Matricial approaches for spatio-temporal control of light in multiple scattering media

Mickaël Mounaix

THÈSE DE DOCTORAT
DE L'UNIVERSITÉ PIERRE ET MARIE CURIE

Spécialité : Physique

École doctorale : "Physique en Île-de-France"

réalisée au :

Laboratoire Kastler Brossel

Présentée par

Mickaël MOUNAIX

Pour obtenir le grade de

DOCTEUR de l'UNIVERSITÉ PIERRE ET MARIE CURIE

Sujet de la thèse :

Matricial approaches for spatio-temporal control of light in multiple scattering media

Soutenue publiquement le 08 novembre 2017

devant le jury composé de :

Prof.	ČIŽMÁR	Tomas	Rapporteur
Dr.	QUÉRÉ	Fabien	Rapporteur
Dr.	BRASSELET	Sophie	Examinateur
Prof.	FINK	Mathias	Examinateur
Prof.	MOSK	Allard	Examinateur
Prof.	GIGAN	Sylvain	Directeur de thèse

Abstract

Optical imaging through highly disordered media such as biological tissue or white paint remains a challenge as spatial information gets mixed because of multiple scattering. Nonetheless, spatial light modulators (SLM) offer millions of degrees of freedom to control the spatial speckle pattern at the output of a disordered medium with wavefront shaping techniques. However, if the laser generates a broadband ultrashort pulse, the transmitted signal becomes temporally broadened as the medium responds disparately for the different spectral components of the pulse.

We have developed methods to control the spatio-temporal profile of the pulse at the output of a thick scattering medium. By measuring either the Multispectral or the Time-Resolved Transmission Matrix, we can fully describe the propagation of the broadband pulse either in the spectral or temporal domain. With wavefront shaping techniques, one can control both spatial and spectral/temporal degrees of freedom with a single SLM via the spectral diversity of the scattering medium. We have demonstrated deterministic spatio-temporal focusing of an ultrashort pulse of light after the medium, with a temporal compression almost to its initial time-width in different space-time position, as well as different temporal profile such as double pulses. We exploit this spatio-temporal focusing beam to enhance a non-linear process that is two-photon excitation. It opens interesting perspectives in coherent control, light-matter interactions and multiphotonic imaging.

Keywords: scattering media, multiple scattering, wavefront shaping, ultrashort pulse, femtosecond laser, spatial light modulator, spatio-temporal focusing, pulse shaping, non-linear imaging.

Résumé

L'imagerie optique à travers des milieux diffusants, comme des milieux biologiques ou de la peinture blanche, reste un challenge car l'information spatiale portée par la lumière incidente est mélangée par les évènements multiples de diffusion. Toutefois, les modulateurs spatiaux de lumière (SLM) disposent de millions de degrés de liberté pour contrôler le profil spatial de la lumière en sortie du milieu, en forme de tavelure (speckle), avec des techniques de modulation du front d'onde. Cependant, si le laser génère une impulsion brève, le signal transmis s'allonge temporellement, car le milieu diffusant répond différemment pour les diverses composantes spectrales de l'impulsion.

Nous avons développé, au cours de cette thèse, des méthodes de contrôle du profil spatio-temporel d'une impulsion brève transmise à travers un milieu diffusant. En mesurant la Matrice de Transmission Multi-Spectrale ou Résolue-Temporellement, la propagation de l'impulsion peut être totalement décrite dans le domaine spectral ou temporel. Avec des techniques de manipulation du front d'onde, les degrés de libertés spectraux/temporel peuvent être ajustés avec un unique SLM via la diversité spectrale du milieu diffusant. Nous avons démontré, de manière déterministe, la focalisation spatio-temporelle d'une impulsion brève après propagation dans un milieu diffusant, avec une compression temporelle proche de la durée initiale de l'impulsion, à différentes positions de l'espace-temps. Nous avons également démontré un façonnage contrôlé du profil temporel de l'impulsion, notamment avec la génération d'impulsions doubles. Nous exploitons cette focalisation spatio-temporelle pour exciter un processus optique non-linéaire, la fluorescence à deux photons. Cette approche ouvre des perspectives intéressantes pour le contrôle cohérent, l'étude de l'interaction lumière-matière ainsi que l'imagerie multi-photonique.

Mots-clés: milieux diffusants, diffusion multiple, façonnage du front d'onde, impulsion brève, laser femtosconde, modulateur spatial de lumière, focalisation spatio-temporelle, façonnage d'impulsions brèves, imagerie non-linéaire.

Contents

Introduction

Who has never dreamed of seeing through walls, or through the fog? Such opaque materials usually appear white to the human eye, as most of the light is back-reflected uniformly over the spectrum. For instance, a thick cloud (from an upcoming storm) appears white on a satellite view (i.e. sunlight back-reflected on the cloud), and dark from the Earth's surface. The latter effect is not due to light absorption, but as few photons are transmitted through the cloud, because of *scattering* effects. On a microscopic scale, when light hits a *scatterer*, an object whose size is on the order of the illumination wavelength, with a different refractive index than the medium's, its direction of propagation is affected by the interaction, and part of the energy is deviated. The typical length on which a significant proportion of the energy is scrambled by scattering effects, the *transport mean free path* $l^\star$, is approximately 10 μm for a sheet of paper for example [Badon et al., 2016]. If the sample thickness is much lower than $l^\star$, scattering effects can be neglected: most of the light propagates in the forward direction. Nonetheless, if the sample thickness is much larger than $l^\star$, light is then strongly scattered: only a small fraction of the energy is transmitted through the scattering medium, while the rest of the energy is back scattered.

Let's consider only a static scattering sample that is not absorptive, such as a white sheet of paper. The distribution of the scatterer's positions is fixed. Under illumination of coherent light, from a laser source for instance, transmitted light takes the form of a spatial random distribution, also known as *speckle* pattern. In essence, it is the result of interferences between a huge number of "optical paths" that light can follow within the scattering medium. This pattern can then be predicted by solving the wave equation: however it would require the exact knowledge of both the position and optical properties of all the scatterers. In practice, this problem is unsolvable. Nonetheless, statistical properties of transmitted light, such as its average intensity and probability distribution of intensity, have been extensively studied over the last 40 years [Goodman, 1976].

Light scattering is usually seen as a detrimental and inevitable process, whether for imaging or for information transfer purposes. Nonetheless, scattering of light is a deterministic and linear process: it can thus be coherently manipulated. *Active wavefront shaping* of light has emerged as a promising tool to control scattered light over the last 10 years, with the use of spatial light modulators (SLM) [Mosk et al., 2012, Vellekoop, 2015, Rotter and Gigan, 2017]. The first experimental demonstration was performed in 2007 [Vellekoop and Mosk, 2007]. In this seminal paper, continuous wave (CW) light was propagating through a thick layer of white paint. The authors demonstrated an enhancement of the light intensity by 3 orders of magnitude in a single output spatial position, via a feedback control between the intensity at the target position and the spatial shape of incident light modulated by the SLM (See Figure 1).

This pioneer work has opened the way for investigating light control in scattering materials, leading to the first experimental measurement of the optical transmission matrix

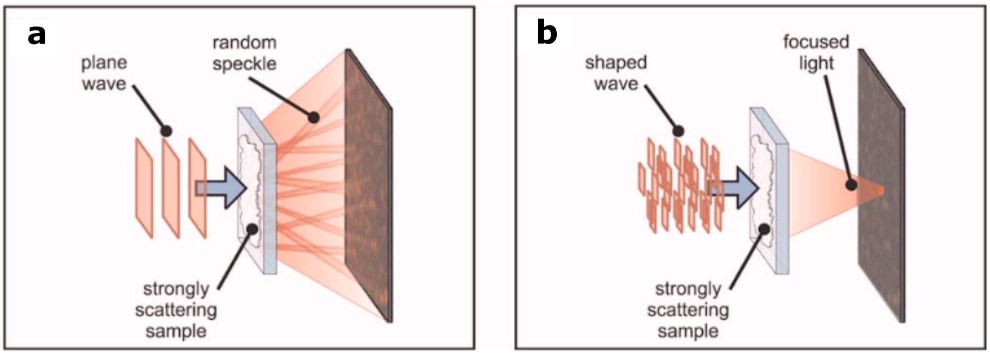

Figure 1 – First wavefront shaping experiment with CW light. (a) Upon a plane wave illumination, transmitted light through a thick layer of white paint takes the form of a random speckle. **(b)** Wavefront shaping the incident beam enables light focusing after propagation through the scattering medium. Image adapted from [Vellekoop and Mosk, 2007]

with CW light [Popoff et al., 2010b]. This operator relates the output field, measured with holographic methods on a CCD camera, directly to the input optical field on the SLM, without *a priori* knowledge of the scattering medium. It has been used, for instance, to focus light [Popoff et al., 2010b] or to transmit images [Popoff et al., 2010a] through the scattering medium. Over the last decade, the wavefront shaping community has also applied different techniques to exploit multiple scattering media, under CW light illumination, as a controllable platform in polarization [Guan et al., 2012], orbital angular momentum [Fickler et al., 2017], and also quantum information [Defienne et al., 2016] with photon pairs.

Temporal control of an ultrashort pulse of light, of large spectral bandwidth, has also been investigated [Mosk et al., 2012]. Multiple scattering effects tends to elongate the pulse duration at the output of the scattering medium, in addition to spatial distortions of light, as each spectral component can generate a different speckle pattern. This spatio-temporal coupling performed by the scattering medium results in a complex spatio-temporal speckle pattern. Different approaches were proposed to perform *spatio-temporal focusing* by exploiting only the spatial degrees of freedom of a single SLM. It consists in focusing light in a single spatial speckle grain, while ensuring that the temporal profile in this specific position has the same ultrashort duration than the input pulse. Spatio-temporal focusing was performed using methods such as feedback-based algorithms based on either a nonlinear optical process [Katz et al., 2011, Aulbach et al., 2012b] or a time-gated signal [Aulbach et al., 2011], and frequency-resolved measurements [McCabe et al., 2011]. More recently, a transmission matrix approach was proposed to adjust the different spectral components, but temporal control of the output pulse was still elusive [Andreoli et al., 2015].

In this context, the objective of this thesis has been to develop a transmission matrix approach to control the spatio-temporal profile of a transmitted ultrashort pulse, through a thick scattering material (See Figure 2). We experimentally demonstrate spatio-temporal control, in particular focusing of the output pulse almost back to its initial duration, with different transmission matrix methods either in the spectral domain, or directly in the temporal domain. We then exploit the developed methods to enhance a non-linear process at the output of the scattering medium, where the low power per speckle grain inherently limits such interactions.

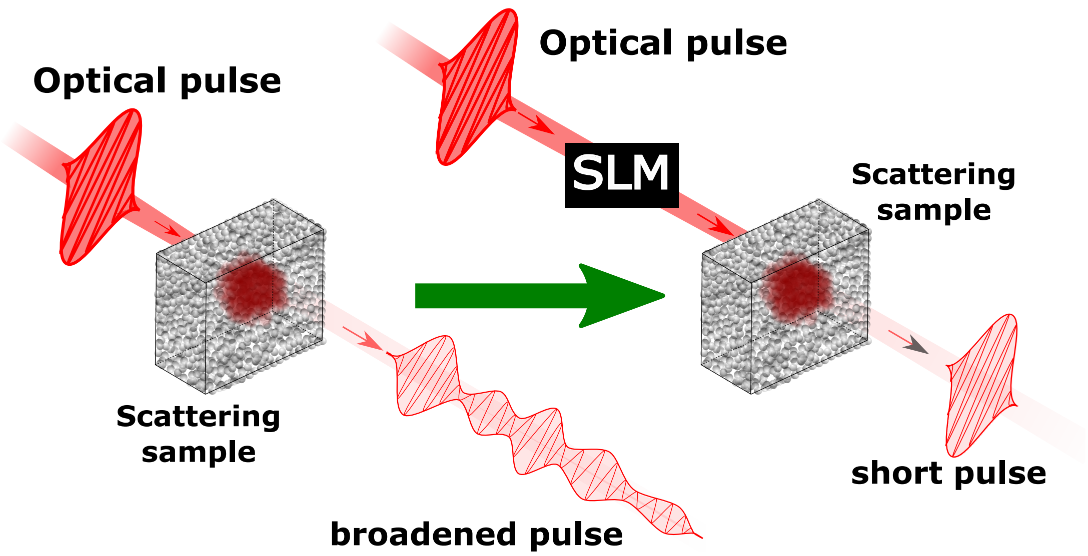

Figure 2 – Extension of wavefront shaping to the temporal control of an ultrashort pulse through scattering media. **(Left)** An ultrashort pulse is propagating through a thick scattering sample. Temporal profile of the transmitted pulse is significantly broadened because of scattering effects.**(Right)** A spatial-only control of the input pulse, via a spatial light modulator (SLM) enables temporal recompression of the output pulse almost back to its initial duration. **In this thesis**, we develop different transmission matrix approaches to compute the corresponding pattern to be displayed on the SLM.

This thesis is organized as follows:

- In Chapter 1, we introduce the background of light propagation in multiple scattering media, for both CW light and an ultrashort pulse. We then describe the state-of-the-art wavefront shaping techniques, to control light in such complex media.

- In Chapter 2, we describe the experimental setup that was conceived in the context of this thesis. In particular, we detail the spatial light modulator properties, as well as the scattering samples that we fabricated, the characteristics of the laser source, and the protocol to simply probe the temporal profile of the spatio-temporal speckle.

- In Chapter 3, we characterize and exploit the Multi-Spectral transmission matrix (MSTM) of the scattering medium. This 3D tensor is a stack of monochromatic transmission matrices, for all the different spectral components of an ultrashort pulse. Once the MSTM is experimentally measured, we exploit it to perform spatio-temporal focusing. We then combine the scattering medium in conjunction with the SLM and the MSTM, to develop a deterministic pulse shaper able to go beyond mere spatio-temporal focusing.

- In Chapter 4, we report the first measurement of the Time-Resolved transmission matrix (TRTM) of the scattering medium, under illumination of an ultrashort pulse of light. This 3D tensor is, by definition, a stack of time-gated transmission matrices, measured at different arrival times of photons after propagation through the scattering medium. We exploit this operator for deterministic spatio-temporal focusing, in arbitrary position in space and time.

- In Chapter 5, we describe an alternative transmission matrix approach, that we coin Broadband transmission matrix (BBTM). In contrast with the above TRTM approach, the BBTM is measured with a self-referencing protocol, rather than using an external reference arm. Although such protocol cannot allow complete spatio-temporal focusing, we interestingly demonstrate a two-fold temporal recompression upon focusing in a single spatial speckle grain, compared with the natural temporal broadening of the output pulse.

- In Chapter 6, we investigate how the different transmission matrix approaches developed in this thesis, allow to excite a non-linear process: two-photon emission fluorescence. We demonstrate enhancement of the non-linear signal upon spatio-temporal focusing. We finally present a point-scanning image of fluorescent beads.

Chapter 1

Light propagation and control in complex media

Contents

In this chapter, we introduce the background of light scattering in disordered media [Rotter and Gigan, 2017]. Upon propagation in heterogeneous media, light interacts with its environment. Transport of light in such a material is complex; nonetheless averaged quantities can be extracted using a diffusion model. Scattering and absorption of light are usually considered as obstacles, typically in microscopy as light gets scrambled during propagation: photons that have not been scattered - ballistic photons - are exponentially attenuated, thus almost inexistent up at depth [Psaltis and Papadopoulos, 2012, Merali, 2015].

After discussing light propagation in free space and with optical aberrations in Section 1.1, properties of scattered light are studied in Section 1.2. Control of monochromatic light through disordered materials is presented in Section 1.3. Propagation of ultrashort pulses is introduced in Section 1.4, and precedes spatio-temporal control of ultrashort pulses in scattering media in Section 1.5.

1.1 Light propagation in free space and with optical aberrations

1.1.1 The easiest scenario: homogeneous media, and the limit of ray optics

When light propagates through an homogeneous medium, ray optics, also known as geometrical optics, provides the means to understand most of common phenomenon. Light is represented as arrows whose tip points in the direction of propagation of its energy. Snell-Descartes laws have been integrated in ray optics. Indeed, when light encounters an interface corresponding to a change of refractive index, graphical methods enable us to find the transmitted direction of propagation, that is valid to explain physical phenomena such as mirage or total internal reflection. Parallel arrows, representing a plane wave, converge to a single point after propagation through a lens, at a distance that is the focal lens away from the lens. This naive representation is sufficient to find both the position and the magnification of the image of a corresponding object with standard optical elements such as lenses or mirrors.

Geometrical optics reaches its limits when the wave nature of light has to be taken into account, such as for interference or diffraction phenomena. Indeed, a focus spot is no longer a single point as ray optics laws would suggest, but a central lobe of diameter d surrounded by concentric disks. This diffraction figure, for a circular aperture, is known as an Airy disc [Born and Wolf, 2013] and its characteristic diameter d reads:

$$d \simeq \frac{1.22\lambda}{2\mathrm{NA}} \tag{1.1}$$

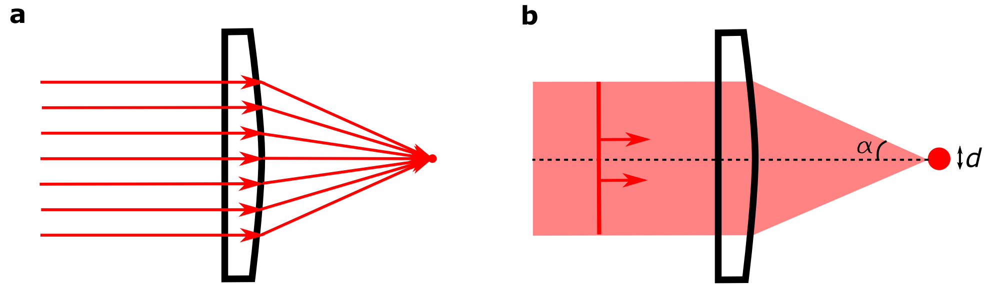

Figure 1.1 – Diffraction-limited spot. Focusing light with a lens. **(a)** Using ray optics, parallel arrows represent an incoming plane wave. The achieved spot has an infinitely small width. **(b)** In reality, for a perfect lens, the spot width is diffraction-limited, with a diameter d

with λ the illumination wavelength, and NA= $n\sin(\alpha)$ the numerical aperture of the lens, defined with n the refractive index of the medium, and α the maximum angle of collection of light as illustrated in Figure 1.1.

Diffraction impacts the resolution of an optical system. Resolution is determined by the size of the focus. Optical reciprocity ensures resolution is diffraction-limited. Therefore, imaging of two incoherent point objects produces an overlapping of diffraction patterns, that might be not resolved depending on their relative distance or angle. Resolution criteria have been proposed, such as Rayleigh's where the first diffraction minimum of the image of one source point coincides with the maximum of another. These criteria do not overcome the diffraction limit, as they are all related to d of Equation 1.1. Nonetheless, a perfect optical imaging system should be able to reach, in principle, this limit.

The Point-Spread Function (PSF) is defined as the image of a point-source by an optical imaging system. In other terms, it describes the impulse response of the imaging system. In general, the PSF depends both on the spatial coordinates in the imaging plane, and the frequency ω. For example, for an isoplanatic system under coherent illumination, the imaging field E_{im} is the convolution of geometrical image $E_{geom.im}$ with the PSF [Goodman, 2005]:

$$E_{im} = aE_{geom.im} * \text{PSF} \tag{1.2}$$

with a a constant term, that depends both on the transmission and on the absorption of the imaging system as well as on the object radiance, and $*$ the convolution operation. A circular aperture PSF is an Airy disc, as in Equation 1.1.

The resolution of an optical system is therefore defined by the width of its PSF, which in practice is usually limited by diffraction. Over the last decades, researchers have been developing *super-resolution* microscopy techniques to overcome this intrinsic diffraction limit, exploiting for example structured illumination [Gustafsson, 2000, Kner et al., 2009, Chaigne et al., 2016], fluorescence [Hell and Wichmann, 1994, Betzig et al., 2006, Dickson et al., 1997] or near field [Harootunian et al., 1986].

1.1.2 Optical aberrations

Paraxial approximation, which consists in using only incoming light close to the optical axis, allows for linearization of propagation equations, which then enables the use of a matrix approach for describing an optical element. However, Snell-Descartes laws cannot be linearized for beams far away from the optical axis of a spherical lens: these beams will converge to different positions, which will tend to widen the PSF: the focus is aberrated.

Optical aberrations can be classified in two different classes: *monochromatic* and *chromatic* aberrations. Chromatic aberrations emerge when optical properties of the medium depend on the wavelength, such as dispersion which quantifies the dependence of the refractive index of the medium with incident frequency. Light composed of different wavelengths will follow different optical paths, and will consequently be focused in different positions. On the other hand, when optical aberrations distort monochromatic light, such as astigmatism, field curvature or tilt, these effects are coined monochromatic aberrations. Mathematically, they can be modeled by Zernike polynomials of different orders [Noll, 1976]. In practice, they induce a small deformation of the incoming beam spatial phase (also known as *wavefront*) during propagation. A direct consequence is a degradation of the PSF, blurring the obtained image according to Equation 1.2.

Furthermore, erratic changes of the medium's refractive index, for example from a change of temperature or due to atmospheric turbulence, stand as obstacles for imaging, as they cannot be predicted and they are time-dependent. Therefore a passive optical control cannot correct these aberrations. In the middle of the 20^{th} century, Babcock proposed an optical setup for correcting atmospheric distortion of light, based on deformable actuators and a wavefront sensor. He named it *astronomical seeing* [Babcock, 1953]. Nowadays this topic, commonly named *Adaptive Optics* (AO), is widely used. In the following, we present AO in astronomy: this technique is implemented in most of the telescopes [Roddier, 1999, Tyson, 2015]. We also present AO for microscopy, which was inspired by astronomy to clear measured images from aberrations [Booth, 2014, Ji, 2017].

Adaptive Optics for astronomy

Adaptive optical astronomy measures in real-time how the atmosphere distorts propagation of light [Roddier, 1999, Tyson, 2015]. Figure 1.2a illustrates a typical setup. Initially, light coming from a reference star, a *guide star*, which acts as a point source, is collected in the telescope. This reference star can either be a natural star or an artificial star. Artificial stars can be created by sending a powerful laser beam, that is either back-scattered by the upper layer of the atmosphere or exciting fluorescence of the mesosphere sodium layer.

A distorted wavefront $\Delta\varphi(x, y)$ is usually measured using a wavefront sensor such as a Shack-Hartmann [Platt and Shack, 2001]. It is composed of a 2D lenslet array, and a camera located at the focal distance. A perfect plane wave from a point source imaged with this sensor system leads to a reference focus array. Displacements of this focus array due to local tilt enable the reconstruction of the wavefront. Correcting the wavefront consists in shaping a deformable mirror, which is located in the conjugate plane of the wavefront sensor, by $-\Delta\varphi(x, y)$, in order to compensate for the reference wavefront in the wavefront sensor. This process is usually named *phase conjugation*. Quality of the achieved correction depends mostly on two parameters. Firstly, the accuracy of the

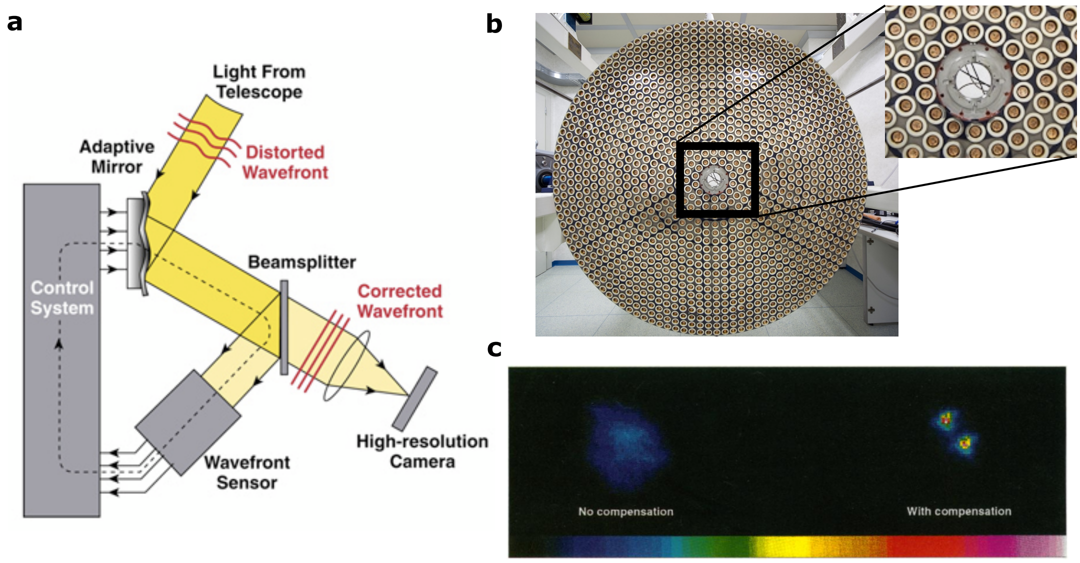

Figure 1.2 – Adaptive optics for astronomy. (a) Principle of adaptive optics in astronomy. The distorted wavefront is measured in real time with a wavefront sensor, connected via a feedback loop to the deformable mirror, blurred by atmospheric turbulence. They adjust correspondingly the wavefront. (Image adapted from Center for Adaptive Optics, UC Santa Cruz) **(b)** Example of a deformable mirror, diameter 1.1m, used for astronomy in the Very Large Telescope in Chile, composed of around 1000 actuators (Image: European Southern Observatory) **(c)** Image of a double star with the Come-on-Plus system on the European Southern Observatory. Turning on the adaptive optics algorithm permits to resolve the binary star, that is initially blurred (adapted from [Hubin and Noethe, 1993])

measurement of $\Delta\varphi(x, y)$ is critical: it depends strongly on the wavefront sensor quality and on the image. Secondly, the process to display the phase conjugate of $\Delta\varphi(x, y)$ on the deformable mirror is mostly limited by the number of actuators. Most of adaptive optical telescopes contain between 10 and 1000 actuators. Figure 1.2b illustrates one of the biggest deformable mirror, containing 1170 elements. Progress in adaptive optical astronomy has enabled astronomers to resolve binary star systems [Hubin and Noethe, 1993], as shown in Figure 1.2c, and the discovery of exoplanets [Serabyn et al., 2010].

Adaptive Optics for microscopy

Similarly, in microscopy, optical aberrations limit the resolution of an optical system. Measuring the imaging system PSF indicates if the system is diffraction-limited or subject to optical aberrations. However it usually requires a point source inside the medium: a guide star. For biological tissues, it can either be fluorescence excitation of an embedded fluorescent bead [Azucena et al., 2011] or from two-photon fluorescence emission from the sample confined in a small volume [Wang et al., 2014]. The deformable mirror adjusts the distorted wavefront to decrease the PSF to the diffraction-limit. Optical aberrations are then corrected: performance of the imaging system can be optimized. These techniques, called *Adaptive optical microscopy*, have improved quality of fluorescence microscopy over the last decade [Booth, 2014, Sinefeld et al., 2015, Ji, 2017], and they correct both aberrations from optical elements and from weak changes of the medium's refractive index.

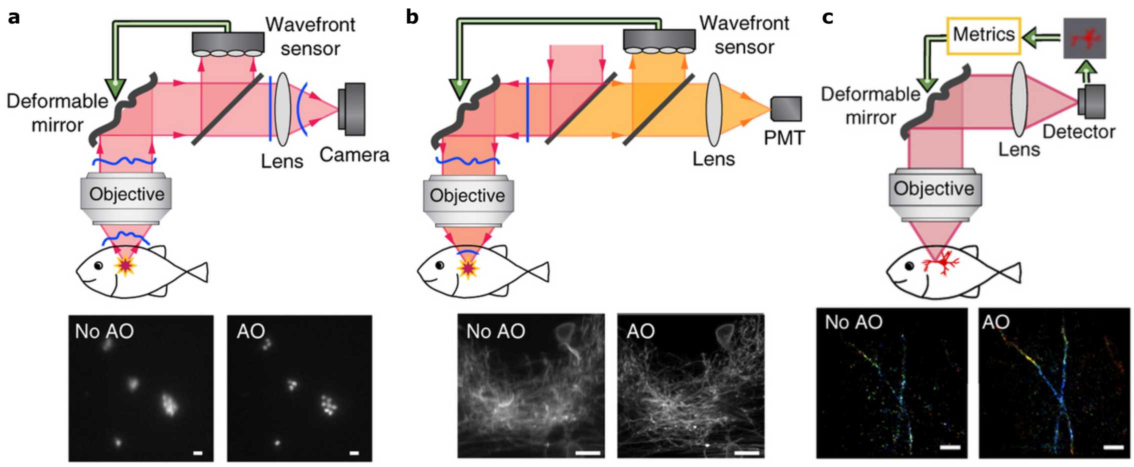

Figure 1.3 – Adaptive optics for microscopy. Top: methods used to adapt the shape of deformable mirrors, to get rid of optical aberrations. Bottom: Corresponding images obtained without adaptive optics (AO) and with AO. **(a, b)** Direct wavefront-sensing-based AO to clear the image of **(a)** beads inside a *Drosophila* embryo implemented in a widefield fluorescence microscope and of **(b)** neurons in *Zebrafish* brain with a two-photon microscope. **(c)** AO without wavefront sensor: a metric-based optimization algorithm converges to clean the image of microtubules. Images are adapted from [Ji, 2017]

Two main approaches have been developed, based on either directly measuring the wavefront, or with an indirect wavefront sensing.

- Figure 1.3a and Figure 1.3b illustrate adaptive optical microscopy with a feedback loop, involving a wavefront sensor and deformable actuators. In Figure 1.3a, the microscope configuration is *widefield*: fluorescence emitted from the guide star propagates through the sample before being imaged on both a camera and a wavefront sensor. In Figure 1.3b, the microscope configuration is *point-scanning*: input light from a laser source is focused on a small volume. However, the input light encounters aberrations and the focus is no longer diffraction-limited. Two-photon fluorescence emitted from the focus volume is collected, and it is analyzed by the wavefront sensor. In both examples, optical aberrations are minimized with the deformable mirror, which improve the contrast of acquired images [Azucena et al., 2011, Wang et al., 2014].

- Figure 1.3c presents an adaptive optical microscopy setup without a wavefront sensor. Aberrations are minimized with a metric to optimize, such as contrast measured on a camera or brightness of total fluorescence measured on a detector. The detector is then directly connected to the deformable mirror with an iterative optimization algorithm [Débarre et al., 2009, Burke et al., 2015].

Such techniques have shown to be efficient in resolving small structures, such as neuronal networks of a mouse cortex up to a depth of 450 μm [Ji et al., 2012], that are normally blurred because of optical aberrations. Similarly to AO for astronomy, the quality of the correction depends on the quality of the deformable mirror, more precisely its number of actuators. This number is approximately the number of Zernike modes on which the linear combination of aberrations can be decomposed in, which is usually on the order of 10-100. AO is thus efficient only in the weak aberration regime. When going deeper in tissue, light encounters stronger heterogeneities of the refractive index. This light scattering outperforms the capacities of adaptive optics, as it requires the control of a much higher number of modes.

1.2 Light propagation in scattering media

Visible light strongly interacts with matter; photons traveling through heterogeneous media are thus carrying information from this interaction. Light gets scattered whenever it encounters an obstacle. The scattering process depends then on the nature of the obstacle, and the heterogeneity of the medium. Usually, *complex media* refers to a medium with a huge number of scatterers (on the order of millions/billions) randomly distributed in a given volume. Light can also be absorbed by the medium. This irremediable loss of energy could come from excitation of a radiative process such as fluorescence, or non-radiative mechanisms such as heat transfer.

In the following, we only consider coherent elastic scattering: both incident and scattered waves have the same optical frequency (wavelength), and a proper phase relationship. Absorption and inelastic scattering, such as fluorescence, are not considered.

Light behavior can be conveniently described by Mie's theory [Mie, 1908] when the obstacle has typical dimensions a compared to the wavelength of light λ. For $a \gg \lambda$, light is usually forward scattered, but if the scatterer size decreases, light radiation becomes more isotropic. A really small scatterer, corresponding to $a \ll \lambda$, is described by Rayleigh's theory of scattering. This theory explains, for instance, the blue color of the sky as light is scattered by gas molecules from the atmosphere.

In essence, transport of light through scattering media can be described at three different scales [van Rossum and Nieuwenhuizen, 1999] that are summarized in Table 1.4:

- <u>Microscopic</u>: Phenomena on a scale $\sim \lambda$ are described by a wave equation, resulting from Maxwell's equations. However, solving wave equation cannot be achieved simply because of the complex structure of the scattering medium: the refractive index map is almost impossible to describe properly.
- <u>Mesoscopic</u>: On a scale of the *transport mean free path* (a microscopic quantity that we will define precisely later), light transport is described by the radiative transfer equation.
- <u>Macroscopic</u>: On a scale much larger than the transport mean free path, the transport equation and diffusion approximations govern the behavior of averaged quantities, such as intensity.

The theory of light scattering draws an analogy with electronic transport in random potentials [Lagendijk and van Tiggelen, 1996, Akkermans and Montambaux, 2007]. Nonetheless this analogy breaks down when looking at the vectorial properties of light, such as polarization [Rotter and Gigan, 2017].

In this Section, we will describe briefly the relevant microscopic quantities that deal with mesoscopic and macroscopic effects. We then add coherent effects that survive multiple scattering effects: under illumination of coherent light, a speckle pattern is observed

Scale	**Microscopic**	**Mesoscopic**	**Macroscopic**
Illustration	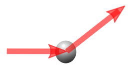	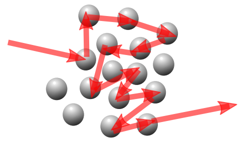	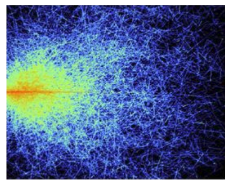
Physical description	Single scattering	Multiple scattering	Transport properties
Typical length scale	Size of scatterers	Scattering / Transport mean free path $l_s, l^\star$	Dimension of the medium L

Table 1.1 – From microscopic to macroscopic scattering. Light scattering on different scales. On a microscopic scale, light (red arrow) is scattered by an obstacle (sphere). Direction of propagation and amplitude can be calculated from the scatterer's properties. Typical scale is the scatterer size, as well as the mean distance between scatterers. On a mesoscopic scale, multiple scattering is occurring. Typical scales are the scattering (l_s) and the transport ($l^\star$) mean free paths. In the macroscopic regime, averaged intensity properties are ruled by $l^\star$ in a medium of thickness L$\gg l^\star$. Illustration of macroscopic scattering adapted from [Pierrat et al., 2014]

after propagation through a scattering sample. We finally introduce the Scattering matrix (S-matrix) formalism which contains information between the input field and the corresponding transmitted and reflected fields by the scattering media.

1.2.1 Diffusion transport: radiative transport equation

Although scattering media exhibit strong heterogeneities regarding their distribution of scatterers, light propagation in such complex systems is, in theory, governed by the wave equation. The medium is defined by its dielectric function, which is position-dependent. Therefore, solving Maxwell's equation requires the exact knowledge about the structure of the medium. Such an accuracy is almost impossible to achieve experimentally. Numerically, it is demanding in computation time for simulations, which would require a large amount of memory. Analytical solutions are then limited to very small systems.

A convenient way to approach this problem is to develop a transport equation from the wave equation. It implies neglecting the wave character of light, and only considering intensity of the electric field. The transport equation takes the form of the the radiative transport equation (RTE) [Chandrasekhar, 2013]. Notwithstanding, wave effects can be included in the RTE [Lagendijk and van Tiggelen, 1996]. When considering coherent scattering, mesoscopic effects can be described such as coherent back scattering [Wolf and Maret, 1985, Akkermans et al., 1986], or phase transition to Anderson localization [Anderson, 1958, Lagendijk et al., 2009, Segev et al., 2013]. Those very important mesoscopic effects stand beyond the scope of this manuscript.

Radiative transport of light describes transport of a flux of photons. The specific intensity $I(\mathbf{r}, \mathbf{u})$ is the average power flux density emitted at a position $\mathbf{r}$ in a direction $\mathbf{u}$ in a system with a density n of scatterers. The specific intensity is directly connected to the radiation energy [Ishimaru, 1999].

Here, we only consider the stationary situation with monochromatic light. A more advanced theory on radiative transport of light can be found in [Ishimaru, 1999]. The specific intensity only depends on the distance of propagation s and the direction of emitted radiation θ. The stationary radiative transfer equation establishes the evolution of the specific intensity $I(\mathbf{r}, \mathbf{u})$ with propagation over a small length ds [van Rossum and Nieuwenhuizen, 1999]:

$$\frac{\mathrm{d}I(\mathbf{r}, \mathbf{u})}{\mathrm{d}s} = n\sigma_{\mathrm{ex}}\Big[-I(\mathbf{r}, \mathbf{u}) + J(\mathbf{r}, \mathbf{u})\Big] \tag{1.3}$$

σ_{ex} is the extinction cross section. In essence, it describes a loss of intensity because of scattering and absorption. These two effects can be treated separately with their own cross sections for scattering σ_{s} and for absorption σ_{a}, leading to $\sigma_{\mathrm{ex}} = \sigma_{\mathrm{s}} + \sigma_{\mathrm{a}}$. In the following, we consider a medium where absorption is negligible: $\sigma_{\mathrm{a}} \ll \sigma_{\mathrm{s}}$. A characteristic length can be extracted from σ_{s}: the scattering mean free path l_s.

$$l_s = \frac{1}{n\sigma_{\mathrm{s}}} \tag{1.4}$$

It gives the average path length between two scattering events, while the average mean distance between two scatterers is given by $\sqrt[3]{n}$. Evolution of the specific intensity during propagation depends on two terms according to Equation 1.3:

- $-n\sigma_{\mathrm{ex}}I(\mathbf{r}, \mathbf{u})$ is a loss term due to scattering in other directions than $\mathbf{u}$ and absorption if not neglected.
- $n\sigma_{\mathrm{ex}}J(\mathbf{r}, \mathbf{u})$ is a gain term. $J(\mathbf{r}, \mathbf{u})$ is the *source function*: it describes radiation arriving from another direction $\tilde{\mathbf{u}}$ and scattered in direction $\mathbf{u}$. It can be derived from the specific intensity [van Rossum and Nieuwenhuizen, 1999], but we are not discussing it.

Scattering regimes

For an unidirectional beam, of direction $\mathbf{u}_0$, the loss term of Equation 1.3 leads to an exponential decay of the specific intensity over $\mathbf{r}$:

$$I(\mathbf{r}, \mathbf{u_0}) = I(\mathbf{0}, \mathbf{u_0}) \exp\left(-|r|/l_s\right) \tag{1.5}$$

This so-called Beer-Lambert law explicits the exponential decay of *ballistic* photons, that have not suffered from scattering. The decay is governed by the scattering mean free path if absorption is neglected. Three different scattering regimes are dictated by the ratio between l_s and the thickness of the scattering medium L:

☞ $L \ll l_s$: ballistic regime

☞ $L \sim l_s$: single scattering regime

☞ $L \gg l_s$: multiple scattering regime

Anisotropy

Anisotropy of the scattering process depends only on the direction of emitted radiation θ. The anisotropy factor $g_{\mathrm{aniso.}}$ is defined as the average cosine of emission angle θ of scattered

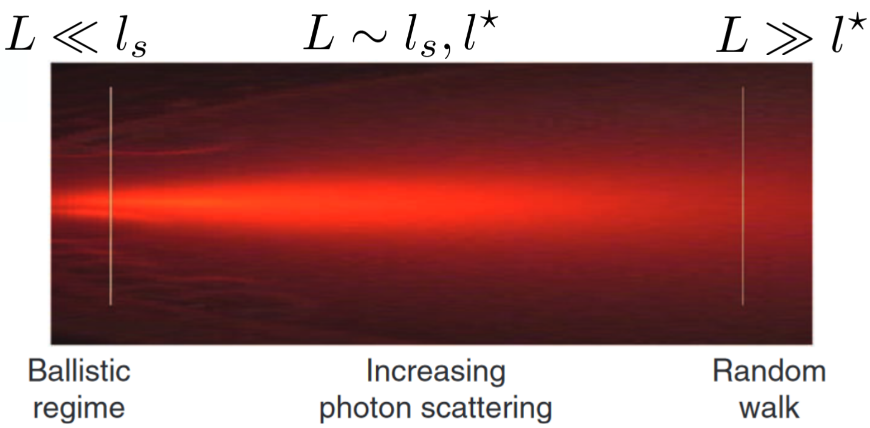

Figure 1.4 – Light propagation in scattering media. Light scattering with increasing thickness of the medium L from left to right at fixed scattering mean free path l_s. In the ballistic regime, light has suffered, in average, less than a scattering event. Increasing L enhances the number of scattering events up to the multiple scattering regime, analogue to a random walk. Image adapted from [Ntziachristos, 2010]

radiation, $g_{\text{aniso.}} = \langle \cos\theta \rangle$. For isotropic radiation $g_{\text{aniso.}}$ is close to 0, whereas for forward scattering $g_{\text{aniso.}}$ is getting close to 1. In biological tissue, $g_{\text{aniso.}}$ takes typically values around 0.9 [Cheong et al., 1990]. The *transport mean free path* $l^\star$ is the mean distance light has to propagate before it loses its initial direction of radiation. $l^\star$ is connected to l_s and to $g_{\text{aniso.}}$, by the following relationship:

$$l^\star = \frac{l_s}{1 - g_{\text{aniso.}}} \tag{1.6}$$

In the multiple scattering regime, transport of light is diffusive, with a diffusion coefficient D, which depends on the energy velocity v_E and the transport mean free path $l^\star$. The diffusion coefficient reads:

$$D = \frac{1}{3} v_E l^\star \tag{1.7}$$

Diffusion in slab geometry

Boundary conditions of the diffusion equation in a slab geometry, that is characterized by its thickness L, leads to the total transmission of light T as a function of L, via the following relationship [van Rossum and Nieuwenhuizen, 1999]:

$$T \sim \frac{l^\star}{L} \tag{1.8}$$

This relationship is the equivalent of Ohm's law for electric conductor. Dependence of T with L enables measurement of $l^\star$ from transmitted light [Genack, 1987, Garcia et al., 1992, Sapienza et al., 2007]. Time-dependence of diffuse transmitted light has also been studied [Patterson et al., 1989]. Another important characteristic quantity of a diffusion process is its characteristic time of diffusion τ_d, related to the Thouless time [Thouless, 1977]. τ_d described the time it takes for the diffusive intensity to leave the scattering medium [Akkermans and Montambaux, 2007]. In other terms, τ_d is the characteristic time when light starts to "feel" the boundaries:

$$\tau_d \sim \frac{L^2}{\pi^2 D} \tag{1.9}$$

Accessing τ_d can be used to extract D or characteristic path length, such as $l^\star$ [Patterson et al., 1989, Thompson et al., 1997]. Once D and $l^\star$ are known, the energy velocity can be estimated with Equation 1.7 [van Albada et al., 1991, Curry et al., 2011].

Wave effects of light were neglected in the RTE. In the following section, we exploit the coherence properties of light. Even though they are not needed to describe transport properties in the diffusive regime, interference effects survive multiple scattering, even in the presence of strong disorder [Goodman, 2007].

1.2.2 Propagation of monochromatic light in scattering media: speckle pattern

In this part we consider monochromatic coherent light propagating through a thick scattering sample. The number of optical modes N_{modes} depends on the size of the illuminated area A and on the wavelength of incident light λ:

$$N_{\text{modes}} \propto \frac{A}{\lambda^2} \tag{1.10}$$

Every mode accumulates a different phase retardation after propagation in the scattering medium, but light keeps its coherence. Transmitted light then results in a very complex interference between all these optical modes. The obtained pattern is called *speckle* [Goodman, 2007]. A typical speckle pattern is illustrated in Figure 1.5a.

The output intensity is not uniform, but has very well defined statistical properties: its probability distribution is spatially varying with an exponential decay. Fluctuation of the speckle intensity δI is equal to the average $\langle I \rangle$: $\langle \delta I^2 \rangle = \langle I \rangle^2$ [Goodman, 2007]. This so-called Rayleigh's law is at the origin of the granular form of the output intensity with strong fluctuations between bright and dark "grains". At the output facet of the medium, the correlation length defines the typical speckle grain size (speckle correlations are defined later in Section 1.2.3). The size of a grain d_{speckle} observed at a distance z depends on the imaging system: it scales as $d_{\text{speckle}} = \lambda z / D_{\text{spot}}$ where D_{spot} is the diameter of the diffusive spot at the output facet [Goodman, 2007]. While we only consider transmitted light in this section, back reflected light from scattering media also gives rise to a speckle pattern [Goodman, 2007].

A bright grain corresponds to a more constructive interference while a dark grain is produced by destructive interference. In essence, the total field in a given output position can be expanded in a superposition of complex phasors [Goodman, 2007], as shown in Figure 1.5b. The speckle is fully developed if the phase distribution of every single phasor is uniformly distributed over 2π. The total field amplitude scales with the magnitude of the sum of phasors. This sum can be related to a random walk because of the very complex distribution of scatterers: every single phasor has acquired an unpredictable phase retardation after propagation through the medium, uniformly distributed over 2π.

Additionally, polarization states are scrambled by propagation through a scattering sample [Yao and Wang, 2000]. The two linear polarization states generate their own speckle

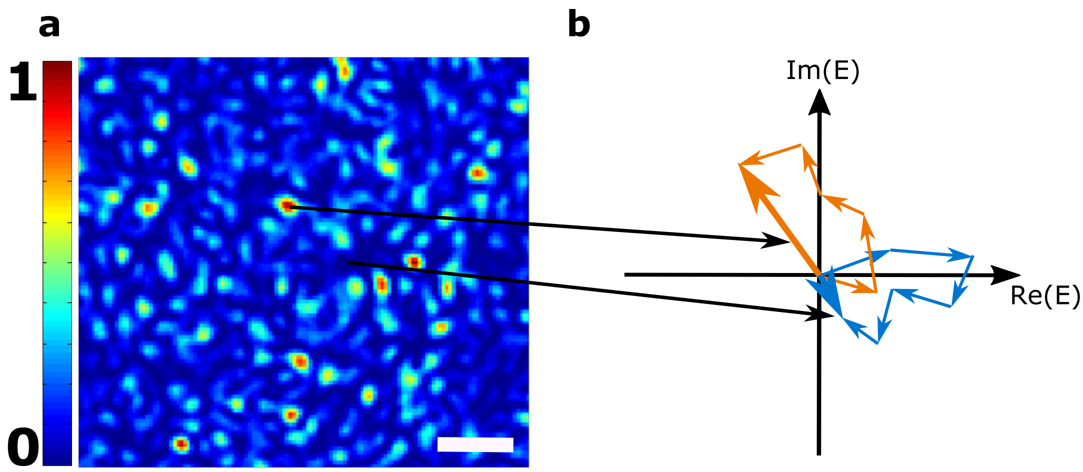

Figure 1.5 – Monochromatic speckle pattern. (a) When monochromatic coherent light is propagating through a scattering medium, interferences between different optical paths give rise to a so-called speckle pattern. In the image: intensity speckle measured with a CCD camera after propagation of continuous wave light through a layer of white paint. Scale bar: 5 μm. **(b)** Simplified representation in the complex plane of the electric field resulting from light scattering in a dark grain (blue) and in a bright grain (orange). Magnitude of the resulting electric field is amplitude of the sum of random phasors.

pattern in the multiple scattering regime. The total output speckle is thus the incoherent sum of these two speckles, resulting in a total speckle of constrast $1/\sqrt{2}$ [Goodman, 2007].

Nonetheless, light scattering is a deterministic process: two different speckle patterns measured at two different times under the same illumination remain identical as long as the medium is *stable* (positions of scatterers stay identical) [Goodman, 1976]. However, tilting the input beam, or illuminating another area of the scattering medium leads to a different and usually uncorrelated speckle pattern. Consequently, the speckle pattern can be coherently modified by adjusting the way light enters the medium. For instance, aligning the sum of phasors will lead to a built-on constructive interference. It should, in principle, enable light that has been multiple scattered to be focused. This light control will be explained in Section 1.3.

1.2.3 S-matrix formalism

Under the assumption of the linearity of the scattering process, the speckle pattern is connected to the input field before propagation through the scattering media. An appropriate tool to describe the relationship between the electric field of incoming light E_{in} and E_{out}, the electric field associated with outgoing scattered photons, is the Scattering-Matrix $\mathbf{S}$, usually named S-Matrix [Rotter and Gigan, 2017], which is defined as:

$$E_{out} = \mathbf{S}E_{in} \tag{1.11}$$

For a slab or a waveguide geometry, which contains two distinct interfaces, light can propagate either from left-to-right (+) or from right-to-left (-). In general, the scattering matrix can be written as:

$$E_{out} = \begin{pmatrix} \mathbf{r} & \mathbf{t'} \\ \mathbf{t} & \mathbf{r'} \end{pmatrix} E_{in} \quad \text{with} \quad E_{in} = \begin{pmatrix} E_{in}^{+} \\ E_{in}^{-} \end{pmatrix} \quad \text{and} \quad E_{out} = \begin{pmatrix} E_{out}^{-} \\ E_{out}^{+} \end{pmatrix} \tag{1.12}$$

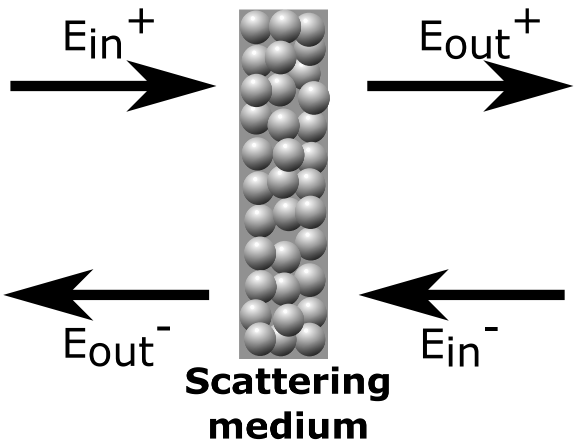

Figure 1.6 – Scattering matrix. Light scattering can be described with the Scattering Matrix $\mathbf{S}$ that gives the relationship between the input field (either on the left side E_{in}^{+} or on the right side E_{in}^{-}) and the output field (either on the left side E_{out}^{-} or on the right side E_{out}^{+})

where E_{in}^{-} (resp. E_{in}^{+}) and E_{out}^{-} (resp. E_{out}^{+}) are illustrated in Figure 1.6. The S-matrix is subdivided in 4 blocks. Submatrices on the diagonal contain the reflection amplitudes for input light coming from the left side ($\mathbf{r}$) and from the right side ($\mathbf{r'}$). On the other hand, the off-diagonal submatrices are composed of transmission amplitudes for light scattering from left to right ($\mathbf{t}$) and from right to left ($\mathbf{t'}$). The S-matrix coefficients are intimately related to Green's functions between all input and output positions [Stöckmann, 2006]. However, the S-matrix does not carry information about evanescent modes, as these do not contribute to the transport of light [Rotter and Gigan, 2017].

The dimensions of the S-matrix are related to the number of propagating modes in the scattering medium. In the literature they are usually referred to as scattering channels [Beenakker, 1997]. The number of modes can be different on the left side (N) and on the right side (M). Reflection matrices are quadratic ($N \times N$ and $M \times M$ for respectively $\mathbf{r}$ and $\mathbf{r'}$) while transmission matrices are rectangular ($M \times N$ and $N \times M$ for respectively $\mathbf{t}$ and $\mathbf{t'}$). $\mathbf{S}$ is thus a squared matrix, of dimension $(N + M) \times (N + M)$.

Experimentally, measuring $\mathbf{S}$ requires one to illuminate the sample on both interfaces, and measure both transmitted and reflected light from all the scattering channels. In optics, the finite numerical aperture of both illumination and detection limits the possibility to detect all the N_{modes} scattering channels [Goetschy and Stone, 2013, Popoff et al., 2014]. An example of full experimental measurement of $\mathbf{S}$ in acoustics is presented in [Gérardin et al., 2014], where N_{modes} is relatively small (22 modes): all the modes can be measured. In practice in optics, only subparts of the full S-matrix are measured, with dimensions significantly lower than N_{modes} [Yu et al., 2013]. Details on the measurement of transmission matrix are explained in Section 1.3.4.

Conservation of energy

Conservation of the energy is included in the scattering matrix $\mathbf{S}$. We suppose an incoming mode on the left side n (a similar approach can be drawn with an incoming mode on the right side). The transmission intensity (resp. reflection intensity) to the outgoing channel m reads $T_{mn} = |t_{mn}|^2$ (resp. $R_{mn} = |r_{mn}|^2$). The total transmission T_n and the total reflection R_n can be then extracted from the S-matrix: $T_n = \sum_{m=1}^{M} T_{mn}$ and $R_n = \sum_{m=1}^{N} R_{mn}$. A scattering process without absorption conserves energy: $T_n + R_n = 1$. This relationship is valid for all the input scattering channels: it implies the scattering matrix will fulfill the unitary condition $\mathbf{S}\mathbf{S}^{\dagger} = 1$ with $\dagger$ the transpose conjugate operation [Rotter and Gigan, 2017].

Transmission/Reflection eigenchannels

Total transmission (resp. total reflection), which reads $T = \sum_n T_n$ (resp. $R = \sum_n R_n$), is also connected to the eigenvalues τ_n (resp. ρ_n) of the matrix $\mathbf{t}^{\dagger}\mathbf{t}$ (resp. $\mathbf{r}^{\dagger}\mathbf{r}$) with the following relationship: $T = \mathrm{Tr}(\mathbf{t}^{\dagger}\mathbf{t}) = \sum_n \tau_n$ (resp. $R = \mathrm{Tr}(\mathbf{r}^{\dagger}\mathbf{r}) = \sum_n \rho_n$) [Rotter and Gigan, 2017]. The distribution of eigenvalues follows, theoretically, a bi-modal with asymmetric distribution for a scattering waveguide [Dorokhov, 1984] if the full matrix $\mathbf{S}$ has been measured. In practice, the distribution of eigenvalues depends strongly on the dimension of the incomplete measured $\mathbf{S}$ [Marčenko and Pastur, 1967, Popoff et al., 2010b, Goetschy and Stone, 2013, Hsu et al., 2017].

Channel of transmission values τ_n and ρ_n are named respectively transmission and reflection eigenchannels. A large eigenvalue τ corresponds to a large transmission eigenchannel, usually named an "open channel", while eigenvalues of low transmission channels are close to 0: they correspond to "closed" channels. The distribution of $\sqrt{\tau_n}$ and $\sqrt{\rho_n}$ can be easily obtained via $\mathbf{t}$ (or $\mathbf{t'}$) and $\mathbf{r}$ (or $\mathbf{r'}$) with a singular value decomposition [Popoff et al., 2010b]. These open and closed channels are hardly impossible to measure in optics because the N_{modes} modes must be accessible [Goetschy and Stone, 2013], but it can be studied using numerical simulations [Choi et al., 2011a]. Open and closed channels have been studied in microwaves [Shi and Genack, 2012, Davy et al., 2015], in acoustics [Gérardin et al., 2014] and in on-chip disordered waveguide optics [Sarma et al., 2016] where N_{modes} is order of magnitude lower (56 modes) than in optical disordered slab. More information on open and closed channels can be found in [Rotter and Gigan, 2017, Shi et al., 2015].

Spatial correlations of transmitted speckle

Although light transmission through a scattering medium looks very complex and disordered, a speckle pattern maintains some statistical correlations in different transmitted modes. Some extensive reviews further detail the physics of these correlations [Berkovits and Feng, 1994, Akkermans and Montambaux, 2007, Rotter and Gigan, 2017].

In their seminal paper, Feng and colleagues discussed how the transmission coefficient T_{mn} from the incoming mode n to the outgoing mode m at a fixed frequency ω is correlated when the distribution of scatterers is randomly changed [Feng et al., 1988]. A meaningful quantity for this study is the correlation function $C_{mnm'n'} = \langle \delta T_{mn} \delta T_{m'n'} \rangle$ where $\delta T_{mn} = T_{mn} - \langle T_{mn} \rangle$ with $\langle T_{mn} \rangle$ the spatially averaged transmission. In essence, this correlation function can be developed at different orders in $1/kl^{\star} \ll 1$:

$$C_{mnm'n'} = C^{(1)}_{mnm'n'} + C^{(2)}_{mnm'n'} + C^{(3)}_{mnm'n'} + \dots \tag{1.13}$$

The first term $C^{(1)}_{mnm'n'}$ is the 0^{th} order of the expansion parameter. Briefly, it describes "short-range" correlations. It is significant especially when incoming and outgoing perpendicular momenta are equal: $C^{(1)}$ correlation is responsible of the granular form of the speckle, as it derives the Rayleigh law $\langle \delta T^2_{mn} \rangle = \langle T_{mn} \rangle^2$ [Feng et al., 1988]. $C^{(1)}$ correlation exhibits also the so-called *memory effect*: a tilt of the incident wavefront results in a shift in the output speckle. This momentum transfer is only available for small angle tilts $\Delta\theta \leqslant \lambda/(2\pi L)$, with L the thickness of the scattering material [Freund et al., 1988]. The memory effect depends on the anisotropy of the scattering media [Schott et al., 2015]. It has also been studied when a shift is applied in the incoming mode instead of a tilt [Judkewitz et al., 2015], or as a combination of both tilt and shift [Osnabrugge et al., 2017]. The memory effect has now been used as a tool for imaging around corners [Freund, 1990], thanks to analysis of speckle autocorrelation [Katz et al., 2012, Bertolotti et al., 2012, Katz et al., 2014a].

The second term $C^{(2)}_{mnm'n'}$ governs "long-range" correlations. Briefly, it indicates correlations for two incoming beams with the same incident direction far apart or for two outgoing scattering channels that are similar [Feng et al., 1988]. $C^{(2)}_{mnm'n'}$ is much smaller than $C^{(1)}_{mnm'n'}$ by a factor $g = \sum_{mn} T_{mn} \sim N_{\text{modes}} l^\star / L$ [Akkermans and Montambaux, 2007]. g is named the conductance, in analogy with the conductance of electron transport [Rotter and Gigan, 2017]. g is an important parameter for mesoscopic light transport [Scheffold and Maret, 1998, Strudley et al., 2013]

The third term $C^{(3)}_{mnm'n'}$ is usually named "infinite-range" correlations, in analogy with the universal conductance fluctuation [Rotter and Gigan, 2017]. It scales as $1/g^2$ in comparison with $C^{(1)}_{mnm'n'}$, which makes it difficult to access, nonetheless achievable [Scheffold and Maret, 1998].

Some other forms of correlations have also been studied. In the presence of a point source inside the scattering medium, some correlations, named $C^{(0)}$ correlations, mainly come from near-field interactions [Shapiro, 1999, Cazé et al., 2010]. Beyond transmission-only correlations, recent works have studied the existence of correlations between reflected and transmitted speckles [Fayard et al., 2015]. Finally, this section was restricted to the monochromatic regime at a fixed frequency. Spectral/temporal effects in the correlation are studied in Section 1.4.3

For most of scattering systems that are studied in this thesis, $g \gg 1$: $C^{(2)}_{mnm'n'}$ and $C^{(3)}_{mnm'n'}$ are then negligible.

If the distribution of scatterers is fixed, light propagation through a thick scattering sample leads to a speckle pattern, that looks very complex but not random: it is a deterministic process. The speckle pattern can be adjusted by controlling the wavefront of incident light. Over the last decade, this control of light propagation has emerged under the name *wavefront shaping*. Its concept is explained in detail in the next Section.

1.3 Control of monochromatic light through scattering media: the opaque lens

Adaptive optics is an efficient method to correct small aberrations, as discussed in Section 1.1.2. It reaches its limit for the strong aberration regime and for light scattering as the number of modes to be controlled, given by Equation 1.10, exceeds the capabilities of deformable mirrors. Recently, spatial light modulators (SLM) have emerged as a tool with millions of degree of freedom, paving the way for extreme adaptive optics: *wavefront shaping*. The first active wavefront shaping experiment in optics was performed in 2007 by Vellekoop and Mosk, to focus monochromatic light through a multiple scattering sample [Vellekoop and Mosk, 2007]. Starting from a speckle pattern, Vellekoop and Mosk demonstrated enhancement of transmitted light intensity in a target position by only controlling the input light, by means of a SLM. This pioneer work has been the inspiration behind much of the research into control of light propagation in scattering media over the last decade, either for focusing purposes or for imaging, that are reviewed in [Rotter and Gigan, 2017, Mosk et al., 2012, Vellekoop, 2015, Shi et al., 2015].

In this Section, the concept of wavefront shaping and the required tools to perform it are first described. We then outline the most common algorithms to control light propagation: iterative optimization algorithms, digital optical phase conjugation, and the optical transmission matrix.

1.3.1 Wavefront modulation and control

While adaptive optical mirrors are limited to a few number of actuators, spatial light modulators (SLM) have turned up as key devices to control light with a huge number of degrees of freedom. Initially conceived for intensity modulation [Konforti et al., 1988], most of SLMs enable phase modulation exploiting more than 10^6 pixels. In this section, we briefly review the main spatial light modulator technologies. Depending on the applications and experimental constraints, SLMs with different speed and accuracy are available. We then provide basics of wavefront shaping techniques based on SLM technology that enable light control over disordered materials.

Spatial Light Modulators

Over the last 20 years, active research on semiconductor technologies has led to devices that can manipulate light: digital spatial light modulators [Savage, 2009]. Most common spatial light modulators are divided in two different categories based on their operating processes: liquid crystal SLM [Lueder, 2010] and micro mirrors SLM [Bifano and Stewart, 2005].

- Liquid Crystal on Silicon-Spatial Light Modulators (LCOS-SLMs) are made of parallel-aligned, or twisted, nematic liquid crystals displayed on a grid of electrodes (around 10^6). The electrodes are deposited on a C-MOS circuit. In their natural state, liquid crystal molecules take the form of sticks oriented parallel to the electrodes, for parallel-aligned LCOS. The liquid crystal state can be tuned by applying a voltage. Liquid crystals molecules are oriented along the propagation direction of light. In essence, the refractive index for light polarized parallel to the liquid crystal molecules changes by an amount $\Delta n(\mathrm{V})$, depending on the voltage V, without any changes in the light intensity and polarization direction. LCOS-SLMs thus provide an efficient phase modulation from 0 to 2π at a given wavelength. Nonetheless, the quantification of addressable voltage induces a staircase approximation, which can limit the efficiency of modulation. LCOS-SLM are usually polarization sensitive.

LCOS-SLMs are mainly limited to slow refresh rate, because of the response time of liquid crystal molecules. Typical rise and fall time of liquid crystal is limiting the frame rate to $\sim$ 10-100 Hz.

- An alternative substitute to LCOS-SLM are Micro-ElectroMechanical-System-SLMs (MEMS-SLMs). This technology is similar to adaptive optical mirrors. MEMS-SLMs are composed of 10μm to 100μm flat movable mirrors. The motion of mirrors can be either translation or rotation achieved with controllable electro-statical forces.

  ☞ Translation motion induces a phase delay and thus a phase modulation from 0 to 2π. In contrast with LCOS-SLMs, the mechanical response of the actuators is typically 10-100μs (Boston Micromachine), corresponding to a refresh rate $\sim$ 10-100 kHz. Nonetheless, the number of actuators is strikingly smaller than LCOS-SLMs ($\sim 10^3$ actuators) and prices are high ($\sim$ 50 k€).

  ☞ Rotation motion can deflect light in two different directions. Digital Micromirror Devices (DMDs) usually have two available states: tilting the mirror (off-state: +12°) to a beam-block or tilting the mirror (on-state: -12°) to let light propagates in the corresponding direction. Light amplitude is then binary modulated.

Technology	**LCOS-SLM**	**MEMS**	**DMD**
Illustration	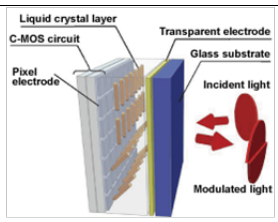	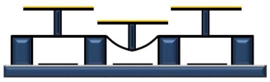	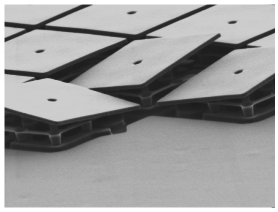
Number of pixels	10^6	10^3	10^5
Speed (Hz)	10^{1-2}	10^4	10^{4-5}
Modulation	Full-phase 0-2π	Full-phase 0-2π	Binary amplitude
Price	10^4 €	10^5 €	10^3 €

Table 1.2 – Comparison of common spatial light modulators (SLM) technologies. Images from : Hamamatsu (LCOS-SLM), Boston Micromachine (MEMS), Texas Instrument (DMD)

Table 1.2 summarizes characteristics of the most common spatial light modulators. Nonetheless, this list is not exhaustive as other SLM technologies exist, such as tip-tilt array (OKOTech) or ferroelectric liquid crystal based SLM (Meadowlark). In principle, both amplitude and phase of light can be controlled with SLMs. Using a phase-only SLM combined with an amplitude-only SLM is not a convenient method as it requires two SLMs and a complex experimental alignment. Some alternative ways have been developed using Fourier optics laws, with complex generated holograms [Arrizón et al., 2007, Conkey et al., 2012b], superpixel techniques [Putten et al., 2008, Goorden et al., 2014] or by exploiting two-pass SLMs [Macfaden and Wilkinson, 2017].

High spatial resolution SLMs are widely used as reconfigurable optical elements in optical microscopy [Maurer et al., 2011], optical manipulation [Čižmár et al., 2010, Padgett and Bowman, 2011, Pesce et al., 2015] and optical information transfer [Gibson et al., 2004].

The high number of degrees of freedom combined with full phase control make LCOS-SLMs convenient tools for beam generation [Conkey et al., 2011, Clark et al., 2016] and pulse shaping [Weiner, 2000] (See Section 1.5.2 for more details on pulse shaping).

Wavefront shaping

In Section 1.2.2, we studied light propagation in scattering media, resulting in a spatial speckle pattern. This speckle is almost impossible to predict because of the complexity of the scattering medium. Nonetheless, light scattering is a deterministic process even for strongly scattering materials. The very complex interference can then be controlled by adjusting phase delays between different optical paths that light follows. In essence, shaping the input wavefront of light deterministically affects the output speckle. Thanks to SLMs, *wavefront shaping* methods have emerged over the last decade to manipulate light propagation in complex media.

Input light is controllable and adjustable by means of a SLM with N_{SLM} degrees of freedom. Light is then propagating with the wavefront patterned on the SLM through the disordered system. Output light (transmitted or reflected by the optical system) is measured with a sensor. A wavefront shaping setup is close to an adaptive optical setup as presented in Section 1.1.2. However, the number of actuators is considerably higher to adjust for scattering effects.

Similarly to adaptive optics, one needs to adjust the N_{SLM} input parameters. Different algorithms have been developed to reach this objective.

- In Section 1.3.2 we present an iterative optimization algorithm. Initially a single input parameter, out of the N_{SLM}, is picked. Modulating this input parameter will influence the output signal, that is measured correspondingly. The input is then set at the position maximizing the output signal. Iteratively, every input parameter is set until the output signal reaches its final maximum value.
- In Section 1.3.3 we present Digital Optical Phase Conjugation (DOPC). Briefly, this method proceeds in two steps: recording the output signal first, and afterwards displaying phase conjugation of the recorded output pattern.
- In Section 1.3.4 we present the optical Transmission Matrix. It consists in measuring a linear matrix relationship between every N_{SLM} input parameters and all the output channels. The displayed input wavefront is then related to the “inversion” of the matrix.

For most of the wavefront shaping experiments, the number of measurements (either iterative or measurement of the Transmission Matrix) scales linearly with the number of SLM pixels N_{SLM} exploited for wavefront shaping, except for DOPC which requires only two steps. Therefore, while DOPC could exploit the full resolution of the SLM ($\sim 10^6$ LCOS-SLM pixels), most of wavefront shaping experiments only exploit $N_{\mathrm{SLM}} \sim 100 - 10000$ SLM pixels. According to Equation 1.10, the number of controlled modes is much lower than the number of optical modes in the scattering medium. Nonetheless, light can still be focused with high intensity compared to the averaged scattered intensity.

Wavefront shaping is not restricted for the study of optical scattering media. It has been inspired by optical radar phase arrays [Bridges et al., 1974] under Coherent Optical Adaptive Techniques (COAT). It is now widely spread in optics such as for surface plasmon polaritons [Gjonaj et al., 2011, Gjonaj et al., 2013, Choi et al., 2017]. Wavefront shaping has also been extended to other electromagnetic regimes such as in microwave with the development of Spatial Microwave Modulator [Dupré et al., 2015, del Hougne et al., 2016].

In the following, we describe more precisely the algorithms discussed above to focus monochromatic light through a scattering medium. Similar algorithms have been developed for controlling broadband light; they are explained in Section 1.5.

1.3.2 Iterative optimization algorithm

In this section, we mainly describe the first pioneering wavefront shaping experiment realized in optics by Vellekoop and Mosk in 2007 [Vellekoop and Mosk, 2007]. The feedback method they employed is an iterative optimization algorithm. Additional details on feedback algorithms can be found in [Vellekoop, 2015].

In their experiment, coherent light from a laser source is imaged on a phase-only spatial light modulator ($N_{\text{SLM}} \sim 3000$ pixels) before propagating in an opaque layer of white paint. The output light is collected and imaged on a CCD camera. Every input mode (i.e. SLM pixels) contributes to the speckle pattern measured on the camera. For focusing purposes in a single position of the CCD camera, the optimization algorithm consists in finding the optimal combination of input modes to reach the maximal intensity at the targeted position.

The optimization process used in [Vellekoop and Mosk, 2007] is composed of two steps for every input mode:

- The phase of the input mode is swept from 0 to 2 π in discrete steps. Consequently, the output signal is sinusoidally modulated.
- The phase of the input mode related to the maxima of the output modulation is recorded and displayed.

The method is iterated for every input mode. The last step consists in displaying on the SLM the correct pattern based on the above measurements. The output fields interfere constructively at the targeted position: a focus is standing over a background speckle, as illustrated in Figure 1.7.

Properties of the achieved focus

The focus size is given by the diffraction-limited speckle grain size, i.e. $C^{(1)}$-correlation as defined in Section 1.2.3. Signal-to-background ratio of focusing η on a single speckle grain is defined as the ratio between the intensity at the focus and the averaged background intensity without shaping. Iterative optimization with N_{SLM} degrees of freedom consists in aligning a random sum of N_{SLM} phasors by adjusting their phases. It corresponds then to an increase of the total field amplitude by an amount $\propto \sqrt{N_{\text{SLM}}}$, and correspondingly to a final intensity that scales linearly with N_{SLM}. For a phase-only SLM, η reads [Vellekoop and Mosk, 2007]:

$$\eta \simeq \frac{\pi}{4} N_{\text{SLM}} \quad \text{with} \quad N_{\text{SLM}} \gg 1 \tag{1.14}$$

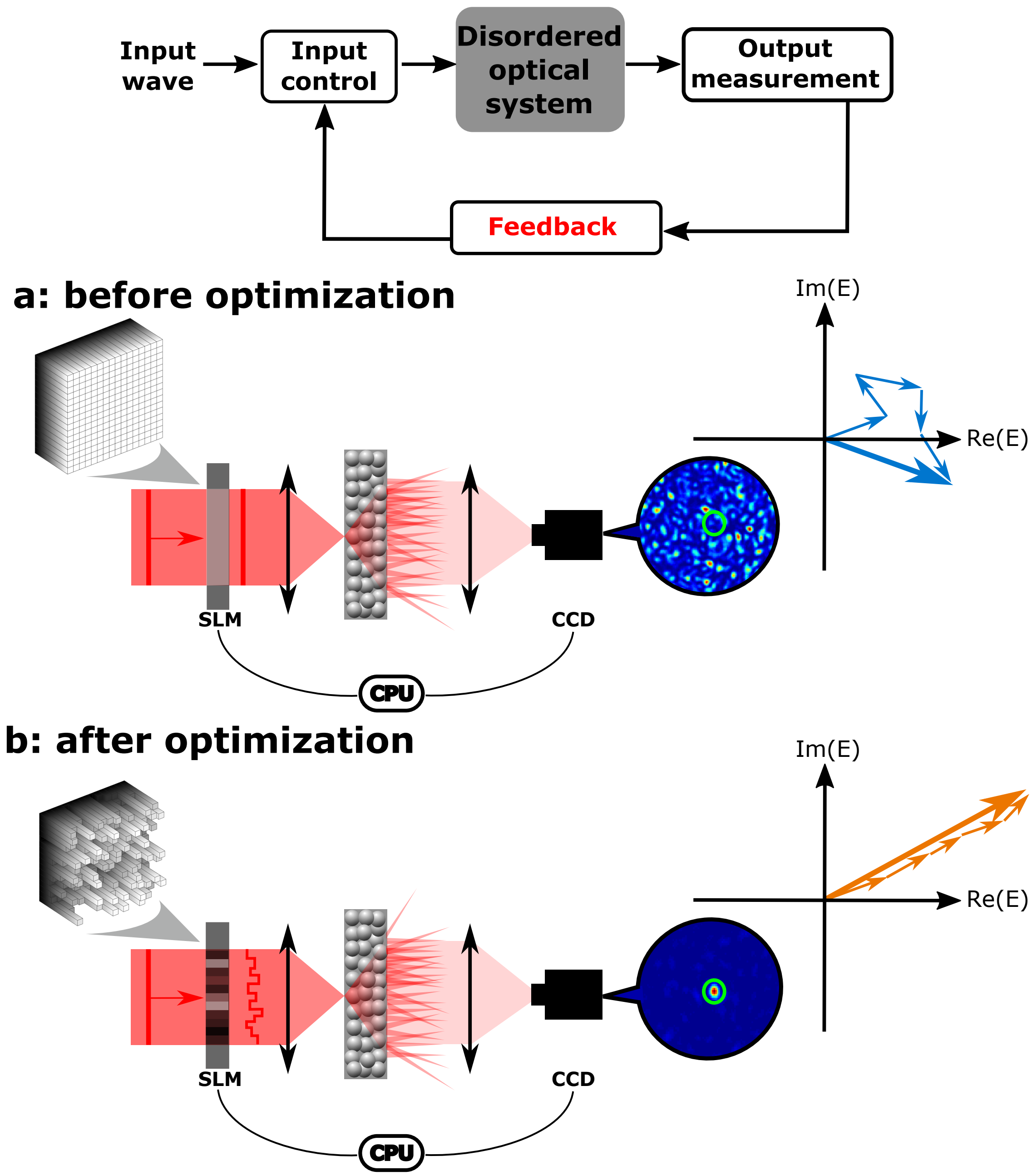

Figure 1.7 – Iterative optimization algorithm to focus light through a scattering medium. (Top) Typical sketch of wavefront shaping setup via an iterative optimization algorithm. **(a)** Coherent light is propagating through a disordered sample. Transmitted light is imaged on a CCD camera. The input wavefront of light can be controlled before propagation in the medium with a SLM. Each pixel of the SLM contributes as a phasor in the output field, with a uniform phase distribution because of scattering. Before starting the optimization algorithm, the SLM pattern is flat: the output field results in a speckle. Field distribution in the target position (center of the green circle) is schematically represented in the complex plane, as in Figure 1.5. **(b)** Iterative optimization algorithm is strongly enhancing the intensity at the target position, by launching a closed loop between SLM pattern and intensity in the target as feedback signal, both connected via a CPU. In the complex plane at the position of the target, the phasors are now aligned in phase, driving a constructive interference which leads to a brighter intensity spot. The final input wavefront is no longer a plane wave, but a distorted wavefront controlled by the SLM. More details about iterative optimization algorithms available in [Vellekoop, 2015]

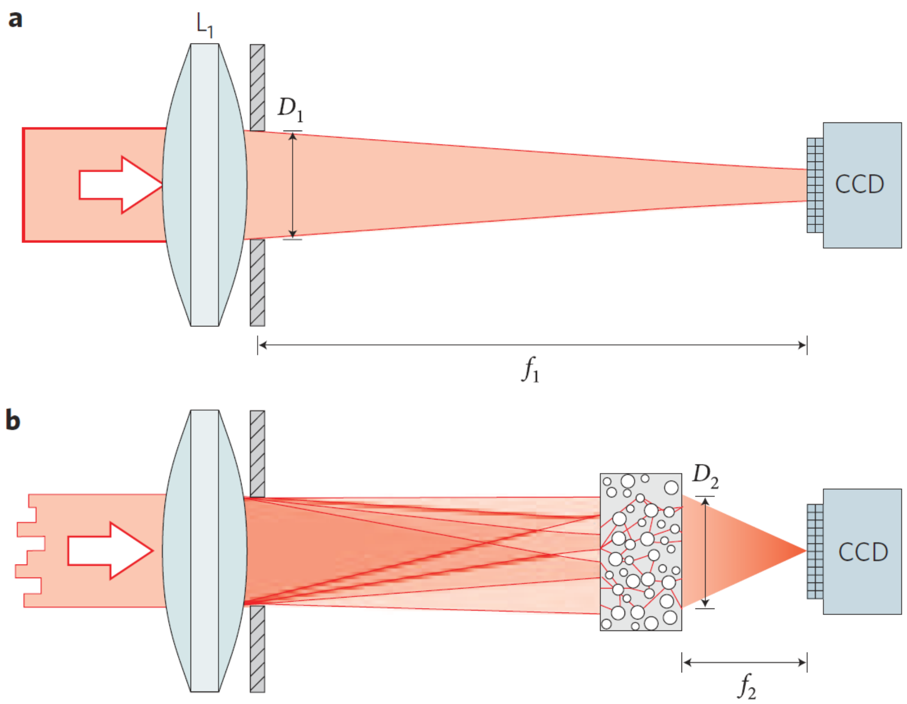

Figure 1.8 – Wavefront shaping turns a disordered material into a scattering lens. (a) Lens L_1 with focal distance f_1 focuses light onto a camera. A pinhole controls the aperture D1 of the lens. The focus is, at best, as sharp as the diffraction limit of the lens. **(b)** A disordered medium at distance f_2 from the camera scatters light. After wavefront shaping, light is focused through the sample to a spot that is narrower than the diffraction limit of the lens. D_2: diameter of the diffuse spot at the back of the sample. Image adapted from [Vellekoop et al., 2010].

In their original paper, Vellekoop and Mosk achieved a final enhancement ~ 2000. Nowadays, fast DMD with 10^6 pixels enables to reach enhancement close to 10^5 [Yu et al., 2017]. Nonetheless, focusing in different positions separated by more than the speckle grain size requires the algorithm to be relaunched entirely, to compute again the input phase mask on the SLM.

The scattering medium is then used as a lens, or more precisely a *scattering lens*. The huge diversity of optical paths provides a high numerical aperture that makes the scattering lens close to a perfect lens, reaching the diffraction limit [Vellekoop et al., 2010, van Putten et al., 2011, Choi et al., 2011b], as illustrated in Figure 1.8. The obtained focus can be sharper with such random scattering [Fink, 2010] than using a standard lens placed before the medium.

Different iterative optimization algorithms

Different algorithms have been developed to robustly reach maximal intensity, depending on noisy experimental conditions [Yılmaz et al., 2013]. The input modulation of a single pixel over the N_{SLM} available pixels, usually named the canonical basis of the SLM, will experience a lower amplitude modulation at the output rather than modulating several pixels simultaneously. Various algorithms have been developed to build on the focus, whether testing individually each pixel, or a set of random pixels simultaneously, to gradually modifying the input phase mask on the SLM [Vellekoop and Mosk, 2008a, Conkey et al., 2012a].

Different metrics to be optimized

Iterative optimization algorithms have been extended not only to focus light on a single point. In their original paper, Vellekoop and Mosk have demonstrated the capability to focus light on different target positions simultaneously with a single phase mask displayed on the SLM [Vellekoop and Mosk, 2007]. In this specific case, the optimization metric was to maximize the intensity of 5 different positions corresponding to 5 different speckle grains. The signal-to-background ratio in each target η_{target} depends on the number of targets N_{target} and on the number of available degrees of freedom N_{SLM}. In essence, the signal-to-background ratio reads:

$$\eta_{\text{target}} \sim \frac{\eta_{\text{single target}}}{N_{\text{target}}} \tag{1.15}$$

with $\eta_{\text{single target}}$ the signal-to-background ratio of a single target given by Equation 1.14. Recent works have also been carried out by optimizing the intensity of an area rather than a single point [Ojambati et al., 2016] in order to increase total transmission and coupling to the so-called open channels [Sarma et al., 2016]. Other studies related to higher order mesoscopic correlation have shown that focusing on a target, with a control on the two polarization states, increases intensity not only in the focus, but also in the background [Vellekoop and Mosk, 2008b].

Iterative optimization algorithms are very simple to implement: it only requires a closed loop between a sensor and the SLM. Its simplicity has lead to the extension to other optical disordered systems such as multi-mode fibers [Čižmár et al., 2010, Leonardo and Bianchi, 2011, Čižmár and Dholakia, 2011]. It has also proven to be efficient with binary amplitude modulation [Akbulut et al., 2011]. The algorithm tends to control the scattering effects in the targeted position by adjusting the input light. This approach is closely related to optical phase conjugation developed in the 1970s [Yariv, 1976], that has been replaced by digital optical phase conjugation, with the use of SLMs, that we now detail in Section 1.3.3.

1.3.3 Digital Optical Phase conjugation

Optical phase conjugation

Optical phase conjugation (OPC) initially comes from the reciprocity of the wave equation. The acoustics analogue of optical phase conjugation is time reversal [Fink, 1997]. An input wave that is scattered can be recovered in two steps: recording the resulting scattered wave, and in second time back propagating its phase conjugate through the complex medium. Time symmetry of the propagation equation ensures focusing back to the point source position.

Although the first experimental use of OPC was the recording of an hologram on a photographic plate [Leith and Upatnieks, 1966], non-linear wave optics processes were implemented as a standard tool in the 1980s for OPC [Fisher, 2012], for example to compensate optical aberrations [Yariv et al., 1979]. Nonetheless, non-linear wave optics

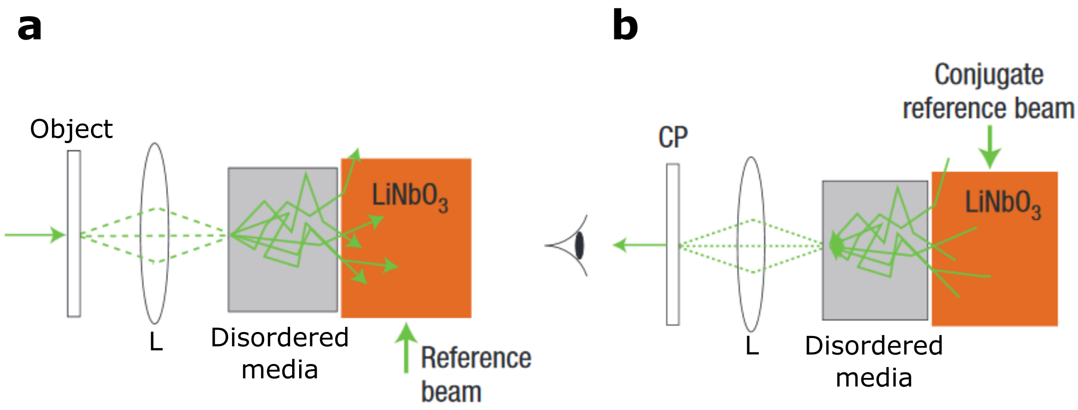

Figure 1.9 – Typical sketch of an optical phase conjugation setup with a photorefractive crystal. **(a)** In the first step, scattered light is recorded. **(b)** Secondly, the optical phase conjugated field is sent back. L: Lens, CP: compensation plate; Image adapted from [Yaqoob et al., 2008].

require non-linear crystals, high-intensity laser sources, and they are selective in the wavelength domain. Photorefractive crystals are a good alternative for OPC. They have been used over the last decade for wavefront shaping through biological tissue [Yaqoob et al., 2008, McDowell et al., 2010, Liu et al., 2015], as they offer high conjugation speeds and simultaneous control of a huge number of modes. A schematic of an OPC experiment with a photorefractive crystal is presented in Figure 1.9.

Optical phase conjugation with spatial light modulators: digital optical phase conjugation

Digital optical phase conjugation (DOPC) has emerged thanks to digital spatial light modulators. Specifically, the two main elements of a DOPC experimental setup are a wavefront sensor (usually a CCD camera, with an off-axis reference beam) and a wavefront actuator (usually a SLM). The operating process of DOPC is explained in Figure 1.10. The sensor and the SLM are in the mirror conjugate planes of a beam splitter: they have to be matched perfectly pixel by pixel, which makes experimental alignment not trivial. A DOPC experiment is performed in two steps:

1. In the first step, the optical scattered light field is recorded. In most of DOPC experiments, interference with a reference beam is used to measure the phase information [Cui and Yang, 2010], as illustrated in Figure 1.10a. Nonetheless, some research groups have been developing reference-free DOPC [Vellekoop et al., 2012].
2. Secondly, a pattern is displayed on the SLM. The reference beam is reflected on the SLM: it transports the phase conjugated wavefront. This beam is then back-propagated through the disordered sample, following the same scattering channels backwards (Figure 1.10b).

DOPC was firstly applied to focus light after propagation through disordered media by Cui and Yang [Cui and Yang, 2010]. It was then extended to focusing through various disordered systems such as thick biological tissues for different polarization states [Shen

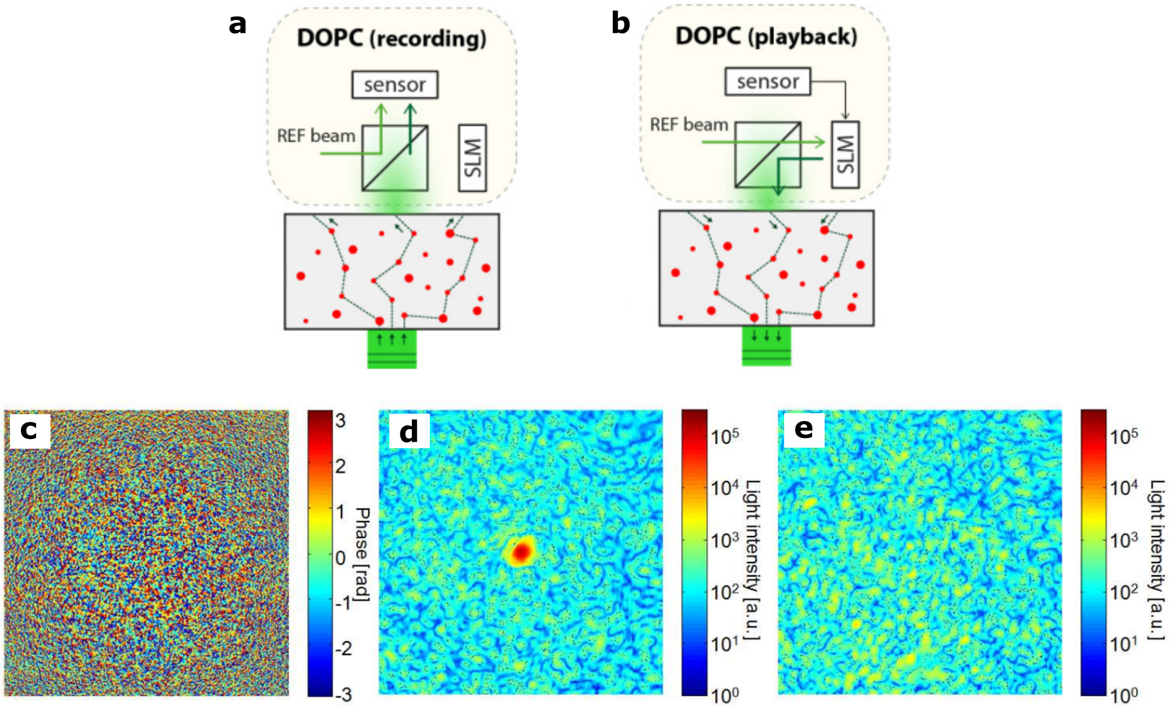

Figure 1.10 – Typical sketch of a digital optical phase conjugation setup. A sensor (usually a CCD camera) and a SLM are located in conjugated planes with respect to a beam splitter. Their respective pixels are matched pixels by pixels. **(a)** In the first step, the scattered field is measured on the sensor via an interference with a reference beam. **(b)** Secondly, the phase map measured on the sensor is displayed on the SLM. The same reference beam is now reflected on the SLM: phase-conjugation operation is digital. The reference beam is propagating in the scattering medium following the same channels used in the first step, but backwards. **(c)** Example of a phase map measured on the sensor. Scattering effects in the disordered material (random polystryrene microspheres here) make the phase map looking very complex, nonetheless measurable. **(d)** Reconstructed focus obtained by phase conjugating the field measured in (c), in log scale. **(e)** Reconstructed image with a flat pattern displayed the SLM. Image (a-b) adapted from [Jang et al., 2015], Image (c-e) adapted from [Cui and Yang, 2010].

et al., 2016] and multi-mode fibers [Papadopoulos et al., 2012] using continuous wave (cw) light. Out of focusing purposes, DOPC also enables delivery of two-dimensional images [Hillman et al., 2013]. Furthermore, iterative DOPC on both side of a scattering medium filters out scattering channels of high transmission, opening the way for the experimental study of open channels [Bosch et al., 2016].

DOPC has several advantages in comparison with conventional OPC. First of all, it can be used with cw light and with pulsed lasers (See Section 1.5.3 for control of broadband light). A DOPC operation can also be performed with controllable power and for a broad spectral range, in opposition to nonlinear optics based OPC techniques. High reflectivity of the SLM does not imply a need of high power source [Jang et al., 2017].

DOPC also takes advantages over iterative optimization algorithms developed above. Indeed, DOPC does not require iterative measurements or computation, but only two steps. Therefore a huge number of degrees of freedom (up to 10^6 SLM pixels) could be exploited in a very short time, in comparison with iterative optimization, where the number of SLM pixels manipulated is mostly limited by the refresh rate of the SLM. For example, it enables light control over dynamic media [Jang et al., 2015, Liu et al., 2017].

Nonetheless, DOPC requires a complex experimental alignment [Jang et al., 2014]. Also, similarly to iterative optimization algorithms, DOPC is not able to extract quantitative information about the scattering media, such as its distribution of eigenvalues.

1.3.4 The monochromatic Transmission Matrix

Another approach to control light propagation in complex media has been experimentally proposed by Popoff *et al.* [Popoff et al., 2010b]. In this paper, they propose a method to measure experimentally the optical transmission matrix (TM) of the scattering medium, and how to exploit it for a more complete control of the transmitted output field. For focusing purposes, an iterative optimization algorithm is efficient, however it needs to be repeated to focus at another target position. In essence, a lot of measured information is not used in the optimization algorithm. For instance, when testing an input pattern, only the modulation at the target position is measured, while the other CCD pixels are not considered. In this regard, the TM approach is more appropriate.

A TM is a subpart of the scattering matrix developed in Section 1.2.3. Because of the linearity of the scattering process, a linear operator establishes the relationship between the input field E^{in} (i.e. on the N SLM pixels before propagation in the disordered sample) and the output field E^{out}(i.e. the scattered field measured on M pixels of a sensor). When the SLM and the output detector, usually a CCD camera, are located on different sides of the scattering medium, this operator is the TM from left-to-right side $\mathbf{t}$, which is related to Green's function of the scattering medium [Fisher and Lee, 1981]. The transmission matrix $\mathbf{t}$ is thus defined as:

$$E^{\text{out}} = \mathbf{t}E^{\text{in}} \tag{1.16}$$

The first experimental measurement of TM in optics for a scattering medium has been realized almost a decade ago by Popoff and colleagues [Popoff et al., 2010b]. This pioneer work demonstrates how to measure easily the TM of a thick layer of white paint under illumination of monochromatic laser source, and how to exploit it to focus light through disordered material. This work has been extended to a multitude of optical disordered systems under illumination of cw light, such as multi-mode fibers [Čižmár and Dholakia, 2012, Carpenter et al., 2014, Plöschner et al., 2015] with potential application in endoscopy [Choi et al., 2012], photonic structures [Akbulut et al., 2016] and linear optical network [Rahimi-Keshari et al., 2013]. The concept of the TM has spread beyond the scope of monochromatic light. Experimental TMs have been measured with quantum light [Defienne et al., 2014, Defienne et al., 2016, Wolterink et al., 2016]. A photo-acoustic TM has been measured with ultrasound detectors as sensors [Chaigne et al., 2014]. Finally, polarization states of scattered light can be adjusted by measuring a vectorial transmission matrix [Tripathi et al., 2012, Yu et al., 2013]

Similar work has been carried out with the Reflection Matrix [Popoff et al., 2011a] inspired by work in acoustics [Aubry and Derode, 2009], where the sensor is located on the same side of the scattering medium as the SLM.

In this Section, we develop how the transmission matrix can be experimentally measured, and how to exploit it to focus light through the scattering medium.

Measurement of the TM of white paint

The transmission matrix is an essential tool to describe light transmission in a scattering medium. Indeed it contains a lot of information such as the eigenvalue distribution of the scattering medium [Popoff et al., 2011b, Skipetrov and Goetschy, 2011], that could be predicted by random matrix theory [Beenakker, 1997].

According to Equation 1.16, measuring the output field on the *m-th* pixel E_m^{out} of the CCD camera provides the means to access the TM coefficients $\mathbf{t} = \{|t_{mn}|e^{i\theta_{mn}}\}$ by modulating individually each of the N SLM pixels:

$$E_m^{out} = \sum_{n=1}^{N} |t_{mn}|e^{i\theta_{mn}} E_n^{in} \tag{1.17}$$

with E_n^{in} the input field on the *n-th* pixel of the SLM. A typical method would be to switch off all the pixels of the SLM except a single one. This process would enable the measurement of its corresponding transmission matrix coefficients related to all the output pixels on the sensor.

However, using this canonical basis, several issues arise, as previously studied with iterative optimization algorithms in Section 1.3.2. In addition to the low output modulation resulting from the modulation of a single SLM segment, a phase-only SLM cannot physically impose a zero-intensity in its pixels. An alternative basis is the *Hadamard* basis [Popoff et al., 2011b]. This orthogonal basis is constituted of N patterns where all the pixels have the same amplitude but a phase difference of π is applied to half of the pixels. Some patterns are illustrated in Figure 1.11 for $N = 256$ SLM segments. The experimental TM, measured in the Hadamard basis, can then be converted to the more convenient canonical basis, by a simple change of basis.

Measurement of the TM requires the ability to measure quantitatively the output electric field. However, most of conventional CCD sensors are only sensitive to intensity measurement. Standard techniques to access the complex output field use holography methods, such as off-axis holography [Cuche et al., 1999]. Such interferometric methods require a

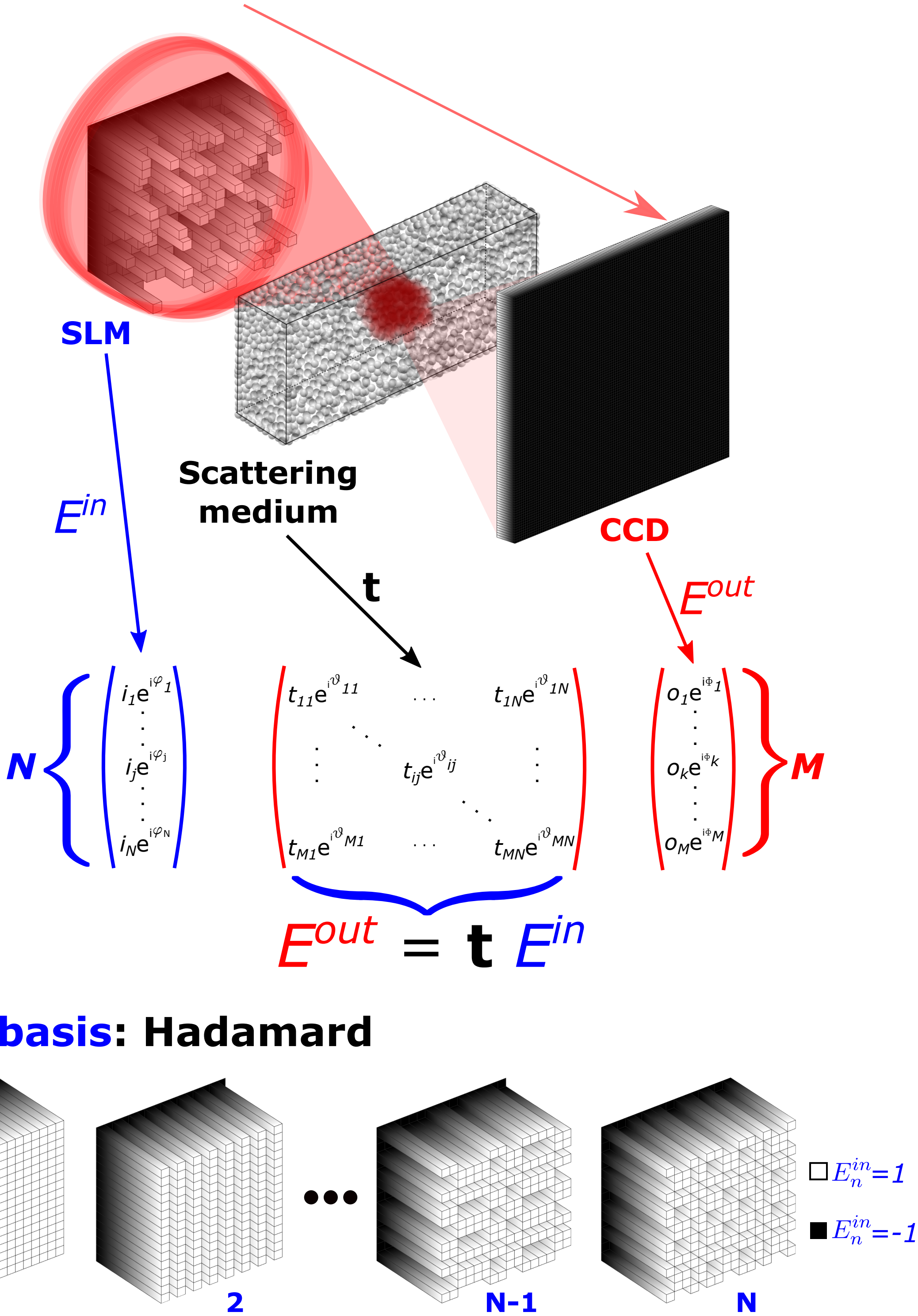

Figure 1.11 – Monochromatic transmission matrix of a scattering medium. (Top) Monochromatic light is transmitted through a spatial light modulator (SLM) before propagating inside a thick scattering medium. Transmitted light is collected with a sensor, usually a CCD camera. While modulating the input field E^{in} on the SLM, the corresponding output field E^{out} is measured using holographic method on the CCD camera. The linear relationship connecting E^{in} and the measured E^{out} is the Transmission Matrix of the scattering medium. **(Bottom)** The input basis used for the measurement of the Transmission Matrix is the Hadamard basis. Some patterns are represented for $N = 256$ input SLM pixels. All the pixels have the same intensity distribution, nonetheless half of them are π phase-shifted with respect to the other half.

reference beam. Nonetheless implementation of an interferometric external arm adds a stability issue. Alternatively, the SLM can be divided in two different parts [Popoff et al., 2010b]:

- A *control part*, whose phase will be modulated. It generates a speckle field $\tilde{E}_{mn} = E_{mn}e^{i\theta_{mn}}$ at the m^{th} output pixel on the CCD created by the n^{th} input SLM pixel.
- A *reference part*, that remains static during the measurement process. It generates a static reference speckle field $\tilde{E}^{\text{ref}} = E^{\text{ref}}e^{i\theta^{\text{ref}}}$ after propagation through the scattering medium. This static speckle can then be used as the reference field for holographic methods.

The two speckle fields from both control and reference part interfere at the output of the scattering medium. If the reference part on the SLM is shifted by a global phase retardation φ, the corresponding reference transmitted speckle, at the output, will experience the same phase shift. The output intensity I^{φ}_{mn}, accessible with a camera, reads:

$$\begin{aligned} I^{\varphi}_{mn} &= |\tilde{E}_{mn} + \tilde{E}^{\text{ref}}e^{i\varphi}|^2 \\ &= |E_{mn}|^2 + |E^{\text{ref}}|^2 + 2\cos\left(\theta_{mn} - \theta^{\text{ref}} + \varphi\right) \end{aligned} \tag{1.18}$$

Phase-shifting holography allows reconstruction of the complex output field with intensity-only measurements [Yamaguchi and Zhang, 1997]. Phase-retrieval algorithms are also another solution [Drémeau et al., 2015], but their long computing time make them inconvenient for a fast measurement of TM. In their original paper, Popoff and colleagues have used 4 phase-shifted intensity images (exploiting $\varphi = [0, \pi/2, \pi, 3\pi/2]$) to reconstruct the transmission matrix coefficients [Popoff et al., 2010b]:

$$\begin{aligned} t'_{mn} &= \frac{I^0_{mn} - I^{\pi}_{mn}}{4} - i\frac{I^{3\pi/2}_{mn} - I^{\pi/2}_{mn}}{4} \\ &= |E_{mn}||E^{\text{ref}}|e^{i(\theta_{mn} - \theta^{\text{ref}})} \\ &= \tilde{E_{mn}}\tilde{E^{\text{ref}}}^* \end{aligned} \tag{1.19}$$

The obtained complex coefficient t'_{mn} contains, as expected, the controlled output field E_{mn}. Nonetheless, the presence of the complex conjugate of the reference field could be detrimental. Indeed, since the reference field is a speckle, it contains both bright grains and dark grains: some reference part will have a low amplitude. The matrix $\mathbf{t'} = \{t'_{mn}\}$ is usually named the *effective transmission matrix*.

Although $\mathbf{t'}$ is convenient for focusing purposes [Popoff et al., 2010b], some applications, such as retrieving a transmitted image through the medium [Popoff et al., 2010a] require the proper transmission matrix $\mathbf{t}$. Some methods developed in [Popoff et al., 2011b] enable the retrieval of only the magnitude of the reference field $|E^{\text{ref}}|$.

Focusing light with the Transmission Matrix

Once the TM has been experimentally measured, it can be exploited to control light propagation through scattering media.

Although many applications have been developed exploiting the TM, such as image transmission [Popoff et al., 2010a] or minimizing total transmission [Tripathi and Toussaint, 2013], in this Subsection we only deal with focusing light in a given target position. Additional applications utilizing the monochromatic TM can be found in [Rotter and Gigan, 2017].

Focusing light with the TM starts from Equation 1.16. The objective is to find the input field $E^{\text{in}}_{\text{SLM}}$ to focus light in a target position $E^{\text{out}}_{\text{target}}$. In essence, solving this problem is equivalent to "inverting" Equation 1.16:

$$E^{\text{in}}_{\text{SLM}} = \text{``}\mathbf{t^{-1}}\text{''} E^{\text{out}}_{\text{target}} \tag{1.20}$$

Re-injecting $E^{\text{in}}_{\text{SLM}}$ in Equation 1.16 leads to $E^{\text{out}} = E^{\text{out}}_{\text{target}}$. Pseudo-inversion is a mathematical operation generalizing the inversion process of a complex matrix: it verifies $\mathbf{t}^{-1} \times \mathbf{t} = \mathbb{1}$. Consequently, this operator looks like a potential candidate to compute $E^{\text{in}}_{\text{SLM}}$. Nonetheless, experimental issues impede the use of pseudo-inversion:

- Experimental noise is inevitably present in the measurement process of $\mathbf{t}$. Although it is not strongly affecting the measurement of $\mathbf{t}$, this noise gets amplified by the inversion process.
- The SLM is only able to shape the phase of the input field. It really limits the efficiency of matching $E^{\text{in}}_{\text{SLM}}$, which usually requires modulation of both amplitude and phase.

Solutions have been developed using Tikhonov regularization [Tikhonov, 1963], taking into account the noise level in the version process.

Another alternative is the transpose conjugate operator $\mathbf{t}^{\dagger}$, similar to phase conjugation developed in Section 1.3.3. Exploiting Equation 1.20, the input field to focus at a given target reads:

$$E^{\text{in}}_{\text{SLM}} = \mathbf{t}^{\dagger} E^{\text{out}}_{\text{target}} \tag{1.21}$$

In contrast with pseudo-inverse process, transpose conjugate operator is stable regarding experimental noise level: instead of amplifying it, the operator is taking into account its phase conjugate. Amplitude of noise after transpose phase conjugation is then similar than during the measurement process of $\mathbf{t}$. After displaying the phase of $E^{\text{in}}_{\text{SLM}}$ on the phase-only SLM, the output field reads:

$$E^{\text{out}} = \underbrace{\mathbf{t} \times \mathbf{t}^{\dagger}}_{\simeq \mathbb{1}} E^{\text{out}}_{\text{target}} \simeq E^{\text{out}}_{\text{target}} \tag{1.22}$$

Focusing through scattering media is equivalent to creating constructive interference at the targeted position, by aligning input modes controllable with the SLM. For focusing in a single target located at pixel m on the CCD camera, the corresponding targeted output field is a null vector except at pixel m whose value is one:

$$E^{\text{out}}_{\text{target},i} = \begin{cases} 0 & \text{for} \quad i \neq m \\ 1 & \text{for} \quad i = m \end{cases} \tag{1.23}$$

We can then evaluate the difference between transpose phase conjugation and an inversion process. While transpose phase conjugation will only phase conjugate the m^{th} line of the TM, the inversion will take care of the intensity of other output pixels, via imposing them a null intensity. The transpose conjugate operator is then more adapted for focusing purposes, as studied in the acoustic regime [Tanter et al., 2000].

Figure 1.12 illustrates a focusing process by using $\mathbf{t}^\dagger$ operator [Popoff et al., 2010b]. With a planar wavefront, a speckle pattern is obtained on the CCD camera. Wavefront shaping after measuring the TM enables focusing in a single target position, with a signal-to-background η similar to the iterative optimization algorithm. η scales linearly with the number of input pixels controlled on the spatial light modulator, as previously studied in Equation 1.14. An advantage of the TM over iterative optimization algorithms is that it contains directly connections between input field on the SLM and output pixels. In other terms, focusing in another CCD pixel does not require to restart an optimization algorithm. TM also enables focusing in N_{target} different multiple output positions. In that case, the targeted output field is a null vector except in the positions where light will be focused. With a fixed number of SLM pixels, the intensity in each foci is thus less bright than focusing on a single target, as explicitly written in Equation 1.15.

Wavefront shaping techniques give the relationship between the input field on the SLM and the desired output field on the CCD camera. Focusing inside the scattering sample would require a feedback signal from inside the medium. Although an optical signal cannot be extracted from inside, ultrasound can propagate without suffering from scattering thanks to their large wavelength. In that sense, photo-acoustics or ultrasonic methods enables light focusing inside a scattering medium, via the photo-acoustic transmission matrix [Chaigne et al., 2014], or ultrasonic-assisted DOPC methods such as Time Reversal of Ultrasound-Encoded (TRUE) [Xu et al., 2011] or Time Reversal of Variance-Encoded Light (TROVE) [Judkewitz et al., 2013].

This Section dealt with monochromatic light. Over the last half century, broadband light sources, such as ultrashort pulse, have been developed and they are now indispensable for many applications such as non-linear optics [Boyd, 2008]. Their high peak power, that cannot be achieved with continuous wave light, has opened the way for study of light-matter interaction. In the next two Sections, we review what an ultrashort pulse of light is, and how they propagate through scattering samples, generating a so-called spatio-temporal speckle. We then review latest state-of-the art research results on the control of an ultrashort pulse through thick disordered materials, mostly thanks to spatial light modulators technologies.

1.4 Propagation of an ultrashort pulse of light in scattering media

At the end of the 1960s, after the first laser was created, short pulse lasers in the picosecond regime were built [DeMaria et al., 1966]. Nowadays, femtosecond and attosecond pulsed lasers are available. The ability to temporally shape ultrashort pulses, brought by arbitrary *pulse shaping* methods developed in the last decades of the 20^{th} century [Weiner et al., 1988, Hillegas et al., 1994, Fetterman et al., 1998] are reviewed in [Weiner, 2000]. They have paved the way for a huge variety of applications such as femtochemistry [Dantus and Lozovoy, 2004], coherent control [Meshulach and Silberberg, 1999], non-linear imaging [Silberberg, 2009] and optical communications [Sardesai et al., 1998] for instance. Nonetheless, ultrashort pulses are sensitive to dispersion and to optical index heterogeneities, and their applications in scattering media remain limited.

In this Section, we describe the basic fundamental mathematics to define and to charac-

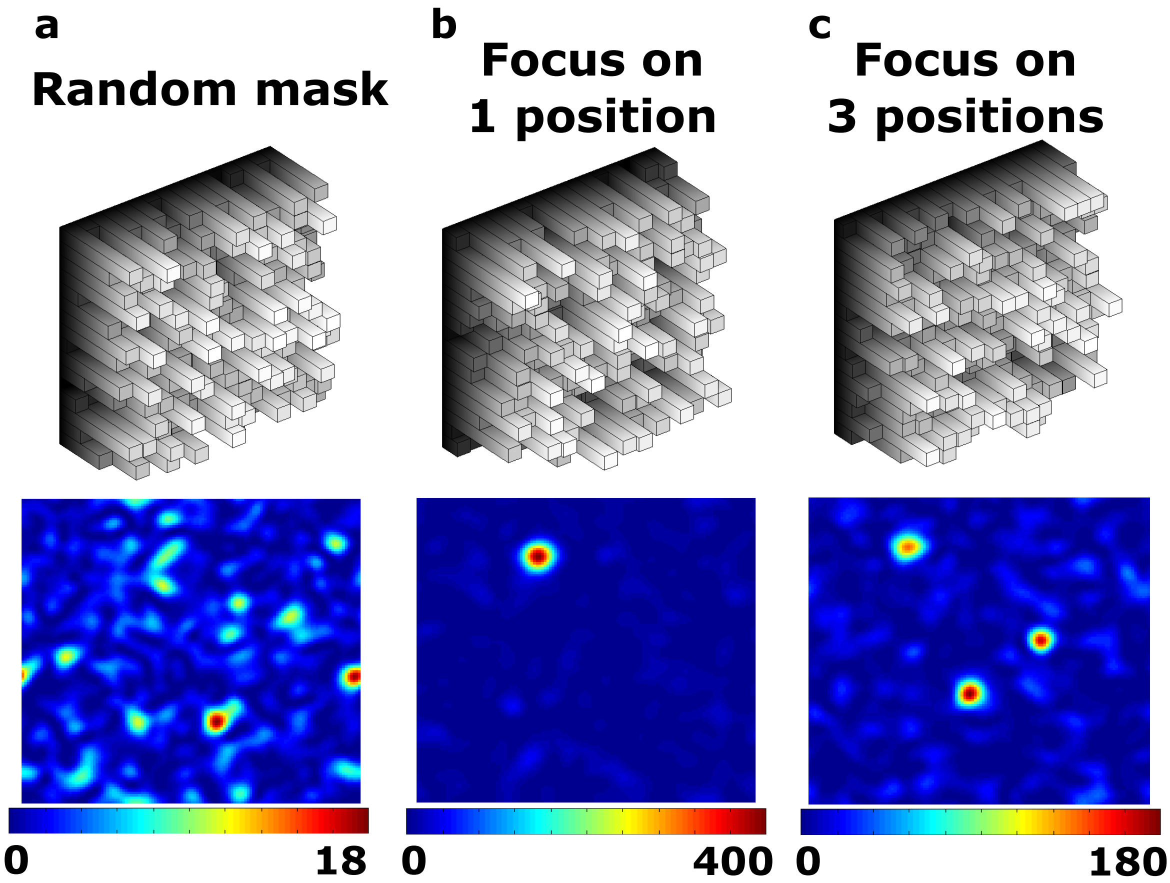

Figure 1.12 – Focusing monochromatic light through a scattering medium via the monochromatic transmission matrix. The monochromatic TM has been measured following the previous protocol developed in Figure 1.11. Phase patterns displayed on the SLM ($N_{\mathsf{SLM}} = 256$) are represented on top. The corresponding output intensity patterns, measured on a CCD camera, are shown on bottom. **(a)** A random input phase pattern is displayed on the SLM. After propagation through the sample, transmitted light takes the form of a speckle pattern, whose mean value intensity is $\langle I \rangle = 2.2$ (arbitrary units). **(b)** Phase conjugation of TM line, corresponding to the target pixel where we want to focus light on, is displayed on the SLM. It results in a focus at the target position $I_{\mathsf{focus}} = 400$, with signal-to-background ratio $\eta = I_{\mathsf{focus}}/\langle I \rangle = 180$, which is proportional to the number of SLM segments controlled. **(c)** The target is now composed of 3 different pixel positions. Signal-to-background ratio in each obtained foci is smaller than in **(b)**. Nonetheless focus intensity at each focus $\propto N_{\mathsf{SLM}}/3$: it remains much higher than averaged intensity in the background.

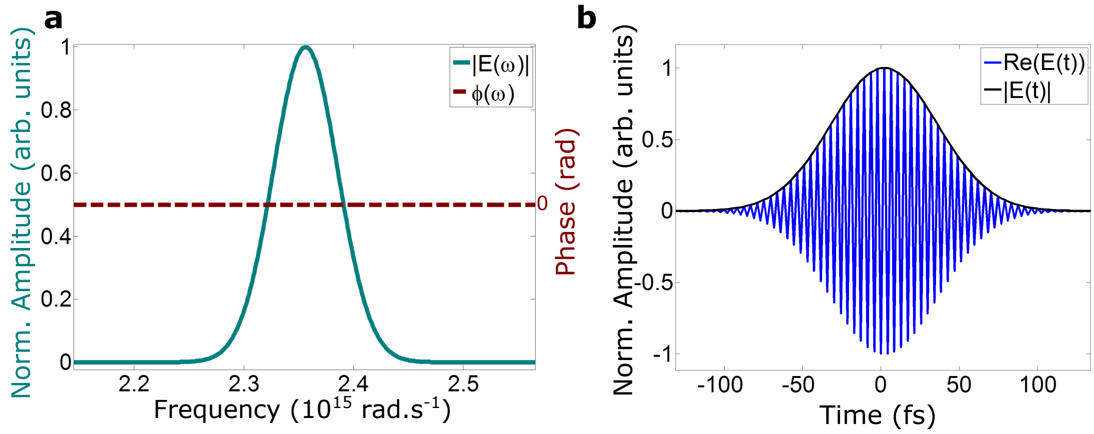

Figure 1.13 – Typical ultrashort pulse of light. Spectral and temporal characteristics of a typical ultrashort pulse. **(a)** Spectral amplitude and spectral phase of the electric field $E(\omega)$, with a center wavelength λ_0=800 nm and a bandwidth of the intensity spectrum $\Delta\omega/\omega_0$=0.02. This ultrashort pulse is Fourier-limited as its spectral phase is flat. **(b)** Corresponding temporal profile of the pulse, obtained with an inverse Fourier transform. Blue line represents the real part of the electric field, while the black line stands for the Gaussian envelope in the time domain. The intensity pulse duration is $\Delta t \simeq$ 70 fs.

terize an ultrashort pulse of light in homogeneous media, mostly based on the following reviews: [Monmayrant et al., 2010, Walmsley and Dorrer, 2009]. We then discuss the propagation of ultrashort pulse through strongly disordered media, and how a transmitted pulse has been impacted by scattering effects.

1.4.1 Definition of ultrashort pulses and propagation in homogeneous media

An ultrashort pulse of light is fully defined by its electric field in the time domain $E(t)$. Although $E(t)$ cannot be easily measured, as standard detectors cannot resolve its temporal behavior, it can be retrieved via $E(\omega)$ the electric field in the spectral domain, with an inverse Fourier transform $\mathcal{F}^{-1}$. $E(\omega)$ is described by its spectral amplitude $|E(\omega)|$ and its spectral phase $\varphi(\omega)$: both contribute to the full characterization of the ultrashort pulse shape. The shortest duration a pulse can achieved corresponds to a flat spectral phase: the pulse is then said to be *Fourier-limited*. Example of an ultrashort pulse is illustrated in Figure 1.13.

Typical ultrashort pulses, generated by Ti:Sapphire mode-locked oscillators, provide a spectral amplitude with large bandwidth, that can usually be fitted with a Gaussian shape [Diels and Rudolph, 2006]. The central wavelength λ_0 of emission, associated to its corresponding frequency $\omega_0 = 2\pi c/\lambda_0$ where c is the speed of light in vacuum, is usually centered around $\lambda_0 \sim 800$ nm [Moulton, 1986]. The spectral bandwidth $\Delta\omega$ is arbitrarily defined at the full width at half maximum (FWHM) of the intensity spectrum $I(\omega) = |E(\omega)|^2$. For most of femtosecond ultrashort pulses, the bandwidth $\Delta\omega/\omega_0$ is on the order of 0.01-0.1. Similarly, the pulse duration Δt is defined as the FWHM of the intensity profile $I(t) = |E(t)|^2$.

The electric field can be seen as a sum of monochromatic waves with their own wavenumber $k(\omega)$, which all acquire a spectral phase $k(\omega)z$ along propagation in the z-axis. The spectral phase plays a decisive role in the general shape of an ultrashort pulse. We expand the spectral phase $\varphi(\omega)$ in Taylor series around the central frequency to analyze the impact of each term:

$$\varphi(\omega) = \varphi(\omega_0) + \varphi^{(1)}(\omega_0).(\omega - \omega_0) + \frac{1}{2}\varphi^{(2)}(\omega_0).(\omega - \omega_0)^2 + \frac{1}{6}\varphi^{(3)}(\omega_0).(\omega - \omega_0)^3 + \dots$$
$$\text{with} \quad \varphi^{(i)}(\omega_0) = \left.\frac{\partial^i \varphi}{\partial \varphi^i}\right|_{\omega_0} \tag{1.24}$$

- The first term $\varphi(\omega_0)$ describes the phase between the envelope of the temporal electric field and oscillation at the carrier frequency ω_0 below the envelope, the Carrier Envelope Phase (CEP). This phase term is crucial in non-linear interactions using few-cycle pulses [Sansone et al., 2006], generally in attosecond physics [Krausz and Ivanov, 2009]. In the following we neglect the impact of this term as we consider many-cycle pulses.
- The linear term $\varphi^{(1)}(\omega_0)$ corresponds to a delay in the time-domain between the pulse and an arbitrary origin of time. This term does not affect the temporal shape of the pulse.
- The quadratic term $\varphi^{(2)}(\omega_0)$, usually named *chirp* or group velocity dispersion, induces an increase of the pulse duration. The group delay $\partial\varphi/\partial\omega$ evolves linearly with frequency: "red" parts of the pulse spectrum propagate faster than "blue" parts for a positive chirp. The larger the pulse spectral width $\Delta\omega$, the more sensitive the pulse duration is to the chirp effect.
- The cubic term $\varphi^{(3)}(\omega_0)$ creates pre- or post-pulses in the time domain, depending on its sign.

Quadratic, cubic and higher orders need to be accurately compensated to generate ultrashort pulse [Fork et al., 1987]. The impact of such high order terms is illustrated in Figure 1.14.

1.4.2 Standard characterization of ultrashort pulses

Optimal time resolution of the fastest photo-diodes is on the order of picoseconds. Therefore typical ultrashort pulses of duration $\Delta t \sim 10 - 100$ fs, as well as an optical cycle, cannot be directly detected with common sensors. Over the last decades, methods have been developed and engineered to characterize ultrashort pulses. In essence, these methods can be classified in three different categories, depending on their accuracy of reconstruction of temporal electric field $E(t)$. Firstly, *incomplete characterization* methods, such as intensity autocorrelation [Monmayrant et al., 2010], are usually easy to implement. Nonetheless they only estimate the pulse duration or the temporal envelope on the electric field, without allowing the measurement of the spectral phase. The other categories manage a complete characterization of the ultrashort pulse, whether using a reference beam, such as spectral or temporal interferometry techniques, or self-references such as frequency-resolved optical gating. In this Section we restrict ourselves to the most widely used techniques. Additional methods and details can be found in [Dudley et al., 2008, Monmayrant et al., 2010].

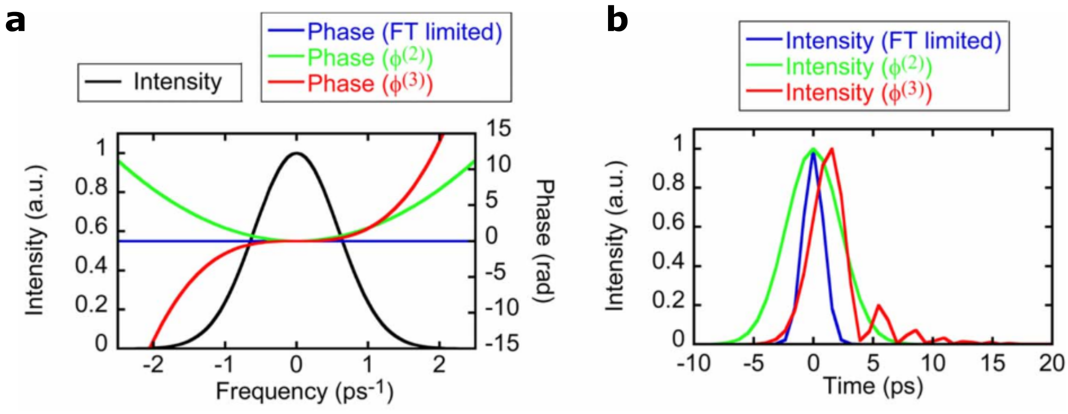

Figure 1.14 – Impact of dispersion terms on the ultrashort pulse duration and shape. (a) Spectral intensity of the considered pulse, associated with three different spectral phases: flat (in blue), quadratic ($\varphi^{(2)}$ term, in green) and cubic ($\varphi^{(3)}$ term, in red). **(b)** Corresponding temporal profiles of pulses. The flat spectral phase leads to a Fourier-limited pulse. The quadratic term increases the temporal duration of the pulse. The cubic term creates post-pulses. Image adapted from [Walmsley and Dorrer, 2009]

Intensity autocorrelation

Intensity autocorrelation is probably the widest method used to characterize an ultrashort pulse because of its simplicity. The scheme of a typical autocorrelation setup is drawn in Figure 1.15a. This method is *self-referencing*: it does not require the use of an external reference beam. The pulse, in a single spatial mode, is split into two time-shifted replicas with a Michelson interferometer. Those two pulses are overlapped and focused on a non-linear crystal. Intensity of the second harmonic signal generated is measured as a function of the time-delay with a slow photo-diode, in comparison with the pulse duration. The obtained signal is given by Equation 1.25. An alternative technique consists in focusing the two replicas with a different angle, and recording only the intensity of the second harmonic signal cross-term.

$$S(\tau) \propto \int |E(t) + E(t-\tau)|^4 dt \tag{1.25}$$

This method provides the autocorrelation function of the intensity envelope. Although the spectral phase information is lost in the process, an a priori knowledge of the pulse shape enables estimation of the pulse duration. Nonetheless, autocorrelation cannot provide information on temporal features below the envelope. In essence, a chirped pulse would give the same signal as a longer Fourier-limited pulse.

Intensity autocorrelation devices are usually simple to implement, they rapidly hint at the pulse duration. They require a high power input signal to generate second harmonic signal from the non-linear crystal, which is naturally provided by most of ultrashort pulse lasers. Nonetheless, propagation through scattering samples, as illustrated in Section 1.4.3, strongly affects the pulse duration and its intensity, which limits the use of autocorrelation methods in that specific scenario.

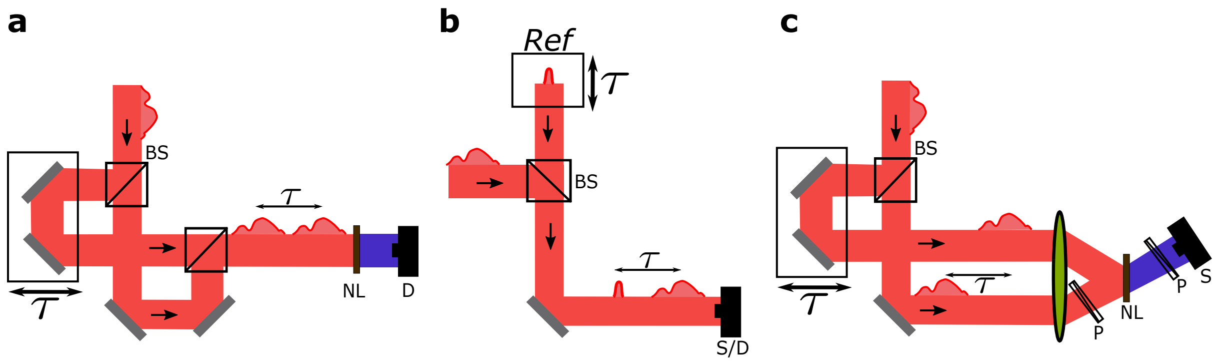

Figure 1.15 – Typical methods to characterize an ultrashort pulse (a) Intensity autocorrelation. **(b)** Spectral or temporal interferometry. **(c)** Polarization-Gated Frequency-Resolved Optical Gating. (BS): beam splitter, (NL): non-linear crystal, (D): photo-detector or camera, (S): spectrometer, (P): polarizer.

Spectral and temporal interferometry

A complete characterization of the ultrashort pulse should provide both the spectral amplitude $|E(\omega)|$ and the spectral phase $\varphi(\omega)$. Spectral interferometry, as drawn in Figure 1.15b provides such characterization, with the use of a known reference signal. This simple setup uses only a spectrometer as a detector. The ultrashort pulse and the reference pulse are overlapped with a controllable delay τ. A spectrometer records the signal, which reads:

$$\begin{aligned} I(\omega,\tau) &= |E(\omega) + E_{\mathrm{ref}}(\omega)e^{i\omega\tau}|^2 \\ &= |E(\omega)|^2 + |E_{\mathrm{ref}}(\omega)|^2 + 2E(\omega)E_{\mathrm{ref}}(\omega)\cos\Big(\varphi(\omega) - \varphi_{\mathrm{ref}}(\omega) - \omega\tau\Big) \end{aligned} \tag{1.26}$$

The cross-term is filtered by taking the Fourier transform of $I(\omega,\tau)$, isolating the component at time τ and inverse Fourier transform back the signal [Lepetit et al., 1995]. As $E_{\mathrm{ref}}(w)$ and $\varphi_{\mathrm{ref}}(\omega)$ are known quantities, one can then retrieve $E(w)$ and $\varphi(\omega)$. To accurately perform the Fourier transform process, the cosine term should be well-resolved, implying conditions on τ and on the spectrometer resolution.

Alternatively, a photo-diode or a CCD camera can be used as sensor instead of a spectrometer: this temporal interferometry consists then in recording the intensity as a function of the delay τ:

$$I(\tau) = \underbrace{\int |E(t)|^2 dt + \int |E_{\mathrm{ref}}(t)|^2 dt}_{\text{baseline}} + \int \Big(E(t)E^*_{\mathrm{ref}}(t-\tau) + c.c.\Big)dt \tag{1.27}$$

This technique is also straightforward to implement, nonetheless it requires stability because of the interferometer, and knowledge of the reference field.

Frequency-resolved optical gating

A complete characterization technique that is self-referenced is Frequency-Resolved Optical Gating (FROG). It consists in interfering the pulse with a gated pulse, that is a small portion of the pulse. The gated pulse is always obtained using a non-linear effect. Many FROG alternative methods have been developed to temporally gate the pulse, that are reviewed in [Trebino et al., 1997]. Figure 1.15c shows polarization-gate FROG, which uses the Kerr effect (third order non-linearity) in a non-linear crystal and crossed polarizers. The obtained gate function is related to the intensity profile of the pulse, as explained more in details in [Trebino et al., 1997].

1.4.3 Spatio-temporal distortion of an ultrashort pulse through highly scattering media

The temporal shape of an ultrashort pulse is strongly dependent on its spectral phase, as emphasized in Figure 1.14. Propagation through a highly disordered media tends to distort the spectral phase of the pulse, as the scattering medium responds differently for each spectral component of the incident pulse. Consequently, transmitted light results in a temporally broadened pulse. In addition to spatial effects developed in section 1.2.2, the ultrashort pulse turns into a complex spatio-temporal speckle field [Mosk et al., 2012], different in every point.

In this section, we present path length distribution of transmitted photons through a thick scattering material. This distribution provides relevant characteristic quantities of the transmitted pulse such as spectral/temporal additional degrees of freedom for a given input pulse. Finally, we illustrate a typical spatio-temporal, or equivalently spatio-spectral, speckle field resulting from propagation of an ultrashort pulse through a scattering medium.

Time-of-flight distribution and spectral correlation

In the multiple scattering regime, light transport is diffusive. Therefore, the averaged transmitted pulse could be obtained by solving the diffusion equation, as developed in section 1.2.1, with an incident short pulse through a scattering medium [Patterson et al., 1989]. Experimental measurements of arrival time distributions of photons are in good agreement with this predicted theory [Genack and Drake, 1990, Johnson et al., 2003]. This so-called time-of-flight distribution is characterized by the exponential decay of its tail, with a characteristic time: τ_m the averaged confinement time of photons described by Equation 1.9. For instance, with a 100 fs ultrashort pulse centered around $\lambda \simeq 800$ nm, typical highly scattering media such as titanium dioxide TiO_2 nanobeads or macroporous gallium phosphide GaP (thickness 20 μm - 100 μm) exhibit $\tau_m \sim 1$ ps - 10 ps [Johnson et al., 2003]. A typical time-of-flight distribution of photons, through a GaP sample, is shown in Figure 1.16.

This time-domain point of view has an equivalent in the spectral domain: time-of-flight distribution is the Fourier transform of the field-field correlation function with frequency C^E defined as $C^E(\Delta\omega) = \langle E(\omega)E^*(\omega + \Delta\omega)\rangle$ via the Wiener-Khinchine theorem [Genack and Drake, 1990]. In essence, for a path of length l, a change of frequency $\Delta\omega$ implies a phase difference in the total accumulated phase $\delta\varphi = 2\pi l\Delta\omega/\omega$. The monochromatic speckle pattern is then λ-dependent.

Experimentally, the intensity-intensity correlation function with frequency $C^I \propto |C^E|^2$ can be measured by correlating speckle pattern intensity images [Shapiro, 1986], that can

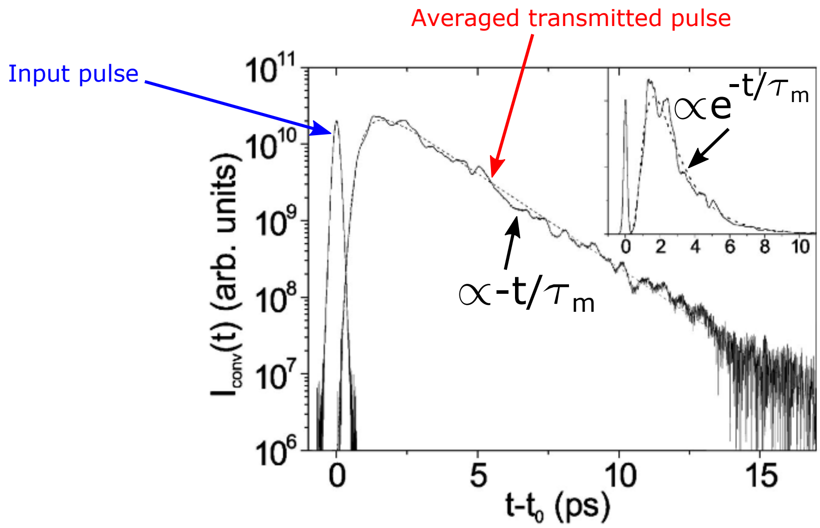

Figure 1.16 – Time-of-flight distribution of photons after propagation through a strong disordered medium. Time-of-flight distribution of photon passing through a thick GaP sample, plotted in log scale. Tail of time-of-flight distribution has an exponential decay (see inset), from which the average confinement time of photons in the scattering medium τ_m can be extracted. Image adapted from [Johnson et al., 2003]

be for instance measured with a CCD camera, for different wavelengths with a tunable cw source [Andreoli et al., 2015]. Examples of C^I are illustrated in Figure 1.17b. Its characteristic width $\delta\lambda_m$ in the wavelength domain, or equivalently $\delta\omega_m = 2\pi c \delta\lambda_m/\lambda_0^2$ in the frequency domain, defines the spectral correlation bandwidth of the scattering medium. In essence, two monochromatic speckle patterns recorded at wavelength λ_1 and λ_2 can be considered uncorrelated if the wavelength difference $\Delta\lambda = \lambda_2 - \lambda_1 \gtrsim \delta\lambda_m$. $\delta\lambda_m$ represents then the characteristic size of a spectral speckle grain, which is the typical fluctuation of intensity at a given position as a function of wavelength [Goodman, 2007]. $\delta\lambda_m$ is inversely proportional to τ_m because of the Fourier relationship between time-of-flight distribution and C^I.

Spectral/Temporal degrees of freedom for a pulse

An ultrashort pulse, that is characterized by its spectral width $\Delta\lambda$, is then spectrally significantly distorted if $\Delta\lambda > \delta\lambda_m$. Similarly, in the temporal domain, an ultrashort pulse of duration δt will be temporally distorted if $\delta t < \tau_m$. Precisely, the number of spectral or temporal speckle grains N_λ within the bandwidth of the pulse is defined as:

$$N_\lambda = \frac{\Delta\lambda}{\delta\lambda_m} = \frac{\tau_m}{\delta t} \tag{1.28}$$

N_λ represents the number of spectral degrees of freedom [Lemoult et al., 2009], which stands for the number of spectral channels. This number not only depends on the scattering medium via $\delta\lambda_m$, but also on the bandwidth of the input ultrashort pulse itself. In essence, the spectral bandwidth of the pulse contains approximately N_λ uncorrelated "spectral" speckle grains. Therefore, when an ultrashort pulse of light, characterized by its spectral width $\Delta\lambda$, is propagating through a scattering medium, characterized by its spectral correlation bandwidth $\delta\lambda_m$, the transmitted pulse can be considered as a superposition of N_λ monochromatic speckle patterns, as shown in Figure 1.17a. The contrast

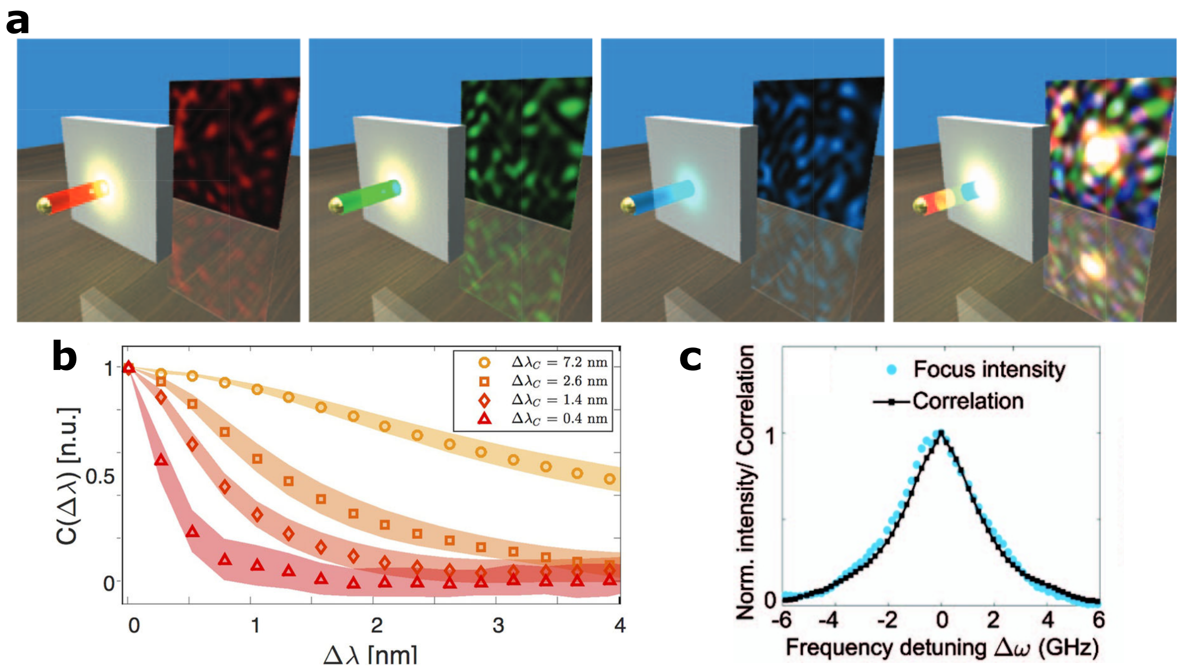

Figure 1.17 – Wavelength-dependent monochromatic speckle. Monochromatic light passing through a scattering medium leads to a speckle that depends on the incident wavelength. **(a)** Three individual different spectral components (on the left) give rise to three uncorrelated speckle patterns. Combination of the three incident colors (last on the right side) generates a complex spatio-spectral speckle, that is the incoherent sum of the previous monochromatic speckle patterns. **(b)** Correlation between monochromatic speckles as a function of spectral detuning, for four samples of different thicknesses with the same $l^{\star}$. Spectral correlation bandwidth of the scattering medium $\delta\lambda_m$ can be extracted. **(c)** A monochromatic focus has the same spectral bandwidth as the medium: light is controlled only for a single spectral channel. Images adapted from **(a)**: [Mosk et al., 2012], **(b)**: [Andreoli et al., 2015], **(c)**: [van Beijnum et al., 2011]

of transmitted light C, that is defined by the ratio between fluctuation of spatial intensity and its mean average, scales as $C = 1/\sqrt{N_\lambda}$. Measuring the contrast is then an alternative method to obtain N_λ [Curry et al., 2011].

Wavefront shaping experiments to focus monochromatic light at wavelength λ_0, as presented in Section 1.3, are then efficient only over a spectral interval centered around λ_0. The spectral width of this interval is precisely $\delta\lambda_m$: only a single spectral channel is controlled [van Beijnum et al., 2011]. In Figure 1.17c, the intensity of a monochromatic focus, obtained with an iterative optimization algorithm at a single wavelength, is plotted as a function of frequency detuning. The measured focus bandwidth is equal to the spectral correlation bandwidth of the medium. This spectral diversity has been used to exploit a strongly disordered medium as an accurate spectrometer [Small et al., 2012, Redding et al., 2013, French et al., 2017].

Spatio-temporal speckle

After propagation through a thick scattering sample, an ultrashort pulse is both distorted in the spatial and in the spectral domain. This spatio-temporal coupling performed by the scattering medium results in a spatio-temporal, or equivalently a spatio-spectral, speckle pattern, as illustrated in Figure 1.18a.

A direct characterization of the spatio-temporal speckle, using methods discussed in section 1.4.2, is challenging, mostly because energy in a single spatial speckle grain is very low. Indeed, for a thick scattering sample of optical thickness $L/l^\star \sim 10$, transmitted energy is around 10% according to Ohm's law (see Equation 1.8). This energy is split over N_{speckle} speckle grains, that is on the order of the number of scattering channels: with $N_{\text{speckle}} \sim 10^4$ grains, the energy per speckle grain is around 10^{-5} lower than the input power. Consequently, characterization techniques that require non-linear crystals, and thus implicitly a high peak power, are then unadapted.

Spectral interferometry techniques enable us to measure accurately both the amplitude and the phase of the spatio-spectral speckle field [Tajalli et al., 2012, McCabe et al., 2011]. The Fourier transform of the spatio-spectral complex electric field along the frequency axis enables the reconstruction of the spatio-temporal speckle. The spatio-temporal speckle can also be measured by exploiting time-resolved methods for 50 ps pulses [Tomita and Matsumoto, 1995]. In the temporal domain at a given spatial position, the intensity fluctuates over a characteristic time-width that is equal to the duration of the input pulse, over a temporal interval $\sim \tau_m$ (see Figure 1.18b). Similarly to the spectral speckle, around N_λ, as defined in Equation 1.28, temporal speckle grains can be found in a temporal interval of duration τ_m.

In order to manipulate the spatio-temporal speckle, one needs, in addition to chromatic aberration corrections [Martinez et al., 2017], to control scattering effects over the spectrum of the input pulse. In the next Section, we discuss how we can use only the spatial degrees of freedom of a single spatial light modulator to perform wavefront shaping experiments with ultrashort pulses.

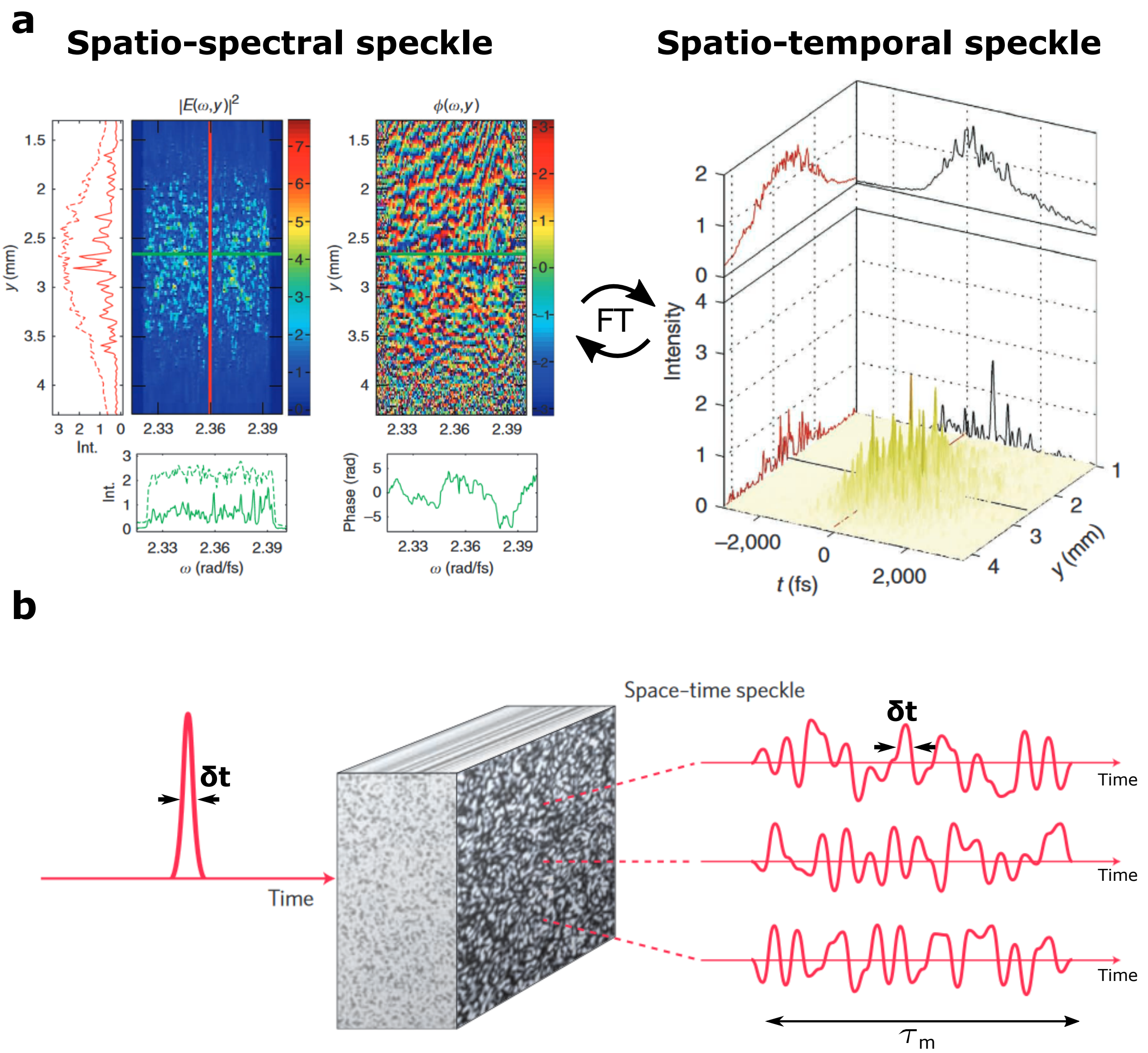

Figure 1.18 – Spatio-temporal/spectral speckle. Propagation of an ultrashort pulse of light through a thick scattering medium leads to both spatial and temporal distortions of light. The corresponding spatio-spectral/temporal speckle pattern results from coupling between spatial and spectral/temporal channels. **(a)** The associated field of the spatio-spectral speckle can be obtained with spatially and spectrally resolved interferometry techniques. Once amplitude and phase are known, a Fourier transform gives access to the spatio-temporal speckle. **(b)** In the temporal domain, a short Fourier-transform limited ultrashort pulse of duration δt is temporally distorted. The temporal profile is different in every output spatial position. This "temporal speckle" smallest feature has a duration equal to the duration of the input pulse. The transmitted pulse is stretched over a temporal interval τ_m, which corresponds to the averaged confinement time of photons inside the scattering medium. Averaging this temporal speckle over spatial position leads to the time-of-flight distribution presented in Figure 1.16. Images adapted from **(a)**: [McCabe et al., 2011]; **(b)**: [Weiner, 2011].

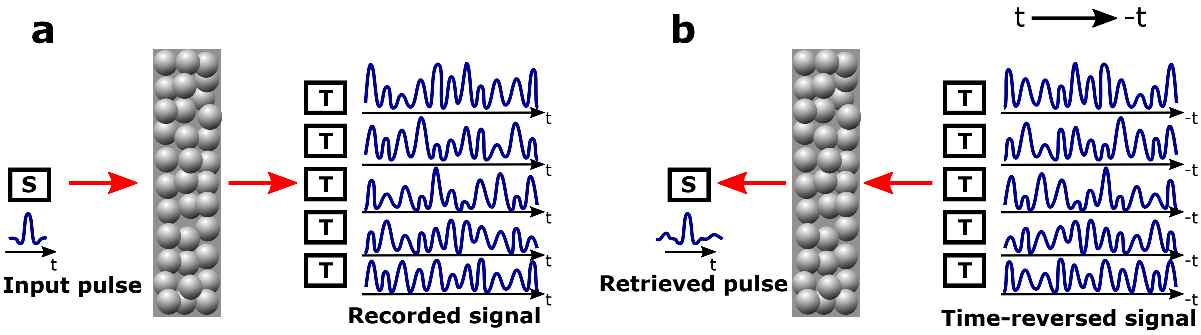

Figure 1.19 – Time-reversal of acoustic waves. Temporal reciprocity of the wave equation is at the origin of time-reversal experiments. **(a)** In a first step, an ultrasound pulse is propagating through a multiple scattering sample, and detected with few transducers on the other side of the medium. Temporal signals are digitally recorded. **(b)** In a second step, temporal signal measured previously are reversed. Transducers are emitting these time-reversed signals back to the sample. At the source location, a short pulse is detected at a given delay time, with similar duration as the input pulse. S: source; T: transducer

1.5 Spatial light modulation of a transmitted ultra-short pulse through highly disordered media: spatio - temporal focusing

Experiments discussed in Section 1.3 exploit spatial light modulators to control a monochromatic speckle pattern, for instance to focus light at a given output position. This approach breaks down when attempting to control an ultrashort pulse of light. Indeed, a monochromatic focus only governs a single spectral channel [van Beijnum et al., 2011], while the corresponding input phase pattern generates a speckle at other spectral components distanced by at least the spectral correlation bandwidth of the medium $\delta\lambda_m$. A spatio-temporal focus requires light to be focused in a given output position and recompression of the stretched pulse back to its initial Fourier-limited duration: one needs to adjust the N_λ spectral/temporal degrees of freedom simultaneously.

Nonetheless, a scattering medium under illumination of an ultrashort pulse of duration $\delta t < \tau_m$, with τ_m the averaged duration of the pulse after the medium, couples both spatial and spectral degrees of freedom. With a single SLM, one can manipulate the spatial degrees of freedom to adjust the delay between different optical paths. Therefore, both spatial and temporal distortions can be compensated using wavefront shaping techniques [Lemoult et al., 2009].

In this Section, we review the methods that have been developed to control an ultrashort pulse of light through turbid media. After a reminder from acoustics on time-reversal experiments, we detail the three main techniques, up to now, that provide spatio-temporal focusing: pulse shaping, digital optical phase conjugation and iterative optimization algorithms.

1.5.1 Time-reversal of waves

In acoustics, spatio-temporal coupling of degrees of freedom have been exploited over the last 25 years to control ultrasound propagation in disordered systems. More precisely, reciprocity of the propagation equation as a function of time has led to an interesting discovery: time reversing the signal received at a given position enables spatio-temporal focusing on the initial source position at a specific time [Prada and Fink, 1994, Fink, 1997]. In a mathematical formalism, if the field $A(\mathbf{r}, t)$ is a solution of the wave equation, the anti-causal field $A(\mathbf{r}, T-t)$ is also a solution, with T an arbitrary time delay.

This so-called *time-reversal* process requires time-resolved measurements of the scattered pulse of many scattering channels, which is much easier in acoustics and microwaves than in optics. A source emits an ultrasound pulse, which is detected on the other side of a random medium (or eventually in a reflection setup where detectors are on the same side as the source) with an array of transducers. Temporal traces are digitally recorded. In a second step, these temporal signals are flipped: time is reversed. Transducers emit backwards time-reversed signals. Reciprocity of the wave equation implies waves follow the same scattering channels backwards: the wave gets focused back onto the source.

An incomplete time reversal, with a few set of ultrasound transducers, eventually enables pulse retrieval, as the method is robust to initial conditions [Derode et al., 1995]. Figure 1.19 illustrates a standard time-reversal process, with an array of transducers to detect, to record, and to back-propagate temporal profiles of the scattered pulse. Similarly to the scattering lens (see Figure 1.8), time reversal increases the resolution of the aperture thanks to multiple scattering, and could enable sub-wavelength focusing using evanescent waves [Lerosey et al., 2007]. Time reversal has been extended to different kind of waves that possess time reversibility of their propagation equation, such as water waves [Bacot et al., 2016]. In optics, time-reversal finds an analogy with phase conjugation [Rotter and Gigan, 2017].

1.5.2 Spectral pulse shaping

Weiner and colleagues pioneered *spectral pulse shaping* techniques in the early 1990s to straightforwardly manipulate both spectral amplitude and spectral phase of an ultrashort pulse [Weiner et al., 1988]. Pulse shaping consists in decomposing an ultrashort pulse into its spectral components by a spectral disperser, usually a grating, and a lens (See Figure 1.20). All the spectral components are then spatially separated: they can be addressed and shaped independently thanks to the spatial degrees of freedom of the SLM, that is located in the Fourier plane of the grating. Symmetrically, the spectrally shaped components are recombined onto another grating with a second lens, or by exploiting back-reflection on the SLM: temporal profile of the output pulse can be designed at will with spectral pulse shaping [Weiner, 2000]. A typical pulse shaping setup is shown in Figure 1.20. Pulse shaping has been extensively exploited over the last decades, for instance in coherent control to enhance multi-photon transitions [Meshulach and Silberberg, 1998, Cruz et al., 2004] or to probe physico-chemical processes [Dantus and Lozovoy, 2004]. Nonetheless, such spectral shaping methods have limitations, such as spectral resolution because of the discretization of the SLM pixels. Also, gaps between SLM pixels lead to replicas of the input beam in the temporal domain, that can be compensated in principle [Monmayrant et al., 2010].

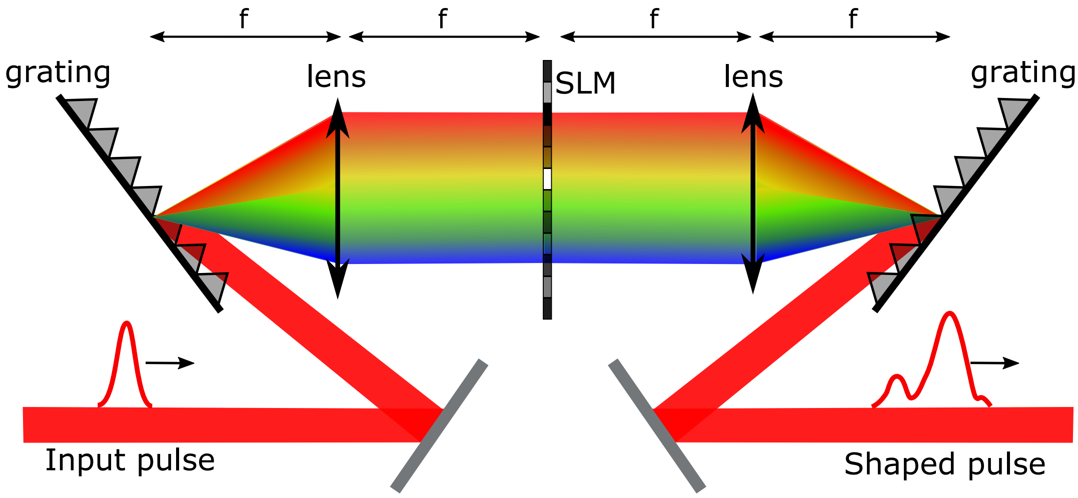

Figure 1.20 – Pulse shaping of an ultrashort pulse. Spectral amplitude and spectral phase of an ultrashort pulse are shaped directly in the spectral domain with a 4f imaging system. The input pulse is focused on a grating, that is imaged with a lens on a spatial light modulator: every spectral components can be adressed independently on the SLM. The SLM is conjugated with another grating via another lens. The obtained pulse can be temporally shaped at will via spectral shaping.

Nevertheless, an ultrashort pulse sees its spectral amplitude and phase blurred after propagation through a scattering medium. If scattering effects on the spectral field can be quantified, then they can be adjusted for all the spectral components with a pulse-shaping technique, similar to Figure 1.20. McCabe and colleagues have realized precisely that experiment [McCabe et al., 2011]. An ultrashort pulse, sent through a thick layer of paint, turns into a spatio-temporal speckle as in Figure 1.18. This spatio-spectral speckle is measured with spatially-and-spectrally resolved interferometry thanks to a reference pulse, both in amplitude and phase. In a second step, a pulse shaper, that is located before the pulse propagates through the scattering sample, adjusts the spectral profile of the ultrashort pulse in a single step. At the output, this corresponding shaped pulse is shown to be compressed temporally close to its initial duration, and spatially focused. Pulse shaping can thus be used similarly to time-reversal mirrors in the optical regime.

1.5.3 Digital Optical Phase Conjugation

In Section 1.3.3, we presented digital optical phase conjugation (DOPC) of a continuous wave distorted by a scattering medium. Exploiting the same principle, this approach has been extended to ultrashort pulse laser sources. For instance, a second harmonic generation (SHG) signal, generated by $BaTiO_3$ nanocrystal under excitation of a 150 fs pulse, was successfully focused back onto the source (the crystal itself) after propagation through a scattering medium via DOPC [Hsieh et al., 2010].

More recently, spatio-temporal focusing of a short pulse was built on with DOPC technique after propagation through a multimode fiber (MMF) [Morales-Delgado et al., 2015]. Figure 1.21 is presenting the experimental set-up and the corresponding results. A 440 fs pulse is propagating through a step-index multi-mode fiber. Modal dispersion of the fiber tends to temporally broaden the output pulse. The output pulse interferes with a reference pulse onto a camera, that is pixel-by-pixel coupled to a spatial light modulator. A delay line in the reference beam enables to time-gate photons at a given arrival time: in essence the cross-term of the interference selects a single temporal speckle grain if the reference pulse is short. The speckle field, at a given delay line position, is measured with off-axis holography on the camera. In a second step, the phase conjugated field is displayed onto the SLM: the reference beam is reflected on the SLM before back propagating through the fiber. The output pulse is measured on both a camera and an interferometric auto-correlator to probe the temporal profile of the pulse. DOPC enables us to both spatially and temporally focus the output pulse: its temporal profile is peaked, and its time-width is almost similar to the input pulse duration. The output pulse can be focused at any arbitrary time in a single measurement, similar to time-reversal. Nonetheless, DOPC experiments requires a meticulous alignment procedure, to precisely match pixels of the camera to pixels of the SLM.

1.5.4 Iterative Optimization algorithm

In Section 1.3.2, different iterative optimization algorithms have demonstrated their efficiency in controlling continuous wave light propagation through disorder. Monochromatic light is composed of a single spectral channel: the different optimization algorithms all converge to the same solution. However, an ultrashort pulse sent through a thick scattering medium generates additional spectral degrees of freedom. Spatio-temporal focusing requires a full control of all the spectral channels, coupled to an accurate control of the spectral phase, to allow temporal compression of the stretched pulse. Optimizing intensity at a given spatial position of the spatio-spectral speckle detected on a camera, similar to cw light condition, will not ensure a temporal compression, but spatial-only focusing as the spectral channels are not individually addressed [Paudel et al., 2013], although some interesting effects arise on the spectrum. Therefore optimization algorithms are trickier to exploit with a broadband source, in comparison with cw light, to achieve spatio-temporal focusing.

One needs to find a metric for the iterative optimization algorithm that provide spatio-temporal focusing. Two relevant methods based on time-dependent feedback signal led to spatio-temporal focusing of an ultrashort pulse, based either on a linear heterodyne detection [Aulbach et al., 2011], and on optimizing a non-linear signal [Katz et al., 2011].

With linear feedback

When the spectrally integrated intensity speckle is used as a CCD-based feedback, spatio-temporal focusing does not occur [Paudel et al., 2013]. Indeed, a transmitted pulse can be spatially focused in a given position, but spectral control is missing. Similarly, a spectrometer-based feedback can enhance light delivery at specific spectral components of the pulse, however the spectral phase of the output pulse cannot be properly adjusted [Paudel et al., 2013]. In order to temporally recompress the pulse to its initial duration, one must simultaneously address either the N_λ spectral channels and their relative spectral phase, or the enhancement of a single temporal channel. While adjusting all the spectral degrees of freedom cannot be performed trivially, a single temporal channel can be filtered using an interferometric external reference arm, which acts as a time-gating technique [Aulbach et al., 2011]. Indeed, when an external ultrashort pulse reference

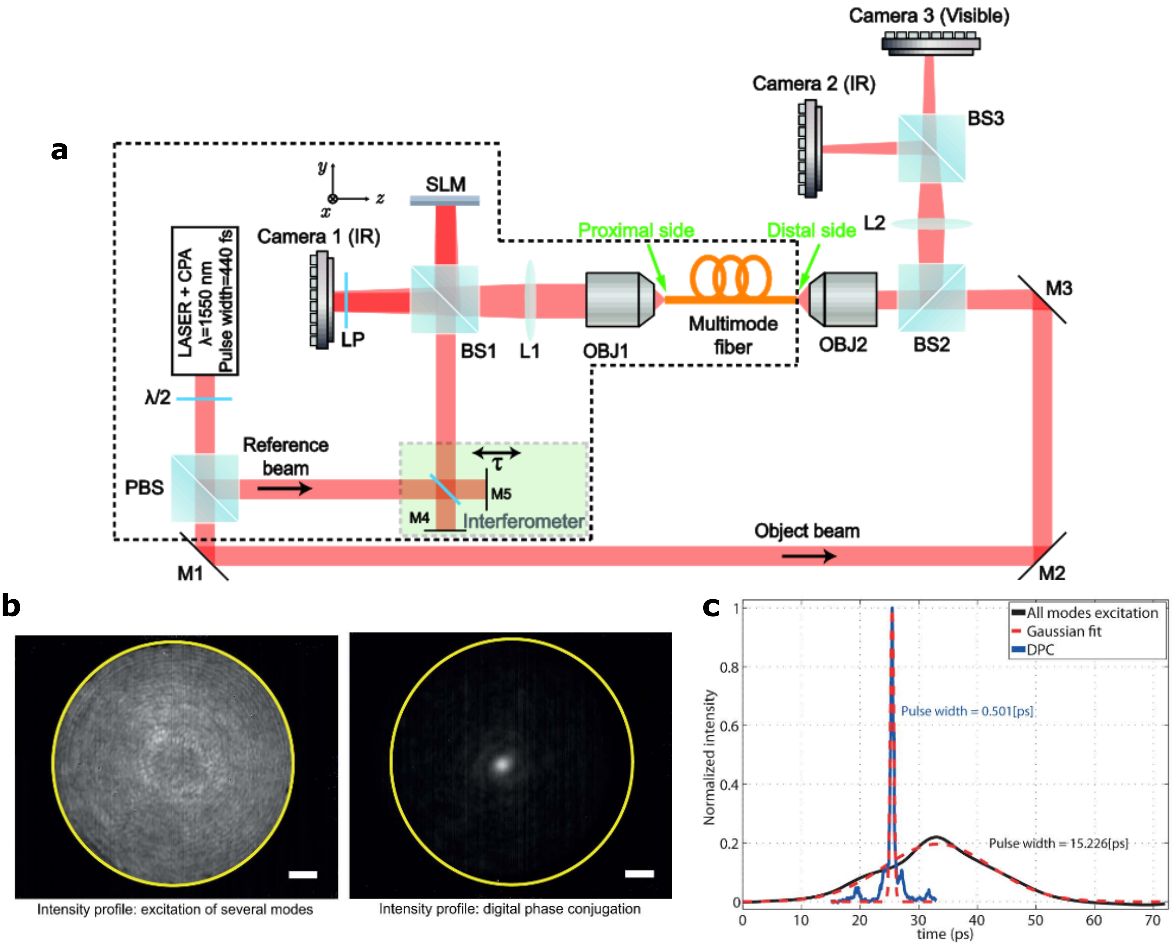

Figure 1.21 – Digital optical phase conjugation of a short pulse. (a) Typical experimental set-up. A 440 fs pulse centered at $\lambda_0 = 1550$ nm is injected into a step-index multimode fiber via a microscope objective OBJ2. The output pulse is interfering with a tilted reference beam. A delay-line in the reference beam enables to filter photons arriving at a given time. An off-axis hologram is recorded at a given time on Camera 1. Its phase conjugate is displayed on the SLM. The reference beam is back propagating into the fiber. The output facet is imaged on camera 2 and an autocorrelator (camera 3). **(b)** Image of the output facet of the fiber without (left) and with (right) DOPC. DOPC is building up a focus among the background speckle. **(c)**Temporal profile without DOPC (in black) and at the focus obtained with DOPC (in blue). The output pulse recovers almost its initial duration with DOPC. Images adapted from [Morales-Delgado et al., 2015]

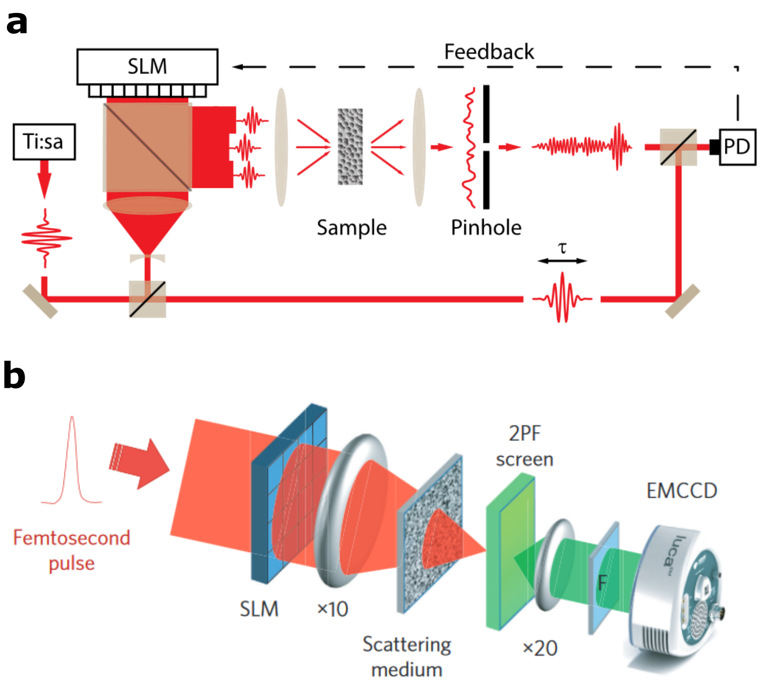

Figure 1.22 – Iterative optimization algorithm with a short pulse for spatio-temporal focusing. Different feedback-based algorithm have been employed. **(a)** With linear heterodyne feedback **(b)** With two-photon fluorescence feedback. Images adapted from: **(a)**: [Aulbach et al., 2011]; **(b)**: [Katz et al., 2011]

beam interferes with the distorted pulse, the heterodyne signal corresponds to the cross-correlation between the spatio-temporal speckle and the reference pulse. In essence, the external arm, as illustrated in Figure 1.22a, acts as a time-gate: the interference term comes from photons arriving only at a chosen delay time dictated by the reference pulse: only a single temporal channel can be chosen. This signal, measured with a photodiode, is then used as a feedback for the optimization algorithm and it converges to spatio-temporal focusing. The spatial position is chosen by inserting a pinhole to spatially filter only a single speckle grain, and the arrival time of the output pulse is fixed with a delay line in the reference arm. Figure 1.22a illustrates the experimental setup.

With non-linear feedback

An alternative feedback signal could come from a non-linear process, such as two-photon absorption. Indeed, two-photon absorption turns into a more intense signal if the pulse is temporally shorter [Zipfel et al., 2003, Helmchen and Denk, 2005]. Two methods exploiting two-photon feedback signal have been developed:

- The two-photon fluorescence signal, emitted from a fluorescent thin capillary named "two-photon screen", is spatially-resolved with a CCD camera, using an experimental set-up similar to Figure 1.22b. An iterative optimization algorithm can enhance the intensity at a given output position to generate a spatio-temporal focusing [Katz et al., 2011, Aulbach et al., 2012b]. Nonetheless, most of two-photon fluorescent microscopy systems are not spatially resolved.
- The total fluorescent signal is recorded with a photodiode, similarly to a non-linear microscopy experiment. Optimizing this signal leads to a spatio-temporal focus,

nonetheless the spatial position of the focus cannot be predicted [Katz et al., 2014b].

Nevertheless, the scattering medium must be thin enough to let sufficient transmitted energy, meaning a sufficient peak power at the focus position, for exciting the non-linear process. Thus, this approach breaks down for very thick scattering media.

1.6 Summary

In this chapter, we presented and described light propagation through highly disordered media. Light gets strongly distorted both in space and time because of scattering effects. Wavefront shaping experiments were developed to control light through scattering media, both spatially and spectrally/temporally, but also its polarization state [Guan et al., 2012] and even its orbital angular momentum [Fickler et al., 2017]. In essence, exploiting the spatial degrees of freedom of a spatial light modulator onto the huge number of scattering modes of a disordered medium transforms the latter into a highly multi-modal platform, that could be useful for imaging, telecoms and optical computing.

In particular, the monochromatic Transmission Matrix enables deterministic light control, in addition to carrying information on light propagation through the scattering medium. Nonetheless, this approach breaks down under illumination of an ultrashort pulse. Indeed the monochromatic transmission matrix would only enable the control of a single spectral channel. The aim of this thesis is to extend the previous monochromatic optical transmission matrix approach to the broadband regime. In contrast with iterative optimization algorithms and DOPC methods, this matrix approach would contain additional information such as the spatio-spectral coupling of light by the scattering medium, or a deterministic control of its temporal profile. Before specifying in detail the developed methods, we present the experimental setup that was developed during this thesis in Chapter 2.

Chapter 2

Elements of the experimental setup

Contents

The objective of this thesis is to demonstrate full control of an ultrashort pulse in multiple scattering media, based on a transmission matrix (TM) approach. Different methods, that will be developed in Chapter 3, Chapter 4 and Chapter 5, are based, with some slight differences, on the same experimental setup.

In this Chapter, we present, in detail, the experimental setup. We first introduce a scheme of the experimental setup, that has been intensively exploited along the thesis. In the next Sections, we describe each part of the experimental setup, including their conceptions and characterizations: multiple scattering medium, non-linear sample, and characterization of the output pulse.

2.1 Experimental setup

In this section, we introduce, in detail, the scheme of the experimental setup, that will be used in the following chapters. Figure 2.1 illustrates the setup. The illumination laser source is a Ti:Sapphire oscillator, whose properties are given in Section 2.1.1. A spectrometer is placed at the output of the laser with a beam splitter to verify the spectrum of light. The laser beam is expanded and filtered with a pinhole in the Fourier plane of a telescope. The beam is split in two different beams with a polarized beam splitter: a reference beam and a signal beam. The ratio between light propagating in either paths is tunable with a half wave plate. The path of each beam is controlled as follows:

- The signal beam is reflected on a phase-only spatial light modulator (SLM), that is described in Section 2.1.2. The SLM is imaged onto the back focal plane of a microscope objective (Olympus UMPlan FI, 10x, numerical aperture 0.3), by exploiting a 4f imaging system (not shown in Figure 2.1). Light is then sent through a scattering medium (See Section 2.2). The transmitted speckle is collected with another microscope objective (Olympus LMPlan FI, 100x, numerical aperture 0.85). The scattering medium output facet is imaged onto a two-photon fluorescent sample (See Section 2.3) with a different microscope objective. Both output linear and fluorescent signals are collected with a fourth microscope objective, similarly to a trans-illumination microscopy setup. A long-pass filter is added between the scattering medium and the non linear sample, to filter out residual autofluorescence of the scattering medium.
- The reference beam contains a delay line, to adjust delay between reference and signal beams. Polarization of the reference beam can be rotated with a half plate wave. The reference beam can be blocked with a computer-controlled shutter (Thorlabs SH05, controller Thorlabs SC10).

The two paths have a similar optical length: both the ultrashort reference pulse and the stretched pulse are overlapped in space and time on a beam splitter. An uncoated bi-convex lens (Thorlabs LB1945) images the linear output intensity on a CCD camera

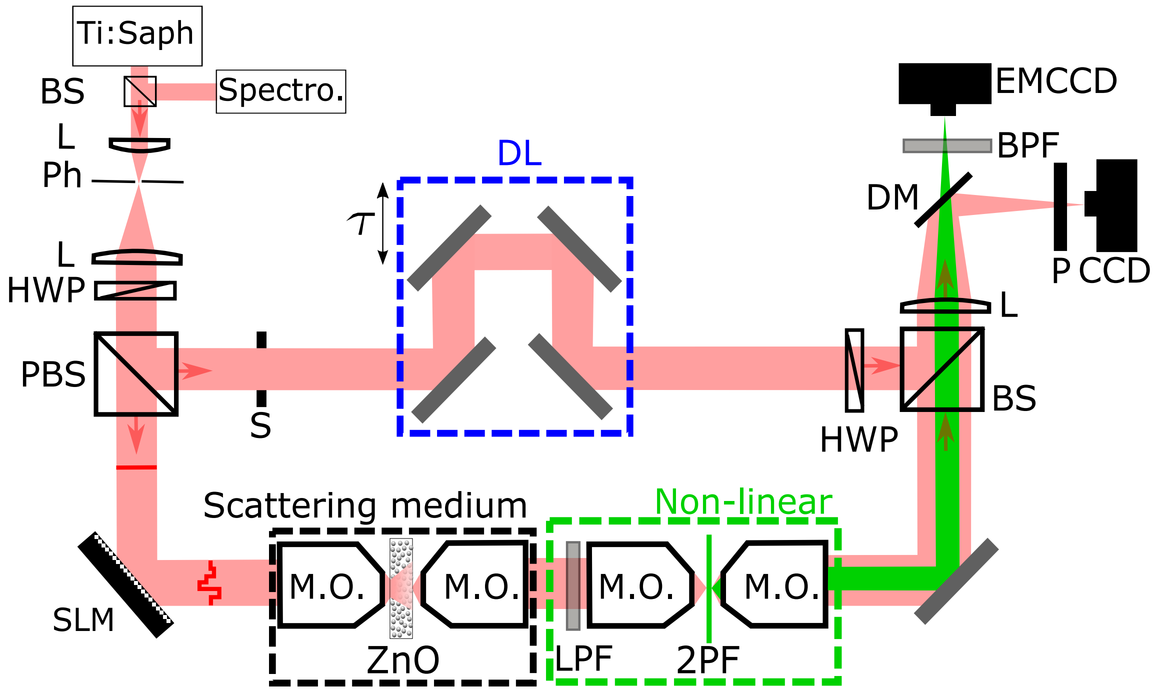

Figure 2.1 – Experimental setup for spatio-temporal control of an ultrashort pulse through a scattering medium. The laser source, emitted from a Ti:Saph oscillator, has two operating modes: either tunable cw, or mode-locking that generates an ultrashort pulse of duration 100 fs at FWHM. Laser beam is expanded and it illuminates a phase-only Spatial Light Modulator (SLM), which is conjugated with the back focal plane of a microscope objective. The scattering medium is a thick (around 100 μm) sample of ZnO nanoparticles, placed between two microscope objectives. The output facet is imaged on a two-photon fluorescence (2PF) sample. A long-pass filter (LPF) allows one to eliminate the autofluorescence of ZnO. A dichroic mirror (DM) separates the two-photon fluorescence signal (imaged with an EMCCD camera) from the linear signal (imaged with a CCD camera). A delay line (DL) is adjusting delay between reference beam and scattered light. A shutter (S) may block the delay line, for instance when performing spectral correlation measurements. Lens (L), pinhole (Ph), half plate wave (HPW), polarized beam-splitter (PBS), delay line (DL), beam splitter (BS), polarizer (P), band pass filter (BPF), spectrometer (Spectro.).

(Manta G-046, Allied Vision, pixel pitch 8 × 8 μm), while the non-linear signal is recorded with an EMCCD camera (iXon Ultra, Andor, pixel pitch 16 × 16 μm, electronic gain: 300). A dichroic mirror (Semrock FF720) separates linear and non-linear signals. An additional band-pass filter, that is located before the EMCCD camera, selects wavelengths between 350 nm and 550 nm, to improve the non-linear signal-to-background ratio. A polarizer is placed before the CCD camera, in order to image a single polarization state of the linear speckle field. While incoming light has horizontal polarization, we image orthogonal polarization state: the few ballistic photons that may have survived through the scattering medium are thus not imaged.

All the devices, including laser source, spectrometer, SLM, delay line, shutter, CCD camera, and EMCCD camera are controlled simultaneously via a Matlab-based automation, that was developed during this thesis.

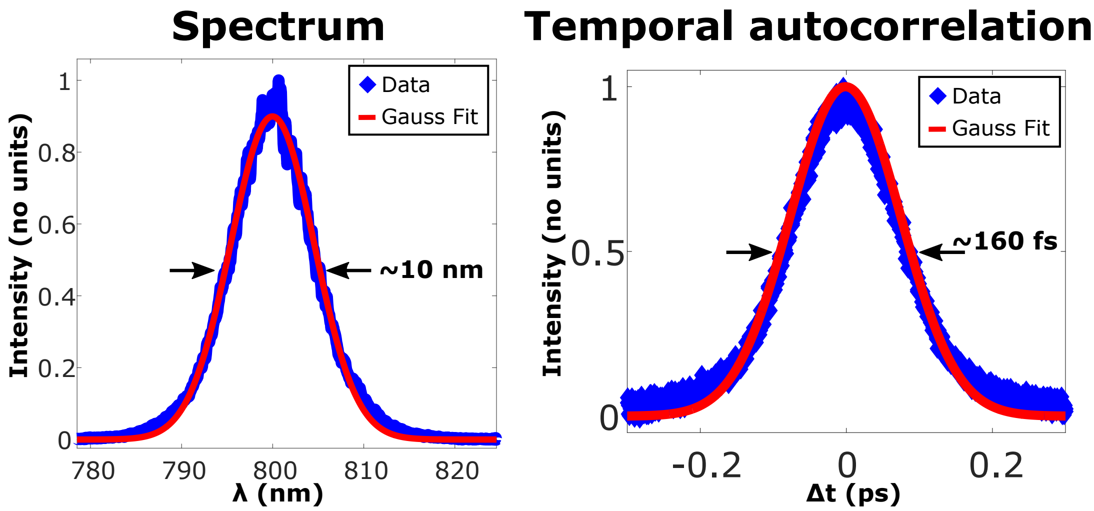

Figure 2.2 – Spectral and temporal characterization of the output pulse from the laser source. Ultrashort pulse laser source properties are verified with an external spectrometer, and an interferometric autocorrelator. Only spectral amplitude is measured: a Gaussian fit leads to a spectral width FWHM $\sim 10\ \mu$m. Envelope of temporal autocorrelation trace can be fitted with a Gaussian or a sech^2 function. FWHM is $\sim$ 160 fs: pulse duration is estimated around 100 fs.

2.1.1 Laser source

A mode-locked Ti:Sapphire oscillator (Mai Tai, Spectra Physics) generates ultrashort pulses, with a repetition rate 80 MHz. The central wavelength is tunable between 700 nm and 900 nm. We arbitrarily fix the central wavelength at 800 nm, as the SLM (See Section 2.1.2) efficiency is at its highest at this wavelength. Averaged power is around 2W when the central wavelength is set to 800 nm. Pulse duration is measured with an interferometric autocorrelator (PulseCheck, APE). We have placed the autocorrelator after propagation in the reference beam, in transmission of the beam splitter of Figure 2.1, after blocking signal path. The envelope of the temporal trace is plotted in Figure 2.2. FWHM is around 160 fs. This measured trace can be fitted with a Gaussian envelope: pulse duration is estimated to be around 100 fs.

The spectrum of the ultrashort pulse is also measured, using a spectrometer (HR 4000, Ocean Optics). Figure 2.2 illustrates the pulse spectrum: the pulse is centered at 800 nm. Its spectral envelope can be fitted with a Gaussian function: FWHM is $\sim$ 10 nm.

The central wavelength of the laser can be tuned. The wavelength components of the pulse are spatially dispersed via a sequence of prisms inside the cavity, and a slit is placed in this dispersed beam. Changing the position of the slit in the dispersed beam tunes the central wavelength of the pulse. This process can be achieved with the software provided with the laser.

Moreover, this laser can be mode-unlocked by closing this slit, whose width defines the spectral width of the output pulse. Closing the width impedes the oscillator to lase in its normal spectral conditions, that is consequently mode-unlocking it. This laser can then be used as a tunable cw source. Although averaged power is reduced, down to 200 mW, this trick enables measurement of the scattering medium spectral correlation (see Subsection 2.2.2), as well as determining monochromatic transmission matrices (See

Chapter 3). The central wavelength is tunable in the same spectral range as in mode-locked operation, and spectral width of monochromatic beam is ~ 0.5 nm.

The position and width of this slit can be adjusted as well via a Matlab-based automation, to control precisely the position of the central peak for both mode-locked and continuous wave operations. The step resolution of the motorized slit is ~ 0.05 nm, however the spectrometer resolution is ~ 0.2 nm. The same program allows mode-locking and mode-unlocking and vice versa: laser operation can be tuned straightforwardly between ultrashort pulses and tunable cw.

2.1.2 Spatial Light Modulator

The SLM (LCOS-SLM, X10468-2, Hamamatsu) used in this setup modulates only the phase of the incident beam on 8 bits. The liquid crystal array is composed of 800×600 pixels. The pixel pitch is $20\ \mu$m $\times$ $20\ \mu$m. The SLM is connected to a computer interface via DVI: it is considered as an additional screen. Phase is coded in 8 bits, between 0 and 255, but modulation from 0 to 2π depends on the central wavelength of the incident beam. The reflectivity at 800 nm is more than 95%: almost all energy is conserved after modulation on the SLM. However, only the horizontal polarization state can be modulated. A telescope to expand beam size is adjusted to match the size of the SLM chip pixel array.

Two characterization steps have to be performed on the SLM for calibration: determine the phase setting for phase modulation from 0 to 2π, and determine the region of the SLM the incident beam is reflected onto.

1. 0-2π modulation characterization. Assuming linearity of the phase response of the SLM, a chessboard is displayed on the SLM while a scattering medium is placed between the set of microscope objectives. A speckle pattern is thus measured on the CCD camera. Half of the pixels remain at 0, and the other half is gradually increased to 255. Transmitted speckle is thus being modulated. When a 2π phase is applied, one should recover the initial speckle. Consequently, plotting the correlation between the initial image and the corresponding measured images as a function of phase "voltage" applied on SLM pixels leads to phase calibration.

2. Beam spot position on the SLM. The horizontal top line of the SLM is modulated with a π-phase difference with the other SLM pixels. The corresponding output speckle is recorded as a function of the line position. The output speckle is not affected if the π-phase line is not into the incident beam spot position on the SLM. However, when the line hits the spot position, the output speckle is experiencing modulation. The central spot position on the SLM, as well as its spatial width, can be then accurately measured by correlating the initial image and all the corresponding measured images as a function of line position. The method is iterated for a vertical line: both horizontal and vertical lines pinpoint 2D position and size of the incident beam.

The Hadamard basis will be displayed on the SLM to measure the TM, as developed in Section 1.3.4. The active zone of the SLM is divided into N_{SLM} macropixels, where N_{SLM} has to be a 2^k with k an even number because of the Hadamard basis. Usually, we exploit $N_{\mathrm{SLM}} = 2^{10} = 1024$ independent SLM pixels.

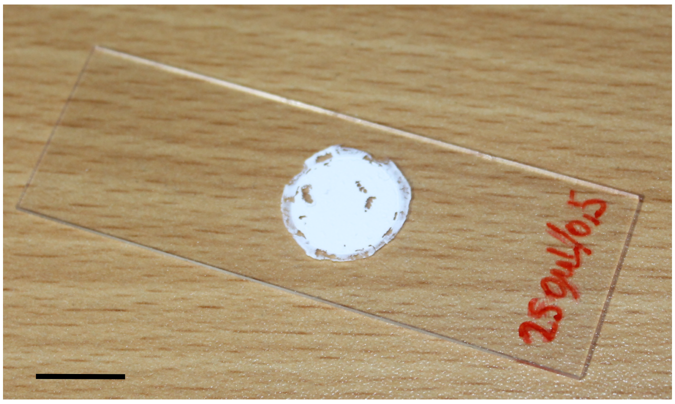

Figure 2.3 – Typical scattering sample. Scattering solution is composed of ZnO nanobeads dispersed in water (on photo: mass concentration$\sim$ 0.5%). A small volume (here 250 μL) is dropped on a microscope slide. Once the sample is dry, the scattering medium looks like a thin layer of white paint. Scale bar: 1 cm.

The SLM refresh rate is slow: it has been found to be $\sim$ 10 Hz. Although a TM measurement lasts experimentally few minutes for $N_{\text{SLM}} \sim 1000$, the SLM's low refresh rate won't be considered as an issue as long as the scattering medium remains stable in the measurement process (See Section 2.2). Nonetheless, this limited working frequency restricts the number of input modes, as the latter scales linearly with TM measurement time.

2.2 Multiple scattering medium

In this thesis, we use multiple scattering media that are prepared in the lab. In this section, we briefly present how we synthesize such scattering media, and their characteristics.

2.2.1 Fabrication

Scattering media fabricated in the lab are mostly thin layers of zinc oxide (ZnO). ZnO powder (Sigma-Aldrich, 205532) is constituted of polydisperse microbeads, of diameter < 5 μm. This white powder is dispersed in water (typically $\sim$ 0.5-1% in mass concentration), and a small volume (typically 200-400 μL) is dropped on a microscope slide. A few hours later, when the sample dries, it takes the form of a thin white layer. Figure 2.3 illustrates a typical scattering sample.

2.2.2 Properties

Spatial, stability and spectral properties are investigated in this Section. Such properties have been deeply studied in the thesis of D. Andreoli [Andreoli, 2014].

Thickness and transport mean free path

Depending on the dropped volume, thickness L of scattering medium varies between 20 μm and 200 μm. The transport mean free path $l^{\star}$ of these samples is conditioned by the concentration of ZnO nanobeads and their size. It has been measured in [Andreoli, 2014], following the method developed in [Curry et al., 2011]: the total transmission is measured with an integrating sphere for scattering samples of various thickness. Fitting the inverse of transmission as a function of thickness to Ohm's law leads to the transport mean free path. Typical $l^\star$ is estimated around $l^\star \sim 3 \pm 2\mu$m, meaning that essentially no ballistic photons are transmitted through such media.

Stability: decorrelation time

The stability of scattering media is an important issue as the SLM refresh rate is low. Stability is measured by correlating the transmitted speckles, measured with a CCD camera upon cw illumination of the scattering sample, as a function of time. Such scattering layers are stable for hours, in opposition to biological tissues, whose decorrelation time are estimated around 1-100 ms [Liu et al., 2015]. Consequently, transmission matrices of the scattering medium can be measured within tens of minutes without decorrelation.

Spectral correlation bandwidth

Spectral correlation bandwidth $\delta\lambda_m$, as defined in Section 1.4.3, is a more relevant quantity to describe a transmitted pulse through scattering media. Indeed, $\delta\lambda_m$ is directly related to the number of spectral degrees of freedom for a given input ultrashort pulse of duration δt, via Equation 1.28.

An example of the measurement of $\delta\lambda_m$ is described in Figure 2.4. The shutter of the external reference arm, in Figure 2.1, is closed for spectral measurements. A pattern on the SLM is fixed during the measurement process: it can be either a random mask, or simply a flat phase pattern. Monochromatic speckle patterns are recorded on the CCD camera while changing the illumination wavelength, using a tunable cw laser whose spectral resolution is ~ 0.25 nm. Correlation between speckle images C_λ is plotted as function of spectral detuning in Figure 2.4b. $\delta\lambda_m$ is defined by convention, as proposed in [Andreoli et al., 2015], as $C_\lambda(\delta\lambda_m) = 0.5$. Typical $\delta\lambda_m$ for ZnO scattering samples are spread between 0.01 nm to 5 nm, depending on the thickness L and transport mean free path $l^\star$. However, $\delta\lambda_m < 0.2$ nm is challenging to measure because of the spectrometer resolution. An alternative way to access $\delta\lambda_m$ is via measurement of time of flight distribution (see Section 2.4), with its characteristic time $\tau_m \propto 1/\delta\lambda_m$.

2.3 Non-linear samples

In Chapter 6, we will study the excitation of non-linear processes after propagation of ultrashort pulses through scattering media. This approach is particularly relevant for non-linear microscopy. Indeed most of the microscopy techniques only exploit ballistic photons, whose number exponentially decreases upon scattering in thick disordered systems. Nonetheless, a large number of scattered photons remain deep in tissue: they can be manipulated with wavefront shaping techniques.

In this Section, we present the two kinds of non-linear samples that have been designed and employed in this thesis. Instead of being used as a feedback signal for wavefront

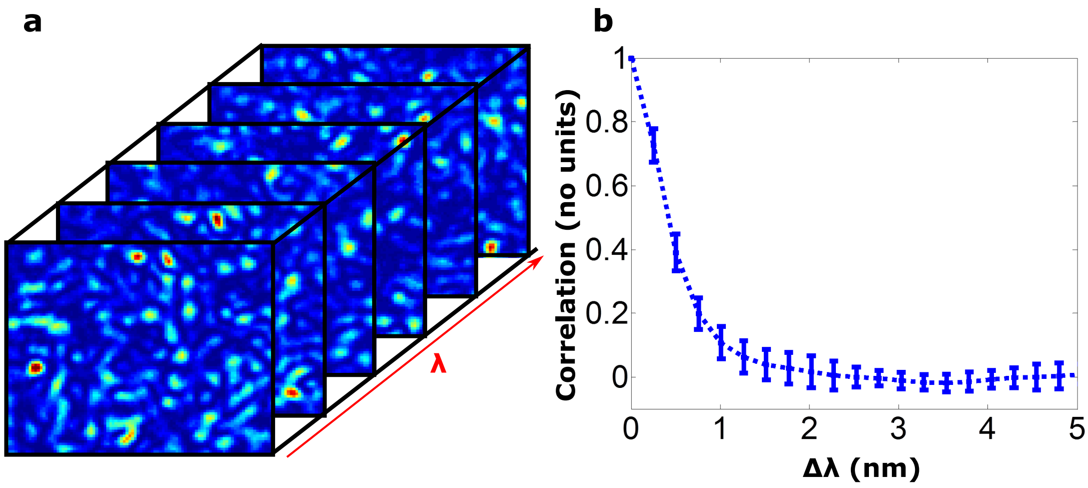

Figure 2.4 – Spectral correlation bandwidth of typical ZnO scattering samples. (a) A stack of monochromatic speckle patterns is recorded as function of illumination wavelength, using tunable cw laser. **(b)** 2D-correlation between monochromatic images C_λ as function of spectral detuning. Spectral correlation bandwidth of the scattering medium $\delta\lambda_m$ is defined as $C_\lambda(\delta\lambda_m) = 0.5$ by convention.

shaping such as in [Katz et al., 2011, Katz et al., 2014b, Aulbach et al., 2012b], the non-linear signal is here measured as a control signal *a posteriori*, for comparison between spatial-only and spatio-temporal focusing. Non-linear samples are placed after propagation through the scattering medium, as presented in Figure 2.1. In this configuration, residual autofluorescence from the scattering medium can be filtered with a low pass spectral filter: only the fluorescence from non-linear sample is detected on the EMCCD camera. Both CCD camera, measuring the "linear" speckle (at $\lambda = 800$ nm), and the EMCCD camera, measuring the "non-linear" speckle (at $\lambda = 400 - 600$ nm), are imaging the same plane.

2.3.1 Two-photon fluorescence

Two photon fluorescence (TPF) involves in general two photons of about the same energy (i.e. from the same laser source) interacting with matter: they are absorbed to produce an excitation similar to absorption of a single photon that has twice the energy. This interaction relies on two photons interacting simultaneously (less than a femtosecond). Its intensity scales quadratically with the incident light intensity. Such interaction is thus preferentially done with ultrashort pulsed lasers, as they provide high peak power with photons concentrated in short temporal intervals [Zipfel et al., 2003].

When focusing through a fluorescent sample, as in multiphoton microscopy [Xu et al., 1996], two-photon excitation is localized in 3D [Zipfel et al., 2003]. Indeed, because of its quadratic dependence on the light intensity, the two-photon absorption probability is much higher in the focal spot compared to unfocused beam and out-of-plane. Two-photon fluorescence is enhanced when pulse duration is shorter: two-photon emission is related to the averaged squared intensity $\langle I(t)^2 \rangle$, that scales linearly with squared averaged intensity $\langle I(t) \rangle^2$ and with $1/\tau$, where τ stands for pulse duration.

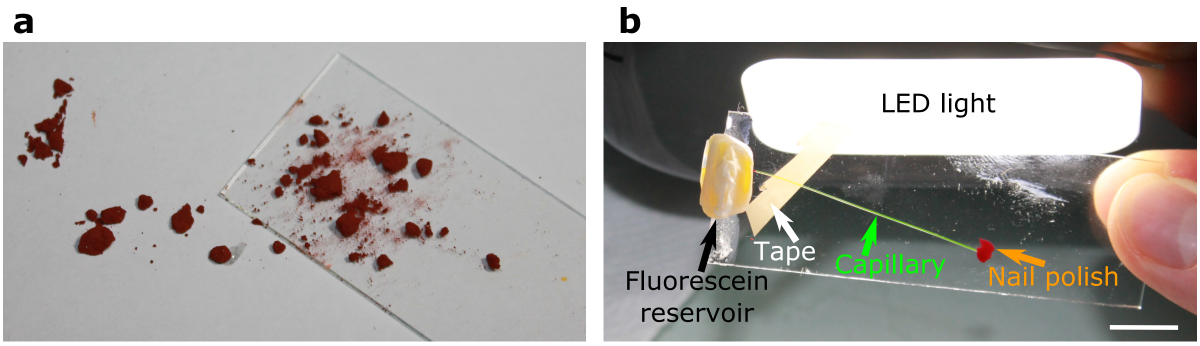

Figure 2.5 – Fluorescein sample. (a) Fluorescein sodium salt appears as a red powder. **(b)** Two-photon screen with fluorescein solution, diluted in ethanol. It is composed of a thin capillary that contains fluorescein solution, and a reservoir. Nail polish seals the extremity of the capillary. Tape fixes the capillary on the microscope slide surface. Upon illumination by a LED light, yellow fluorescein solution in the capillary turns green as it fluoresces. Scale bar: 1 cm.

2.3.2 Two-photon screen

A two-photon screen has been introduced in the context of scattering media by Katz and colleagues in [Katz et al., 2011]. A fluorescent solution is injected in a thin glass capillary. Two-photon fluorescence is then emitted under illumination of an ultrashort pulse. In this section, we present the fluorescein, a highly fluorescent molecule, that we exploit in Chapter 6 for two-photon fluorescence. We then develop the protocol, inspired by [Katz et al., 2011], to inject a fluorescein solution in a small glass capillary, in order to build our own two-photon screen.

Fluorescein

Two-photon fluorescence is emitted from fluorescein red powder (fluorescein sodium salt $C_{20}H_{10}Na_2O_5$). Fluorescein is soluble in water and in ethanol. A solution of fluorescein is inserted in a thin glass capillary (CM Scientific, 20 μm $\times$ 200μm $\times$ 5 cm). Two-photon fluorescence is emitted between 500 nm and 520 nm, under incident illumination of a Ti:Saph oscillator. The protocol to prepare the two-photon screen [Katz et al., 2011] is explained in the next subsection. For a very low fluorescein concentration in a solvent, the number of fluorescent molecules is too low to generate a non-linear signal under a constant illumination power. However, a compromise should be found between the thickness of the TPF sample and its concentration. Indeed, if the fluorescein concentration is too large, the emitted signal is reabsorbed, which leads to a total decrease of the detected TPF signal. For a given sample thickness (here 20 μm) upon illumination of a 100 fs pulse centered at 800 nm with averaged power 1.7 W, maximum detected TPF signal has been measured with a mass concentration of fluorescein in ethanol solvent $\sim 0.9\%$.

Sample preparation

The fluorescein solution seeps into the capillary via capillary action. However, ethanol is volatile: within few hours the capillary dries up. We have thus developed a protocol to prevent the capillary from drying:

1. Cut top off of a 1.5 mL microfluidic reservoir (Eppendorf): it will be used as fluorescein reservoir for the capillary.
2. Fill the reservoir with fluorescein solution ($\sim 70\ \mu$L), and close it with parafilm.
3. Stick the closed reservoir on the edge of a microscope slide.
4. Pierce a tiny hole in the reservoir with sharp tweezers, and insert an empty capillary: it gets filled. Seal the hole with nail polish.
5. Seal the other capillary extremity with nail polish.
6. Tape capillary on the microscope slide surface close to the reservoir: capillary is in contact with the slide on almost all its length.

Figure 2.5 illustrates fluorescein sodium salt as well as the assembled two-photon screen. In the experiment, the two-photon screen is placed after propagation through the scattering medium, between a pair of identical microscope objectives. Therefore fluorescence is emitted from different speckle grains within the two-photon screen. The depth of field z_R of an objective is defined as $z_R \simeq \lambda n/(\mathrm{NA}^2)$ [1], with NA the numerical aperture of the objective, λ the illumination wavelength and n the refractive index (without immersion: n=1). It should then approximately match the thickness of the two-photon screen to minimize out-of-focus fluorescence. Nonetheless, a compromise must be found between the longitudinal size of a speckle grain and the quantity of detected transmitted light. Therefore, we picked microscope objectives characterized by a magnification factor of 20, and a numerical aperture 0.4: we thus have $z_R \sim 5\mu$m.

2.3.3 Fluorescent beads

An alternative sample to use is fluorescent nanobeads. We use polystyrene beads in solution. We have tested beads of different diameters in the experimental setup shown in Figure 2.1: 200 nm, 1 μm and 2 μm. The fluorescence cross-section was too low for the 200 nm beads, requiring an extremely long exposure time to detect a two-photon fluorescent signal. The two-photon fluorescence emitted by the larger beads were easier to detect. In this thesis, we only focus on beads with nominal diameter 1 μm (F8852, Thermo Fisher).

Two-photon emission ranges in a similar spectral interval as fluorescein. A droplet of the solution containing nanobeads is dropped and spread on a microscope slide: beads are then isolated from each other. Once liquid from the solution has dried, an aqueous gel (Fluoromount Aqueous mounting medium, Sigma-Aldrich) is injected on to the beads to reduce the change in refractive index between air and the collection microscope objective, which is oil immersed. Therefore the bead positions are sensitive to temperature drift in the lab: the same sample of beads can be exploited for the experiments within $\sim$ few days. Total fluorescence is detected in transmission on the EMCCD camera.

Such fluorescent nanobeads require a pair of microscope objectives with high numerical aperture to maximize light collection. We have selected the emission objective (Olympus

[1] Nikon Microscopy U, https://www.microscopyu.com/microscopy-basics/depth-of-field-and-depth-of-focus

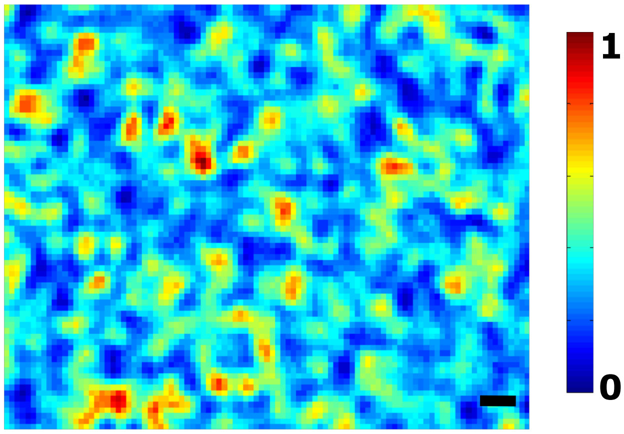

Figure 2.6 – Spatio-temporal speckle spectrally/temporally integrated, measured with an ultrashort short pulse on a CCD camera. Transmitted pulse through ZnO scattering medium is imaged on a CCD camera. The measured intensity pattern corresponds to integration of spatio-temporal speckle over time. This speckle is low contrasted: C=0.22, corresponding to an incoherent sum of $1/\mathrm{C}^2 \sim 20$ monochromatic speckles. Scale bar: 2 μm.

MplanFL N, 100x, NA 0.85) and the collection objective (Nikon Plan Apo VC, 60x, NA 1.4 oil immersion) consequently. We thus have $z_R \sim 500$ nm.

2.4 Linear characterization of transmitted pulse through scattering media

After propagation of an ultrashort pulse through thick scattering media, a spatio-temporal speckle emerges. While spatial properties of the spatio-temporal speckle can be straightforwardly measured with a standard CCD camera, spectral and temporal fluctuations are challenging to characterize. In this Section, we present linear techniques we have adapted to properly characterize, both spectrally and temporally, transmitted ultrashort pulses through scattering media.

2.4.1 Spatial content

The intensity pattern measured on the camera corresponds to the integration of the spatio-temporal speckle over time. Therefore, we cannot distinguish between a spatial focus, corresponding to enhancing intensity in a single spatial speckle grain without controlling spectral/temporal degrees of freedom, and a spatio-temporal focus. That is, a single temporal speckle grain is high in intensity.

Figure 2.6 shows a transmitted pulse intensity pattern of a spatio-temporal speckle after propagation through a thick ZnO layer, measured using a CCD camera. The number of spectral degrees of freedom N_λ can be estimated with the speckle contrast C, as $N_\lambda = 1/\mathrm{C}^2$. With C$\sim 0.22$, $N_\lambda \sim 20$: the output speckle is the incoherent sum of N_λ monochromatic speckle patterns [Curry et al., 2011].

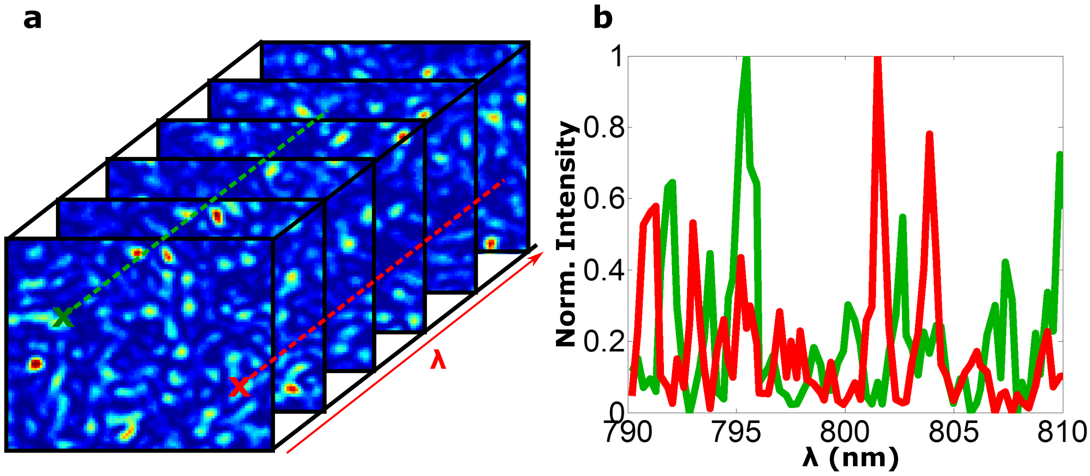

Figure 2.7 – Spectral content of a spatio-temporal speckle, measured with tunable cw light and a CCD camera. A random input pattern is displayed on the SLM. **(a)** Similarly to Figure 2.4, monochromatic speckle images are recorded for the different spectral components, over a spectral interval corresponding to the input pulse spectrum. **(b)** Monochromatic intensity in two different spatial positions (x in (a)) is plotted as function of illumination wavelength. Spectral intensity is fluctuating, with characteristic feature $\delta\lambda_m$ corresponding to the spectral correlation bandwidth of the scattering medium.

2.4.2 Spectral content

The spectral content of a spatio-spectral speckle can be quantified with a 2D-SSI-spectrometer, similarly to [McCabe et al., 2011]. Afterwards, a spatio-temporal speckle is indirectly retrieved, via a Fourier transform of the spatio-spectral field. Nonetheless, such methods have not been used in this thesis, as we have developed techniques to probe directly the envelope of the spatio-temporal speckle in the time domain (See Section 2.4.3).

Nevertheless, the spectral content of the transmitted pulse can be measured with the experimental setup shown in Figure 2.1. The Ti:Saph is mode-unlocked: monochromatic speckle images are recorded for the different spectral components of the transmitted pulse, without a reference beam. Spectral features of the spatio-spectral speckle are thus accessible for all the spatial speckle grains simultaneously. Figure 2.7 presents spectral speckle in two different spatial positions, measured with tunable cw source and a CCD camera. Spectral speckles differ between different spatial positions, illustrating the complex spatio-spectral coupling of light by the scattering medium. The spectral-width of spatio-spectral speckle features corresponds to $\delta\lambda_m$, the spectral correlation bandwidth of the medium, developed in Section 2.2.2.

2.4.3 Temporal profile: Interferometric Cross Correlation

Techniques probing the temporal profile of an ultrashort pulse, developed in Section 1.4.2, are challenging to perform after propagation through scattering media. Indeed, due to the very low averaged power per spatial speckle grain, standard nonlinear characterization methods are inappropriate, for example to excite a non-linear crystal. Nonetheless, temporal and spectral interferometry are linear techniques that do not require a high peak power threshold [Lepetit et al., 1995, Monmayrant et al., 2010]. In this section, we present the full field version of temporal interferometry through scattering media, that we name Interferometric Cross-Correlation (ICC) technique. The method is illustrated in Figure 2.8. It is performed with the experimental setup developed in Figure 2.1. In essence, it enables measurement of the spatio-temporal speckle temporal envelope for all the speckle grains on the RoI of the CCD camera, spatially resolved, as well as the time-of-flight distribution.

Interferometric Cross-Correlation relies on the interference between an ultrashort pulse, here from the external arm of Figure 2.1, and an unknown pulse, here the spatio-temporal speckle. ICC involves in measuring a cross correlation between the ultrashort reference pulse and temporally stretched pulse by scanning a delay line in the reference arm. This cross correlation profile would then be larger than the actual duration of the temporal speckle, as we measure the temporale profile of a speckle grain convuleted by the reference ultrashort pulse. As we are only interested in the temporal envelope, phase measurements are not required: the spectral phase of the reference pulse does not need to be known. We refer to $E(t)$ as the complex electric field. A reference pulse, with a controllable delay τ, and the stretched pulse are overlapped spatially on a beam splitter, and they are coherent. They are imaged on a CCD sensor. As a CCD camera is a slow detector, in comparison with the sort pulse duration, it only measures integrated signals. For a given delay τ, the CCD signal at spatial position x reads:

$$\begin{aligned} S(x,\tau) &= \int |E_{\text{sig}}(x,t) + E_{\text{ref}}(x,t-\tau)|^2 dt \\ &= \underbrace{\int |E_{\text{sig}}(x,t)|^2 + |E_{\text{ref}}(x,t-\tau)|^2 dt}_{\text{baseline}} + 2\underbrace{\int E_{\text{sig}}(x,t)E^*_{\text{ref}}(x,t-\tau)dt}_{\text{cross-correlation}} \end{aligned} \tag{2.1}$$

Recording interferogram as function of delay

An interferogram is recorded as function of τ: CCD images are recorded while the delay line is continuously translated, via a motorized stage (Newport, translation speed: 2 μm/s). The left-hand term of Equation 2.1 corresponds to the interferogram baseline. The right-hand term is a cross-correlation between a reference pulse and a spatio-temporal speckle. This term is directly proportional to the amplitude of the spatio-temporal speckle field. Indeed, the magnitude of reference pulse with delay τ, $|E_{\text{ref}}(t-\tau)|$, has only non-zero terms within its duration, which is $\sim$ 100 fs. The interferometric setup is thus exploited as a coherence gating in the temporal domain.

An example of an interferogram in a given spatial position of the spatio-temporal speckle, after propagation of a 100 fs pulse through ZnO sample, is presented in Figure 2.8. We observe temporal fluctuations, whose temporal widths are on the order of the pulse duration. Its envelope is directly related to the temporal envelope of spatio-temporal speckle field: it is temporally spread over τ_m the averaged confinement time of photons in the scattering medium.

Filtering the envelope

Before filtering the interferogram to only keep its envelope, the interferogram is normalized by subtracting the averaged baseline, and by dividing it by $2\sqrt{I_{\text{ref}}I_{\text{sig}}}$. I_{ref} (resp. I_{sig})

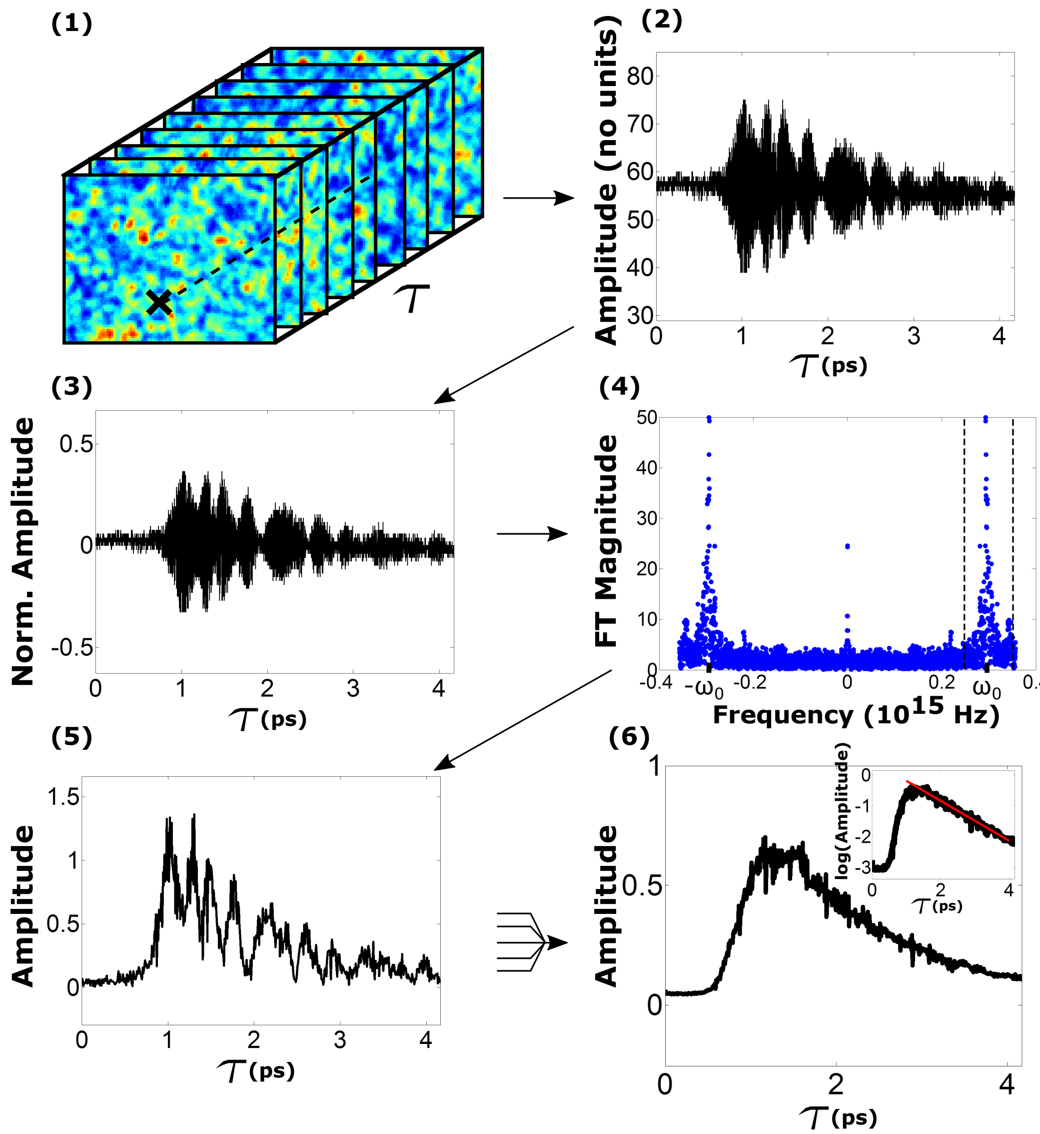

Figure 2.8 – Interferometric Cross-Correlation characterizes temporal fluctuation of spatio-temporal speckle. Interferometric Cross-Correlation (ICC) is performed using experimental setup presented in Figure 2.1. An ultrashort reference pulse, whose arrival time is controllable with a delay line, is overlapped spatially and temporally with spatio-temporal speckle. The two beams are coherent. **(1)** Interference images are recorded as function of delay τ, by scanning the delay line. **(2)** Interferogram at a given spatial position, defined by the black cross in (1). Intensity of the cross-term between reference pulse and stretched pulse is linearly related to the amplitude of spatio-temporal speckle field at this specific position. **(3)** Normalized interferogram by subtracting baseline, and by dividing over both amplitude of reference and signal beams. **(4)** Fourier transform of the normalized interferogram. Peak at ω_0, the central frequency of the ultrashort pulse, is filtered with a band-pass filter, and shifted down to DC. **(5)** Inverse Fourier transform of the filtered signal. Only envelope of interferogram is remaining: we directly access temporal speckle at a given spatial position. Approximately N_λ temporal speckle grains are present. **(6)** Averaging over N=1000 spatial speckle positions leads to time-of-flight distribution. Its tail has an exponential decay, of characteristic time $\tau_m \propto 1/\delta\lambda_m$ is the averaged confinement time of photons in the scattering medium. Inset: time-of-flight distribution in semilog diagram. Linear fit of the tail (red line) gives access to τ_m, via the inverse of its slope.

corresponds to the intensity of the reference beam (resp. speckle) at the position where the interferogram is recorded, integrated over time on the CCD camera. It is measured by blocking the signal arm (resp. the reference arm). Normalizing signals enable comparison between different interferograms, as well as averaging.

Filtering the envelope is performed with a Fourier transform of the interferogram, that is shown in Figure 2.8. Three peaks, at respective frequencies $-\omega_0$, 0 and ω_0, are revealed. ω_0 corresponds to the central frequency of the pulse. The term at ω_0 contains the information. It is filtered with a band-pass filter and then shifted down toward DC. The inverse Fourier transform leads directly to the interferogram envelope.

ICC enables probing the temporal profile at position x on the CCD camera. In parallel, ICC can also be measured for multiple spatial positions , as the CCD detector has spatial resolution. In essence, the ICC technique gives an access simultaneously to the full field temporal profile of the transmitted pulse, with a single measurement of $S(x,\tau)_x$ for all spatial speckle grains in positions x on the CCD camera. Averaging temporal envelopes over spatial position leads to a time-of-flight distribution, as described in Section 1.4.3.

Time-of-flight distribution

An example of a measured time-of-flight distribution, obtained by averaging temporal profile of 1000 spatial speckle grains, is shown in Figure 2.8. Its tail has an exponential decay, with characteristic time τ_m. This is defined as the average confinement time of photons in the scattering medium. τ_m can be extracted with a linear fit on a semilog plot. τ_m typically scales $\sim$ 700 fs - 10 ps with a ZnO scattering medium, depending on the sample thickness for a given transport mean free path $l^\star$. Measurement of $\tau_m > 2$ ps is more accurate with this ICC method than spectral correlation, as the corresponding $\delta\lambda_m$ is smaller than the spectral resolution of the spectrometer.

Temporal field autocorrelation

Time-width of a temporal speckle grain can be estimated via calculating the autocorrelation of the measured temporal profile (as in Figure 2.8(5)). As we studied in Figure 1.18, the duration of a temporal speckle grain is approximately the duration of the input ultrashort pulse δt. With the experimental setup of Figure 2.1, we can verify this statement.

The spatial resolution of the ICC technique enables to measure multiple temporal profiles with a single scan of the delay line, as we did to retrieve the time-of-flight distribution above. Instead of averaging the envelopes, we store them (in this example 100 temporal envelopes) in lines of a 2D array. We then compute the autocorrelation by calculating the inner products between columns, in comparison with a reference column. This reference column is arbitrary chosen at a delay time when the time-of-flight distribution reaches its maximum, that is $\tau = 1.2$ ps from Figure 2.8(6). The resulting temporal autocorrelation is shown in Figure 2.9. Duration of a temporal grain is approximately the duration of the input pulse $\delta t \sim 100$ fs at FWHM.

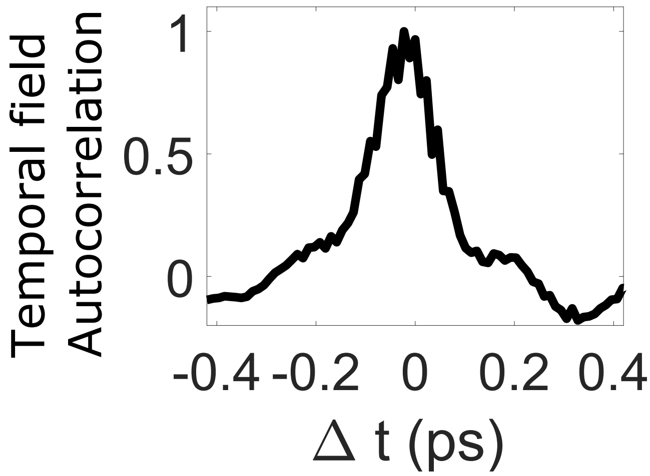

Figure 2.9 – Temporal field autocorrelation of the temporal envelope retrieved via ICC. 100 different temporal envelopes, retrieved via ICC, are stored in lines of a 2D array. Temporal autocorrelation is retrieved by calculating the inner products of columns, with a reference arrival time arbitrary chosen at $\tau = 1.2$ ps (See Figure 2.8), corresponding to the maximum of the time-of-flight distribution. Time-width of this autocorrelation gives the duration of smallest feature of the temporal speckle, that is $\sim$ the duration of the input pulse $\delta t \sim 100$ fs.

2.5 Summary

In this Chapter, we introduced all the experimental elements of the setup. We developed with details the principle devices that are used in the following chapters: the spatial light modulator, the laser source, the scattering samples and the fluorescent samples.

In the following Chapters, we exploit the experimental setup, that is presented in Figure 2.1, to control the spatio-temporal speckle by means of a SLM. More precisely, in Chapter 3, Chapter 4, Chapter 5 and Chapter 6, we exploit this setup to perform deterministic spatio-temporal control of an ultrashort pulse after propagation through a thick scattering medium. Either with multi-spectral control, that is the aim of Chapter 3, or with a time-resolved approach, detailed in chapter 4, a transmitted pulse can be focused in an arbitrary space-time position. In Chapter 5, we demonstrate that a broadband transmission matrix approach, measured with a co-propagative reference beam, enables focusing of the pulse with interesting spectral/temporal properties. Finally, in Chapter 6, we exploit the previously developed matrix approaches to enhance two-photon fluorescence after propagation through a thick scattering sample.

Chapter 3

Coherent spectral control of the output pulse: Multi - Spectral Transmission Matrix

Contents

Propagation of coherent light through a scattering medium produces a speckle pattern at the output, due to light scrambling by multiple scattering events. Phase and amplitude information of light are spatially mixed, as we developed in Section 1.2. Temporally, photons exit a scattering medium at different times, giving rise to a broadened pulse at its output. In Section 1.4.3, we studied temporal spreading of the original pulse: it is characterized by its averaged confinement time, τ_m. Equivalently, from a spectral point of view, the scattering medium responds differently to distinct spectral components of an ultrashort pulse, with a spectral correlation bandwidth $\delta\lambda_m \propto 1/\tau_m$, giving rise to a very complex spatio-temporal speckle pattern. However, one can manipulate the spatial degrees of freedom, using a single SLM, to adjust the delay between different optical paths. Therefore spatial and temporal distortions can be both compensated using wavefront shaping techniques, as we developed in Section 1.5.

In this Chapter, we introduce an extension of the monochromatic transmission matrix to the broadband regime. The measurement of monochromatic Transmission Matrices (TMs) of the scattering medium for all its spectral components constitutes the Multi - Spectral Transmission Matrix (MSTM). This 3D dataset allows for both spatial and spectral control at any position in space using a single SLM, as demonstrated during the PhD of Daria Andreoli [Andreoli, 2014]. However, if the spectral phase relation between the different frequency responses of the medium is known, it also gives access to a full spatio-temporal control of an ultrashort pulse propagating in the disordered medium. This Chapter is organized as follows: in Section 3.1, we define the MSTM formalism, and we discuss a protocol to measure it, with the experimental setup that is fully developed in Chapter 2. We then exploit the MSTM to adjust the spatio-spectral speckle in Section 3.2, via multi-spectral focusing in multiple spatial positions. We extend this approach in Section 3.3 to control the temporal profile of the output pulse, via a well-defined spectral shaping. In particular, we demonstrate spatio-temporal focusing as well as a deterministic shape of the temporal profile of the output pulse: the scattering medium can thus be used as a controllable pulse shaper.

3.1 Formalism and measurement of the Multi - Spectral transmission matrix

The monochromatic TM cannot allow spectral control of the output pulse. Indeed, phase-conjugating a single line of the TM focuses only a single spectral channel [van Beijnum et al., 2011]. Full spatio-spectral control requires adjusting the N_λ spectral degrees of freedom, as we explicitly described in Section 1.4.3. In this Section, we introduce the formalism of the Multi-Spectral Transmission Matrix of a scattering medium, the extension of the monochromatic TM for all the spectral components of an ultrashort pulse of light.

3.1.1 From the monochromatic Transmission Matrix to the Multi - Spectral Transmission Matrix

At a single frequency ω, the relationship between transmitted light after propagation through a scattering medium and its corresponding input field can be described with a TM formalism, $\mathbf{t}$ [Popoff et al., 2010b], using Equation 1.16. Nonetheless, in Section 1.4.3 we developed the spectral dependence of the speckle pattern. In essence, the spectral correlation bandwidth of a scattering medium, $\delta\lambda_m$, defines the minimum difference in input wavelength to produce uncorrelated speckle patterns using CW light from a monochromatic laser source. Consequently, the monochromatic TM approach breaks down to describe light propagation, of broadband light whose spectral width, $\Delta\lambda$, satisfies the following condition: $\Delta\lambda > \delta\lambda_m$.

More precisely, when such light propagates through a scattering medium, transmitted light takes the form of a complex spatio-temporal structure. This spatio-temporal speckle can be understood as a sum of $N_\lambda = \Delta\lambda/\delta\lambda_m$ independent monochromatic speckle patterns, where N_λ is the number of spectral degrees of freedom. While a single monochromatic TM allows control of a single spectral degree of freedom, describing the content of an ultrashort pulse propagation through a scattering medium requires the measurement of N_λ monochromatic TMs.

The Multi-Spectral Transmission Matrix (MSTM) of a scattering medium, whose formalism is introduced below, corresponds to the extension of the monochromatic TM for an ultrashort pulse of light. Substantially, it corresponds to a spectrally-resolved Transmission Matrix. Ideally, MSTM would be a continuous stack of monochromatic TMs over the spectral bandwidth of the input ultrashort pulse. Nonetheless, the spectral correlation bandwidth of the scattering medium $\delta\lambda_m$ allows for spectral discretization of the MSTM. Indeed, a monochromatic TM measured at wavelength λ_k enables control of light over a spectral interval $\delta\lambda_m$ centered around λ_k [van Beijnum et al., 2011]. Therefore, measuring the full spectral content requires only on the order of N_λ monochromatic TMs, rather than a redundant continuum of spectral matrices. Indeed, a continuum of spectrally-resolved TM has a similar spectral correlation bandwidth as the scattering medium, as expected [Andreoli et al., 2015]. Here, each individual monochromatic TM is essentially uncorrelated with the other monochromatic TMs, since they are separated in the spectral domain by at least $\delta\lambda_m$.

The MSTM of a scattering medium is thus a 3D tensor of dimension $N_{\text{out}} \times N_\lambda \times N_{\text{SLM}}$. While N_{SLM} corresponds to the number of spatial degrees of freedom on the SLM, i.e. the number of independent SLM segments used in the measurement process of the MSTM, N_{out} stands for the number of spatial speckle grains measured on the CCD camera, i.e. the number of CCD pixels.

This tensor relates the broadband input field E^{in}, which is constituted of $N_\lambda \times N_{\text{SLM}}$ spatio-spectral components, to the transmitted broadband output field E^{out}, that is characterized by its $N_\lambda \times N_{\text{out}}$ spatio-spectral components. The output field is connected to the input field for all the spectral content of the ultrashort pulse via the MSTM coefficients, with the following relation:

$$E_j^{\text{out}} = \sum_{m=1}^{N_{\text{SLM}}} \sum_{l=1}^{N_\omega} |h_{jml}| e^{i\varphi_{jl}} E_m^{\text{in}}(\lambda_l) \tag{3.1}$$

where E_j^{out} represents the value of the output field at the j-th pixel of the CCD camera, $E_m^{\text{in}}(\lambda_l)$ the value of the input field at the l-th SLM pixel at wavelength λ_l, $h_{jml} = |h_{jml}|e^{i\varphi_{jl}}$ are the coefficients of the MSTM with φ_{jl} the spectral phase component.

The MSTM contains information on the spatio-spectral coupling of light by the scattering medium. For instance, knowledge of the spectral phase distortion could lead to spatio-temporal focusing if it is properly compensated. In the next section, we detail how the MSTM can be measured with the experimental setup that is detailed in Figure 2.1.

3.1.2 Experimental measurement of the Multi - Spectral Transmission Matrix

The MSTM can be measured with the experimental setup that we developed in Chapter 2, without the presence of non-linear samples. First of all, the MSTM is a signature of an ultrashort pulse propagation through a given scattering medium. It is valid as long as the medium remains stable. In practice, according to Section 2.2, a measured MSTM can be exploited for many hours with ZnO scattering samples.

In order to quantify N_λ, the third dimension of the MSTM, spectral correlation bandwidth of the scattering medium $\delta\lambda_m$ has to be measured. The experimental protocol is developed in Section 2.2. Typical values of $\delta\lambda_m$ for our samples scale between 0.5 nm - 2 nm. Ultrashort pulses generated by the Ti:Saph laser source of the experimental setup have a spectral width $\sim$ 10 nm at FWHM. Therefore $N_\lambda \sim$ 5 - 20 monochromatic TMs have to be measured, with a spectral step $\delta\lambda_m$. In practice, we measure the MSTM over a spectral width $\sim$ 13 nm centered at the central wavelength of the ultrashort pulse. This larger width, compared to FWHM of the pulse spectrum, enables a better spectral control of the pulse, by including some part of the Gaussian envelope tail (See Figure 3.1).

Measuring the set of monochromatic transmission matrices

For the measurement, the Ti:Saph laser is mode-unlocked and is used as a tunable CW source. The MSTM is equivalent to a stack of uncorrelated discrete monochromatic TMs. A schematic representation of the MSTM is illustrated in Figure 3.1. In the following, we briefly describe the experimental protocol to measure the MSTM with the setup described in Figure 2.1.

Firstly, the laser is set to wavelength $\lambda_1 = \lambda_0 - (N_\lambda \times \delta\lambda_m)/2$. The monochromatic $\text{TM}(\lambda_1)$ is measured as follows: a set of Hadamard patterns is displayed on the SLM, and the corresponding output field is measured on the CCD camera using digital phase-shifting holography (See Section 1.3.4). In practice, $N_{\text{SLM}} = 1024$ SLM segments and $N_{\text{out}} \sim 10^4$ CCD pixels are typically exploited. CCD pixels can be binned according to the spatial speckle grain size. Measurement time of $\text{TM}(\lambda_1)$, using $N_{\text{SLM}} = 1024$ SLM pixels, is mostly limited because of the refresh rate of the SLM. In practice, $\text{TM}(\lambda_1)$ is acquired in $\sim$ 8 min.

Once $\text{TM}(\lambda_1)$ has been measured, the incident wavelength is switched to $\lambda_2 = \lambda_1 + \delta\lambda_m$: $\text{TM}(\lambda_2)$ is recorded similarly to $\text{TM}(\lambda_1)$. The operation is iterated for the N_λ different spectral components of the ultrashort pulse, that are spectrally separated by $\delta\lambda_m$. A complete set of matrices $\mathbf{H} = \{\text{TM}(\lambda_l)\}_{\lambda_l}$ forms the MSTM of the scattering medium.

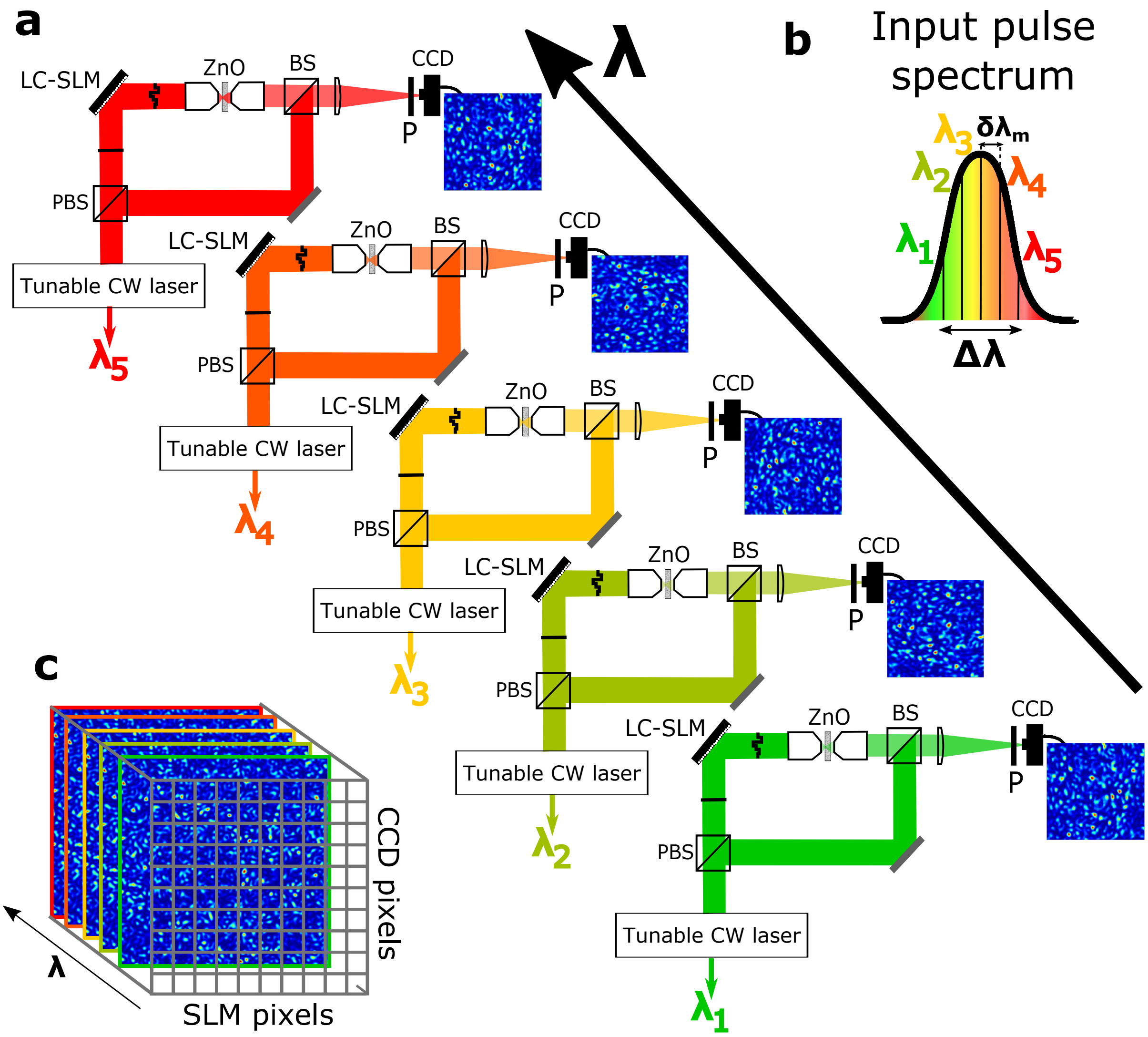

Figure 3.1 – Multi-Spectral Transmission Matrix measurement. Scheme of the Multi-Spectral Transmission Matrix of a scattering medium. N_λ stands for the number of spectral degrees of freedom. **(a)** Measurement of the MSTM is discretized: N_λ monochromatic TMs are measured, at wavelengths separated to each other by $\delta\lambda_m$ that corresponds to the spectral correlation bandwidth of the medium. The experimental setup is simplified from the real one that is presented in Figure 2.1. For clarity, we chose $N_\lambda = 5$ in this representation. (LC-SLM) : Liquid-Crystal Spatial Light Modulator; (PBS): Polarized Beam Splitter; (BS): Beam Splitter; (P): Polarizer; (CCD): Charged Coupled Device; (ZnO): Zinc Oxide scattering medium. **(b)** The N_λ wavelengths are represented with black lines over the spectrum of the input pulse. $\Delta\lambda$ stands for the spectral bandwidth of the ultrashort pulse. **(c)** Typical schematic representation of the Multi-Spectral Transmission Matrix, of dimension $N_{\text{out}} \times N_\lambda \times N_{\text{SLM}}$, where N_{out} stands for number of CCD pixels, and N_{SLM} the number of SLM pixels exploited in the measurement of TMs. Each monochromatic TM has been measured at a different wavelength, that is represented with a chosen color. In practice $N_{\text{out}} \sim 10^4$ pixels, $N_{\text{SLM}} \sim 1024$ pixels and $N_\lambda \sim 20$ spectral degrees of freedom.

In all this Chapter, the scattering medium is constituted of randomly distributed ZnO nanoparticles, as presented in Section 2.2. Spectral correlation bandwidth $\delta\lambda_m$ is measured ~ 0.5 nm: 21 monochromatic TMs are recorded to form the MSTM. For instance, such MSTM measured on a RoI zone of the CCD camera of $(133 \times 135 = 17955)$ CCD pixels represents a ~ 8 Gb dataset of complex numbers.

Measuring the relative spectral phase between matrices

According to Equation 1.19, the measured complex coefficients of a monochromatic TM are cross products between the reference beam and the modulated beam. Therefore, the measured phase φ_{jl} at the j-th pixel on the CCD camera at wavelength λ_l can be decomposed as follow:

$$\varphi_{jl} = \varphi_{jl}^M - \varphi_{jl}^R \tag{3.2}$$

where φ_{jl}^M corresponds to the phase term of the signal, i.e. distorted because of scattering effects, and φ_{jl}^R the phase term induced by the reference beam. These two terms cannot be separated, as they are inherent to the measurement process. Therefore, the reference beam will be of utmost importance, when controlling the input pattern on the SLM via the MSTM, as the quantity that requires adjustment is φ_{jl}^M. Two different kinds of reference beams can be used to measure a monochromatic TM:

- As it was presented in Section 1.3.4 and in the PhD thesis of Daria Andreoli [Andreoli, 2014], a subpart of the SLM is not being modulated: this co-propagative reference beam leads to a static but unknown reference speckle pattern.
- A plane wave can be set as a reference beam, with the use of an external arm.

Although the co-propagative reference beam is more convenient than the external arm as it is simple to implement experimentally, the reference speckle, and consequently φ_{jl}^R, varies as a function of incident wavelength λ_l. More precisely, relationship between φ_{jl}^R and $\varphi_{j(l+1)}^R$ cannot be predicted nor be measured individually because of scattering effects. Therefore, a measurement of the MSTM with a co-propagative reference cannot allow coherent control of the temporal profile [Andreoli et al., 2015], since φ_{jl} cannot be set unambiguously for the various wavelengths. Nonetheless, spatio-spectral control of the speckle pattern remains possible: Section 3.2 deals with manipulation of the spectral degrees of freedom with such a MSTM, measured with a co-propagative reference beam.

In contrast, the use of an external arm produces a well-defined plane wave as reference signal, with a well-defined spectral phase relationship. The phase of the plane wave φ_j^R is dictated by the arrival time of the reference pulse, that is set by the delay line. For all the spectral components of the pulse, we have $\varphi_{jl}^R = \varphi_j^R$. Although φ_j^R is known up to a global phase, the relative phase $\delta\varphi_{jl} = \varphi_{jl} - \varphi_{j(l+1)} = \varphi_{jl}^M - \varphi_{j(l+1)}^M$ does not depend on the reference term. Coherent spectral control is then achievable: in Section 3.3, deterministic control of the temporal profile of the output pulse is demonstrated, via spectral shaping using spatial-only degrees of freedom of a single SLM.

Here, we call a measured MSTM with an external arm is called *full* MSTM (as its spectral phase can be accessed) in contrast with an *incomplete* MSTM, which has been measured with a co-propagative reference beam.

At a chosen output pixel, the spectral phase has been scrambled because of multiple scattering. Consequently, transmitted pulse is no longer a Fourier-limited pulse, but its temporal profile has been broadened, as it was developed in Section 1.4.3. Nonetheless, this spectral phase distortion is deterministic, as long as the scattering medium is stable. If the spectral phase information can be measured, while measuring the MSTM, the spectral phase alteration could be compensated with wavefront shaping on the SLM. In addition to what was presented in Section 1.5, in the following we present a Multi-Spectral Transmission Matrix approach to control the spatio-spectral speckle, leading to spatio-temporal focusing.

3.2 Exploiting spectral degrees of freedom of the medium for Multi-Spectral focusing

We assume the MSTM of a scattering medium, that is constituted of randomly distributed ZnO nanobeads, has been measured, following the protocol that is detailed in Section 3.1.2. In this Section, we demonstrate how the MSTM can be exploited to control the spatio-spectral speckle, even with an incomplete MSTM.

3.2.1 Focusing a single frequency of the pulse

Firstly, we present how a single frequency component λ_s of the ultrashort pulse can be controlled. It consists in only exploiting $\mathrm{TM}(\lambda_s)$ of the MSTM. The protocol is as follows:

1. We extract from the MSTM the monochromatic $\mathrm{TM}(\lambda_s)$.
2. We calculate the complex conjugate of the monochromatic matrix associated to this wavelength λ_s. We then multiply it by the targeted spatial output E_{target} (See Equation 1.23), which is a null vector everywhere except in the targeted output position, which has a value of 1 [Popoff et al., 2010b].
3. As the SLM is only able to modulate the phase of the input field, we display on the SLM the phase of the previously calculated solution.

In the following, we investigate spectral and temporal properties of this monochromatic focusing.

Spectral properties of the monochromatic focus

The laser is mode-unlocked and it is used as tunable CW source. The CW laser source wavelength is set to λ_s. Similarly to what was presented in Section 1.3.4, monochromatic signal-to-background ratio ($\mathrm{SBR}_{\mathrm{mono}}$) of focusing at wavelength λ_s is defined as the intensity at the focus position over the spatially averaged background speckle intensity. In Figure 3.2, MSTM has been measured with $N_{\mathrm{SLM}} = 256$ SLM pixels. The achieved focus is characterized by its $\mathrm{SBR}_{\mathrm{mono}} \sim 100$. Spectral properties of the focus are explored by probing the focus intensity as function of incident wavelength. Figure 3.2 illustrates the experimental results. Maximal focus intensity is detected at wavelength λ_s, as expected. Furthermore, focus intensity follows almost exactly the spectral decorrelation of the speckle pattern as function of spectral detuning, as it was demonstrated with monochromatic iterative optimization focusing [van Beijnum et al., 2011]. Therefore,

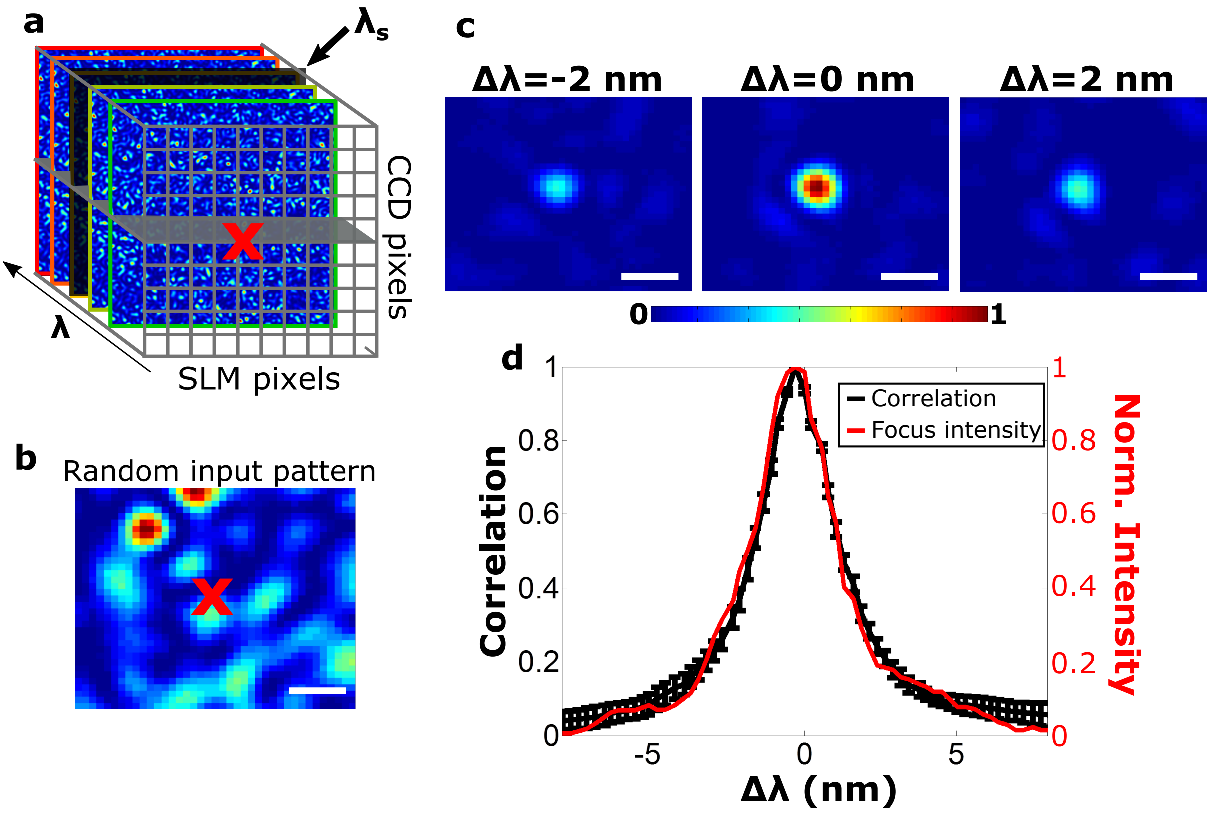

Figure 3.2 – Focusing a single wavelength of an ultrashort pulse via the MSTM through a scattering medium - spectral properties. (a) A single monochromatic TM(λ_s) (black vertical cross-section) is extracted from the measured MSTM. The scattering medium is characterized by $N_\lambda \sim 5$. Focusing light at wavelength λ_s is achieved via phase-conjugating a chosen line, which corresponds to the targeted spatial position (grey horizontal cross-section). Phase of the solution is displayed on the SLM. **(b)** Typical speckle pattern observed with CW light, with a random phase pattern on the SLM. Red cross corresponds to the targeted position for focusing. Its position is represented by the gray cross-section in the MSTM in (a). **(c)** Phase pattern to focus light at wavelength λ_s is displayed on the SLM. Monochromatic intensity images are recorded on the CCD camera as function of spectral detuning $\Delta\lambda$ from λ_s. 3 monochromatic speckle patterns are represented, for respectively $\Delta\lambda$ = -2 nm, $\Delta\lambda$ = 0 nm, and $\Delta\lambda$ = 2 nm with the same colorbar. At central wavelength (i.e. $\Delta\lambda$ = 0 nm), in CW SBR$_{\text{mono}}$ $\sim$ 100 using $N_{\text{SLM}} = 256$ SLM pixels. **(d)** Normalized intensity of the focus, as well as spectral correlation, are plotted as function of spectral detuning $\Delta\lambda$. Scale bar: 4 μm

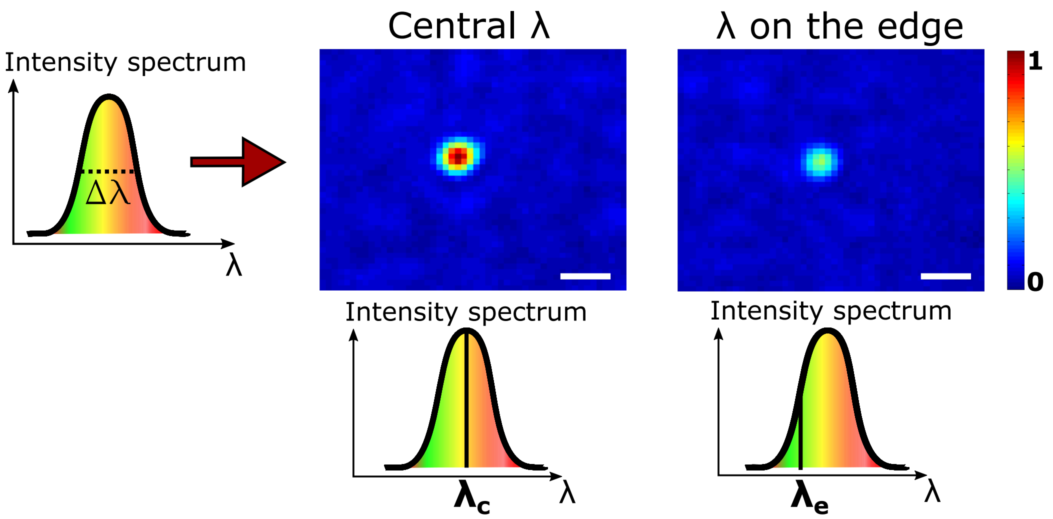

Figure 3.3 – Monochromatic focusing of different individual wavelength of the ultrashort pulse spectrum. Phase pattern is displayed on the SLM to focus either central wavelength of the pulse λ_c, or wavelength on the edge λ_e, where spectral amplitude of the pulse is half of the maximum. Laser is now emitting an ultrashort pulse of light. SBR of focusing at $\lambda_c \sim 13$, while SBR at $\lambda_e \sim 7.5$. MSTM has been measured with $N_{\text{SLM}} = 1024$ SLM pixels, for a scattering medium that is characterized by $N_\lambda \sim 20$. Scale bar: 4 μm

monochromatic focusing allows spectral control of a single spectral degree of freedom: light is focused over a spectral interval centered at λ_s of spectral width $\sim \delta\lambda_m$.

Monochromatic focusing while laser source is mode-locked

The laser source is now turned into mode-locked operation. The same input phase pattern remains displayed on the SLM. The signal-to-background ratio (SBR) is defined as focus intensity over the averaged background intensity under illumination of an input ultrashort pulse, while SBR_{mono} was defined with CW light. Automatically, the focus SBR decreases, as illustrated in Figure 3.3. Indeed, monochromatic focusing consists in exploiting all the spatial degrees of freedom to enhance the constructive interference at the focus position and at the chosen wavelength λ_s. When the laser source generates ultrashort pulses of light, only a single spectral degree of freedom is adjusted. The other spectral components of the pulse contribute to the speckle background: $(N_\lambda - 1)$ speckle patterns are incoherently summed on top of the monochromatic focusing pattern, producing a low-contrast background. Therefore, signal-to-background ratio with mode-locked laser of monochromatic focusing SBR scales $\sim \text{SBR}_{\text{mono}}/N_\lambda$ [Curry et al., 2011]. In Figure 3.3, monochromatic focusing (central wavelength of the pulse) through a thick scattering medium, that is characterized with $N_\lambda \sim 20$, under an ultrashort pulse illumination exhibits typical SBR ~ 13. In that experiment, the monochromatic TM was measured with $N_{\text{SLM}} = 1024$ SLM pixels.

In principle, every individual spectral component of the pulse can be focused through the scattering material as long as the MSTM has been measured. In Figure 3.3, either the central wavelength λ_c or the wavelength on the edge of the spectrum λ_e, where spectral amplitude of the pulse is half maximum amplitude, are focused individually while the laser is mode-locked. Although similar monochromatic SBR_{mono} are observed at their

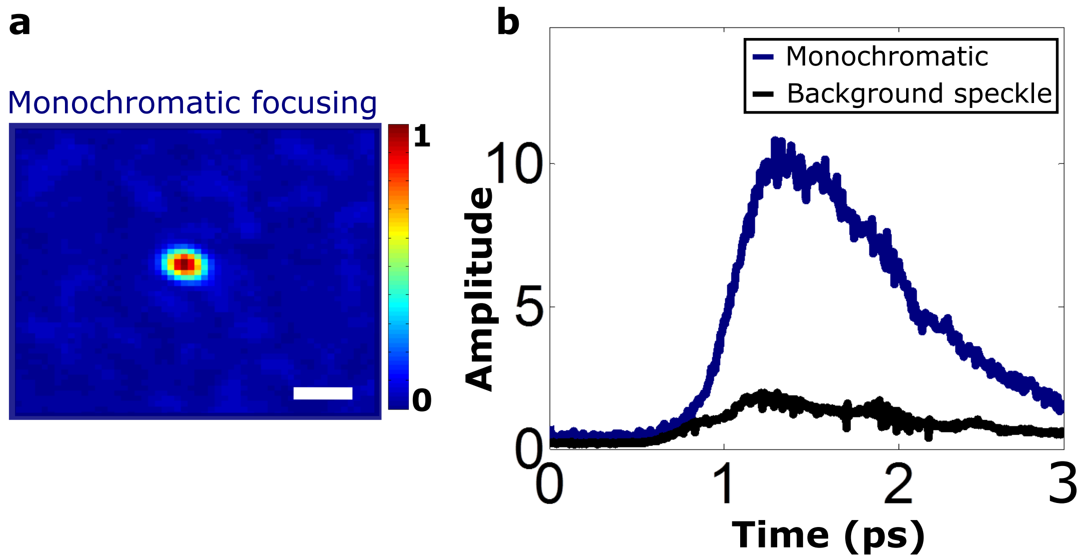

Figure 3.4 – Focusing a single wavelength of an ultrashort pulse via the MSTM - temporal properties. **(a)** CCD image of monochromatic focusing (central wavelength of the pulse) in a given output spatial position, while the laser is mode-locked. Intensity is normalized. **(b)** Temporal profile of monochromatic focusing is recorded with Interferometric Cross-Correlation (ICC) technique. In blue: averaged temporal profiles of monochromatic focusing over 9 spatial positions. In black: averaged temporal profiles of spatial speckle grains with a random input phase mask on the SLM, over 200 positions: the scattering medium is characterized by its confinement time of photon $\tau_m \sim 1.8$ ps. Amplitude of monochromatic focusing is higher, but temporal compression is missing, as only a single spectral degree of freedom over N_λ is controlled.

own respective wavelengths, focusing at λ_c is more efficient when comparing its SBR to focusing at λ_e, because of the Gaussian envelope of the pulse spectrum amplitude.

Temporal properties of the monochromatic focus: spatial-only focusing

Finally, we investigate the temporal properties of the achieved monochromatic focusing. Once the input pattern for monochromatic focusing is displayed on the SLM, the temporal profile of the focus is probed with an Interferometric Cross Correlation (ICC) technique. This technique is presented in details in Section 2.4.3. Figure 3.4 presents the averaged temporal profile over nine different spatial positions for better visibility. The observed intensity is higher than the averaged background speckle because the pulse is spatially focused. Nonetheless, the resulting focus remains temporally broadened as only one wavelength of the output pulse is controlled: the pulse is thus spatially-only focused.

Impact of the reference is not an issue for monochromatic focusing, as we only consider a single degree of freedom. In the following, an incomplete MSTM can be exploited for Multi-Spectral focusing.

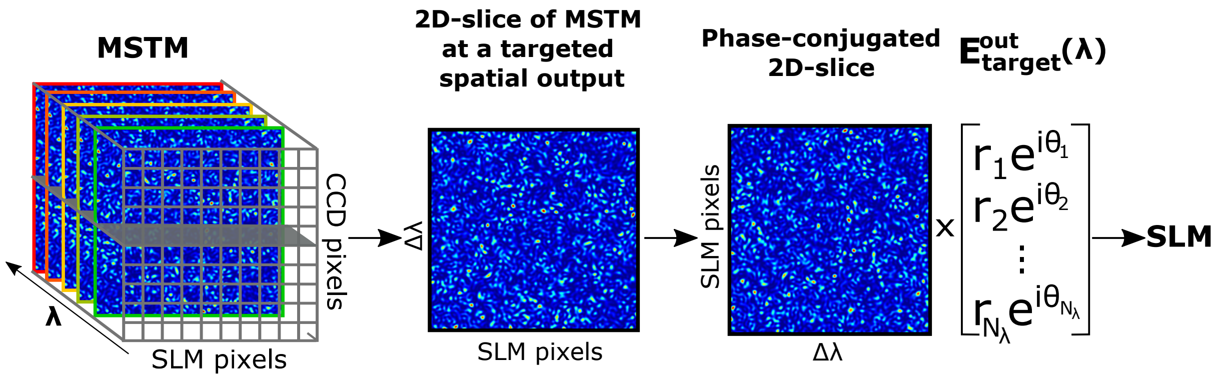

Figure 3.5 – Algorithm for Multi-Spectral focusing in the same spatial position via the MSTM. Scheme of the algorithm used to arbitrary shape the output pulse at a given output position. Both amplitude (r_k) and phase (θ_k) relations between the N_λ wavelengths are imposed at the output of the scattering medium by the user, and the corresponding input is calculated. Incomplete MSTM allows proper spatio-spectral control only of spectral amplitude, while full MSTM enables spatio-temporal control of the output pulse via spectral phase adjustment.

3.2.2 Multi - Spectral focusing: using the scattering medium as a controllable grating

In the previous Section, we demonstrated light focusing of a single spectral degree of freedom, at a chosen wavelength. By exploiting the MSTM, we have access to both S_1 and S_2, complex solutions of dimension N_{SLM}, to independently focus light at either individual wavelength either λ_1 or λ_2, via phase-conjugation of either TM(λ_1) or of TM(λ_2). The problematic now reads: can we focus simultaneously λ_1 and λ_2 with a single phase mask on the SLM ?

In Section 1.3.4, we studied monochromatic light focusing in N_s different spatial speckle grains. This result is obtained by adding coherently the N_s corresponding individual complex input fields, with the use of a targeted output field vector $E^{\mathrm{out}}_{\mathrm{target}}$ (See Equation 1.23), leading to a total solution S of identical dimension N_{SLM}. Once its phase is displayed on the SLM, N_s focus spots are then observed on the CCD camera (See Figure 1.12). Other equivalent solutions exist, such as splitting the SLM in N_s independent sub-zones, which are individually dealing with their respective targets.

Similarly, simultaneously focusing several spectral components of the ultrashort pulse is achievable via the MSTM. For instance, λ_1 and λ_2 can be focused with a single phase mask on the SLM, that is the phase of the incoherent sum S of the two individual solutions S_1 and S_2: $S = S_1 + S_2$. This approach can be generalized for $N_s \leq N_\lambda$ different spectral components.

In this Section, we demonstrate simultaneous focusing of several spectral components of the pulse spectrum, using a single phase mask on the SLM. The different wavelengths of the pulse can either be focused in the same spatial position, or in multiple spatial speckle grains.

Multi - Spectral focusing in the same spatial position

Firstly we consider focusing $N_s \leq N_\lambda$ spectral components of the ultrashort pulse in the same output spatial position via the MSTM. Figure 3.5 explains the algorithm to achieve such Multi-Spectral focusing, which reads as follows:

1. Targeted output spatial position corresponds to a cross-section of the MSTM. This cross-section, which a 2D-slice of the MSTM of dimension $N_\lambda \times N_{\mathrm{SLM}}$, is extracted (gray plan in Figure 3.5). This matrix-slice is denoted $\mathbf{M}$: it contains the relation between the input field and the different wavelengths of the output pulse at this specific spatial output position.

2. By analogy to Equation 1.22, we use the transpose conjugate of $\mathbf{M}$ to determine the spatial shape of the input field. In this case, the targeted output field $E^{\mathrm{out}}_{\mathrm{target}}$ is a vector $E^{out}_{target}(\lambda)$ giving the desired amplitude (r_k) and phase relation (θ_l) between the different wavelengths of the output pulse:

$$E^{\mathrm{out}}_{\mathrm{target}}(\lambda) = \begin{pmatrix} r_1 e^{i\theta_1} \\ r_2 e^{i\theta_2} \\ \vdots \\ r_{N_\lambda} e^{i\theta_{N_\lambda}} \end{pmatrix} \tag{3.3}$$

3. As the SLM is only able to modulate the phase of the input field, we display on the SLM the phase of the previously calculated solution.

The phase term (θ_l) corresponds to the specific desired spectral phase relation between the different wavelengths components at the targeted output position. As we have seen, the relative spectral phase cannot be properly set with an incomplete MSTM. Section 3.3 deals with such spectral shaping via the full MSTM. In this Section, we only consider amplitude contribution (r_k) of $E^{\mathrm{out}}_{\mathrm{target}}(\lambda)$.

Monochromatic focusing at wavelength λ_s can be retrieved using this algorithm. Indeed, $E^{\mathrm{out}}_{\mathrm{target,mono}}(\lambda)$ would be a null vector except at line corresponding to λ_s, where $r_{\lambda_s} = 1$. Multi-Spectral focusing consists in picking N_s non-null term in $E^{out}_{target}(\lambda)$ [Andreoli et al., 2015].

Figure 3.6 shows experimental results using $N_s = N_\lambda$ spectral components. Two-different spectral amplitude profiles are applied in $E^{out}_{target}(\lambda)$: either a squared amplitude or a Gaussian amplitude. A squared amplitude consists in coherently summing the N_λ with the same amplitude weight (i.e. $r_1 = \cdots = r_{N_\lambda} = 1$), while the applied Gaussian amplitude fits the Gaussian profile of the ultrashort pulse spectrum amplitude (i.e. $r_l \propto e^{-(\lambda_0 - \lambda_l)^2/(2\Delta\lambda^2)}$, with λ_0 central wavelength of the ultrashort pulse). The SBR are obtained by averaging the focus over 9 different spatial positions. Choosing Gaussian amplitude exhibits a slightly higher SBR ~ 15 than squared amplitude (SBR ~ 13.5), but should result in a narrower spectrum. Indeed, while the top-hat spectral amplitude tends to reproduce the initial spectral pulse shape, the Gaussian amplitude (r_l) is adding more weight in the total solution for wavelengths close to the central wavelength of the pulse rather than in the tail. Although the spectral amplitude of the focus is now the squared spectral amplitude of the input pulse, thus a narrower Gaussian function, the SBR is slightly increased.

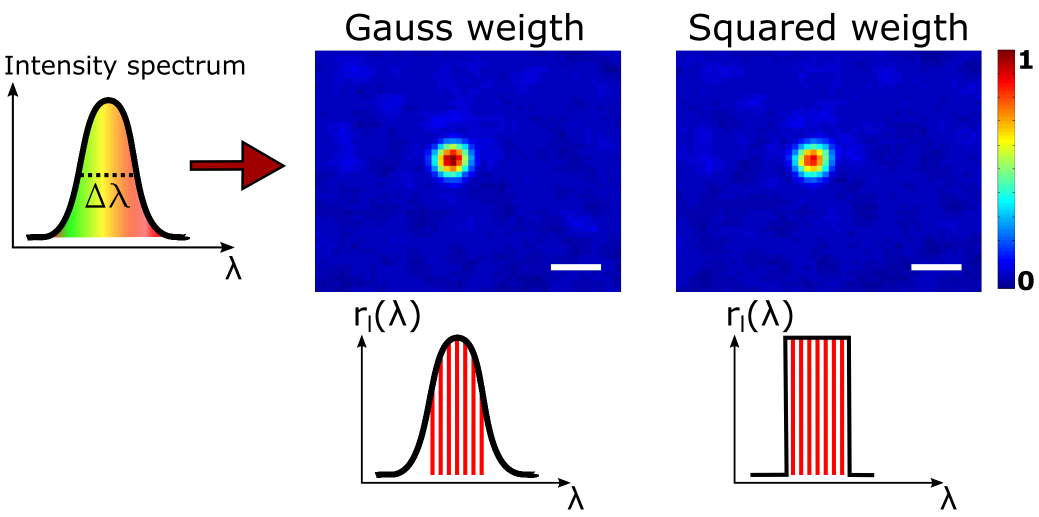

Figure 3.6 – Multi-Spectral focusing of all the spectral components of the ultrashort pulse. N_λ monochromatic solutions are incoherently summed for focusing all the spectral components of the pulse with different spectral amplitude functions (r_k). Either a Gaussian weight function (left) or a squared weigth function (right) is applied while summing individual monochromatic solutions. Gaussian focusing is characterized by a slightly better SBR $\sim$ 15 than squared focus (SBR $\sim$ 13.5). MSTM was measured with $N_{\mathsf{SLM}} = 1024$ SLM pixels for $N_\lambda = 20$ different wavelengths. Scale bar: 4 μm

Comparison with monochromatic focusing

When focusing either the central wavelength (Figure 3.3) or the full spectral content of the pulse (Figure 3.6), we observe similar signal-to-background ratio of focusing. We can easily evaluate the expected SBR of Multi-Spectral focusing in the same spatial position. In analogy with monochromatic focusing on different spatial targets (See Equation 1.15), N_λ spectral targets are focused exploiting N_{SLM} SLM segments. For a squared amplitude $E^{\mathrm{out}}_{target}(\lambda)$, each spectral component would thus have, on average, a SBR $\sim N_{\mathrm{SLM}}/N_\lambda$ under a pulse illumination. Incoherent sum of these N_λ solutions leads to the same SBR at the focus $\sim N_{\mathrm{SLM}}/N_\lambda$. We thus find a similar SBR as for monochromatic focusing that we have studied in Section 3.2.1.

Similarly to monochromatic focusing, such Multi-Spectral focusing cannot be temporally recompressed at the output of the scattering medium. Indeed, although all the spectral components are addressed, their relative spectral phases could not have been properly set as the reference field is λ-dependent. In this case, Multi-Spectral focusing corresponds to focusing all the wavelengths at a given spatial output position without controlling the spectral phase relation. Although the solutions are coherently summed, it results in a spatial focus, but the temporal signal remains broadened at the focus position. An alternative way to generate such a spatial-only focusing beam relies on exploiting the full MSTM. An equivalent result can be achieved by deliberately imposing a random spectral phase relation (θ_l) between the different spectral components being focused.

The temporal profile of the focus, retrieved with ICC, is shown in Figure 3.7 for the three methods described above: monochromatic focusing, and Multi-Spectral focusing at the same output position with either the incomplete MSTM or the full MSTM with a deliberate random spectral phase (θ_l). Figure 3.7 shows that the three approaches give equivalent results in terms of temporal broadening. In all cases, the average temporal

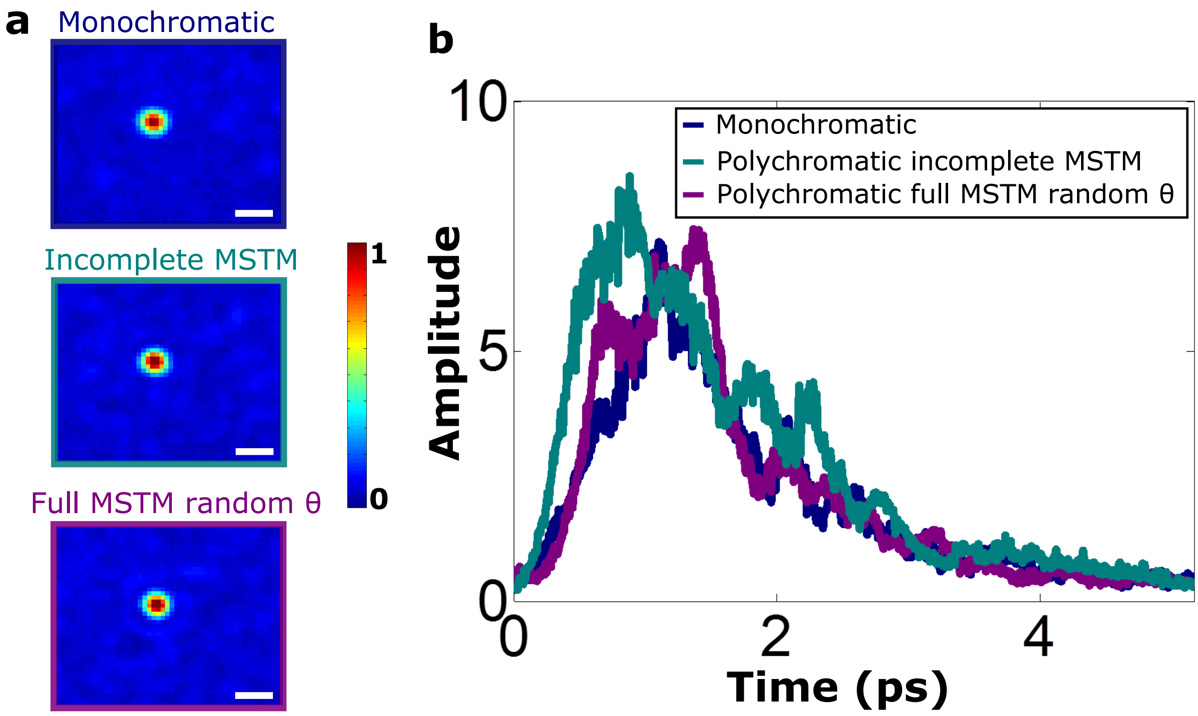

Figure 3.7 – Temporal profiles of spatial-only focusing of an ultrashort pulse via the MSTM. Measurement of the temporal broadening of the focus obtained by different methods of spatial-only focusing: (magenta) spatial-only polychromatic focusing obtained with the full MSTM, setting deliberately a random spectral phase relation (θ_l); (green) spatial-only focusing using the incomplete MSTM measured with a co-propagating reference speckle, setting in vain a flat spectral phase; (blue) spatial-only focusing obtained by phase-conjugating only the central wavelength of the pulse. **(a)** CCD images of spatial-only focusing, that are normalized by maximum of monochromatic focusing CCD image. The three methods leads to similar SBR. Scale bar: 5 μm. **(b)** Corresponding temporal profiles, retrieved with ICC technique. All the plots are spatially averaged over 9 different spatial positions. The three methods lead also to similar temporal profiles.

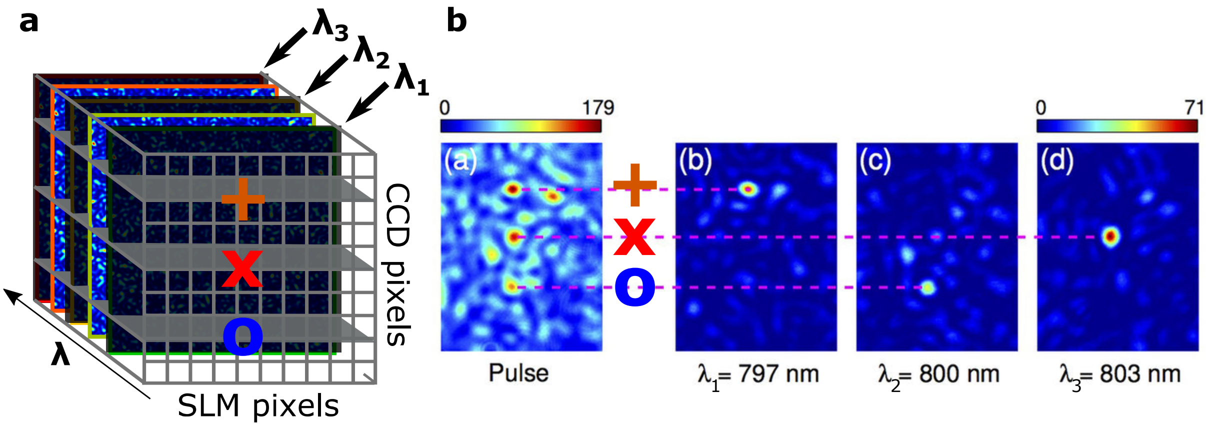

Figure 3.8 – Turning the scattering medium into a controllable grating. Multi-Spectral focusing of 3 different spectral components ($\lambda_1, \lambda_2, \lambda_3$) within an ultrashort pulse spectral bandwidth, in 3 different spatial positions (+, x, and o). **(a)** The 3 corresponding monochromatic TMs (black planes) are extracted from the MSTM. The SLM pattern corresponds to the phase of incoherent superposition of three solutions. Each one of them is obtained by phase-conjugating a chosen line (one of the three symbols corresponding to horizontal cross-sections that are represented with gray planes): each wavelength is spatially focused in a different position. **(b)** When the ultrashort pulse is sent through the scattering medium, 3 spatial focus are observed. While the same pattern is displayed on the SLM, the laser is turned to tunable CW source. The 3 images are measured respectively at λ_1, λ_2 and λ_3. Each focus corresponds to an individual focus, whose position is represented with dashed line in accordance with selected cross-sections in the MSTM. The medium is thus used as a controllable dispersive element. Image adapted from [Andreoli et al., 2015].

profile of the focus corresponds to the natural confinement time of the medium. Therefore, spatial-only focusing can be equivalently achieved with a Multi-Spectral focusing (using the complete or incomplete MSTM) or with a monochromatic phase-conjugation.

Multi-Spectral focusing in multiple spatial positions

Alternatively, the spectral components of the ultrashort pulse can be individually focused in multiple spatial positions via the MSTM [Andreoli et al., 2015]. Instead of cross-sectioning the MSTM at a single spatial position, N_s monochromatic focusing solutions are deterministically summed up, corresponding to multiple spatial output positions. For instance, in Figure 3.8, three different wavelengths of the output pulse are focused in three different spatial positions. Here the spatial positions are deliberately chosen aligned, nonetheless they can be deterministically set. When the laser generates ultrashort pulses, 3 focus spots are observed on the CCD camera, with a similar individual SBR. When scanning the incident wavelength with a tunable CW source, each spot indeed corresponds to a single spectral degree of freedom of the ultrashort pulse.

The scattering medium can then be used as a controllable dispersive element, such as a grating. Its spectral resolution is given by $\delta\lambda_m$ the spectral correlation bandwidth of the medium. Spatial resolution is given by the spatial speckle grain size, that is diffraction-limited: it is then limited by the numerical aperture of the imaging system. Efficiency of focusing is determined by the number of spatial degrees of freedom exploited on the SLM.

Similar results were achieved using an iterative optimization algorithm, using a scattering medium as an accurate spectrometer (See Section 1.4.3).

3.3 Shaping the temporal profile of the output pulse via spectral shaping

In the previous Section, we used the spectral degrees of freedom of the scattering medium to perform Multi-Spectral focusing. This approach interestingly turns a scattering medium into a controllable dispersive element, even if the MSTM is incomplete. In this Section, we assume the full MSTM has been measured: the relative phase (θ_k) between spectral components can thus be adjusted upon focusing. We demonstrate the use of the scattering medium as a controllable pulse shaper.

3.3.1 Control of the spectral phase of the output pulse

In Section 3.2.2, we discussed the algorithm to perform Multi-Spectral focusing. We note φ_{jl} the phase measured on the j-th output spatial position, under illumination at wavelength λ_l (See Equation 3.2). As we have seen, the incomplete MSTM, measured with a co-propagative reference beam, cannot allow a proper control of the spectral phase.

Controlling the spectral phase requires a reference beam whose spectral phase is known. The use of an external reference arm is meeting this requirement, as we detailed in Section 3.1.2. The phase of the reference beam $\varphi_{jl}^R = \varphi_j^R$ depends then only on the output spatial position, and on the delay-line position in the external reference arm, which is fixed in the measurement process of the MSTM. As a consequence, the relative phase at the j-th pixel between two neighbor wavelengths $\delta\varphi_{jl} = \varphi_{jl} - \varphi_{j(l\pm1)} = \varphi_{jl}^M - \varphi_{j(l\pm1)}^M$ does not depend on φ_j^R anymore.

At this stage, we want to use the MSTM to generate a particular temporal profile at a given output spatial position, via spectral shaping. In contrast with pulse shaping techniques [Weiner, 2000, McCabe et al., 2011], the spectral degrees of freedom are not matched with the spatial degrees of freedom of the SLM. Indeed, each pixel of the SLM is not matched to a given wavelength of the pulse spectrum, as in [McCabe et al., 2011], but is illuminated by the full spectrum since the incident ultrashort pulse has not been dispersed prior to the SLM plane. As we studied in Section 3.2.1, the input pattern for focusing a given wavelength λ_l at a given position can be simply obtained by phase-conjugating the corresponding line of the monochromatic TM(λ_l) [Popoff et al., 2010b]. However this focus corresponds to a spatial-only focus, without any temporal compression (See Figure 3.7). The algorithm developed in Section 3.2.2, enables focusing multiple wavelengths with a well-defined spectral phase (θ_l) with a single SLM pattern. For example, to achieve spatio-temporal focusing, all the frequencies are focused into a specific output spatial position,

The content of this Section has been published as: Mickael Mounaix, Daria Andreoli, Hugo Defienne, Giorgio Volpe, Ori Katz, Samuel Grésillon, and Sylvain Gigan, "Spatiotemporal Coherent Control of Light through a Multiple Scattering Medium with the Multispectral Transmission Matrix", *Phys. Rev. Lett.*, **116**, 253901 (2016) [Mounaix et al., 2016a].

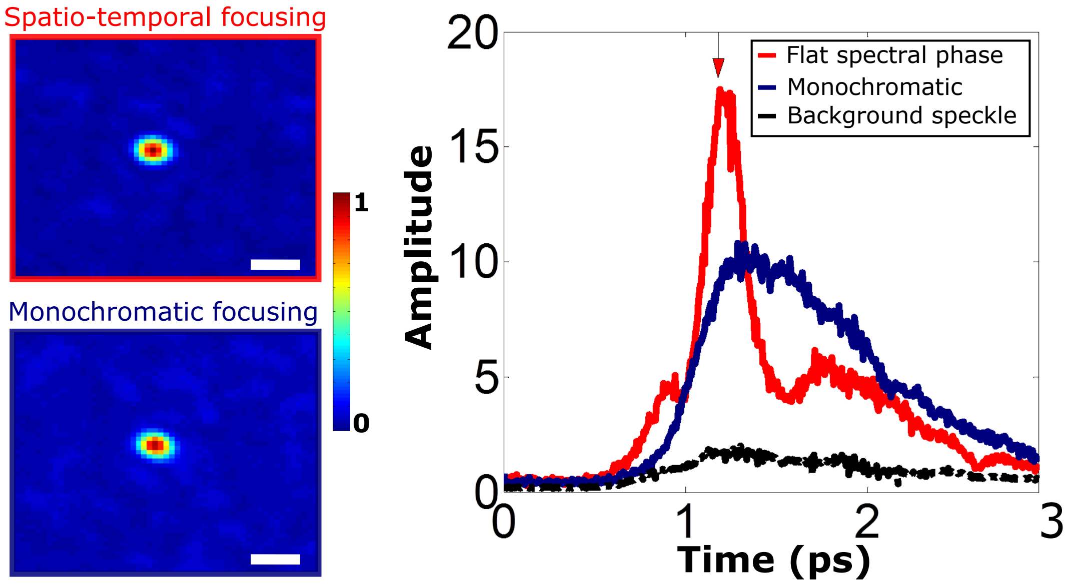

Figure 3.9 – Spatio-temporal focusing is achieved with the MSTM via imposing a flat spectral phase at a given output spatial position. The MSTM was measured with $N_{\text{SLM}} = 1024$ SLM pixels for $N_\lambda = 21$ wavelengths. **(left)** CCD images when displaying on the SLM a phase pattern to impose either a flat spectral phase for all the spectral components of the pulse (top, red square) or phase-conjugating the central frequency of the pulse (bottom, blue square). Both images are sharing the same color-map. The two focus have similar signal-to-background ratio of focusing ~ 19. **(right)** Temporal profiles of the two focus, retrieved with Interferometric Cross-Correlation. Data are averaged over 9 different spatial positions. Imposing a flat spectral phase leads to spatio-temporal focusing of the output pulse, almost back to its initial duration ($\sim$ 150fs at FWHM), at the delay time where the MSTM has been measured (top red arrow). Scale bar: 3 μm.

while simultaneously ensuring that their relative phases are equal: $\theta_1 = \cdots = \theta_{N_\lambda}$. Since the SLM is phase-only, the optimal phase pattern to display is simply the argument of the solution, which would be almost as efficient as amplitude and phase modulation [Aulbach et al., 2012a].

In the following Sections, we demonstrate deterministic temporal shaping of the transmitted pulse, exploiting the full MSTM while adjusting the spectral phase (θ_l) between the different spectral components of the pulse, that have suffered from multiple scattering. We notably demonstrate spatio-temporal focusing of the pulse, almost to its initial duration.

3.3.2 Spatio-temporal focusing of the pulse in a given spatial speckle grain

To go beyond the Multi-Spectral focusing developed in Section 3.2.2, we demonstrate the ability to adjust the spectral phase between the different spectral components of the ultrashort pulse. For instance, the simplest way to achieve spatio-temporal focusing, at a given j-th pixel on the CCD camera, is to impose a flat phase profile. Therefore, the phase relation (θ_l) of Equation 3.3 should read $\theta_1 = \cdots = \theta_{N_\lambda}$, while the spectral amplitude (r_l) should have a Gaussian shape with similar properties to the input pulse spectrum, as we have shown in Figure 3.6. In other terms, the N_λ monochromatic solutions are coherently summed in order to adjust their relative phase, whereas for the Multi-Spectral spatial-only focusing the N_λ solutions were incoherently added. The transmitted pulse should then recover its Fourier-limited duration, as shown in Section 1.4.1.

Experimental results are presented in Figure 3.9. CCD images show no differences between a flat spectral phase pulse and a spatial-only focusing, that is achieved by phase-conjugating the central wavelength of the pulse. Indeed, as we discussed in Section 3.2.2, we expect similar SBR from Multi-Spectral focusing with a random spectral phase relation, and monochromatic focusing. Nonetheless, these CCD images are only sensitive to the integrated temporal profile of transmitted pulse. We cannot distinguish a spatio-temporal focus from a spatial-only focus, as we do not observe any apparent difference between the two types of focusing.

However, if we observe the temporal profiles of these two output pulses shown in Figure 3.9, that are retrieved with an ICC measurement, we clearly achieve spatio-temporal focusing in the latter case. All temporal curves are averaged over 9 different spatial positions for better visibility. Imposing a flat spectral phase at a chosen spatial position at the output, we observe spatio-temporal focusing at a time determined by the delay line position where the MSTM was previously measured, corresponding to the top arrow in Figure 3.9. Temporal compression of the output pulse is obtained almost to its Fourier limited time-width (150 fs at FHWM), while spatial-only focusing is temporally broadened. Nonetheless, the Gaussian spectral amplitude that we imposed in $E^{\mathrm{out}}_{\mathrm{target}}(\lambda)$ of Equation 3.3 might also slightly increase the pulse duration, as the focus spectrum is narrower. The maximum amplitude of the spatio-temporal focus profile is related to temporal amplitude enhancement η [Aulbach et al., 2011], which is defined as amplitude of the electric field at time where the pulse is focused, over the corresponding averaged background at that time. More precisely, $\eta \simeq \sqrt{\frac{\pi}{4} N_{\mathrm{SLM}}}$, as amplitude of the electric field is probed and SLM is modulating phase of the input field, as demonstrated in optimization [Aulbach et al., 2011]. Here, since $N_{\mathrm{SLM}} = 1024$ SLM pixels were exploited in the MSTM measurement, the measured $\eta \sim 20$ is in agreement with expected value.

We now discuss the temporal background signal. The shape of the pulse around the peak is not due to artifacts but can be explained from the 10 nm spectral window used in the MSTM measurement. It gives a cardinal sine form with an expected rebound at 400 fs from the arrival time of the pulse. One could also attribute the increase of the background to long-range correlations. However, the thick sample of ZnO used in the experiment is characterized by its confinement time of photons $\tau_m \sim 1.8$ ps. With a transport mean free path $l^\star \sim 1$ μm - 5 μm [Andreoli, 2014, Curry et al., 2011] and thickness L ~ 20 μm - 100 μm, the optical conductance g, as defined in Section 1.2.3, can be estimated[1]: $g \gg 1$. Even if long-range correlations exist in such samples, measuring them directly with a single input polarization state would be challenging [Vellekoop and Mosk, 2008b]. Imprecision of the spectral phase measurement, spectral discretization of the MSTM, as well as errors in transmission matrix measurements, would result in same spatial focusing but no temporal compression, thus might explain this increase of the background for different times. We also point out that the tails of the pulse spectrum

[1] With a section S $\sim L^2 \sim 100\mu\mathrm{m}^2$ and central wavelength $\lambda_0 = 800$ nm, the number of transmitted modes through the scattering sample scales as $N_{\mathrm{modes}} \sim 10^4$. Therefore, the optical conductance can be estimated as $g \sim N_{modes} l^\star / L$ [Akkermans and Montambaux, 2007](Equation 12.10), leading to $g \sim 10^3$ with an optical thickness $L/l^\star \sim 10 - 15$.

are missing in the content of the MSTM, as we have only measured frequencies over a spectral interval $\Delta\lambda$ where spectral amplitude was above $\sim 40\%$ of the maximum value.

In addition to spatio-temporal focusing, the MSTM gives also access to more sophisticated spectral shapes, via a proper adjustment of (θ_l). The control of this information allows any kind of spectral shape at the output of the scattering medium [Weiner, 2000], without any additional measurement. In essence, the scattering medium in conjunction with the spatial light modulator can be used as a deterministic pulse shaper. In the next Section, we list a series of examples of such experimental pulse shaping.

3.3.3 Using the scattering medium as a controllable pulse shaper

In this Section, we demonstrate temporal shaping of the output pulse, via a deterministic control of its spectral phase (θ_l). Spectral amplitude (r_l) follows the Gaussian shape of the input pulse, as we studied in Multi-Spectral focusing (see Section 3.2.2). By imposing a specified phase relation (θ_l) between spectral components, we demonstrate spatio-temporal focusing at chosen space-time position using the exact same experimentally measured MSTM, as well as more advanced temporal profiles. The corresponding input SLM pattern for each example is retrieved with the protocol presented in Section 3.2.2 for Multi-Spectral focusing, except that we now control (θ_l).

Delaying or advancing the pulse

A linear spectral phase relation (θ_l) enables spatio-temporal focusing of the output pulse pulse at a specific delay time relatively to the flat spectral phase pulse, as we studied in Equation 1.24. The slope of (θ_l) imposes the arrival time of the output pulse:

$$\theta_l = \frac{(l-1) - \dfrac{N_\lambda}{2}}{N_\lambda}\delta\phi \tag{3.4}$$

with l the index of each individual N_λ wavelength over a spectral interval $\Delta\lambda$ centered around λ_0, varying from 1 to N_λ, and $\delta\phi$ the phase difference between the first and the last wavelength. By tuning the slope of the imposed spectral phase ramp [Weiner, 2000], the ultrashort pulse can be temporally shifted with a controllable delay τ in comparison with an imposed flat phase, that reads:

$$\tau = -\frac{\delta\phi\ \lambda_0^2}{2\pi c\ \delta\lambda} \tag{3.5}$$

with c the speed of light. Therefore, by tuning $\delta\phi$ and its sign, the arrival time of the output pulse is controllable.

In Figure 3.10a and Figure 3.10b, two different spectral phase ramp profiles are presented, as well as their corresponding measured temporal profiles, retrieved with ICC. The predicted arrival time of pulses are indicated by top arrows on each plot. The ultrashort pulse is focused in the same output spatial position, but its arrival time has been changed. In these examples, we chose the phase ramps to impose $\tau_a = -256$ fs and $\tau_b = 171$ fs.

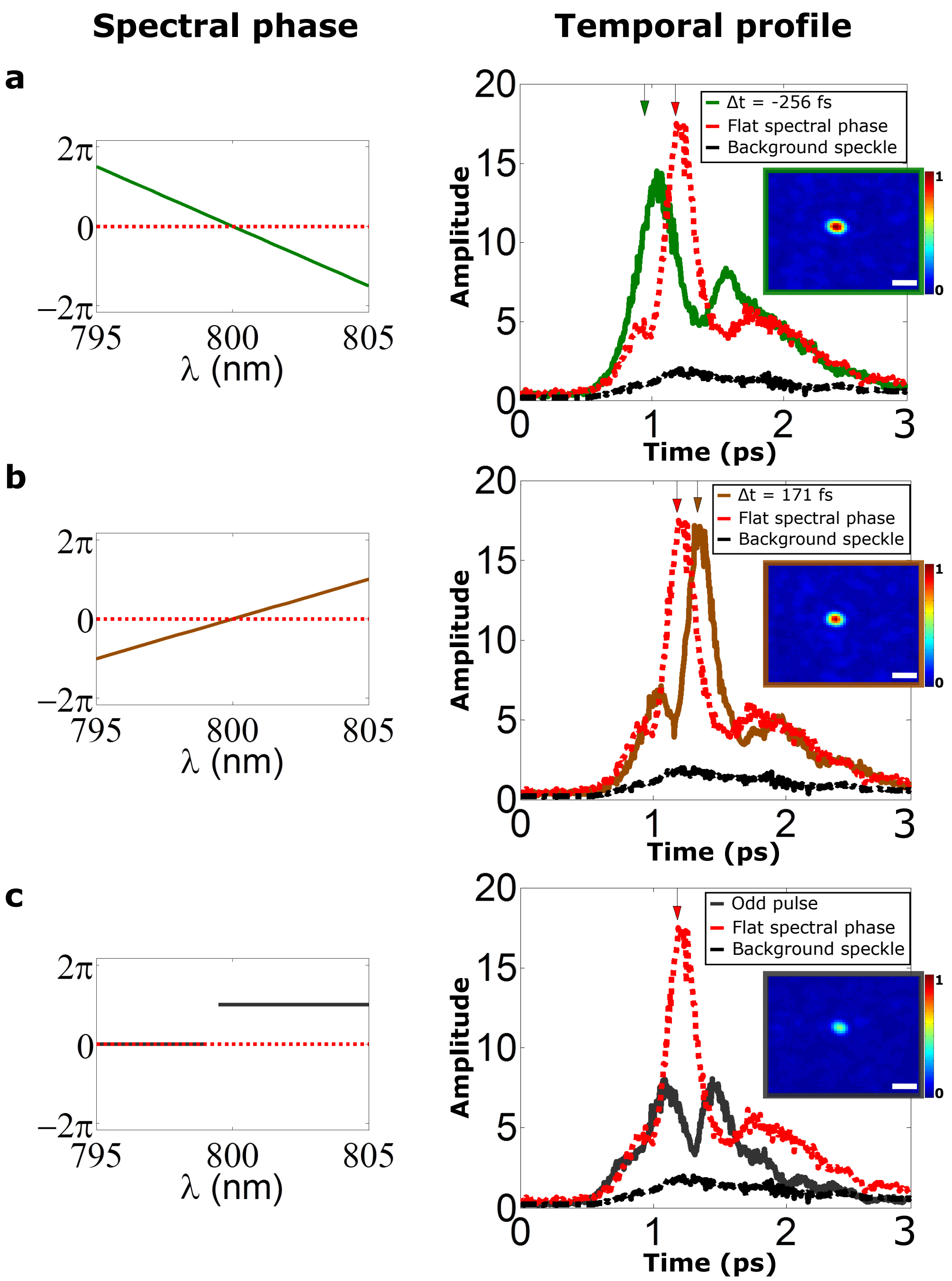

Figure 3.10 – Controllable pulse shaping with the full MSTM. A set of different spectral phase distributions (θ_l) is applied on $E^{\text{out}}_{\text{target}}(\lambda)$ with similar spectral amplitude (r_l), that is fitting a similar Gaussian shape as the input pulse spectrum. Spectral phase distribution is shown on left, and the corresponding measured temporal profile of focus, retrieved with ICC technique and averaged over 9 different focus positions, is shown on right. Red top arrow indicated delay line position where MSTM has been measured. **(a-b)** A spectral phase ramp is applied. Slope of the ramp is tuning the pulse arrival delay time related to flat spectral phase pulse, while its sign indicates if the output pulse is being advanced or retarded. Colored top arrows indicate expected arrival time according to applied spectral phase slope. **(c)** An odd pulse is obtained by imposing a π-phase step in the spectrum. A dip appears in the temporal profile instead of a peak. Insets: CCD image of focusing for each spectral phase relation, normalized by CCD intensity of flat spectral phase pulse. Scale bar: 5 μm.

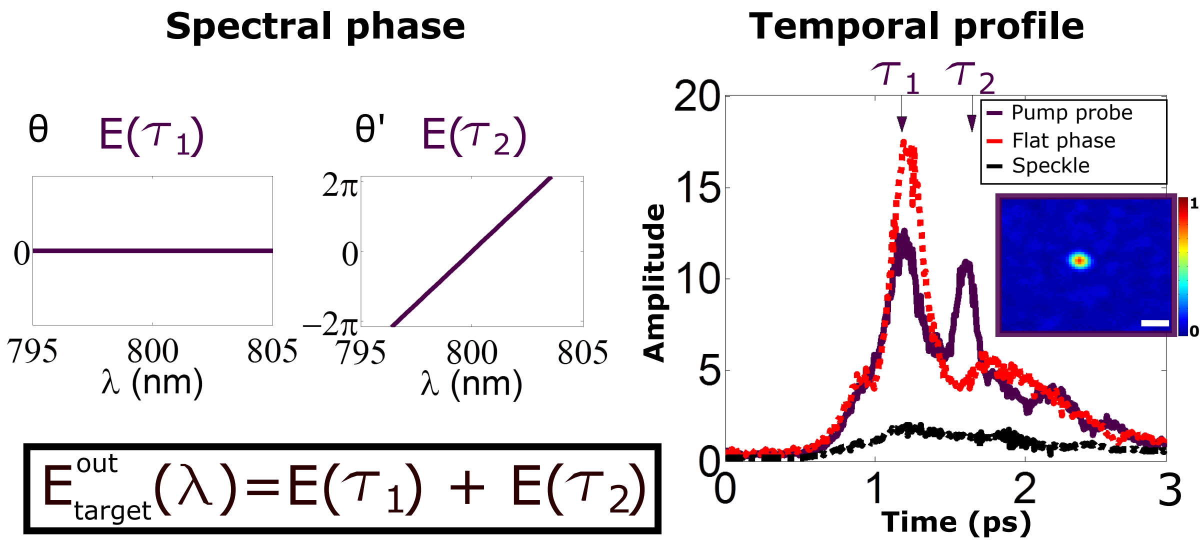

Figure 3.11 – Pump probe pulse profile with the full MSTM. A double pulse can be achieved with $E^{out}_{target}(\lambda)$ that is the sum of two spatio-temporal focus, in the same spatial position but at different delays. **(left)** The global $E^{out}_{target}(\lambda)$ corresponds to the sum of two spatio-temporal focusing whose spectral phase (θ_l) and (θ_l') are shown. **(right)** Temporal profile of the achieved pulse, retrieved with ICC and averaged over 9 different focus positions. In the same spatial position, two pulses at delay time τ_1 and τ_2 are focused. Expected arrival times are shown with top arrows, whose delay times are calculated according to (θ_l) and (θ_l'). Inset: CCD image of a pump-probe focusing experiment. Light is focused in a single spatial position. Intensity is normalized by maximum of CCD image corresponding to a flat spectral phase pulse.

Odd pulse

Another example consists in imposing a π-phase step between the two halves of the spectrum. The operation induces a pulse with a dip in its temporal profile rather than a peak. This so-called odd pulse [Weiner and Heritage, 1987, Weiner et al., 1992] can be extremely useful for coherent control [Meshulach and Silberberg, 1999]. The experimental result is shown in Figure 3.10c, averaged over 9 different focal points. As expected, a dip is present in the temporal profile at the delay time where the MSTM was measured.

Double pulses with controllable delay

In the previous Section, we demonstrated how to focus the output pulse at a specific position in space and time. We now exploit the linearity of the system to focus the output pulse at one given spatial position but at two different times. For this purpose, the targeted output field $E^{out}_{target}(\lambda)$ is a linear superposition of two spectral phase ramp pulses at the same spatial position. Such targeted output allows the arrival of two pulses with a controllable delay. $E^{out}_{target}(\lambda)$ reads:

$$E^{out}_{target}(\lambda) = \underbrace{\begin{pmatrix} r_1 e^{i\theta_1} \\ \dots \\ r_{N_\lambda} e^{i\theta_{N_\lambda}} \end{pmatrix}}_{\tau_1} + \underbrace{\begin{pmatrix} r'_1 e^{i\theta'_1} \\ \dots \\ r'_{N_\lambda} e^{i\theta'_{N_\lambda}} \end{pmatrix}}_{\tau_2} \tag{3.6}$$

where the linear phase relation between (θ_l) corresponds to a focus at time τ_1, and (θ_l') at time τ_2. The spectral amplitudes (r_l) and (r_l') are identical: they follow the Gaussian shape of the input pulse, as we have imposed for spatio-temporal focusing in Section 3.3.2.

As an example, we show in Figure 3.11 two pulses separated by Δt = 513 fs. The phase ramps are chosen to impose delay $\tau_1 = 0$ fs (flat phase) and $\tau_2 = 513$ fs. Data are averaged over 9 different focal positions. The intensity of each pulse is lowered by a factor of 2 compared to the situation when individually focusing each pulse, since the number of degrees of freedom N_{SLM} is the same. Such a temporal profile could allow pump-probe excitation for imaging [Matthews et al., 2011] or spectroscopy [Woutersen et al., 1997].

Quadratic dispersion

As a last example, a quadratic spectral phase relation (θ_l) enables control of the group velocity dispersion of the output pulse, with an adjustable chirp, leading to a well-defined temporal broadening of the pulse. As we studied in Section 1.4.1, the quadratic term $\varphi^{(2)}$ of Equation 1.24 stands for group velocity dispersion. For a Gaussian ultrashort pulse, duration of the chirped pulse δt can be calculated as a function of the Fourier limited pulse duration δt_0 and the added chirp $\varphi^{(2)}$ [Diels and Rudolph, 2006]:

$$\frac{\delta t}{\delta t_0} = \frac{\sqrt{\left(\delta t_0\right)^4 + 16\left(\ln(2)\varphi^{(2)}\right)^2}}{\left(\delta t_0\right)^2} \tag{3.7}$$

In Figure 3.12, we focus the output pulse and impose a quadratic spectral phase profile. The MSTM was measured for a different scattering medium, that is characterized by $\tau_m \sim 1$ ps: $N_\lambda = 11$ monochromatic TMs constitute the MSTM.

For 9 different spectral curvatures $\varphi^{(2)}$, we probe the corresponding temporal profiles at the focus position with ICC technique. For each imposed $\varphi^{(2)}$, the temporal envelop is averaged over 9 different focus positions, which allows for measuring the corresponding pulse duration. An imposed flat spectral phase relation $(\theta_1 = \cdots = \theta_{N_\lambda})$ enables measurement of δt_0, that is estimated around 200 fs in this experiment.

In Figure 3.12c, we compare the measured pulse duration for each chirped pulse, with the theoretical prediction from Equation 3.7. The pulse duration evolves with the chirp as expected: the experiment results follows the theoretical prediction for the output pulse duration.

3.4 Summary

In this Chapter, we extended the monochromatic approach to all the spectral components of an ultrashort pulse, via the Multi-Spectral Transmission Matrix. Although measurement of the MSTM is lengthy and requires tunable CW source, the spectral diversity of the scattering medium allows for full Multi-Spectral control of transmitted light. We thus exploit the scattering medium, in conjunction with the SLM, as a controllable grating, with spectral resolution $\delta\lambda_m$ corresponding to the spectral correlation bandwidth of the

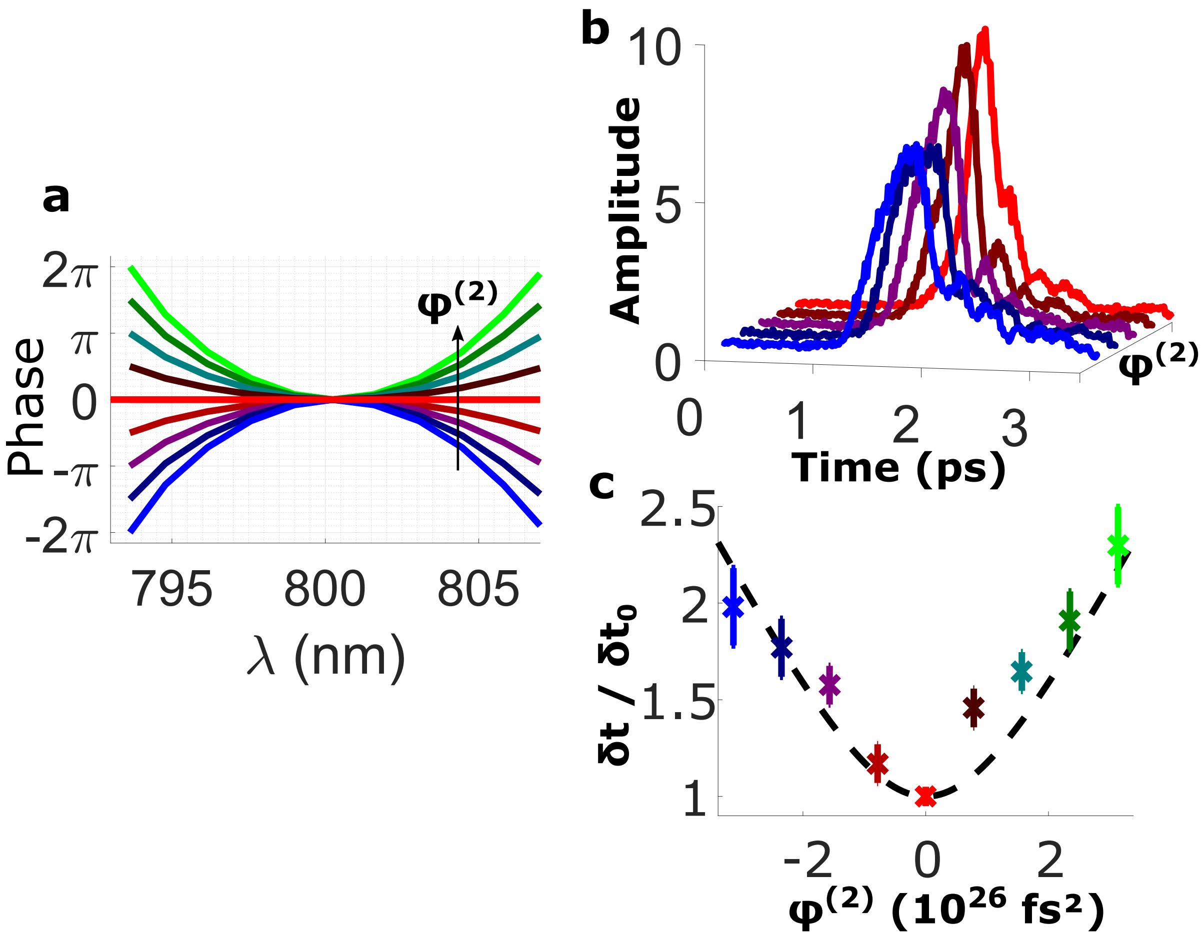

Figure 3.12 – Adjustable chirped pulse via a quadratic spectral phase distribution with the full MSTM. A quadratic spectral phase can be implemented in $E^{\text{out}}_{target}(\lambda)$: we deliberately add group velocity dispersion to the output pulse. The MSTM is measured here on a scattering sample characterized by $\tau_m \sim 1$ ps: the MSTM contains then $N_\lambda = 11$ monochromatic TMs, with $N_{SLM} = 1024$ SLM pixels. **(a)** 9 different quadratic spectral phase distributions (θ_l) are applied on $E^{\text{out}}_{target}(\lambda)$, for different values of chirp $\varphi^{(2)}$. **(b)** For each chirp, the temporal profile, measured with ICC technique, is averaged over 9 focus positions. In the plot we only display 4 averaged temporal profiles (for clarity), for negative chirps and (red) the flat spectral phase temporal profile. Duration of the corresponding chirped pulses δt are extracted. **(c)** δt is plotted for the different $\varphi^{(2)}$. We note $\delta t_0 \sim 200$ fs the duration of the measured flat spectral phase pulse. Theoretical prediction of $\delta t/\delta t_0$ is plotted in black dashed line.

medium. Spatial resolution is given by the spatial speckle grain size, which is diffraction-limited. If the MSTM is measured with an external arm, the relative phase between different spectral components can be recorded and adjusted with the SLM. It enables us to exploit the scattering medium, in conjunction with the SLM, as a deterministic pulse shaper, to achieve for instance spatio-temporal focusing.

As these examples indicate, any temporal shape is achievable, with a resolution given by the temporal duration of the pulse, over a temporal interval related to τ_m the confinement time of the medium. It can be achieved using only spatial degrees of freedom of a single SLM. This temporal control could enable coherent quantum control [Meshulach and Silberberg, 1998], or the excitation of localized nano-objects: enhancement of a non-linear process with the MSTM is studied in Chapter 6.

Full control of the spectral phase with the MSTM also opens interesting perspectives for the study of light-matter interaction, non-linear imaging in multiple scattering media, and more fundamental insights such as light transport properties [Wang and Genack, 2011]. Another potential application could be engineering spectrally-dependent point spread functions of an imaging system. In [Boniface et al., 2017], the monochromatic transmission matrix has been exploited to design the PSF of the imaging system via filtering the TM in a virtual Fourier plane. The use of the MSTM could extend this result in the spectral domain.

Chapter 4

Direct temporal control of the output pulse: the Time - Resolved Transmission Matrix

Contents

In Chapter 3, deterministic control of an ultra-short pulse of light propagating through a multiple-scattering medium, that is naturally distorted both in space and time because of scattering effects, was achieved by measuring its Multi-Spectral Transmission Matrix (MSTM). This tensor characterizes light propagation for all the different wavelengths that compose the incoming pulse, and enables a deterministic spatio-temporal control of the scattered pulse at the output, by exploiting the time-frequency duality. This approach has nevertheless an important practical drawback, in that it requires the full knowledge of the spectral information, i.e the full measurement of the MSTM that includes N_λ monochromatic transmission matrices (with N_λ the number of spectral degrees of freedom), to control accurately the output temporal speckle. If the same laser source is used, one should be able to exploit it both in CW and mode-locked operation, which is far from trivial. Moreover, using ZnO scattering media as described in Section 2.2, N_λ can easily scale up to 10 - 30: MSTM measurement is lengthy, as it requires few hours. Also, most of the information content of the MSTM is superfluous if one is only interested in manipulating light at a specific arrival time at the output.

Other approaches based on the measurement of a time-resolved reflection matrix have also been proposed for focusing [Choi et al., 2013] or imaging [Kang et al., 2015, Badon et al., 2016] at a target depth, inside a scattering medium. In this regime, the time-gated detection of back-scattered photons aims at selecting a certain depth of the scattering sample, essentially by selecting ballistic photons, similarly to optical coherence tomography [Huang et al., 1991, Dubois et al., 2004]. However, when light propagates through a disordered medium with an optical thickness larger than several transport mean free paths, the diffusive regime is reached in transmission and no ballistic photons can be detected at the output.

In this Chapter, we described the Time-Resolved Transmission Matrix (TRTM) of a scattering medium in the diffusive regime, using a coherent time-gated detection with the experimental setup that is detailed in Section 2.1. Unlike the MSTM approach, we demonstrate that a TRTM measured for a given arrival time of photons enables an efficient spatio-temporal focusing of the pulse at precisely that time, in transmission. We then show that the full knowledge of the TRTM allows for shaping more sophisticated spatio-temporal profiles of the pulse at the output of the scattering medium, such as pump-probe profiles.

This Chapter is organized as follows: in Section 4.1, we first introduce the Time-Resolved Transmission Matrix, and the protocol to measure it experimentally, by utilizing the setup shown in Figure 2.1. We then exploit the TRTM to demonstrate spatio-temporal focus-

Most of the content of this Chapter has been published as: Mickael Mounaix, Hugo Defienne, and Sylvain Gigan, "Deterministic light focusing in space and time through multiple scattering media with a time-resolved transmission matrix approach", *Phys. Rev. A*, **94**, 041802 (R) (2016) [Mounaix et al., 2016b].

ing at chosen space-time positions in Section 4.2. We complement these experiments by showing complex spatio-temporal profiles, by combining a couple of time-gated transmission matrices in Section 4.3. For instance, we show pump-probe-like temporal profiles at the output of the scattering medium. We finally complete the study of the TRTM by analysing its singular values in Section 4.4.

4.1 Formalism and measurement of the Time-Resolved Transmission Matrix

As we have developed in Chapter 1 and in Chapter 3, an ultra-short pulse of light propagating through a multiple scattering medium follows a large distribution of optical diffusive paths determined by the exact position of the scatterers. All these optical paths interfere at the output and generate a complex spatio-temporal speckle pattern. Herein, we present the Time-Resolved Transmission Matrix, an operator that directly probes the connection between the input field on the Spatial Light Modulator (SLM) and the output field for photons arriving at a given delay time outside the scattering medium, in transmission.

4.1.1 From the Multi-Spectral Transmission Matrix to the Time-Resolved Transmission Matrix

Spatial and temporal features of the speckle are characterized respectively by the size of a speckle grain, and by the traversal time of the medium, related to its confinement time of photons τ_m. This characteristic time depends only of the medium properties and refers to the duration during which the photons stay confined inside the medium, due to the broad path length distribution in the sample, as presented in Section 1.4.3. In the spectral domain, features of the related spatio-spectral speckle are characterized by the spectral correlation bandwidth of the medium $\delta\lambda_m$, which is the minimal difference in input wavelengths required to generate uncorrelated speckle patterns at the output. The number of spectral/temporal degrees of freedom N_λ is defined as the ratio between the spectral width of the input pulse and $\delta\lambda_m$: it probes the number of spectral speckle grains within the pulse spectral width.

In Chapter 3, we defined the Multi - Spectral Transmission Matrix of the scattering medium as a 3D tensor describing light propagation for all the spectral components of an ultrashort pulse of light. Temporal control of the output pulse has been achieved via a proper spectral shaping. Although such pulse shaping is controllable, in a sense that in principle whatever temporal profile should be accessible via spectral shaping, measurement process is lengthy (typically $\sim$ 3 hours for $N_\lambda = 20$ spectral degrees of freedom and $N_{\text{SLM}} = 1024$ SLM pixels), if the user wants to exploit the MSTM only for spatio-temporal focusing.

Instead of measuring transmission matrices for all the spectral content, one can also access transmission matrices for all photons arriving at a specific delay time. This information is carried within the MSTM if it has been measured at many closely spaced wavelengths via a Fourier transform operation [Carpenter et al., 2016]. Alternatively, it can be accessed directly in the time domain, with a coherence-gated transmission matrix approach. The coherence gate is provided by an external reference pulse, that is the input ultrashort pulse itself: they thus have similar duration and identical spectral bandwidth. The optical field measured at a given arrival time τ_a , defined by the coherence gate position and its width, at the output is then linearly linked to the input field by the formula:

$$E^{\text{out}}(\tau_a) = \mathbf{H}(\tau_a)E^{\text{in}} \tag{4.1}$$

where E^{in} is a complex vector containing the global amplitude and phase values of the ultrashort pulse for each input mode (i.e a SLM pixel); $E^{\text{out}}(\tau_a)$ is a complex vector containing the global amplitude and phase values of the transmitted pulse for each output mode (i.e a CCD camera pixel) measured at a specific arrival time, τ_a, within the coherence gate; and $\mathbf{H}(\tau_a)$ is the transmission matrix measured at τ_a connecting these two quantitites. We name $\mathbf{H}(\tau_a)$ the Time-Gated Transmission Matrix (TGTM), measured at time τ_a. A complete set of matrices $\{\mathbf{H}(\tau_a)\}_{\tau_a}$ forms the full Time-Resolved Transmission matrix (TRTM) of the scattering medium.

Compared to the MSTM, the TRTM should contain the same information directly in the temporal domain on the spatio-temporal coupling of light performed by the scattering medium. Its dimension is thus similar to the MSTM one: the TRTM is a 3D tensor of dimension $N_{\text{out}} \times N_\lambda \times N_{\text{SLM}}$. The full TRTM is composed of N_λ individual time-gated Transmission matrices, that are separated in the time domain by the feature of the temporal speckle, which is the duration of the input pulse δt and of the time gate.

In the next section, we detail how the TRTM can be measured with the experimental setup that was presented in Figure 2.1.

4.1.2 Experimental measurement of the Time-Resolved Transmission Matrix

The TRTM can be directly measured with the experimental setup that was developed in Chapter 2. As we discussed in the above Section, the TRTM is composed of a set of individual time-gated Transmission Matrices. In this Section, we present the protocol to measure a single time-gated Transmission Matrix. After measuring in succession time-gated transmission matrices, we thus access to the TRTM.

Measuring a single time-gated transmission matrix

In the following, the laser is mode-locked: ultrashort pulses of duration $\delta t \sim 100$ fs are propagating through a thick layer of a ZnO scattering sample. Firstly, we measure the time-of-flight distribution of photons in the scattering medium, as we discussed in Section 2.4.3. A random pattern is displayed on the SLM, and the temporal profile of all the speckle grains are simultaneously measured, using ICC technique. Time-of-flight distribution is retrieved by averaging spatially the temporal profile of speckle grains. A typical time-of-flight distribution is shown in Figure 4.1: the characteristic confinement time of photons $\tau_m \sim 2$ ps can be estimated from this plot.

In a second step, the targeted detection time τ_a is set by adjusting the delay line position, as we illustrate in Figure 4.1b. The delay line remains fixed during the measurement process of $\mathbf{H}(\tau_a)$. The matrix is measured column by column by recording the output fields for a set of N_{SLM} SLM patterns at the input. Each transmitted field is retrieved

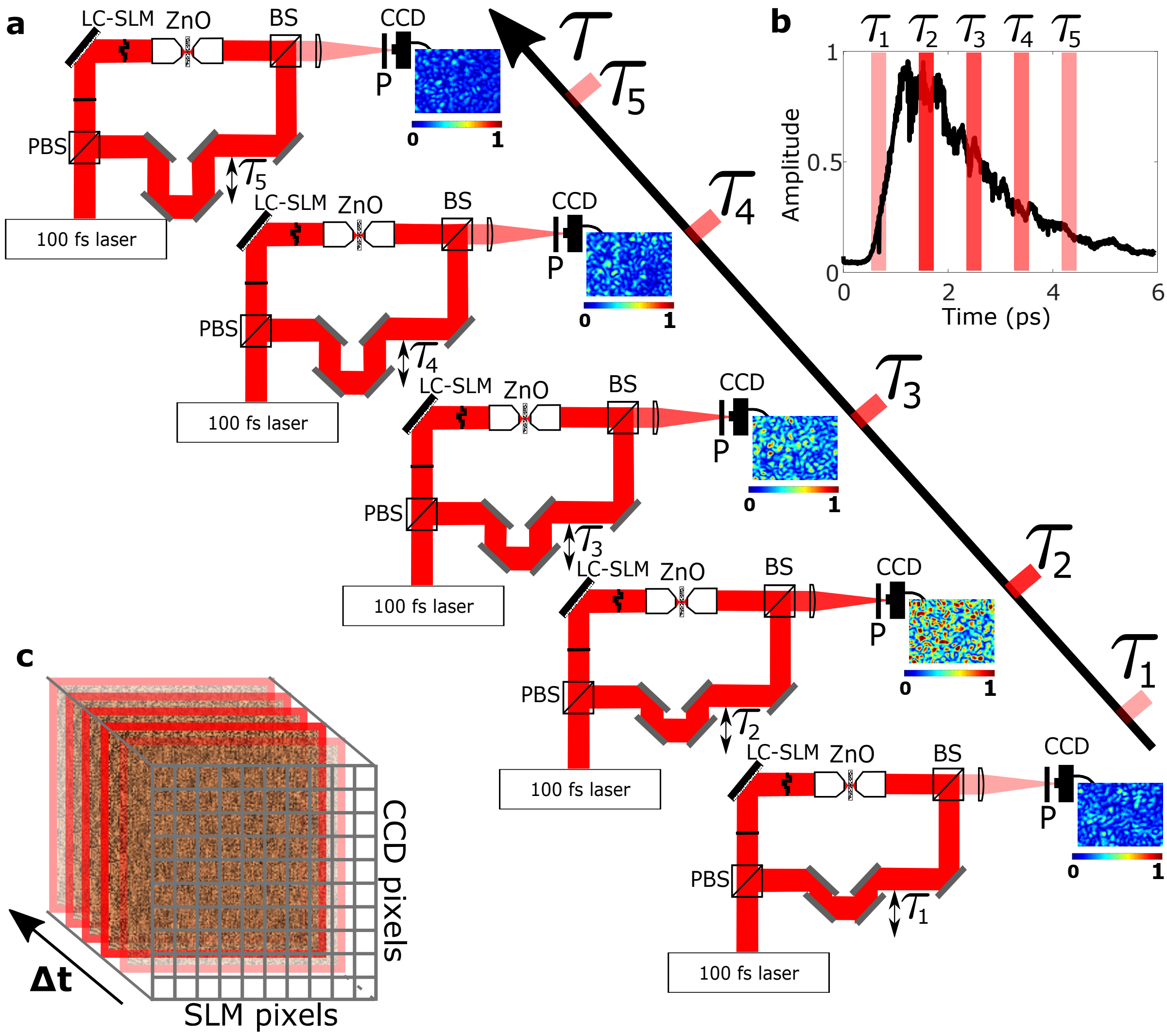

Figure 4.1 – Time-Resolved Transmission Matrix measurement. N_λ stands for the number of temporal degrees of freedom. Only 5 time-gated transmission matrices (TGTMs), measured at delay time (τ_a) are represented for clarity. **(a)** Measurement of the Time-Resolved Transmission Matrix (TRTM) is discretized: N_λ TGTMs are measured, at different arrival times (τ_a) that are separated to each other by δt the duration of the input ultrashort pulse. τ_a is set by adjusting the delay line position, in the external reference arm. Cross-product between the transmitted output pulse and the delayed reference pulse, that is proportional to TGTMs coefficients, is represented on the CCD camera for a flat pattern on the SLM. Color-bar and amplitude are normalized to maximum of cross-product at time τ_2. For each fixed delay line position at time (τ_a), the matrix is measured by setting a series of N_{SLM} pattern on the SLM, and measuring the corresponding output field with phase-stepping holography. (LC-SLM) : Liquid-Crystal Spatial Light Modulator; (PBS): Polarized Beam Splitter; (BS): Beam Splitter; (P): Polarizer; (CCD): Charged Coupled Device; (ZnO): Zinc Oxide scattering medium. **(b)** Typical time-of-flight distribution of photons in the ZnO scattering medium, measured with Interferometric Cross-Correlation. The five delay time (τ_a) are represented on top of the plot. We estimate from this plot $\tau_m \sim 2$ ps the confinement time of photons in the medium. **(c)** Typical schematic representation of the Time-Resolved Transmission Matrix, of dimension $N_{\text{out}} \times N_\lambda \times N_{\text{SLM}}$, where N_{out} stands for number of CCD pixels, and N_{SLM} the number of SLM pixels exploited. In practice $N_{\text{out}} \sim 10^4$ pixels, $N_{\text{SLM}} \sim 1024$ pixels and $N_\lambda \sim 20$ temporal degrees of freedom.

from intensity measurements on the CCD camera at the output, using a phase-stepping holographic process, as in the monochromatic case [Popoff et al., 2010b]. However, in contrast with [Popoff et al., 2010b], the ultrashort reference pulse, from the external arm, provides a time-gating since the interference can only come from a time-window given by the pulse duration δt.

$\mathbf{H}(\tau_a)$ coefficients are the result of the cross-product between the scattered pulse associated field, and the reference pulse associated field at delay time τ_a, as the phase-shifting holography is similar to the monochromatic transmission matrix case (See Equation 1.19). Hence, $\mathbf{H}(\tau_a)$ coefficients are of higher amplitude when τ_a is set close to the maximum of the time-of-flight distribution, where magnitude of the spatially averaged transmitted output field reaches its maximum value.

Typically, in our experiment, $\mathbf{H}(\tau_a)$ is measured in approximately ~ 8 min when $N_{\text{SLM}} = 1024$ SLM pixels are exploited. In essence, the recording process of a single time-gated transmission matrix is as lengthy as the measurement time of a monochromatic transmission matrix fitting the exact same dimension ($N_{\text{SLM}} \times N_{\text{out}}$). This measurement time is mostly limited by the refresh rate of the slow LCOS-SLM. N_{out} depends on the number of speckle grains that are recorded on the CCD camera. Usually, $N_{\text{out}} \sim 10^4$ CCD pixels.

Measuring the set of time-gated transmission matrices

The full TRTM is analogous to a stack of uncorrelated time-gated transmission matrices. Figure 4.1 illustrates the measurement protocol. Once an individual $\mathbf{H}(\tau_a)$ has been measured, the delay line is being shifted to set the targeted detection time to τ_b. $\mathbf{H}(\tau_b)$ is recorded with the same protocol as $\mathbf{H}(\tau_a)$. The operation is iterated for the different arrival time of photons, that are separated by δt, the ultrashort pulse duration.

The number of single time-gated transmission matrix to be measured, in order to form the TRTM, scales with the number of temporal degrees of freedom N_λ, defined in Equation 1.28. Our scattering samples have typical characteristic confinement time $\tau_m \sim 2$ ps: the TRTM is then typically composed of ~ 20 individual time-gated transmission matrices.

A single time-gated transmission matrix $\mathbf{H}(\tau_a)$ contains the relationship between the input field on the SLM, and the transmitted field on the CCD camera, only for photons arriving at τ_a. Therefore, spatio-temporal focusing could be achieved with a single time-gated transmission matrix, rather than exploiting the full MSTM. In the next Section, we demonstrate such spatio-temporal focusing via the TRTM.

4.2 Spatio-temporal focusing with a single temporal degree of freedom

The TRTM of the scattering medium was measured following the protocol that was developed in the above section. In this Section, we demonstrate how the TRTM can be exploited to deterministically achieve spatio-temporal focusing in arbitrary space-time position.

4.2.1 Exploiting a single time-gated transmission matrix: spatio-temporal focusing at the same delay time in different spatial positions

In this Section, we demonstrate spatio-temporal focusing at delay time τ_a using the TRTM.

Protocol for spatio-temporal focusing at delay time τ_a via the TRTM

Spatio-temporal focusing at delay time τ_a consists in exploiting only $\mathbf{H}(\tau_a)$. The corresponding protocol reads:

1. We extract the time-gated transmission matrix $\mathbf{H}(\tau_a)$ from the TRTM.
2. The pattern to be programmed on the SLM, for focusing light in space and time, is then calculated using a phase conjugation approach as in [Popoff et al., 2010b]:

   $$E^{\text{in}} = \mathbf{H}^{\dagger}(\tau_a) E_x^{\text{target}} \tag{4.2}$$

   where $\mathbf{H}^{\dagger}(\tau_a)$ is the conjugate transpose of $\mathbf{H}(\tau_a)$ and E_x^{target} (See Equation 1.23) is a null vector with a coefficient 1 at the row corresponding to the targeted position x on the camera.
3. As the SLM is phase-only, we display on the SLM the phase of E^{in}.

Performing a digital phase conjugation in Equation 4.2 corresponds to controlling the phase of the input modes - and then consequently the global phase of the speckle patterns they generate at the output. Thus we precisely set these speckles to interfere constructively at the targeted output position. Thanks to the time gating due to the reference pulse during the measurement of $\mathbf{H}(\tau_a)$, this constructive interference process occurs only for a specific arrival time. $\mathbf{H}^{\dagger}(\tau_a)\mathbf{H}(\tau_a)$ acts then as a time reversal operator [Prada et al., 1996] for the arrival time τ_a with a spatial-only control, and light is focused both in space and time at the output [Derode et al., 1995, Aulbach et al., 2011].

Experimental results of spatio-temporal focusing

Experimental results of spatio-temporal focusing of an ultrashort pulse of light, that is transmitted through a thick layer of ZnO nanobeads randomly distributed, are shown in Figure 4.2. The time-gated matrix $\mathbf{H}(\tau_a)$ is measured using a set of $N_{\text{SLM}} = 256$ SLM pixels, at the arrival time $\tau_a = 1$ ps as indicated by the top arrows, in approximately ~ 2 minutes. Temporal profile of the output pulse at the targeted spatial position is reconstructed with an ICC measurement. In this example, τ_a corresponds to the arrival time where time-of-flight distribution reaches its maximum.

As presented in Figure 4.2a, the temporal profile of the resulting focused pulse (red) shows a peak of intensity centered at τ_a with a temporal width of ~ 150 fs, close to the width of the Fourier-limited incoming pulse (~ 100 fs). The spatial content is measured with a CCD camera: light is focused on the chosen speckle grain. Spatio-temporal focusing has thus been achieved with the TRTM. As a comparison, black line of Figure 4.2a represents the time-of-flight distribution. Although the transmitted pulse naturally suffers

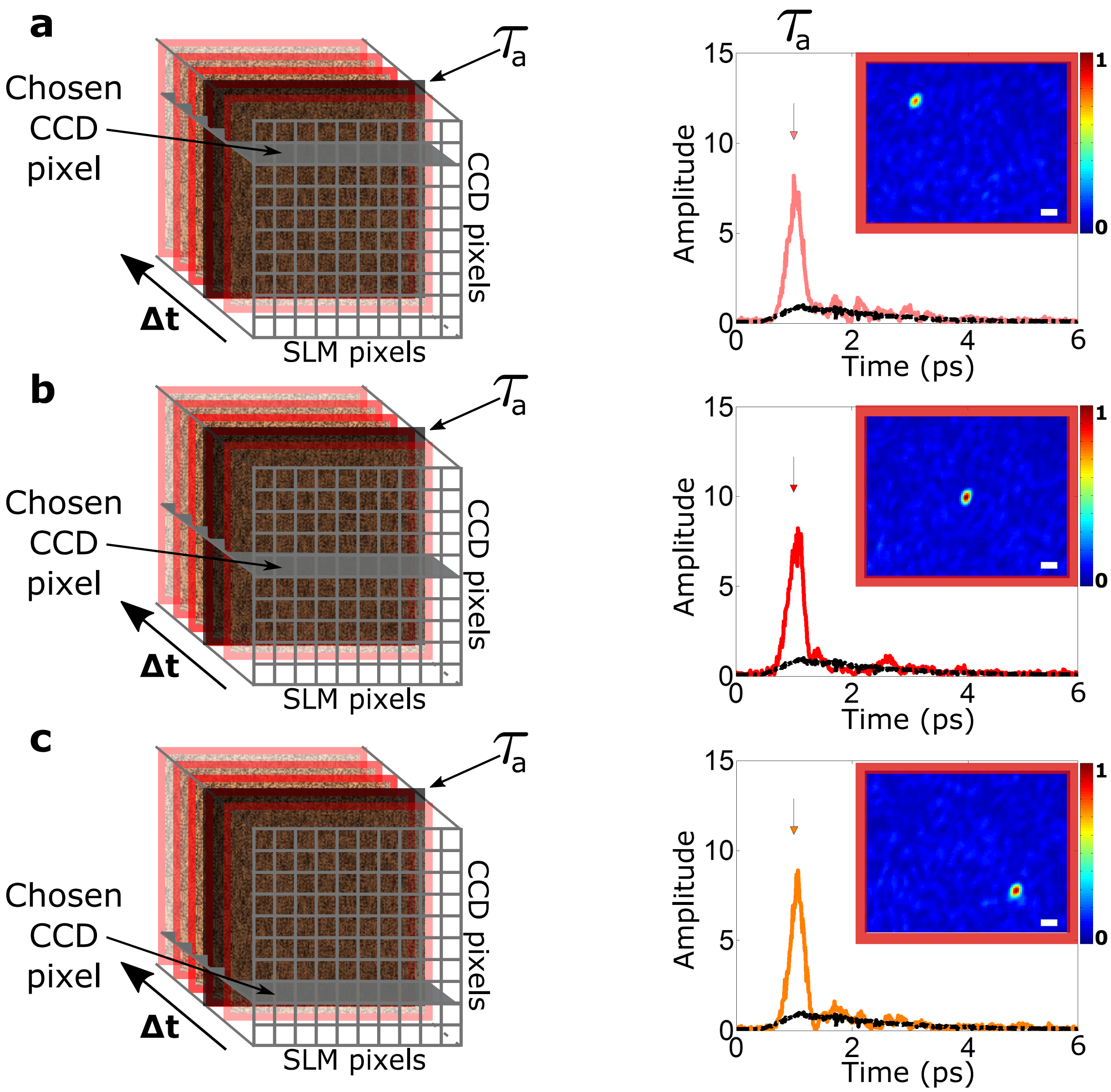

Figure 4.2 – Spatio-temporal focusing with a single time-gated Transmission Matrix. A single time-gated Transmission Matrix $\mathbf{H}(\tau_a)$ (black vertical plan), corresponding to $\tau_a = 1$ ps, is extracted from the TRTM, that was measured with $N_{\mathsf{SLM}} = 256$ SLM pixels. TRTM is illustrated on the left side. Spatial targeted position is represented by the gray horizontal cross-section on the TRTM. Temporal profile of the achieved spatio-temporal focusing is retrieved with ICC measurement. Focusing is achieved by phase-conjugating $\mathbf{H}(\tau_a)$. **(a)** A chosen targeted spatial position is selected on top left corner of the CCD camera. The target position is visible on the CCD image in inset. Temporal profile at this spatial position shows a peak at time τ_a, whose duration $\sim$ 150 fs is close to the duration of the input pulse. The time-of-flight distribution (black line) is obtained by averaging temporal profiles over 100 different speckle grains at the output. The confinement time of photons inside the medium is evaluated from this averaged profile to be about $\tau_m \simeq 2$ ps. **(b - c)** Temporal profiles and the corresponding CCD camera images for spatio-temporal focusing processes performed at two different spatial positions, using the same transmission matrix $\mathbf{H}(\tau_a)$. Averaged temporal profiles are drawn in black. Intensity of CCD images are normalized by maximum of CCD image of (b). Scale bar: 5 μm.

from temporal broadening, wavefront shaping with the spatial light modulator allows for spatio-temporal focusing with spatial-only degrees of freedom. Signal-to-background ratio of focusing is analyzed in Section 4.2.3.

By changing E_x^{target} in Equation 4.2, the output pulse can be focused at any arbitrary output spatial position. As presented on Figure 4.2b and Figure 4.2c, the resulting temporal profiles for focusing at two different spatial positions show the same temporal compression at the arrival time $\tau_a = 1$ ps. As expected, the intensity enhancements, observed on the CCD camera, are also similar (See insets).

When comparing the temporal profiles obtained with the MSTM (See Figure 3.9) and with the TRTM (See Figure 4.2), temporal width of the achieved pulses are similar. Nonetheless, the temporal signal out of τ_a is much lower using the TRTM. More precisely, it follows the averaged background speckle. Indeed, the time-gating measurement only control light over a temporal interval that is δt, the duration of the ultrashort pulse, centered around τ_a. The shaped input pattern is thus generating speckle for the other arrival times, while any error in the spectral phase control in the MSTM increases the background. As we can expect, TRTM is thus more adapted for spatio-temporal focusing than the full MSTM. Furthermore, we stress out that measuring $\mathbf{H}(\tau_a)$ takes approximately 2 minutes with $N_{\text{SLM}} = 256$ SLM pixels, rather than an additional factor N_λ for the full measurement of the MSTM.

4.2.2 Exploiting different time-gated transmission matrices at the same spatial position: spatio-temporal focusing at different delay times

In the previous section, we exploited a single time-gated transmission matrix $\mathbf{H}(\tau_a)$ from the TRTM to demonstrate spatio-temporal focusing, at different spatial positions but occurring at the same arrival time τ_a. In this Section, we demonstrate spatio-temporal focusing in the same spatial position x, at different delay time τ.

Following the same protocol that was developed in the above section, transmitted light can be focused in the same spatial position x but at different arrival time τ. In the first step of the protocol, the time-gated transmission matrix $\mathbf{H}(\tau)$ has to be extracted rather than $\mathbf{H}(\tau_a)$.

Figure 4.3 illustrates the experimental results. Three different time-gated transmission matrices, at arrival times τ_1= 2.1 ps, τ_2= 3.3 ps and τ_3= 4.5 ps are exploited for spatio-temporal focusing in the same position x, at these three different times. τ_1 has been selected such that $\tau_1 > \tau_a$. On the CCD image, light is focused in position x, as expected. Nonetheless, intensity at the focus is lower than in Figure 4.2. Indeed, the chosen arrival time τ_1 corresponds to a lower averaged transmitted intensity. The temporal profile in the focus position, retrieved with ICC measurement, reveals a peak at time τ_1. Amplitude of the maximum is slightly lower than in Figure 4.2, because of the conservation of temporal enhancement [Aulbach et al., 2011] which is defined as the ratio between amplitude of the focus and the averaged background speckle amplitude at the same arrival time (See Section 3.3.2).

Figure 4.3b and Figure 4.3c illustrate as well spatio-temporal focusing in the same spatial position but at different arrival times τ_2 and τ_3. The CCD image of focusing with $\mathbf{H}(\tau_2)$

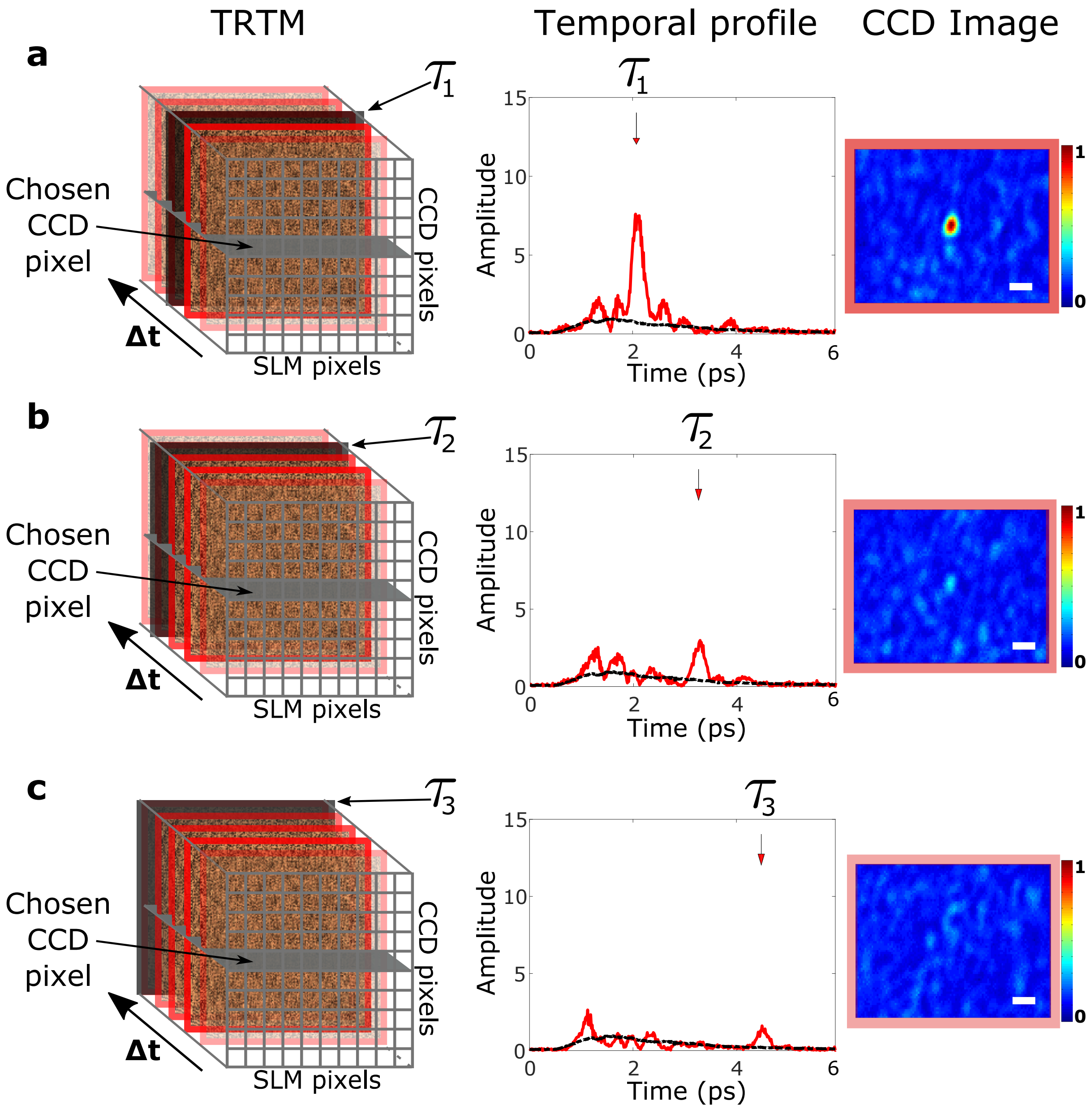

Figure 4.3 – Spatio-temporal focusing with different time-gated transmission matrices. Light is focused in the same spatial position, but at different arrival times. 3 time-gated transmission matrices are extracted from the TRTM, at arrival times τ_1= 2.1 ps, τ_2= 3.3 ps and τ_3= 4.5 ps, that were measured with $N_{\text{SLM}} = 256$ SLM pixels. Temporal profiles are retrieved with ICC measurement on the focus position. **(a)** Phase-conjugation of $\mathbf{H}(\tau_1)$ leads to spatio-temporal focusing at arrival time τ_1 in the selected spatial position. The target position is visible on the CCD image. **(b-c)** Spatio-temporal focusing in the same spatial position at times τ_2 and τ_3. Intensity of the focus, detected by the CCD camera, decreases as it follows the time-of-flight distribution for a fixed number of N_{SLM} SLM pixels. Scale bar: 5 μm.

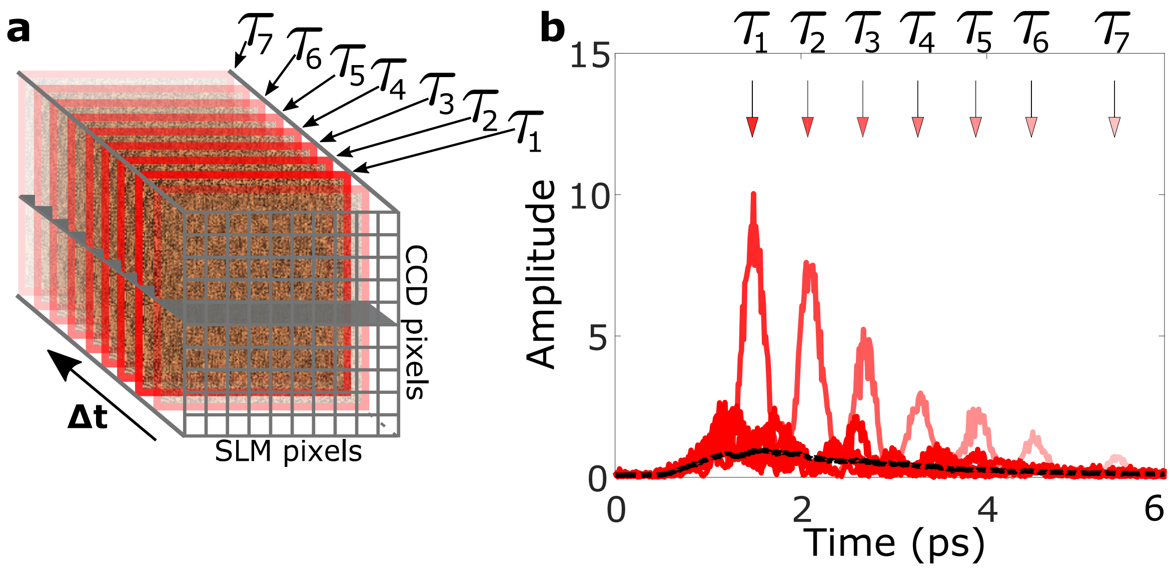

Figure 4.4 – Spatio-temporal focusing with different single time-gated Transmission Matrices, at different delay times. Spatio-temporal control of light with the Time-Resolved Transmission Matrix, that was measured with $N_{\text{SLM}} = 256$ SLM pixels. **(a)** Simplified scheme of the TRTM. 7 individual time-gated transmission matrices are selected, whose arrival times are distributed between $\tau_1 = 1.5$ ps and $\tau_7 = 5.4$ ps. **(b)** Superposition of temporal profiles acquired with ICC measurement, using spatio-temporal focusing processes at the same output position and different arrival times (colored arrows). The time-of-flight distribution is used as a reference temporal profile (black curve).

reveals a focus with low signal-to-background ratio, as the averaged background speckle amplitude at time τ_2 scales as 40% of the time-of-flight distribution maximum. Temporal profile of the focus reveals a peak precisely at τ_2. An extreme scenario is presented with phase-conjugation of $\mathbf{H}(\tau_3)$, where time-of-flight distribution amplitude at time τ_3 is 5 times lower than its maximum. On the CCD camera, no focus is detected. Nonetheless, the temporal profile at spatial position x is revealing a low amplitude temporal peak, exactly at time τ_3, whose amplitude is ~ 10 times lower than temporal profiles of Figure 4.3. The amount of experimental noise level in the tail of the time-of-flight distribution induces a decrease of the temporal enhancement at such delay times [Aulbach et al., 2011].

In Figure 4.4, 7 time-gated transmission matrices were recorded at 7 different arrival times distributed between $\tau_1 = 1.5$ ps and $\tau_7 = 5.4$ ps. The time gap between two targeted arrival times $|\tau_i - \tau_j|$ is set larger than the time-width of a temporal speckle grain, which corresponds also to the time-width of the initial input pulse (See Section 2.4.3), to ensure the matrices are well uncorrelated with each other. As presented in Figure 4.3, each matrix of the set can be independently used to perform spatio-temporal focusing at the different arrival times. Spatio-temporal focusing can then be achieved in arbitrary space-time positions, by phase-conjugating a chosen line of the corresponding time-gated transmission matrix. Resolution of the focus is defined by the time-width of the temporal peak, which is the duration of the input pulse. The temporal interval over which spatio-temporal focusing can be performed is limited by τ_m the confinement time of photon inside the scattering medium.

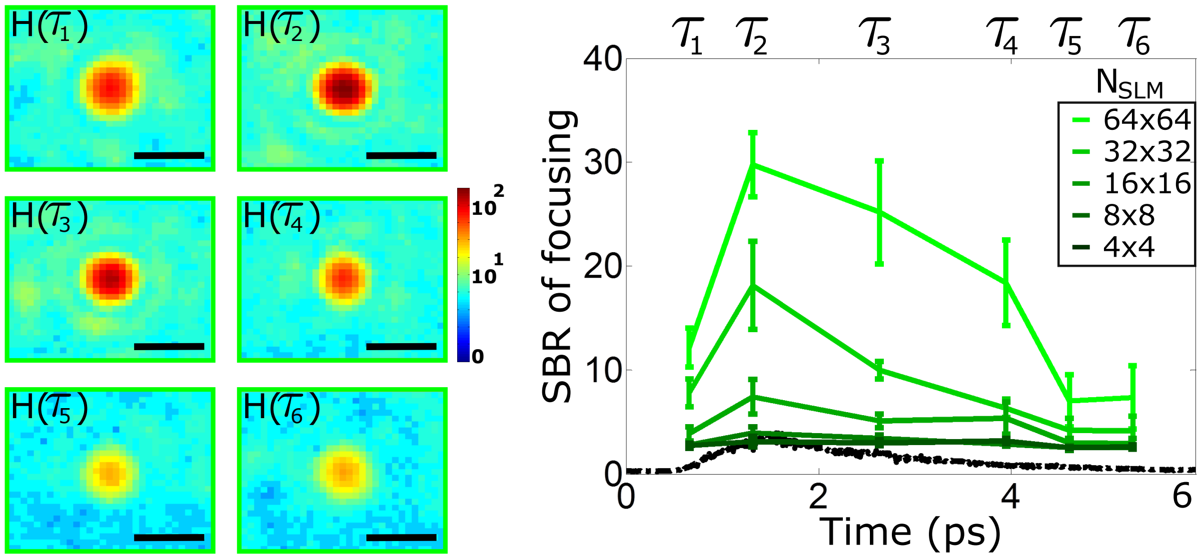

Figure 4.5 – Signal-to-background ratio upon focusing with a single time-gated transmission matrix. Signal-to-background ratio (SBR) measured on the CCD camera for different targeted arrival times, and different number of modes controlled at the input N_{SLM}. The SBR is the ratio of the intensity at the targeted pixel of the CCD camera and the mean intensity value of the full speckle image. **(left)** CCD images of focusing using a 6 different time-gated transmission matrices (TGTMs) at 6 arrival times $\mathbf{H}(\tau_k)$. The corresponding TGTMs were measured with $N_{\mathrm{SLM}} = 64 \times 64$ SLM segments. Intensity is represented in log scale. Scale bar: 5 μm. **(right)** SBR of focusing measured on the CCD camera at 6 different arrival times τ_k, and different N_{SLM}. Error bars are standard deviation for SBR over 9 different focus positions.

4.2.3 Signal-to-background ratio of spatio-temporal focusing

The efficiency of the spatio-temporal focusing process can be analyzed by measuring signal-to-background ratio (SBR) on the CCD images recorded at the output. The SBR is defined here as the ratio of the intensity at the targeted pixel of the CCD camera over the mean intensity value of the full speckle image, integrated over the acquisition time of the camera (the CCD images are thus not time-resolved). Figure 4.5 shows experimental results for a set of focusing varying two parameters: either the arrival time of the focus, or the number of N_{SLM} SLM pixels used in the measurement process of the TRTM.

At the arrival time when transmitted light is focused, the time-resolved intensity at the focus scales linearly with the number of modes controlled at the input, N_{SLM} [Aulbach et al., 2011]. Indeed, all the spatial degrees of freedom are exploited only in a single temporal speckle grain: we then obtain similar SBR as the monochromatic focusing, but just for this time. However, the temporally-integrated CCD image of the focus reveals a lower SBR, as the contribution of the background is increased due to the other temporal speckle grains. SBR values depend both on the targeted arrival time and on the number of modes controlled at the input. For a given arrival time, the SBR increases with the number of controlled modes (also verified in [Aulbach et al., 2011]). For a fixed number of controlled modes, maximal values of SBR are always reached for the targeted arrival time that corresponds to the maximum of the time-of-flight distribution. Interestingly, we observe that spatio-temporal focusing may be achieved even for very long arrival time ($\tau_7 \approx 5.4$ ps, see also Figure 4.4) where the photon rate is very low, provided the number of modes controlled is sufficiently high. As the input light is broadband, values of SBR measured in this experiment are much lower than the one observed in the monochromatic case, that we already studied in Chapter 3. Besides, SBR is much lower than the peak to background intensity that would be obtained at the target time τ_a.

The obtained SBR also depends on the scattering medium, by means of its characteristic confinement time of photons, τ_m. For a fixed number of controlled modes at the input, and a fixed arrival time, the SBR decreases with τ_m. Indeed, the equivalent spectral point of view indicates that the number of spectral/temporal degrees of freedom N_λ scales with τ_m: only a single temporal scattering channel is controlled over N_λ upon focusing.

4.3 Advanced pulse shaping with the Time-Resolved Transmission Matrix

In the previous section, we exploited a single time-gated transmission matrix, from the Time-Resolved Transmission Matrix, in order to perform spatio-temporal focusing at arbitrary space-time positions. Similarly to the Multi-Spectral approach developed in Section 3.2.2 with the Multi-Spectral Transmission Matrix, we demonstrate some more advanced spatio-temporal focusing profiles with the Time-Resolved Transmission Matrix.

4.3.1 Spatio-temporal focusing of two pulses in the same spatial output position

In Section 4.2.1, we developed a protocol to achieve spatio-temporal focusing via a single time-gated transmission matrix, that is extracted from the TRTM. The TRTM can also be used to shape more complex spatio-temporal profiles at the output.

Protocol for focusing two pulses in the same spatial position with the TRTM

In analogy with the targeted output field $E^{\text{out}}_{target}(\lambda)$ that was set in Equation 3.3 for spectral shaping in a given spatial position x, we can introduce an equivalent protocol for temporal pulse shaping:

1. Targeted output spatial position x corresponds to a cross-section of the TRTM. This cross-section, which a 2D-slice of the TRTM of dimension $N_\lambda \times N_{\text{SLM}}$, is extracted (gray plan in Figure 4.6a). This matrix-slice is denoted $\mathbf{T}$: it contains the relation between the input field and the different arrival delay times of the output pulse at this specific spatial output position.
2. By analogy to Equation 4.2, we use the transpose conjugate of $\mathbf{T}$ to determine the spatial shape of the input field. In this case, the targeted output field $E^{\text{out}}_{\text{target}}$ is a vector $E^{\text{out}}_{target}(\tau)$ of dimension N_λ, which is a null vector except at delay time (τ_k), where k corresponds to the delay times where the pulse is focused, whose value is one:

$$E^{\text{out}}_{\text{target}}(\tau) = \begin{cases} 0 & \text{for} \quad i \neq k \\ 1 & \text{for} \quad i = k \end{cases} \tag{4.3}$$

3. As the SLM is only able to modulate the phase of the input field, we display on the SLM the phase of the previously calculated solution.

$E^{out}_{target}(\tau)$ enables then to select the arrival times for focusing the output pulse: its general form can be used to focus up to N_λ pulses, with a single input phase pattern on the SLM. Here we demonstrate simultaneous focusing of two pulses at delay times τ_1 and τ_2, similarly to the pump probe-like temporal profile that was demonstrated in Figure 3.11. $E^{\text{out}}_{\text{target}}(\tau)$ contains then only two non-null values. Equivalently, such spatio-temporal focusing is achieved using a combination of the matrices $\mathbf{H}(\tau_1)$ and $\mathbf{H}(\tau_2)$. The corresponding input pattern on the SLM reads:

$$E^{\text{in}} = \mathbf{H}^\dagger(\tau_1)E^{\text{target}}_x + \mathbf{H}^\dagger(\tau_2)E^{\text{target}}_x \tag{4.4}$$

where E^{target}_x is a null vector containing a coefficient 1 at the line that corresponds to the position x of the camera.

Experimental results

Figure 4.6a shows results of spatio-temporal focusing with $\tau_1 = 1$ ps and $\tau_2 = 2.2$ ps. On the CCD camera, we observe light focusing on a single speckle grain. Temporal profile in this specific spatial position is retrieved with ICC measurement. Logically, we observe that the intensity values of the two successive peaks are approximately half the intensities obtained for the same arrival times using a simple spatio-temporal focusing process presented in Figure 4.4, with the same number of input modes ($N_{\text{SLM}} = 256$ SLM pixels). Such a deterministic pump-probe-like pulse has an interesting potential for applications in light-matter interaction in scattering media [Sapienza et al., 2011].

4.3.2 Spatio-temporal focusing of two pulses in two different spatial output positions

An extension of the previous result is to perform such spatio-temporal focusing (two pulses with delays τ_1 and τ_2) in two different spatial positions x_1 and x_2, rather than in the same spatial speckle grain. The corresponding input pattern to be displayed on the SLM then reads:

$$E^{\text{in}} = \mathbf{H}^\dagger(\tau_1)E^{\text{target}}_{x_1} + \mathbf{H}^\dagger(\tau_2)E^{\text{target}}_{x_2} \tag{4.5}$$

where $E^{\text{target}}_{x_1}[E^{\text{target}}_{x_2}]$ is a null vector containing a coefficient 1 at the line that corresponds to the position $x_1[x_2]$ of the camera. Figure 4.6b shows experimental results obtained by generalizing this process to the case $x_1 \neq x_2$. The output speckle is now focused simultaneously at two different times ($\tau_1 = 1$ ps and $\tau_2 = 2.2$ ps, visible on temporal profiles) and at two different speckle grains (visible on the CCD image).

The amplitude of temporal peaks are similar whether the output pulse is focused in one or two different spatial speckle grains, as it only depends on the number of spatial degrees of freedom N_{SLM}.

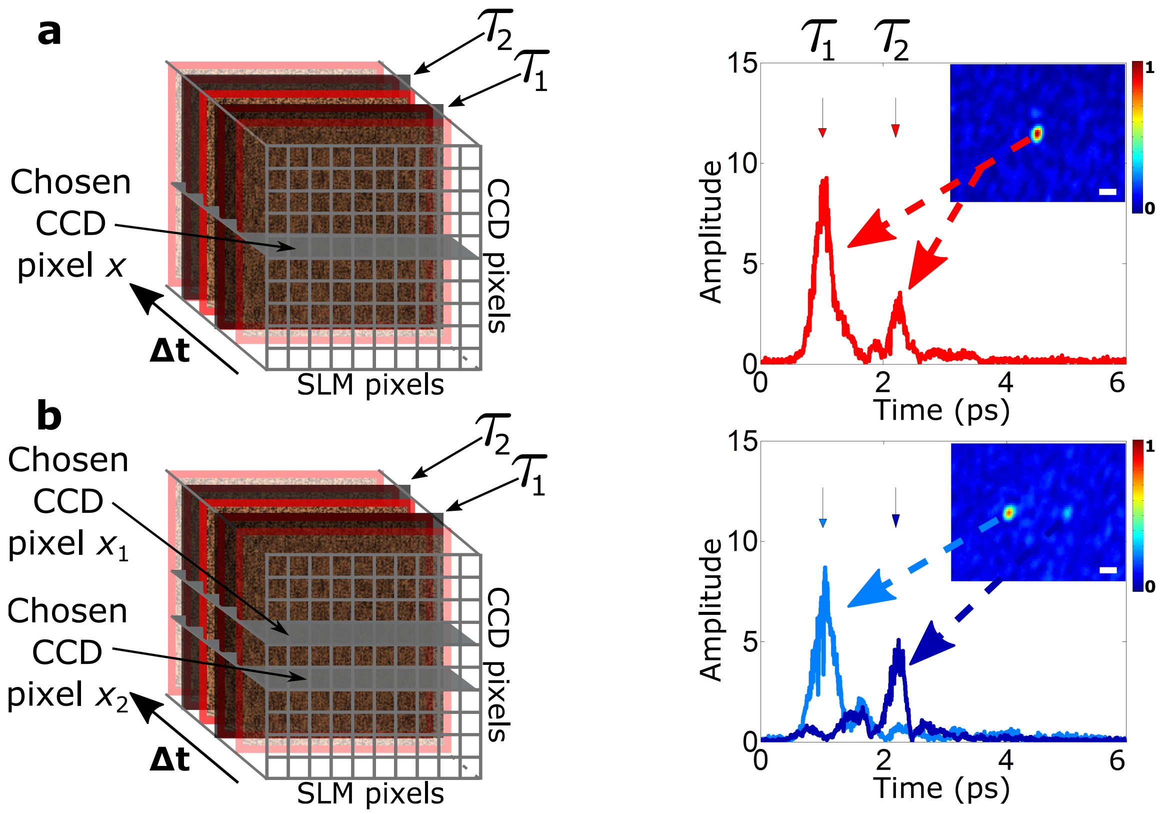

Figure 4.6 – Complex spatio-temporal shaping by exploiting the full TRTM. Two time-gated transmission matrices at delay times τ_1 and τ_2 are extracted from TRTM. **(a)** Temporal profile recorded using a spatio-temporal focusing process at one spatial position x (gray horizontal plane on the TRTM) and at two different arrival times $\tau_1 = 1$ ps and $\tau_2 = 2.2$ ps. CCD image in inset shows the position of the spatial target. **(b)** Temporal profiles recorded using a spatio-temporal focusing process at the same two different arrival times, $\tau_1 = 1$ ps and $\tau_2 = 2.2$ ps, and at two different spatial positions, x_1 and x_2 (gray horizontal planes the TRTM), visible on the CCD image in inset. CCD is normalized by maximum intensity of **(a)**. Scale bar is 5 μm.

4.4 Singular value decomposition of the Time-Resolved Transmission Matrix

Previously, the TRTM was exploited for focusing purposes, via phase-conjugation of time-gated transmission matrices. However, it should be emphasized that the TRTM contains information about light propagation that goes beyond focusing. For instance, with a monochromatic transmission matrix, singular value decomposition provides an access to the distribution of energy in the measured scattering channels [Popoff et al., 2011b]. In the monochromatic regime, recent works have demonstrated transmittance enhancement by either iteratively optimizing total transmission [Popoff et al., 2014, Ojambati et al., 2016], or by propagating singular vectors through the scattering medium, that are associated to the highest singular values of the TM [Choi et al., 2011a, Kim et al., 2012, Hsu et al., 2017].

Using an ultrashort pulse of light, light transmission can be enhanced by coupling to open transmission channels with iterative DOPC [Bosch et al., 2016]. Recent works reported an increase of the frequency width of open channels in scattering media, either in optics [Bosch et al., 2016] or in microwave regime [Wang and Genack, 2011, Shi and Genack, 2015]. Nonetheless, no recent work, to our knowledge, is specifically reporting enhancement of light transport only at a chosen arrival time of photons after propagation through multiple scattering media.

In this Section, we analyze the singular value decomposition of an experimentally measured TGTM $\mathbf{H}(\tau)$. We exploit it to enhance transport of light at a chosen time τ via the singular vectors of $\mathbf{H}(\tau)$ associated to the highest singular values, without focusing on a speckle grain.

4.4.1 Introduction to singular value decomposition

Singular value decomposition of a transmission matrix

A transmission matrix (TM), that is either monochromatic or time-gated, is unique as it describes light propagation, monochromatic or broadband, for a given scattering sample. If we translate the scattering sample, to illuminate another part of it, it would lead to an uncorrelated measured TM, that would nonetheless look as random as the previous TM. These two matrices might have some similar properties, such as transmission eigenvalues, which cannot be trivially accessed.

Singular Value Decomposition (SVD) generalizes diagonalization of a matrix, regardless of its dimensions and its diagonalizability. Considering a TM, that we note $\mathbf{H}$, of dimension $N_{\text{out}} \times N_{\text{SLM}}$, SVD allows for decomposing the TM as:

$$\mathbf{H} = \mathbf{U}\mathbf{S}\mathbf{V}^{\dagger} \tag{4.6}$$

where $\dagger$ stands for the conjugate transpose operation. $\mathbf{S}$ is a diagonal matrix of dimension $N = \min(N_{\text{out}}, N_{\text{SLM}})$, whose coefficients are real and positive numbers. They are named singular values and denoted λ_m: these values are the square root of energy transmission coefficients of the so-called transmission channels [Rotter and Gigan, 2017]. The singular values of $\mathbf{S}$ are sorted in descending order. $\mathbf{U}$ and $\mathbf{V}$ are unitary matrices, of dimension respectively $N_{\text{out}} \times N_{\text{out}}$ and $N_{\text{SLM}} \times N_{\text{SLM}}$: they are the *left* and the *right* singular vectors of $\mathbf{H}$. $\mathbf{U}$ and $\mathbf{V}$ are related to transmission channels output and input modes with associated singular values. Therefore, SVD provides an essential tool study how the incident energy is being split through the scattering channels.

Nonetheless, we stress out that the extracted transmission channels from the transmission matrix do not directly correspond to the "physical" channels of the medium. Indeed, while singular vectors are orthogonal by construction, physical modes would be orthogonal only if we measure them in totality. Our measurement protocol gives access to a single side of the medium, with a limited numerical aperture. As the number of modes, according to Equation 1.10, can scale up to 10^4 with a medium section $\sim 100\mu\text{m}^2$, we cannot distinguish physical modes from TM channels: each TM channel is a complex combination of a huge number of physical channels of the medium.

In our experiments, the singular vectors do not enable an access to the so-called open channels, as we measured only a subpart of the total number of scattering channels [Goetschy and Stone, 2013] (See Section 1.2.3). Still, this repartition of singular values can be studied. In the regime of low mode control, the transmission matrix is equivalent to a random matrix without correlations [Popoff et al., 2011b]. Random matrix theory can then be applied to study statistics of singular values [Aubry and Derode, 2010].

Marcenko-Pastur law

Random matrix theory is valid for a TM with independent variables: short range correlations (See Section 1.2.3) and energy conservation thus break this hypothesis. Nonetheless, impact of short range correlations can be eliminated by performing binning of the TM output modes by a factor that is the typical speckle grain size: in that way, every output modes would be independent. Energy conservation is furthermore not verified in our experimentally measured TM, as for instance we have only access to one side of the scattering sample. Random matrix theory predicts that the statistical distribution of the normalized singular values follows the Marcenko-Pastur law $\rho(\tilde{\lambda})$ [Marčenko and Pastur, 1967] for a matrix whose elements are independent variables with identical Gaussian distribution. Therefore, $\mathbf{H}$ should verify the Marcenko-Pastur law, as demonstrated for monochromatic transmission matrix in [Popoff et al., 2010b]. Normalized singular values $\tilde{\lambda}_m$ are defined as follows:

$$\tilde{\lambda}_m = \frac{\lambda_m}{\sqrt{\frac{1}{N}\sum_{j=1}^{N}\lambda_j^2}} \tag{4.7}$$

By denoting $\gamma = N_{\text{out}}/N_{\text{SLM}}$, $\rho(\tilde{\lambda}_m)$ from Marcenko-Pastur law reads:

$$\rho(\tilde{\lambda}) = \frac{\gamma}{2\pi\tilde{\lambda}}\sqrt{(\tilde{\lambda}^2 - \tilde{\lambda}^2_{\text{min}})(\tilde{\lambda}^2 - \tilde{\lambda}^2_{\text{max}})} \tag{4.8}$$

where $\tilde{\lambda}_{\text{min}}$ and $\tilde{\lambda}_{\text{max}}$ stands for the minimum and maximum normalized singular values.

In the next section, we analyze the distribution of normalized singular values of the Time-Resolved transmission matrix. We verify that its distribution is in agreement with Marcenko-Pastur law, and study the result of sending singular vectors through the scattering medium.

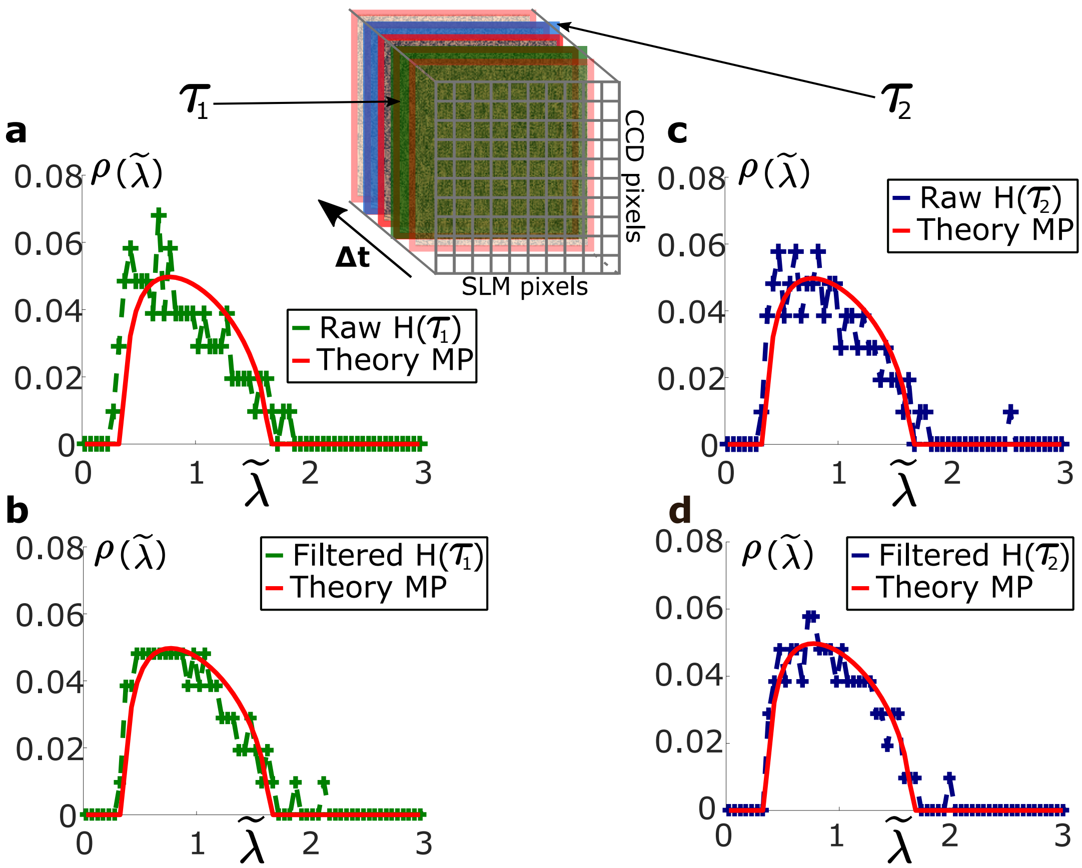

Figure 4.7 – Distribution of normalized singular values of a single time-gated transmission matrix. The full TRTM has been measured with $N_{\text{SLM}} = 256$ SLM pixels and $\gamma = 2.5$, for a thick scattering medium, that is characterized by $\tau_m \sim 2$ ps. **(a)** A single TGTM $\mathbf{H}(\tau_1)$ is extracted from the TRTM at arrival time τ_1. After binning the output pixel by the typical speckle grain size, leading to a matrix $\mathbf{M}(\tau_1)$, the distribution of its normalized singular values is plotted (green), in comparison with theoretical prediction from Marcenko-Pastur (MP) law (red). **(b)** $\mathbf{M}(\tau_1)$ is filtered by normalizing its lines and columns: fidelity with theoretical prediction is improved. **c-d** The protocol is iterated for an uncorrelated time-gated transmission matrix $\mathbf{H}(\tau_2)$, that is extracted from the same TRTM, at arrival time τ_2.

4.4.2 Analysis of the singular value decomposition of a time-gated transmission matrix

In this Section, we assume the Time-Resolved transmission matrix of the scattering medium, which is characterized by its confinement time $\tau_m \sim 2$ ps, was measured with $N_{\text{SLM}} = 256$ SLM pixels. From this tensor, we extract a single time-gated transmission matrix $\mathbf{H}(\tau_1)$ (See Figure 4.7).

Before studying the SVD, we have to extract a submatrix from $\mathbf{H}(\tau_1)$ to ensure the output components are properly uncorrelated [Popoff et al., 2011b]. From the original $\mathbf{H}(\tau_1)$, we extract $\mathbf{M}(\tau_1)$ by only picking a single pixel per speckle grain in the output coordinates of the matrix, which corresponds to matrix lines. This filtering process ends up with a rectangular matrix of factor $\gamma \simeq 2.5$.

After computing the SVD of $\mathbf{M}(\tau_1)$, the statistics of its singular values are studied in Figure 4.7a. We plot the distribution of the normalized singular values, as well as the

$\rho(\tilde{\lambda})$ that represents the prediction from Marcenko-Pastur law (See Equation 4.8) in Figure 4.7a. Experimental data $\rho_{\text{exp}}(\tilde{\lambda})$ shows a good agreement with the theoretical prediction. The normalized root-mean-square E_r [Popoff et al., 2011b], which quantifies the deviation to Marcenko-Pastur law, is defined as:

$$E_r = \frac{\sqrt{\frac{\sum_{j=1}^{N}\left(\rho_{\text{exp}}(\tilde{\lambda}_j) - \rho(\tilde{\lambda}_j)\right)^2}{N}}}{\max(\rho(\tilde{\lambda}))} \tag{4.9}$$

Here, we observe that E_r is lower than the deviation observed for a monochromatic TM measured with a co-propagative reference beam [Popoff et al., 2011b]. Indeed, the speckle reference produces additional correlations, that might induce a divergence to the predicted distribution of normalized singular values. This kind of additional correlations should not influence the experimental distribution of normalized singular values of the TGTM, as the reference beam, when measuring $\mathbf{H}(\tau_1)$, is external. Nonetheless, illumination on the SLM is not homogeneous, because of the Gaussian shape of the beam, which could add some correlations in the matrix coefficients. Filtering by normalizing lines and columns of $\mathbf{M}(\tau_1)$ by their root mean square [Popoff et al., 2011b] could be performed onto $\mathbf{M}(\tau_1)$ to reduce E_r (See Figure 4.7b), which then goes down to 11%. Also, we only have a single realization of the disorder, by means of a single TGTM. E_r could be reduced by measuring TGTMs at the same arrival time but at different sample positions, with the same scattering medium. The presence of singular values above $\tilde{\lambda}_{\text{max}}$, which is effectively increasing E_r, is complex to interpret in such scattering media. Indeed, highly normalized singular values are typically existing in weakly heterogeneous media: the presence of ballistic contributions can be associated to high eigenvalues, or strong scatterers in reflection. DORT methods, standing for decomposition of the time reversal operator [Prada and Fink, 1994], allow to focus onto such scatterers [Popoff et al., 2011a].

The same protocol is presented on Figure 4.7c for a different time-gated transmission matrix $\mathbf{H}(\tau_2)$, that is extracted from the same TRTM, but at a different arrival time τ_2 . With an identical binning of the output pixels, leading to the same γ coefficient and a matrix $\mathbf{M}(\tau_2)$, the distribution of normalized singular values reaches a similar fidelity with Marcenko-Pastur law than $\mathbf{H}(\tau_1)$. The comparison is explicitly shown in Figure 4.7c. A similar filtering on the lines and columns of $\mathbf{M}(\tau_2)$ reduces deviation from Marcenko-Pastur prediction (See Figure 4.7d). Table 4.1 compares E_r for the 7 TGTMs, with and without filtering, that were exploited in Figure 4.4.

$\mathbf{H}(\tau_i)$	τ_1	τ_2	τ_3	τ_4	τ_5	τ_6	τ_7
τ_i(in ps)	1.5	2	2.6	3.3	3.9	4.5	5.4
E_r (%)	19.2	20.0	18.1	14.3	15.3	12.6	14.8
E_r with filtering (%)	15.6	11.7	10.3	9.1	10.0	9.7	8.5

Table 4.1 – Deviation from Marcenko-Pastur law for 7 time-gated transmission matrices, measured at different arrival times. Normalized root-mean-square error E_r between experimental normalized singular values distribution and Marcenko-Pastur law for 7 different time-gated transmission matrices extracted from the same TRTM than in Figure 4.4. Figure 4.7a,c show $\mathbf{H}(\tau_2)$ and Figure 4.7b,d show $\mathbf{H}(\tau_4)$ from this table.

Every single TGTM of the full TRTM is following qualitatively the random matrix theory prediction from [Marčenko and Pastur, 1967]. Deviation from the theory, that is quantified

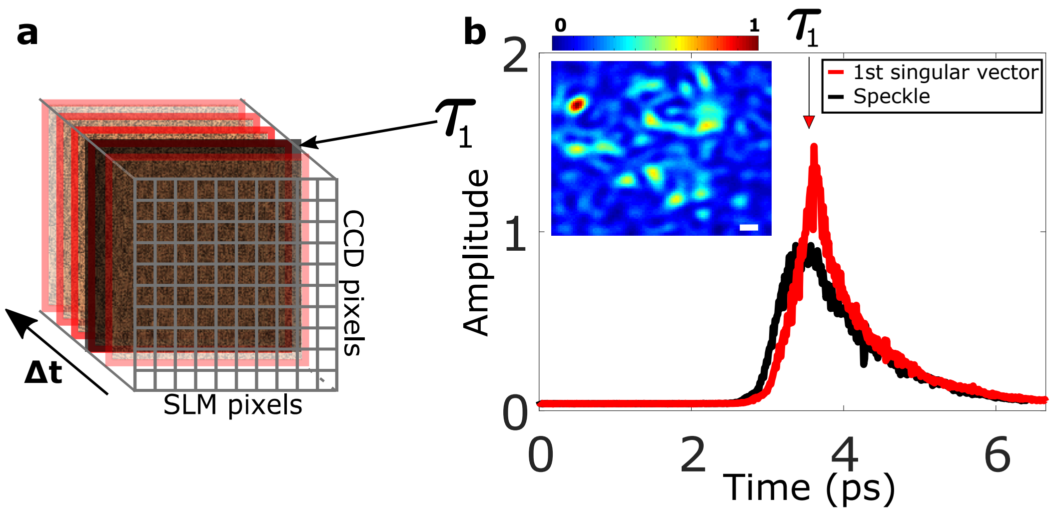

Figure 4.8 – Propagation of the first singular vector, associated to the highest singular value of $\mathbf{H}(\tau_1)$. The scattering medium is characterized by $\tau_m \sim 1.1$ ps. **(a)** The TGTM $\mathbf{H}(\tau_1)$ is extracted from the TRTM, which was measured with $N_{\mathsf{SLM}} = 1024$ SLM pixels and $N_{\mathsf{CCD}} \sim 100$ speckle grains. Its SVD is being computed to extract singular vectors. **(b)** Spatially averaged temporal profile of the first singular vector (red), associated to the largest singular value of $\mathbf{H}(\tau_1)$. As a comparison, the time-of-flight distribution is plotted in black. Top red arrow corresponds to arrival time τ_1. Inset: Normalized CCD image of transmitted first singular vector. Scale bar: 2 μm.

by E_r could have many origins, such as the influence of a single SLM pixel on the different output pixels [Popoff et al., 2011b], or long-range correlation [Hsu et al., 2017].

We note that E_r notably decreases when the time-gate is set to later arrival times. This might be interpreted as an increase of light mixing at longer arrival times, as light has suffered in average more scattering events than photons exiting the medium at early arrival times, such as snake photons [Das et al., 1993].

4.4.3 Propagating singular vectors of a time-gated transmission matrix through the scattering medium

In this section, we propagate singular vectors, extracted from the SVD of a time-gated transmission matrix $\mathbf{H}(\tau)$ measured with the experimental setup shown in Figure 2.1, that are associated to the highest singular values. Similarly to the previous work using CW light enhancing light transmission [Kim et al., 2012], we exploit the SVD to enhance broadband light transport only at the arrival time τ set during the measurement process of $\mathbf{H}(\tau)$. We verify the temporal profiles of such transmitted light with ICC technique.

The full Time-Resolved transmission matrix was here measured with $N_{\mathrm{SLM}} = 1024$ SLM pixels, and the scattering medium is characterized by its confinement time $\tau_m \sim 1.1$ ps.

At a time τ_1 where time-of-flight distribution gets close to its maximum value

We first consider a single time-gated transmission matrix $\mathbf{H}(\tau_1)$, with $\tau_1 = 3.5$ ps (see Figure 4.8), corresponding to the arrival time where the time-of-flight distribution reaches

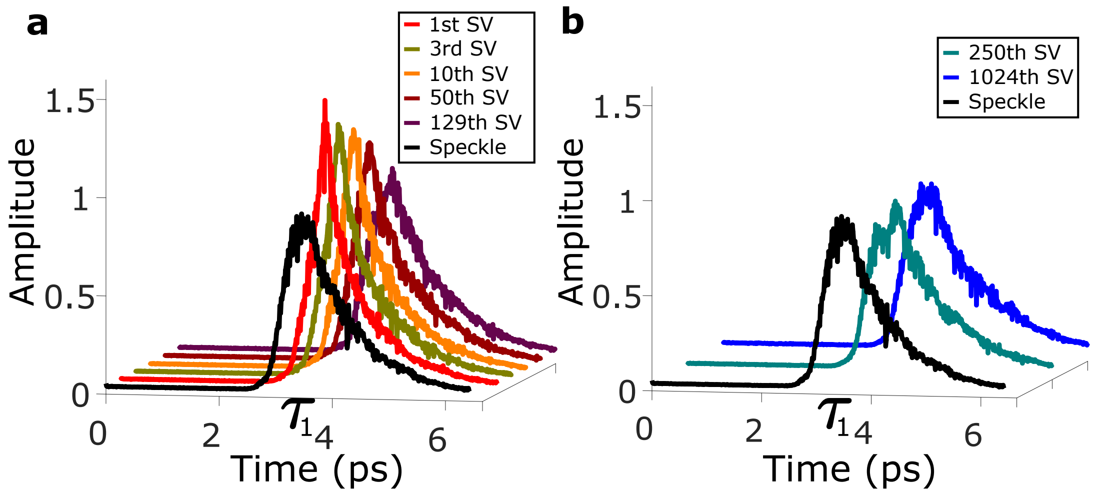

Figure 4.9 – Propagation of singular vectors of $\mathbf{H}(\tau_1)$. Normalized singular values $\tilde{\lambda}$ of $\mathbf{H}(\tau_1)$ are sorted in descending order. In particular for $\mathbf{H}(\tau_1)$, $\tilde{\lambda}_i = 1$ for $i = 166$. **(a)** Propagation of singular vectors of $\mathbf{H}(\tau_1)$, whose associated singular values are larger than unity. **(b)** Propagation of singular vectors of $\mathbf{H}(\tau_1)$, whose associated singular values are lower than unity.

its maximal value. After computing the SVD of $\mathbf{H}(\tau_1)$, we display on the phase-only SLM the phase pattern of the first *right* singular vector, that is associated to the largest singular value of $\mathbf{H}(\tau_1)$. The measured CCD image is shown in Figure 4.8. Light is not spatially focused, as expected. The averaged intensity has been enhanced by a factor $\sim$ 2-3 in comparison with the averaged intensity without shaping (or by displaying a set of random patterns on the SLM). This transmission enhancement is expected to affect only photons arriving at delay time τ_1. Yet, the temporal profile of all the speckle grains are recorded simultaneously with an ICC measurement. The spatially averaged temporal profile of the first singular vector (red line) is presented on Figure 4.8. The top red arrow corresponds to the arrival time τ_1: light intensity has been enhanced only at time τ_1 in comparison with the time-of-flight distribution. Both plots are following a similar exponential decay: the tail is not affected.

Figure 4.9 presents the spatially averaged temporal profiles of other high singular vectors from the same time-gated transmission matrix $\mathbf{H}(\tau_1)$. In Figure 4.9a, a set of five high singular vectors, whose associated normalized singular values are large, are propagating through the scattering sample. Their respective spatially averaged temporal profiles are shown: they all present an amplitude enhancement at time τ_1, which gradually decreases with the index of the singular vector.

Temporal profiles of transmitted singular vectors whose associated $\tilde{\lambda}$ are lower than average are illustrated in Figure 4.9b. No temporal enhancement is observed around τ_1 for the presented two modes. Their average spatial intensities are lower than without shaping, as these two modes are related to low energy scattering-channels [Choi et al., 2011a] (“closed” channels for monochromatic TMs).

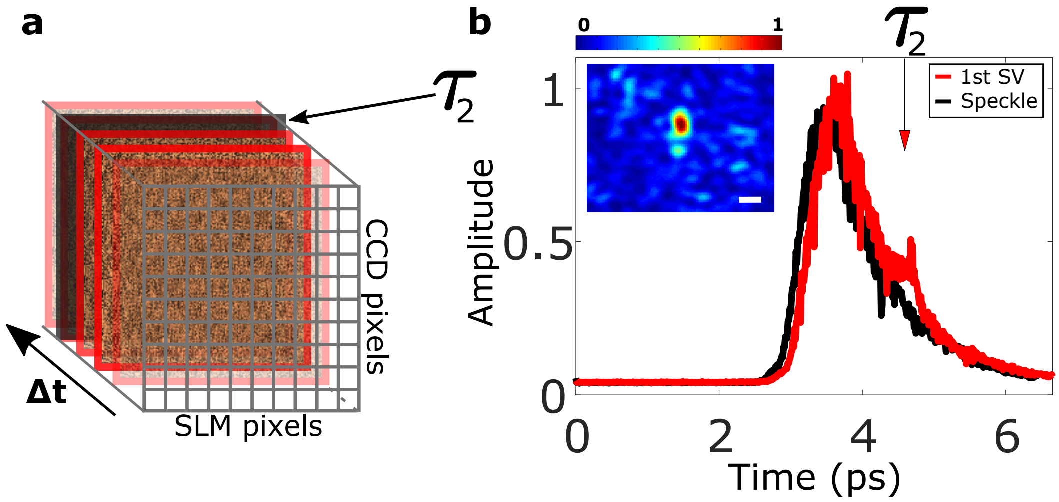

Figure 4.10 – Propagation of the first singular vector, that is associated to the highest singular value of $\mathbf{H}(\tau_2)$. The scattering medium is characterized by $\tau_m \sim 1.1$ ps. **(a)** The TGTM $\mathbf{H}(\tau_2)$ is extracted from the TRTM. Singular vectors are extracted via SVD. **(b)** Spatially averaged temporal profile of the first singular vector (red), associated to the largest singular value of $\mathbf{H}(\tau_2)$. As a comparison, the time-of-flight distribution is plotted in black. Top red arrow corresponds to arrival time τ_2. Inset: Normalized CCD image of transmitted first singular vector. Scale bar: 2 μm.

At a later time τ_2

The exact identical protocol is presented for a different time-gated transmission matrix $\mathbf{H}(\tau_2)$. This TGTM is extracted from the same TRTM, with $\tau_2 = 4.7$ ps (see Figure 4.10) corresponding to a late arrival time. In Figure 4.10, the CCD image corresponding to the first singular vector of $\mathbf{H}(\tau_2)$ is shown. Its mean intensity is larger than without shaping, but it remains lower than the CCD image associated to the first singular vector of $\mathbf{H}(\tau_1)$. The first singular mode temporal profile is plotted and compared to the averaged background speckle without shaping. The temporal profile follows the time-of-flight distribution except at time τ_2 where amplitude is enhanced.

Figure 4.11 is presenting temporal profiles of different singular vectors of $\mathbf{H}(\tau_2)$. Similarly to what was shown in Figure 4.9 for $\mathbf{H}(\tau_1)$, transport of light is enhanced only at delay time τ_2 for singular vectors whose associated $\tilde{\lambda}$ are large.

4.5 Summary

In this Chapter, we introduced and measured the Time-Resolved transmission matrix of a scattering medium with a coherence-gated technique. This 3D tensor is composed of a stack of individual time-gated transmission matrices at various arrival times (τ_k). It contains information on the spatio-temporal coupling of light propagating through the scattering medium. With the use of a single time-gated transmission matrix, we demonstrated deterministic spatio-temporal focusing of an ultrashort pulse of light in arbitrary space-time position. Combining several scattering matrices from the full TRTM enable spatio-temporal focusing at different arrival times, using a single SLM. First results of study of the SVD of a TRTM were presented, highlighting the interest of the approach,

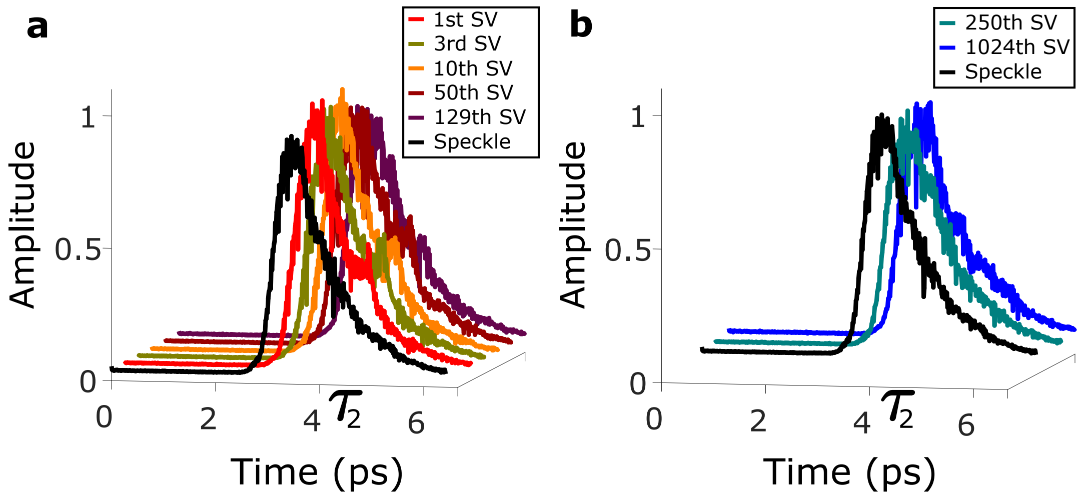

Figure 4.11 – Propagation of singular vectors of $\mathbf{H}(\tau_2)$. Similarly to $\mathbf{H}(\tau_1)$, normalized singular values $\tilde{\lambda}$ of $\mathbf{H}(\tau_2)$ are sorted in descending order. In particular for $\mathbf{H}(\tau_2)$, $\tilde{\lambda}_i = 1$ for $i = 208$. **(a)** Propagation of singular vectors of $\mathbf{H}(\tau_2)$, whose associated singular values are larger than unity. **(b)** Propagation of singular vectors of $\mathbf{H}(\tau_1)$, whose associated singular values are lower than unity.

for light delivery for instance. It could have potential interests in the study of open/closed channels on a “thin” scattering medium, with a large number of controlled modes on the SLM.

It is interesting to compare the TRTM approach demonstrated in this Chapter, to the Multi-Spectral approach of Chapter 3. Although the MSTM and the TRTM contains in principle the same information, the most adapted depend on the experiment to be performed. While the MSTM could address the spectral dispersion by a phase control on all the spectral components of the output pulse, the TRTM enables a direct temporal refocusing by adjusting the optical paths with the same arrival time τ at the output of the medium. Clearly, re-compressing the pulse at the output at a given time is much easier and faster using the TRTM, as it requires measuring a single time-gated transmission matrix, rather than measuring the MSTM for all the spectral components, and then recombining them accordingly. Nonetheless, narrowband focusing as well as more refined pulse control, in phase and in amplitude, of the output pulse is more straightforward using the MSTM.

Chapter 5

Extension of the optical transmission matrix to the broadband regime: Broadband Transmission Matrix

Contents

In the previous Chapters, we measured either the Multi-Spectral transmission matrix (Chapter 3) or the Time-Resolved Transmission Matrix (Chapter 4). These two approaches enabled spatio-temporal control of the output pulse, by either controlling the N_λ spectral degrees of freedom, or a single temporal channel.

Nonetheless, these two methods present drawbacks. Measuring multiple transmission matrices with spectral resolution requires very long measurement time. A time-gated transmission matrix requires an external interferometric reference arm, which implies stability issues. In this Chapter, we study a single linear operator, that we name Broadband transmission matrix. This matrix is measured for a broadband pulse with a co-propagating reference, similarly to [Popoff et al., 2010b] but with broadband light instead of continuous wave light. As we will demonstrate, this operator naturally allows for spatial focusing. Interestingly, it generates a two-fold temporal recompression at the focus compared with the natural temporal broadening, despite an intentional lack of control on the spectral degrees of freedom because of the reference beam.

This Chapter is organized as follows: in Section 5.1 we discuss the state of the art on experiments carried out with broadband light that exploit a co-propagative reference beam. Interestingly, some unexpected properties appears upon wavefront shaping. In Section 5.2, we introduce the Broadband transmission matrix, which connects the broadband input field on the SLM, to the output "broadband field" on the camera with a co-propagative reference beam. We then exploit this operator in Section 5.3 for focusing purposes. More precisely, we analyze the spatial, temporal and spectral features of the achieved focus.

5.1 State of the art on broadband wavefront shaping with co-propagative reference through scattering media

In Chapter 1, we discussed wavefront shaping experiments under illumination of monochromatic coherent light in a multiple scattering medium. Despite the complex structure of speckle patterns, each speckle grain has a deterministic relation to the input fields. Over the last decade, wavefront shaping has turned to be an efficient tool to control monochromatic light through highly scattering systems, notably by exploiting the monochromatic transmission matrix (See Section 1.3.4).

Under illumination with a source of large bandwidth, each spectral component can generate a different speckle pattern, as we studied in Chapter 1 and in Chapter 3. Therefore

This Chapter has been mostly taken from : Mickael Mounaix, Hilton B. de Aguiar, and Sylvain Gigan, "Temporal recompression through a scattering medium via a broadband transmission matrix" *Optica*, **4** (10), 1289-1292 (2017) [Mounaix et al., 2017]). Additional discussions are presented.

one needs to adjust these additional spectral/temporal degrees of freedom to temporally control the output pulse. This can be achieved using methods such as nonlinear optical processes [Katz et al., 2011, Aulbach et al., 2012b], time-gating (Time - Resolved transmission matrix in Chapter 4 or with iterative optimization methods [Aulbach et al., 2011]), and frequency-resolved measurements (spectral pulse shaping [McCabe et al., 2011] or Multi-Spectral transmission matrix in Chapter 3). However, these methods underly either low signal-to-noise measurements (non-linear processes), or stability issues as they require lengthy acquisition procedures [Carpenter et al., 2016] and the need of external reference.

An alternative approach is to use self-referencing signals with a co-propagating reference beam, at the expense of lacking control on spectral degrees of freedom. Recently, such "broadband wavefront shaping" experiments reported outcomes different from what is expected from monochromatic wavefront shaping. For instance, in [Paudel et al., 2013], Paudel and colleagues demonstrated focusing of the broadband pulse with a linear iterative optimization approach and a co-propagative reference beam. Although no spatio-temporal focusing is evidenced, the achieved linear enhancement $\eta_{\text{exp.}}$ is higher than the expected $\eta_{\text{th.}} = \eta_{\text{monochromatic}}/N_\lambda$ [Curry et al., 2011]. As the number of spatial degrees of freedom is fixed by the SLM, it implies the number of independent spectral degrees of freedom was reduced at the focus. This number of spectral degrees of freedom can also be reduced because of long-range correlations when enhancing the total broadband transmission [Hsu et al., 2015].

Another interesting feature with broadband wavefront shaping is the recovery of pure polarization states [Aguiar et al., 2017]. After propagation through thick (several transport mean free paths) multiple scattering media, the achieved "broadband focus", resulting from a broadband wavefront shaping, survives natural polarization scrambling, in contrast with the background speckle. This effect is not present for monochromatic light. Notably, these results could have an impact on biomedical imaging [de Aguiar et al., 2016].

Nonetheless, temporal and spectral properties of the obtained output pulse via broadband wavefront shaping remain elusive. Because the setup we developed in Figure 2.1 gives access to temporal features of transmitted light through scattering media, we introduce and report the first characterization of the so-called Broadband transmission matrix of a scattering medium. This operator is experimentally measured with a co-propagative reference beam. In the next Section, we develop its formalism and measurement protocol. We then exploit this operator to focus light in an arbitrary speckle grain, and we analyze and explain with a simple model its corresponding temporal/spectral properties.

5.2 Definition, formalism and measurement of the Broadband Transmission Matrix

In this Section, we present the concept of the Broadband Transmission Matrix. We first define the formalism of the matrix. We then explicit a protocol to measure experimentally the operator, with the setup of Figure 2.1.

5.2.1 Definition of the Broadband Transmission Matrix with a co-propagative reference beam

Reminder on the monochromatic transmission matrix measured with a co-propagative reference beam

In order to measure a transmission matrix, one needs to measure the output field (as in Equation 1.16). A convenient method consists in using phase-stepping interferometry of the speckle with a speckle reference field [Popoff et al., 2010b] (as in Equation 1.19). The method we present here is exactly the same as in [Popoff et al., 2010b] except that the source is broadband rather than cw. Figure 5.1 illustrates the principle of the measurement of the Broadband Transmission Matrix using a co-propagative ("internal") reference field. The phase-only SLM is divided into a reference zone "iR" and an active zone "iM", which is modulated with respect to the reference part [Popoff et al., 2010b]. The reference (resp. modulated) part on the SLM creates a reference (resp. modulated) speckle "oR" (resp. "oM") at the output of the scattering medium. These two speckles "oR" and "oM" cannot be separated on the CCD camera, as the active zone of the phase-only SLM cannot be switched off.

For a monochromatic input beam at wavelength λ_0, the measured output field at a pixel x, via holographic methods, can be directly related to the input field on the SLM plane at a pixel y with a linear relationship, that is the monochromatic transmission matrix $\mathbf{t}(\lambda_0, x, y)$ (see Equation 1.16). The experimental measurement of the TM with a co-propagative reference leads to an effective transmission matrix $\mathbf{t'}(\lambda_0) = \mathbf{S}^*_{\text{ref}}\mathbf{t}(\lambda_0)$ [Popoff et al., 2010b], where $\mathbf{S}_{\text{ref}}$ is a diagonal matrix related to the contribution of the reference field in amplitude and phase and * represents the phase-conjugation operation. We will now explain how the Broadband Transmission Matrix differs.

Formalism of the Broadband transmission matrix

We now assume the input source is broadband, and the reference beam is co-propagative, as illustrated in Figure 5.1. Transmitted light through the scattering medium, measured with a CCD camera without spectral resolution, results in a low-contrasted intensity speckle. Indeed, this speckle can be seen, for the sake of simplification, as the incoherent superposition of N_λ uncorrelated monochromatic speckles (See Section 1.4.3). Each monochromatic speckle can be decomposed as a coherent sum between a reference field $E^{\text{out,R}}$ and a modulated field $E^{\text{out,M}}$ over a spectral interval $\delta\lambda_m$.

The transmitted intensity can be decomposed as a static term I_0, which contains all field-squared terms, and the incoherent sum of N_λ uncorrelated cross-terms between reference and modulated fields. In essence, each individual cross-term is related to its corresponding monochromatic TM coefficient at a given wavelength λ_i: $E^{\text{out,M}}(\lambda_i) = \mathbf{t}(\lambda_i)E^{\text{in}}(\lambda_i)$, where $E^{\text{in}}(\lambda_i)$ is the controlled input field at the SLM pixel (see iM in Figure 5.1). Thus, the

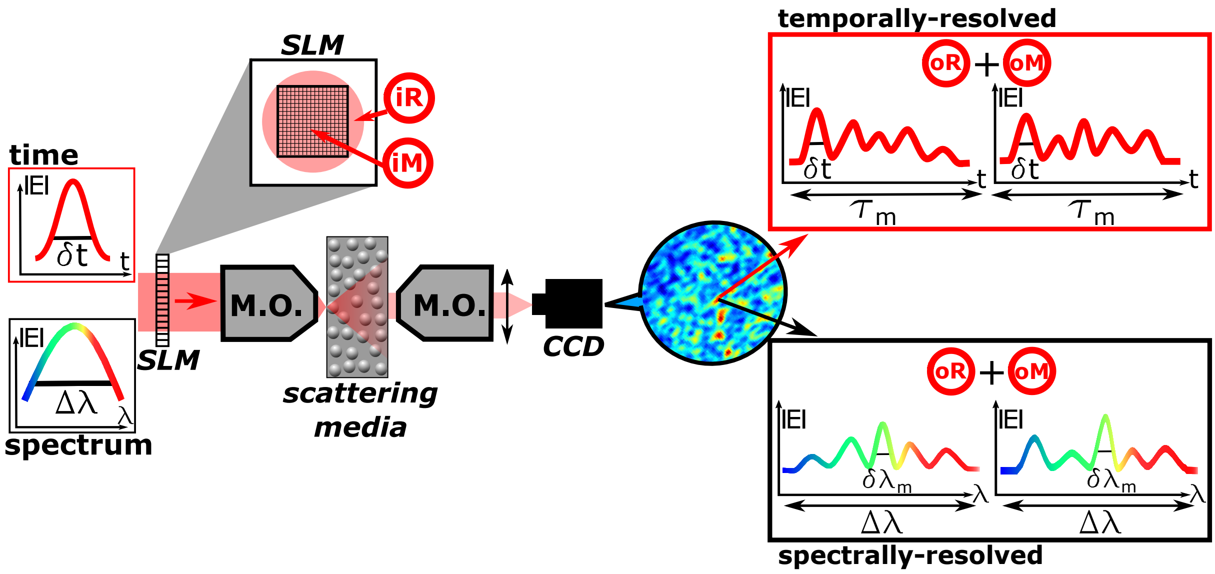

Figure 5.1 – Principle of the measurement of the Broadband transmission matrix. An input pulse of duration $\delta t \sim 100$ fs (spectral width $\Delta\lambda \sim 10$ nm) illuminates a spatial light modulator (SLM) before propagation through a thick scattering medium via a microscope objective (MO). The active part of the SLM will modulate a subpart of the input beam iM with respect to a static reference part iR. The transmitted light results in an intensity speckle with low contrast $C_0 \simeq 1/\sqrt{N_\lambda}$, with N_λ the number of spectral degrees of freedom, on a CCD camera. Every single grain is the resulting broadband interference of the transmitted speckle from the input reference part oR and from the input modulated part oM. The BBTM is the linear relationship connecting iM to oM. In the temporal domain, the speckle grain is characterized by its temporal feature δt, and by the averaged traversal time of photons through the medium τ_m. In the spectral domain, the speckle has a characteristic width $\delta\lambda_m$, which is the spectral speckle correlation bandwidth of the medium.

transmitted intensity reads:

$$\begin{aligned}
I = \sum_{\lambda_i=1}^{N_\lambda} I(\lambda_i) &= \sum_{\lambda_i=1}^{N_\lambda} |E^{\text{out,R}}(\lambda_i) + E^{\text{out,M}}(\lambda_i)|^2 \\
&= I_0 + \sum_{\lambda_i=1}^{N_\lambda} \left[\left(E^{\text{out,R}}(\lambda_i) \right)^* E^{\text{out,M}}(\lambda_i) \quad + \text{c.c.} \right] \\
&= I_0 + \sum_{\lambda_i=1}^{N_\lambda} \left[\underbrace{\left(E^{\text{out,R}}(\lambda_i) \right)^* \mathbf{t}(\lambda_i)}_{\mathbf{t}'(\lambda_i)} E^{\text{in}}(\lambda_i) \right]
\end{aligned} \tag{5.1}$$

A retardation is now applied on the modulated part of the broadband input field on the SLM. As long as the pulse can be considered narrowband, meaning $\Delta\lambda/\lambda_0 \ll 1$ with $\Delta\lambda$ the spectral width of the pulse and λ_0 its central wavelength, this retardation translates into a phase shift φ that is identical for all the spectral components of the input pulse: $\forall \lambda_i \in \Delta\lambda, \varphi(\lambda_i) = \varphi$. Consequently, the N_λ spectral modes will experience the same phase shift φ. Therefore, modulating the phase of a pixel of the SLM implies the modulation of the output broadband intensity speckle. A complex, although measurable, linear operator is then connecting the phase of every controllable pixel on the SLM, and the output intensity. We coin this operator the Broadband Transmission Matrix $\mathbf{B}$ (BBTM), which as evident from Equation 5.1 is the incoherent sum of N_λ monochromatic effective TMs: $\mathbf{B} = \sum_{\lambda_i=1}^{N_\lambda} \mathbf{t}'(\lambda_i)$.

5.2.2 Measurement of the BBTM

The experimental protocol to measure $\mathbf{B}$ is similar to the measurement of the monochromatic transmission matrix developed in [Popoff et al., 2010b] and in Section 1.3.4. Nonetheless, the laser source is generating ultrashort pulses of duration $\delta t \sim 100$ fs rather than continuous wave light.

We exploit the setup shown in Figure 2.1, for measuring the Broadband transmission matrix $\mathbf{B}$. As the reference beam is co-propagative, the shutter S in the external reference arm is closed. In practice, $\mathbf{B}$ is measured using the Hadamard basis on the SLM, with $N_{\text{SLM}} = 1024$ SLM pixels for the modulated part in the center of the illumination spot, and the rest of the SLM surface for the reference part (See Figure 5.1). For every input pattern on the SLM, the corresponding output "broadband field" is retrieved from phase-stepping-holography methods exploiting 4 intensity images (the same formula as in Equation 1.19 is exploited). Typical number of CCD pixels used in the measurement of $\mathbf{B}$ is $N_{\text{CCD}} \sim 10^4$ pixels. $\mathbf{B}$ is experimentally measured in ~ 8 minutes, which corresponds to similar measurement time to a single time-gated transmission matrix, or a monochromatic transmission matrix, with an identical number of SLM pixels N_{SLM}. An *a posteriori* change of basis enables to get the BBTM in the canonical basis of the SLM pixels.

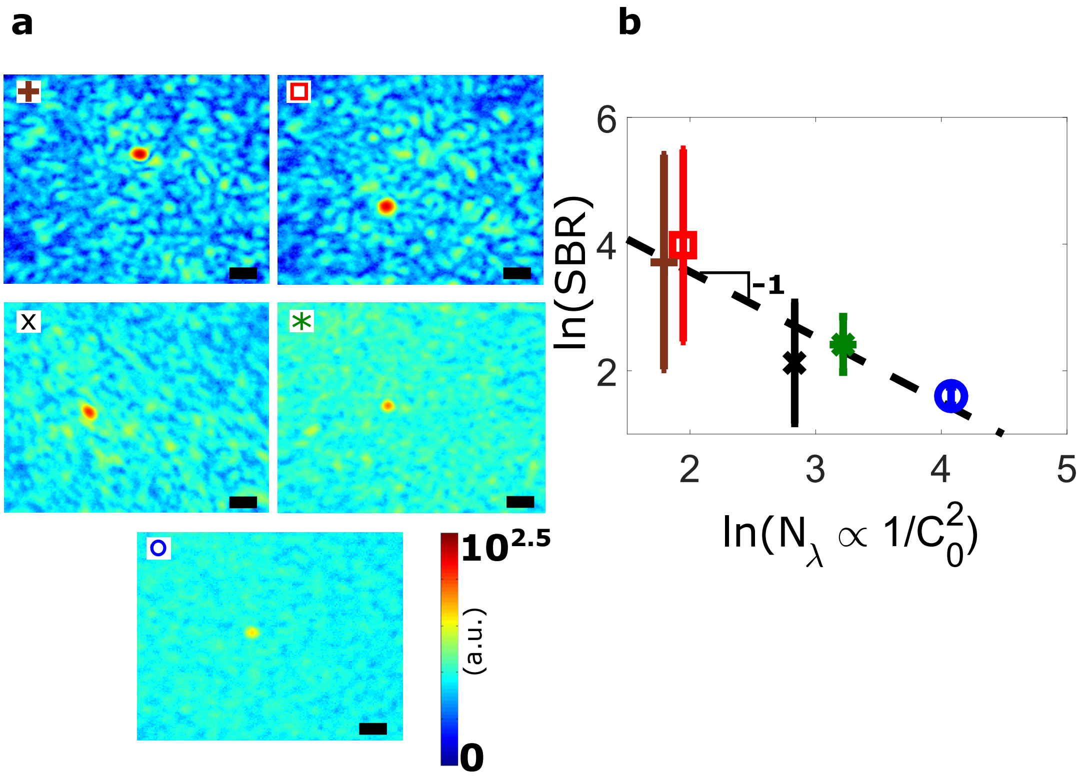

Figure 5.2 – Signal-to-background ratio of focusing with the Broadband transmission matrix. Phase-conjugation of the BBTM enables spatial focusing in a given speckle grain, whose efficiency is inversely related to N_λ. **(a)** The images show the results for 5 different scattering samples whose spectral degrees of freedom $N_\lambda \propto 1/C_0^2$, with C_0 the contrast of transmitted speckle without shaping, are indicated with corresponding markers in (b). The color bar is in log scale. Scale bar: 2 μm. **(b)** Log of signal-to-background-ratio (SBR) is plotted as a function of log(N_λ). Error bars are standard deviation for SBR over 50 different focus positions. Dashed line: linear fit, with a -1 slope.

5.3 Focusing the output pulse with the Broadband Transmission Matrix

We now consider the Broadband transmission matrix of the scattering medium measured, with $N_{\text{SLM}} = 1024$ SLM pixels. Similarly to the monochromatic transmission matrix, transmitted light can be focused at an arbitrary position by exploiting the transpose-conjugate of $\mathbf{B}$. Nonetheless, in contrast with the Multi-Spectral or a single time-gated transmission matrix, the spectral degrees of freedom were neglected in the measurement process of $\mathbf{B}$: no Fourier-limited temporal focusing can thus be expected from $\mathbf{B}^\dagger$.

In this Section, we quantify both spatial and spectral/temporal properties of focusing with the BBTM.

5.3.1 Spatial properties of the focus

We first quantify the conventional focusing properties of the BBTM in the spatial domain. Figure 5.2 shows representative results for 5 samples of ZnO powder of different thicknesses, while the transport mean free path remains constant. We thus vary the number of spectral degrees of freedom of the scattering medium N_λ. This quantity can be easily accessed via measuring the contrast of the "broadband speckle" C_0 without prior wavefront shaping [Curry et al., 2011]. Similarly to the monochromatic approach, phase-conjugating a line of the BBTM enables focusing the output pulse in a chosen speckle grain.

Signal-to-background ratio (SBR) of the achieved broadband focus is defined as the ratio between I^{focus} intensity at the focus and $\langle I^{\text{random}} \rangle$, the average background speckle intensity. Using a broadband source, the values of SBR is expected to scale as $\propto N_{\text{SLM}}/N_\lambda$ [Lemoult et al., 2009]. In Figure 5.2, the dependence of SBR regarding N_λ is experimentally verified, as expected. The increase in the standard deviation for scattering samples with low N_λ comes from the fact that the reference speckle is highly contrasted. The lower the contrast (N_λ), the higher the relative fluctuations in the reference speckle. The effect of the reference speckle in the monochromatic regime (N_λ=1) was studied in detail in [Tao et al., 2015].

5.3.2 Temporal profile of the achieved focus

In this Section, we analyze the temporal properties of the achieved focus. After acquiring $\mathbf{B}$ and focusing, the temporal profile of the output pulse in the focus can be measured with a linear Interferometric Cross-Correlation technique (See Section 2.4.3). The shutter S in the external arm of Figure 2.1 is now opened to allow the external reference ultrashort pulse to sample either the focus, or random speckle grains.

Figure 5.3b shows representative time-domain results for a thick scattering medium, with $N_\lambda \simeq 60$ spectral degrees of freedom. Examples of typical temporal profiles of a single grain, retrieved with ICC, are presented without wavefront shaping (black line) and at the focus (red line). As the ICC technique has high spatial resolution, the temporal profile of different speckle grains can be recorded simultaneously for a single scan of the delay line. Figure 5.3c illustrates 25 different temporal profiles recorded in different speckle grains simultaneously with a random input pattern on the SLM. Nonetheless, scanning the delay line has to be iterated for recording temporal profiles of different focus. Figure 5.3d shows 25 different temporal profile of foci, via phase-conjugating $\mathbf{B}$, in different spatial positions. From these sets of data, two different information can be retrieved:

- Averaging spatially (i.e. over lines of Figure 5.3c and Figure 5.3d) the temporal profiles leads to time-of-flight distribution of the medium, and thus to τ_m, the confinement time of photons inside the medium.
- The autocorrelation of temporal profiles (i.e. inner products of columns of Figure 5.3c and Figure 5.3d) gives access to the smallest feature of the temporal profiles, that is the time-width of a single temporal speckle grain.

Before performing a quantitative analysis in the upcoming sections, one can observe that the temporal signal from Figure 5.3d, when light is focused via the BBTM, seems to contribute mostly at short times, i.e. around the arrival time corresponding to maximum

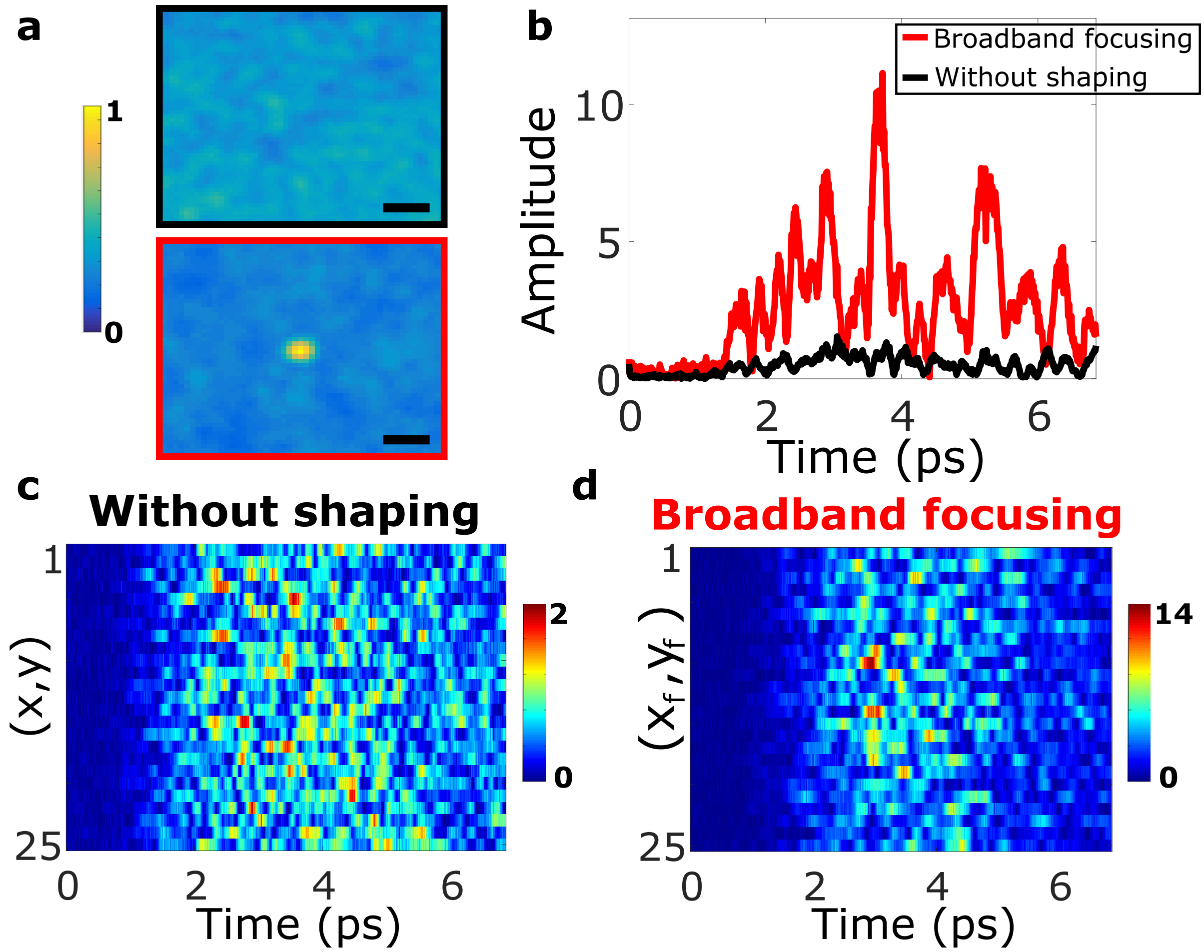

Figure 5.3 – Temporal profile when focusing with the Broadband transmission matrix. The scattering medium is characterized by its confinement time $\tau_m \sim 6$ ps. **(a)** CCD images measured with the shutter of the external arm S closed. Top: Without wavefront shaping, or equivalently with a random input phase pattern on the SLM, a low-contrasted speckle is measured. Bottom: The output pulse is focused on the central spatial speckle grain. Scale bar: 5 μm. **(b)** Time-of-flight distributions retrieved with ICC, in a single speckle grain in the case of (red) focusing with the BBTM and (black) without shaping. **(c-d)** Temporal profiles over 25 different spatial positions (x,y) either without shaping (in **(c)**) or in different focus in positions (x_f,y_f) (in **(d)**) with the same scattering sample. Colormap stands for the amplitude of the temporal profile at chosen spatial position and arrival time.

of the time-of-flight distribution. A consequence would be a decrease of the confinement time of photons contributing to the focus. Another observation is related to the time-width of the averaged temporal speckle grain, that appears bigger when focusing with **B** than without wavefront shaping.

In the following, we analyze those two aspects of the temporal profiles, averaging and autocorrelation, without wavefront shaping or when focusing with **B**.

Spatial averaging: time-of-flight distribution of photons at the focus

Averaging over many spatial grains enables to retrieve the time-of-flight distribution of the medium, and consequently τ_m the average confinement time of photons. Identically, averaging temporal profiles of foci over different realizations enables to retrieve τ_f, the average temporal duration at the focus. τ_m and τ_f can be retrieved by averaging Figure 5.3c and Figure 5.3d over their respective lines, which corresponds to different realizations of focusing.

In Figure 5.4a, we first compare the spatially averaged temporal envelop of the pulse for focusing either with the Broadband transmission matrix **B** (red line), and two single time - gated transmission matrices measured at delay time τ_1 and τ_2 with the same number of spatial degrees of freedom N_{SLM}. In essence, the only difference between a single time - gated transmission matrix and **B** lies in the reference beam, that is either external (shutter S of the external arm opened with chosen delay) or co-propagative (shutter S of the external arm closed). Figure 5.4a illustrates clearly the absence of peak in the temporal profile when focusing with **B**, as expected.

In Figure 5.4b, we analyze the envelope of focusing for a scattering medium whose $\tau_m \sim 6$ ps. The obtained spatially averaged temporal profile is plotted in semilog scale. Remarkably, with the very same sample we obtain a shorter time $\tau_f \simeq 3$ ps $< \tau_m$ when focusing with the BBTM. Therefore, the focus is temporally shorter than the medium. We repeated the experiment on different multiple scattering samples, whose τ_m are spread over an order of magnitude, from 700 fs to 6 ps. Fig. 5.4c shows the corresponding observed values of τ_f and τ_m. The dashed black line represents the expected $\tau_m = \tau_f$, from a spatial-only focusing experiment. Clearly, we observe that τ_f is systematically smaller than τ_m, more precisely $\tau_f/\tau_m = 0.5$.

This ratio of 2 can be easily understood: the BBTM coefficients are inherently cross-terms between reference and modulated broadband speckles, as written in Equation 5.1. These two speckles have both similar time-of-flight distributions with a decay, on average, of the form $\propto e^{-t/\tau_m}$. Therefore this cross-term has a decay of the form $\propto e^{-2t/\tau_m}$ on average. The corresponding temporal duration at the focus $\tau_f \simeq \tau_m/2$ is consequently two times lower.

Autocorrelation: time-width of the temporal feature at the focus

The results analyzed above are averaged properties of temporal profiles, which are related to the smallest features in the frequency-domain. Another relevant, yet independent, information is located in the fast variation of the temporal fluctuations, which is the temporal speckle grain. Without wavefront shaping, this quantity scales approximately as the duration of the input pulse, as we studied in Section 2.4.3.

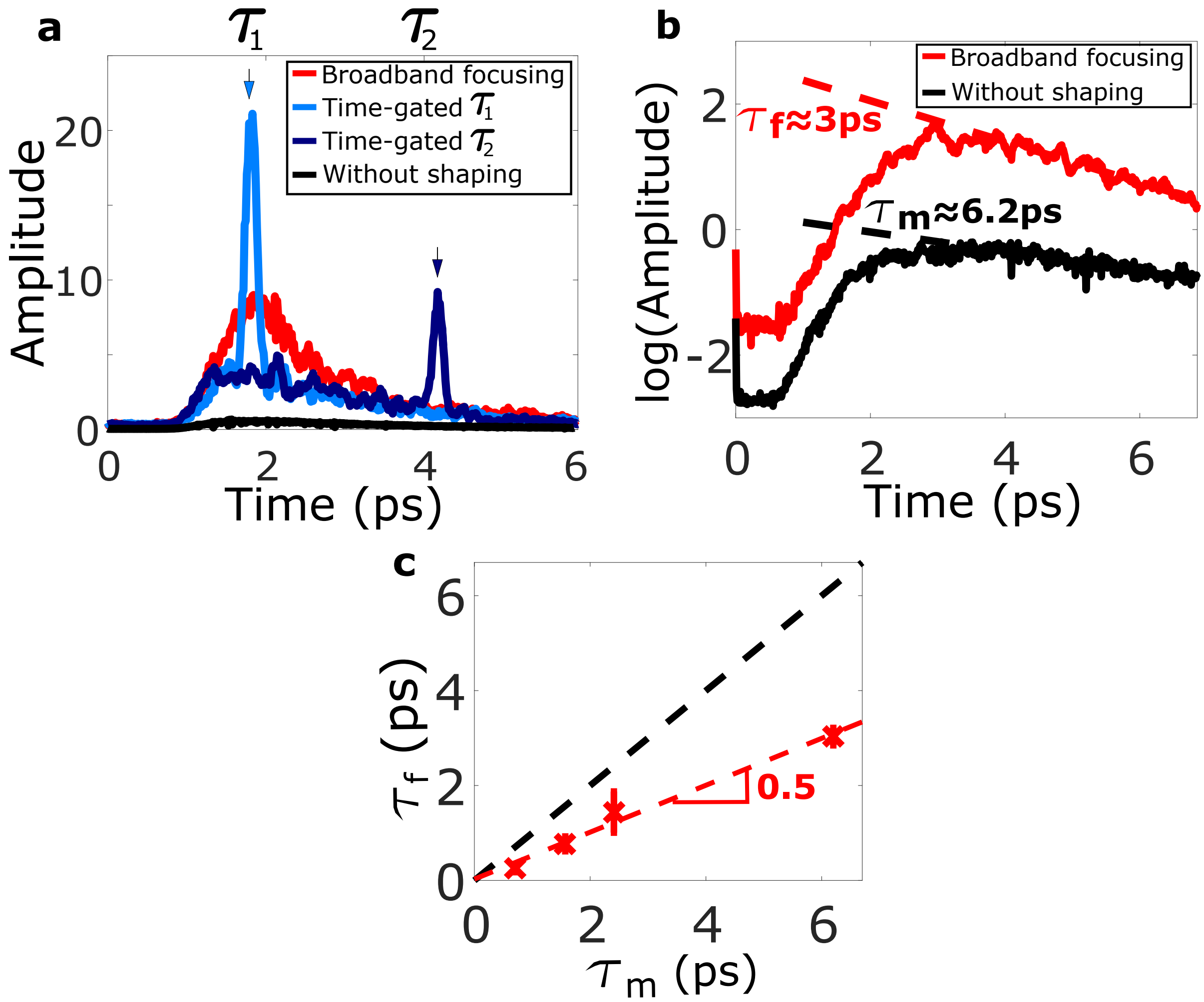

Figure 5.4 – Averaged temporal profiles of focusing with the Broadband transmission matrix. (a) Comparison of averaged temporal profiles when focusing with the Broadband transmission matrix (red) and two single time - gated transmission matrices (blue) measured respectively at delay time τ_1 and τ_2 with the external reference arm, with the same number of SLM pixels ($N_{\text{SLM}} = 1024$). Data are averaged over 9 focus. Time-of-flight distribution of the scattering medium is obtained via averaging over 200 temporal envelop of speckle grains without wavefront shaping (black): we retrieve $\tau_m \sim 2.5$ ps for this scattering sample. **(b)** Averaged time-of-flight distributions over 25 different foci plotted in semilog of a thicker scattering sample. τ_m (without shaping, black line) and τ_f (broadband focusing, red line) are measured with a linear fit. **(c)** Comparison between τ_m and τ_f for various scattering samples. While dashed black line represents the expected $\tau_m = \tau_f$, experimental data (red markers) evidences τ_f is twice smaller than τ_m. Red dashed line represents a linear fit and error bars indicate the standard deviation for estimation of τ_f.

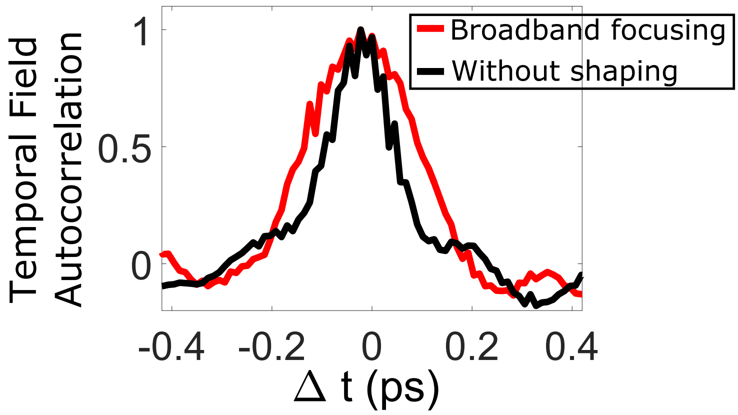

Figure 5.5 – Temporal field autocorrelation when focusing with the Broadband transmission matrix. Temporal field autocorrelation of both (red) focus averaged over 25 different foci and (black) without shaping averaged over 200 speckle grains. We arbitrary chose the reference arrival time $\tau = 3$ ps from the set of data presented in Figure 5.3c and Figure 5.3d, which corresponds then to Δt=0. The temporal width of the autocorrelation peak for the focus is broader than without shaping: $\delta t_f > \delta t_m$.

To extract this quantity from Figure 5.3c and Figure 5.3d, temporal autocorrelations are plotted in Fig. 5.5 for both focusing with $\mathbf{B}$ and speckle grains corresponding to a random input pattern. The autocorrelations are extracted from Figure 5.3c and Figure 5.3d by calculating the inner products between columns, with an arbitrary reference column chosen at time $\tau = 3$ ps. Interestingly, the typical time-width of a temporal speckle grain is larger when focusing with the BBTM than without shaping: $\delta t_f > \delta t_m$. This time-width is related to the spectral-width of the pulse spectrum in the focus: as $\delta t \propto 1/\Delta\lambda$, a direct consequence is the spectral narrowing of the bandwidth (See Section 5.3.3). In the next Section, we investigate the spectral properties of the focus, in order to verify if the spectral envelop is reduced when focusing with the BBTM in comparison to the input pulse spectrum.

5.3.3 Spectral content of the focus

We now investigate on the frequency-domain response of the focus. For spectral characterization of the focus, the laser is mode-unlocked, and it is used as a tunable cw source. The shutter in the external reference arm is closed. For every single wavelength, a CCD image is recorded either when focusing or for a random input mask. We thus have spatial resolution when scanning the incident wavelength. The scattering medium we used in this Section is characterized with $N_\lambda \simeq 20$. Indeed, we cannot exploit a scattering medium with a larger N_λ, as its spectral correlation bandwidth $\delta\lambda_m$ would be lower than the spectral resolution of the spectrometer (0.2 nm).

Figure 5.6 shows a typical spectral intensity profile of a single speckle grain for a random input phase pattern, and at a focus. Figure 5.6b illustrates 100 different spectral profiles recorded in different speckle grains with a single spectral scan, by exploiting the spatial resolution of the method. Nonetheless, the process has to be iterated for focusing in different spatial speckle grains. In Figure 5.6c, 100 different spatial foci are scanned spectrally and their corresponding monochromatic intensity profiles are plotted as a function of illumination wavelength.

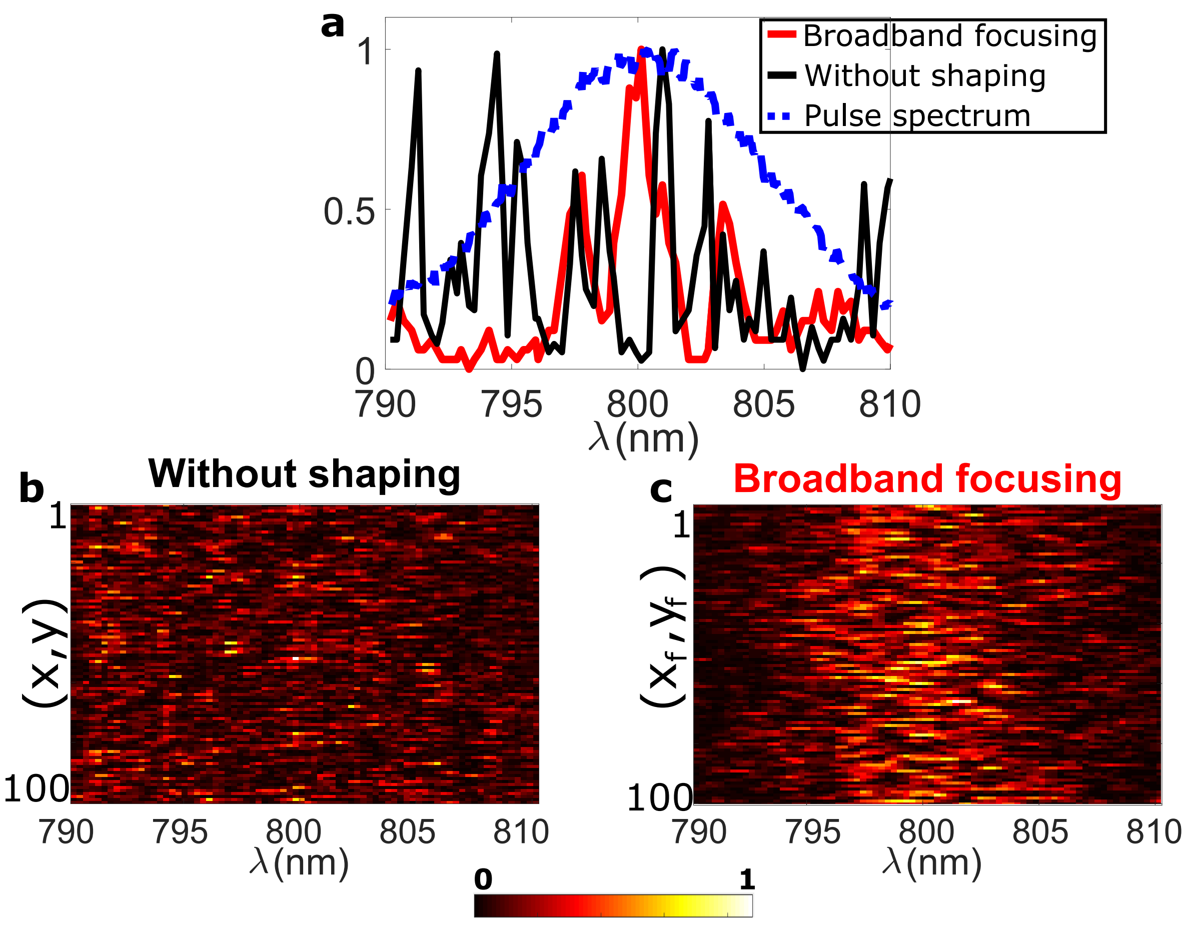

Figure 5.6 – Spectral intensity measurement when focusing with the Broadband transmission matrix. (a) Spectral intensity measurement. Monochromatic intensity in a single grain (with or without shaping) is recorded on a CCD camera as function of λ with a tunable cw laser. Plots are spectral intensities (black) without wavefront shaping, and (red) at the focus. (blue) Intensity spectrum of the input pulse is recorded with a spectrometer at the output of the laser. **(b-c)** Monochromatic intensity over 100 different spatial positions (x,y) either without shaping (in **(b)**) or in different focus positions (x_f,y_f) (in **(c)**) with the same scattering sample. Color-map stands for the spectral intensity at a chosen spatial position and incident wavelength.

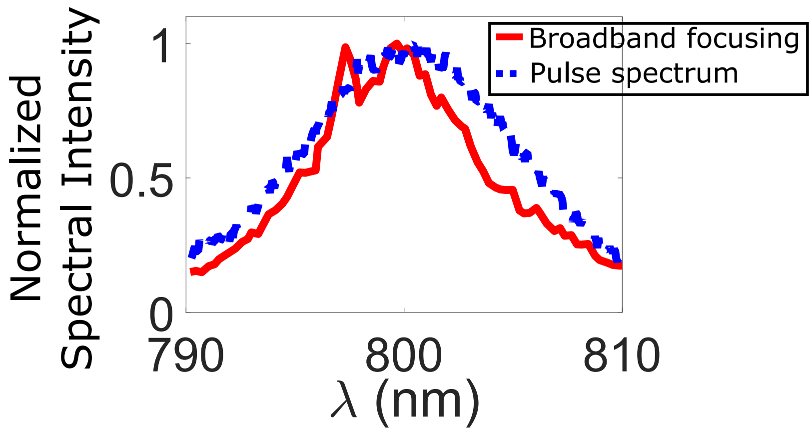

Figure 5.7 – Averaged spectral intensity of the achieved focus with the Broadband transmission matrix. (red) The averaged spectral intensity of focusing, via the BBTM, is obtained by averaging monochromatic intensity as a function of incident wavelength over 100 different focus positions. (blue) It is compared to the intensity spectrum of the input pulse, recorded with the spectrometer. On average, the output pulse has a narrower spectrum than the input pulse

As expected, around N_λ spectral grains, that can be identified by the number of spectral fluctuations, can be seen within the pulse spectral width with a random input pattern on the SLM. Conversely, for the focus, we observe fewer grains, and moreover they are mostly contributing to the central frequency of the output pulse.

In the following, we quantitatively analyze the data from Figure 5.6b and Figure 5.6c, with a similar methodology that we developed for the temporal profiles in Section 5.3.2. More precisely, we investigate the average over different foci to retrieve the spectral envelope at the focus, and we plot the spectral autocorrelation to measure $\delta\lambda_m$ at the focus.

Spatial averaging: averaged spectral envelope at the focus

The average over 100 different foci is plotted in Figure 5.7. It shows a narrower spectrum $\Delta\lambda_f$ than the Gaussian spectrum of the input pulse $\Delta\lambda_m$. A Gaussian fit leads to $\Delta\lambda_f \simeq 10.8$ nm $\pm$ 0.5 nm at FWHM at the focus, and $\Delta\lambda_m \simeq 12.5$ nm $\pm$ 0.1 nm without shaping.

Accordingly, this observation can be explained using Equation 5.1. Both reference and modulated speckles have the same spectral profile as the input pulse, which is a Gaussian centered at λ_0 over a span $\Delta\lambda_m$. Therefore, the cross product is a narrower Gaussian with $\Delta\lambda_f = \Delta\lambda_m/\sqrt{2}$ at FWHM, which is consistent with experimental data of Figure 5.7. This spectral narrowing is in agreement with the increase of temporal autocorrelation presented in Figure 5.5.

Autocorrelation: spectral-width of the spectral speckle at the focus position

Another independent feature of the spectral intensity when focusing with $\mathbf{B}$ is the spectral-width of the smallest feature of the spectral speckle, $\delta\lambda_f$. Without wavefront shaping, this quantity corresponds to $\delta\lambda_m$ the spectral correlation bandwidth of the scattering medium.

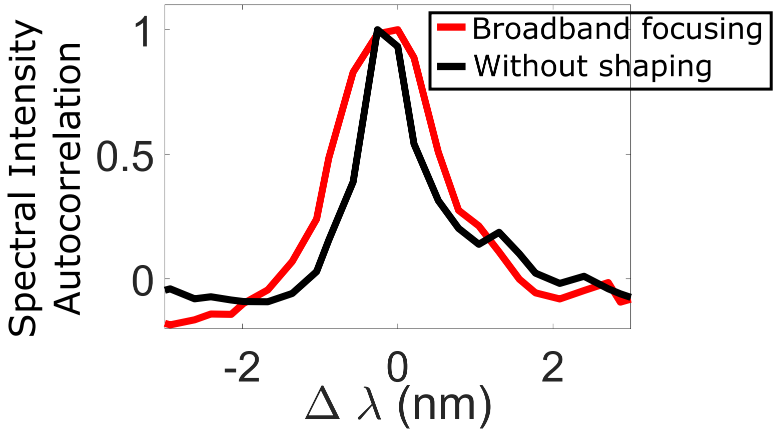

Figure 5.8 – Spectral intensity autocorrelation when focusing with the Broadband transmission matrix. Spectral intensity autocorrelation of both (red) focus averaged over 100 different foci and (black) without shaping averaged over 200 speckle grains. We arbitrary chose the reference wavelength $\lambda_0 = 800$ nm the central wavelength of the pulse, from the set of data presented in Figure 5.6b and Figure 5.6c, which corresponds then to $\Delta\lambda$=0. The spectral width of the autocorrelation function for the focus is broader than without shaping: $\delta\lambda_f > \delta\lambda_m$.

A method to access $\delta\lambda_f$ is to plot the spectral intensity autocorrelation, that is presented in Figure 5.8.

The autocorrelations are extracted from Figure 5.6b and Figure 5.6c by calculating the inner products between columns, with an arbitrary reference column chosen at central wavelength of the pulse $\lambda_0 = 800$ nm. Clearly from Figure 5.8, we observe that $\delta\lambda_f$ larger than $\delta\lambda_m$, which makes sense with the decrease of τ_f compared to τ_m studied in Figure 5.4c, as $\tau_m \propto 1/\delta\lambda_m$. In essence, the autocorrelation of spectral intensity is an alternative method to confirm the same information than averaging temporal profiles: the decrease of τ_f and the increase of $\delta\lambda_f$, with respect to τ_m and $\delta\lambda_m$.

Recent works have shown a broadening of the spectral correlation when exciting the so-called open channels [Bosch et al., 2016, Shi and Genack, 2015]. Here, with an effective diffuse spot area $S \simeq L^2 \simeq 50 - 100\mu m^2$, with L the thickness of our scattering samples, the number of scattering modes $N_{\text{modes}} \simeq S/\lambda^2 \simeq 10^4$ (See Equation 1.10) largely exceeds the degree of control N_{SLM}. As shown in [Goetschy and Stone, 2013], this limited control of the degrees of freedom in our experiment makes it unlikely that we are sensitive to the recently reported broadening of the spectral speckle correlation of open/closed channels.

5.4 Summary

In this Chapter, we introduced the concept of Broadband transmission matrix, measured with co-propagative reference. We analyzed spatial, temporal and spectral properties of the achieved focus, which leads to surprising results. Indeed, with a Gaussian input pulse, we have shown that focusing with BBTM enables to reduce the effective N_λ at the focus by a factor $\sim 2\sqrt{2}$, which comes from a factor 2 in the increase of spectral correlation bandwidth, and a factor $\sqrt{2}$ in the shortening of the spectral envelope. This result may have practical implications in nonlinear microscopy for deep imaging, as in practice it allows relaxing the need to control the spectral degrees of freedom at few mm-thickness specimens [Katz et al., 2011].

Complementary analysis could be performed on the measured BBTM. Indeed, in this Chapter we only exploited this operator for focusing purposes, but one could analyze its singular value decomposition SVD. This operator could be promising for non-linear microscopy because of its simple measurement protocol, as well as for more fundamental study of broadband light matter interactions.

Chapter 6

Enhancing a non-linear process through scattering media with spatio-temporal focusing

Contents

In the previous Chapters, we developed the Multi-Spectral transmission matrix (Chapter 3), the Time-Resolved transmission matrix (Chapter 4) and the Broadband transmission matrix (Chapter 5) to control a transmitted ultrashort pulse through multiple scattering media. More precisely, the ability to adjust both spatial and temporal properties of the pulse can be useful for multiphotonic through disordered systems, such as biological tissues [Ntziachristos, 2010, Gigan, 2017]. However, the fast decorrelation time of biological tissues, in the order of 1 ms - 100 ms [Liu et al., 2015, Jang et al., 2015], prevents the use of such scattering media in our optical setup, mainly because of the low refresh-rate of our LCOS-SLM: the speckle would decorrelate faster than a single step of wavefront shaping.

In this Chapter, we want to study the ability to exploit this spatio-spectral control of an ultrashort pulse for non-linear microscopy purposes: we excite two-photon fluorescence emission after propagation of an ultrashort pulse through ZnO scattering media. As we discussed in Section 2.3, the fluorescent sample is placed after the scattering medium, in order to filter the auto-fluorescence of the scattering medium. Two fluorescent samples were used in this Chapter: either a "two-photon screen" (See section 2.3.2) or fluorescent microbeads (See section 2.3.3). As a proof of principle, we exploit the various transmission matrix approaches, developed in the previous Chapters, to focus light on the two-photon sample. We also study the dependence of the excitation on the temporal/spectral shape of the output pulse. For instance, we demonstrate enhancement of the non-linear signal thanks to spatio-temporal focusing, which paves the way for deep non-linear microscopy.

This Chapter is organized as follows: in Section 6.1, we briefly introduce the "two-photon" signal resulting from a speckle illumination on the fluorescent sample. Most of the presented results in this Chapter exploit the fluorescent microbeads, except in Section 6.2.1. In Section 6.2, we analyze non-linear signals under spatio-temporal focusing, obtained with the Multi-Spectral transmission matrix and a single time-gated transmission matrix. In Section 6.3, we quantitatively compare the non-linear signals from the various transmission matrix approaches developed in this thesis. We then present an application of this spatio-temporal focusing in Section 6.4: point-scanning imaging of fluorescent microbeads, based on a single time-gated transmission matrix,

6.1 "Two-photon" signal

In this Section, we describe how the two-photon signal is probed and quantified, with the setup shown in Figure 2.1, without prior wavefront shaping on the SLM. In this configuration, a speckle pattern, named "linear" speckle (at $\lambda = 800$ nm) in this Chapter, is sent through the fluorescent sample via a microscope objective. The linear speckle is then exciting two-photon fluorescence (2PF) in the non-linear sample: a "two-photon" signal is observed on the EMCCD camera [Katz et al., 2011]. Both transmitted linear

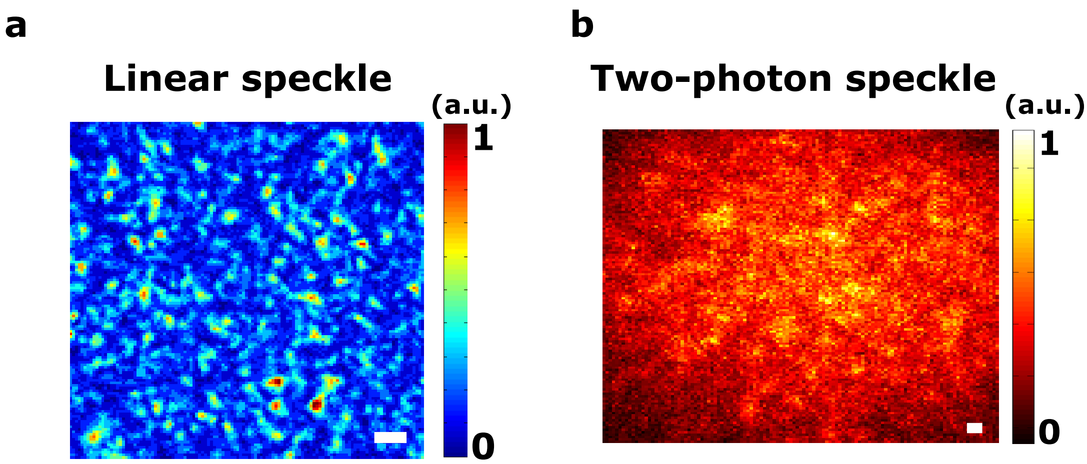

Figure 6.1 – Two-photon speckle pattern from fluorescein within a two-photon screen. A random pattern is displayed on the SLM. The scattering medium is characterized by $\tau_m \sim$ 500 fs. A capillary of thickness 20 μm, filled with fluorescein, is inserted in the experimental setup. Transmitted light is collected with a microscope objective (x20, NA=0.4). Linear signal (speckle at $\lambda = 800$ nm) and non-linear signal (fluorescence at $\lambda = 400 - 600$ nm) are separated with a dichroic mirror. **(a)** "Linear" speckle pattern recorded with the CCD camera, after propagation through the scattering medium and the two-photon screen. **(b)** Corresponding fluorescence pattern, revealing a two-photon speckle, measured on the EMCCD camera, with a gain 300 and exposure time T$_e$ = 2 s. Scale bars: 5 μm.

pulse, from the linear speckle pattern, and "non-linear" fluorescent signal (at λ = 400-600 nm) are collected with another microscope objective.

Two different fluorescent samples are tested: either a "two-photon screen" of fluorescein, as introduced by Katz et al. [Katz et al., 2011] (See Section 2.3.2 for description of the sample's preparation), or fluorescent microbeads of inner diameter 1 μm (See Section 2.3.3 for more description on the microbeads).

6.1.1 From a two-photon screen: two-photon speckle

A layer of fluorescein, prepared with the protocol developed in Section 2.3.2, is inserted in the experimental setup (Figure 2.1). It acts effectively as a "two-photon" screen. In this Section, the scattering medium is characterized by its confinement time $\tau_m \sim$ 500 fs.

In Figure 6.1a, a typical linear speckle pattern, measured on the CCD camera after propagation through the corresponding scattering medium is shown, for a random phase pattern on the SLM. The linear speckle is then imaged on the capillary to excite 2PF. The 2PF signal is recorded with the EMCCD camera, with an electronic gain 300 and exposure time T$_e$ = 2 s, as shown in Figure 6.1b. Although some "two-photon speckle grains" can be observed in Figure 6.1b, the two-photon speckle is not well contrasted. Indeed, 2PF is emitted from different planes within the capillary. Its thickness, 20 μm, is much larger than the depth of field of the observation microscope objective (20x, NA 0.4) $z_R \sim 5\mu$m. Therefore, the 2PF originates from a few speckle planes. As reported in Katz et al. [Katz et al., 2011], the off-plane contributions are increasing the background of 2PF signal.

From the two-photon signal presented in Figure 6.1b, we can extract the average two-photon speckle intensity $\langle I_{\text{NL,background}}^{\text{2P screen}} \rangle$, under speckle illumination, by spatially averaging the intensity measured on the EMCCD camera of the two-photon intensity. We average this quantity over different illumination patterns on the SLM (~ 10). This "average non-linear background intensity" will be useful to quantify the signal-to-background ratio of focusing for the non-linear signal.

6.1.2 From fluorescent microbeads

In other series of experiments, the capillary is replaced by micrometer size fluorescent beads spread on a microscope slide (diameter 1 μm, see Section 2.3.3). The pair of microscope objectives is changed as well to maximize the collection efficiency (see Section 2.3.3 for more details).

Two-photon fluorescence from the beads is drastically more challenging to probe than 2PF from the two-photon screen. Indeed, while the two-photon screen fluoresces in volume, with a speckle illumination, 2PF from a single bead is emitted when the corresponding input speckle grain has a non-zero intensity, i.e. for a "bright" speckle grain, and is typically low. A way to reduce the speckle intensity fluctuations, i.e. a low-contrasted speckle, in order to facilitate detection is to use a thick scattering medium (See Section 1.4.3). The background resulting from the sum of monochromatic speckle patterns reduces the number of dark grains. However it comes at the price of lower power per speckle grain despite high numerical aperture, as the output pulse is temporally spread. A longer exposure time is required to detect 2PF: a compromise must be found between signal and contrast.

In the following, the scattering medium, used in this Section, is characterized by a confinement time $\tau_m \sim 1$ ps.

Beads location in the imaging plane

In order to find the microbeads' location, we mimic a uniform illumination by averaging the transmitted light over different illuminations with the SLM. In essence, we display different (100) random patterns on the SLM, and we measure the corresponding speckle patterns on the CCD camera. Figure 6.2a shows the mean speckle image. For instance, in Figure 6.2a, $N_b = 12$ individual beads can be counted. The microbeads' location is identified in Figure 6.2a with a slightly higher intensity than the average. In conjunction with a lower intensity around the bead, we interpret this effect as a fisheye lens effect.

Two-photon signal from isolated fluorescent beads

Figure 6.2b shows a typical two-photon signal from the same set of microbeads, under a single speckle illumination. The electronic gain on the EMCCD camera is 1000, and the exposure time is $\mathrm{T}_e = 1000$ s. From Figure 6.2b, we can identify 4 distinct zones on the EMCCD where signal is detected. It matches the 4 corresponding clusters of beads that

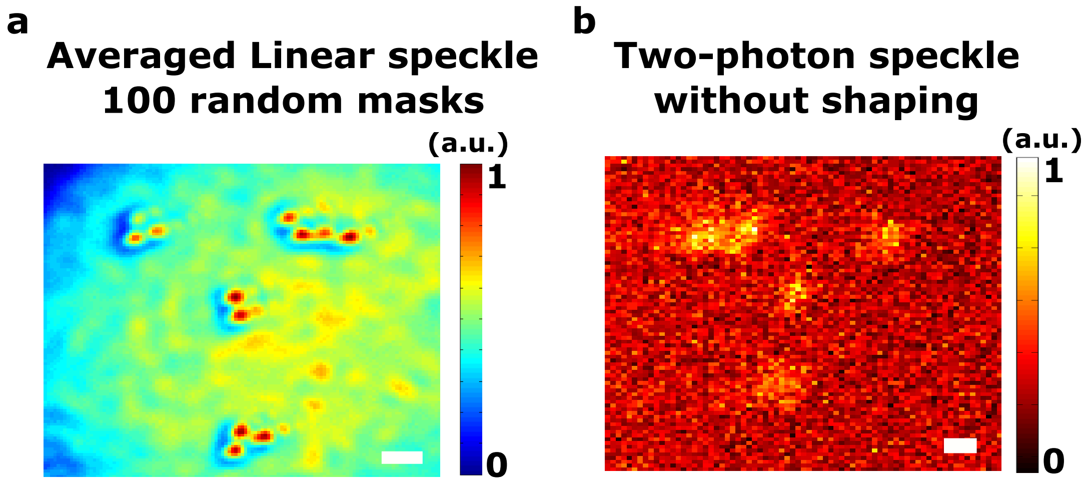

Figure 6.2 – Two-photon signal from fluorescent microbeads. The scattering medium is characterized by $\tau_m \sim 1$ ps. Fluorescent microbeads (diameter 1 μm) are spread over a microscope slide, and inserted in the experimental setup. Transmitted light is collected with an oil immersion microscope objective (x60, NA=1.4). **(a)** Mean linear speckle image, obtained by averaging over 100 different speckles (from different random patterns on the SLM) measured with the CCD camera. We thus mimic homogeneous illumination with the setup: $N_b = 12$ beads are identified in the imaging zone. **(b)** Two-photon signal measured on the EMCCD camera with a random pattern on the SLM. Gain=1000 and exposure time $T_e = 1000$ s. Scale bars: 2 μm.

we identified in Figure 6.2a, as the non-linear sample plane is both imaged on the CCD camera and on the EMCCD camera.

Nonetheless, we cannot distinguish the 12 individual spots, for several reasons. Indeed, as the input beam on the non-linear sample is a single speckle pattern, some beads might be illuminated by dark grains, thus it would require a longer exposure time to detect them. Secondly, the depth of field of the microscope objective is lower ($z_R \sim 500\mu$m) than the diameter of a single bead (1 μm): signal from part of beads might be out of the detection plane. Therefore, the considered two-photon signal is the spatially integrated signal on the EMCCD camera, in a zone around the beads location, similar to typical confocal two-photon microscope [Helmchen and Denk, 2005] that uses a photomultiplier tube (PMT). We justify this choice as we will exploit, in the next Sections, a spatio-temporal focus to excite fluorescence. It is then equivalent to a point source excitation, that does not require spatial resolution for detection. Figure 6.2b corresponds to this RoI (region of Interest) on the EMCCD camera.

Non-linear background

From this image, we extract the average non-linear background intensity, under a single speckle illumination, for the $N_b = 12$ microbeads in the imaging zone identified in Figure 6.2a. Although it could be average over different illuminations with the SLM, we only measure it for a single random SLM pattern, as the exposure time for a single EMCCD image is ~ 20 min. We estimate the non-linear background $\langle I^{\text{beads}}_{\text{NL,background}} \rangle$ by:

$$\langle I^{\text{beads}}_{\text{NL,background}} \rangle = \frac{1}{N_b} \sum_{i}^{N_{\text{pixels}}} I_{\text{EMCCD}}(i) - \bar{I}_{\text{noise,bg}} \tag{6.1}$$

with $I_{\text{EMCCD}}(i)$ the measured intensity on the *i-th* pixel of the EMCCD camera, $\bar{I}_{\text{noise,bg}}$ the offset noise background (dark) inherent from the camera (measured on a zone without signal), and N_{pixels} the number of pixels of the EMCCD camera within the RoI of the zone of interest on the EMCCD camera.

Two-photon signal from microbeads after propagation through different scattering samples and wavefront control

In the next Sections, the two-photon signal from the microbeads will be measured after propagation through two different scattering samples, and focusing spatially and temporally:

- A "thin" scattering sample, characterized by its confinement time $\tau_m \sim 550$ fs, and its spectral correlation bandwidth $\delta\lambda_m \sim 2$ nm. The EMCCD characteristics to measure the two-photon signal, after focusing with a transmission matrix, are: gain = 300; exposure time $\text{T}_e = 3$ s.
- A "thick" scattering sample, similar to the one used in Figure 6.2, characterized by its confinement time $\tau_m \sim 1$ ps. The EMCCD characteristics to measure the two-photon signal, after focusing with a transmission matrix, are: gain = 1000; exposure time $\text{T}_e = 10$ s.

6.2 Spatio-temporal focusing on two-photon fluorescence sample after propagation through scattering media

In the previous Section, we described the non-linear samples, either the two-photon screen or microbeads, with the experimental setup shown in Figure 2.1. We then probed 2PF under random speckle illumination with an EMCCD camera.

In this Section, we measure the 2PF under shaped wavefront illumination. More precisely, we exploit the Multi-Spectral transmission matrix (MSTM) and the Time-Resolved transmission matrix (TRTM) to enhance 2PF with spatio-temporal focusing. The Broadband transmission matrix (BBTM) cannot lead to a Fourier-limited spatio-temporal focus (See Chapter 5): we are thus deliberately not studying the BBTM in this Section. It will be analyzed in Section 6.3.

6.2.1 Spatio-temporal focusing via flattening the spectral phase of the output pulse with the MSTM

In Chapter 3, we introduced the Multi-Spectral transmission matrix. In particular, imposing a linear relative spectral phase relationship to the output pulse leads to spatio-

The results we present in Section 6.2.2 and in Section 6.2.3, as well as Section 6.3 and Section 6.4 were obtained in the context of DucMinh Ta's master internship project, in March-August 2017.

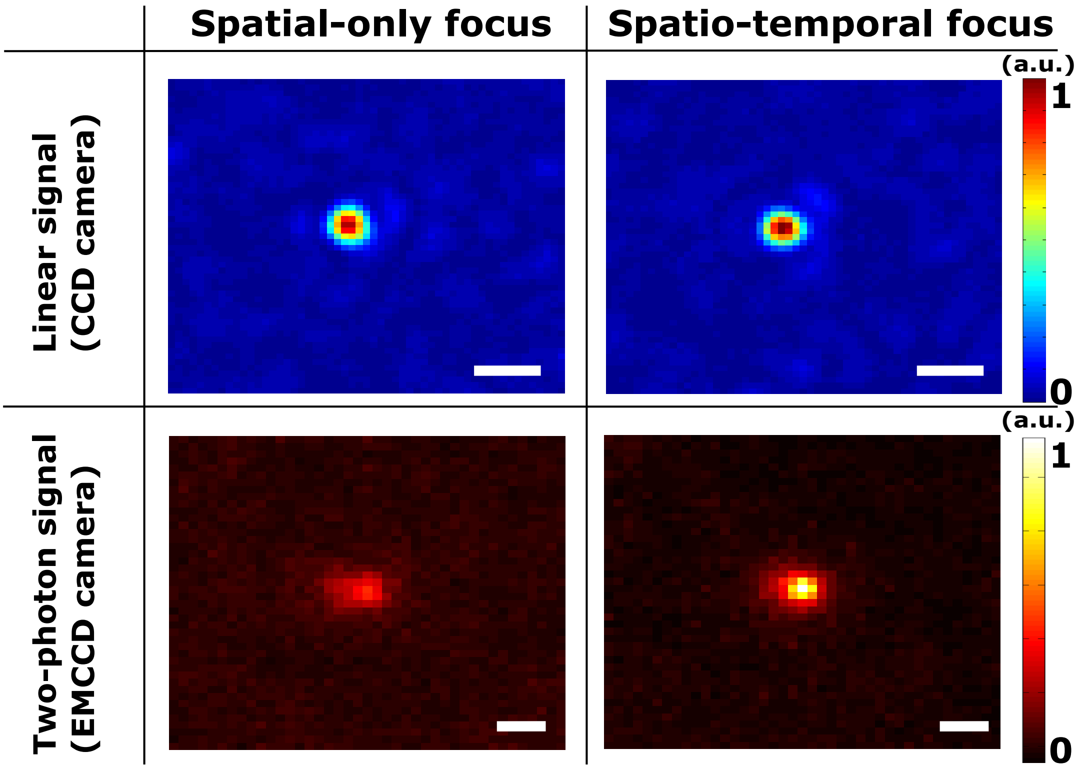

Figure 6.3 – Comparison of both linear and two-photon excitations for spatial-only focusing, and spatio-temporal focusing, with the MSTM. A two-photon screen is used to excite 2PF. The scattering medium is characterized by its spectral correlation bandwidth $\delta\lambda_m \sim 2$ nm. Spatial-only focusing is achieved by focusing only the central wavelength of the output pulse. **Top line:** Linear signal measured with the CCD camera. **Bottom line:** Corresponding two-photon signal, measured with the EMCCD camera. Colorbars are normalized to the maximum intensity of spatio-temporal focusing. Scale bar: 5 μm.

temporal focusing. Spatial-only focusing is achieved via either deliberately imposing a random spectral phase relationship between the spectral components of the pulse, or via focusing a single wavelength of the output pulse. The output pulse is then focused in a given spatial speckle grain, but it remains temporally broadened. In this Section, we compare the 2PF signal under illumination of both a spatial-only pulse and a spatio-temporal focusing pulse, using only the two-photon screen.

The "thin" scattering medium is characterized by its spectral correlation bandwidth $\delta\lambda_m \sim 2$ nm: the MSTM is measured with 6 monochromatic transmission matrices, with $N_{\text{SLM}} = 1024$ SLM pixels. This scattering medium is relatively thinner than the scattering media exploited in other Chapters, in order to increase both the collected 2PF intensity and the two-photon contrast, at the price of lower temporal broadening of the output pulse. The external reference arm was opened for the measurement of the MSTM, and then closed for the following measurements (both linear and 2PF signals).

A similar signal-to-background ratio of linear focusing between spatial-only and spatio-temporal focusing

Figure 6.3 shows the experimental results for a single focusing position. The spatial-only focus is arbitrarily performed via focusing only the central wavelength of the pulse. For the two different focusing profiles, we show both linear and two-photon signals.

As we already studied in Figure 3.9, the linear signal-to-background ratios ($\mathrm{SBR_L}$) of focusing are similar for both spatial-only focusing ($\mathrm{SBR_{L,spatial}} \simeq 42$), and spatio-temporal focusing ($\mathrm{SBR_{L,spatio\text{-}temporal}} \simeq 45$). $\mathrm{SBR_L}$ values only depend on the number of spatial degrees of freedom (i.e. N_{SLM}) and the number of spectral degrees of freedom N_λ.

Averaging over 9 different focus positions, with the same scattering medium, leads to $\overline{\mathrm{SBR}}_{\mathrm{L,spatial}} \simeq 39 \pm 3$ and $\overline{\mathrm{SBR}}_{\mathrm{L,spatio\text{-}temporal}} \simeq 40 \pm 3$.

Enhancing the two-photon signal with spatio-temporal focusing

Figure 6.3 also presents the two corresponding 2PF signals, for the same focus position. We extract the two-photon signal-to-background ratio ($\mathrm{SBR_{NL}}$) for both spatial-only focusing ($\mathrm{SBR_{NL,spatial}} \simeq 8.5$), and spatio-temporal focusing ($\mathrm{SBR_{NL,spatio\text{-}temporal}} \simeq 19.6$) at the output of the scattering medium. When the light is spatio-temporally focused, the SBR of the two-photon signal is about 2.5 times higher, at this focus position, compared to the case where the light is spatially focused, while linear signals are similar. Indeed, the total intensity of the 2PF signal is proportional to the square of the excitation intensity (i.e. $\propto$ the square of the linear signal), and also to the inverse of its time-width [Zipfel et al., 2003]. Therefore, with an equivalent spatial focusing, a temporal compression corresponds to a higher two-photon signal.

Averaging over 9 different focus positions, with the same scattering medium, leads to $\overline{\mathrm{SBR}}_{\mathrm{NL,spatial}} \simeq 11 \pm 3$ and $\overline{\mathrm{SBR}}_{\mathrm{NL,spatio\text{-}temporal}} \simeq 15 \pm 4$. While the increase in the SBR of the two-photon signal is unequivocally due to temporal recompression, one can see that the value of the SBR is still far from the theoretical value for a quadratic process. It can be attributed to the two-photon screen finite thickness (20 μm), which means that the camera records the two photon fluorescence corresponding to several speckle grain planes simultaneously in our experiment. The measured 2PF enhancement with the two-photon screen is then underestimating the real 2PF enhancement in the focus plane, which should scale as the square of the linear SBR, times the temporal compression of the output pulse. Thickness of the two-photon screen thus increases the background intensity, and also enlarges the apparent two-photon focus size [Katz et al., 2011]. A more quantitative analysis with a the fluorescent microbeads, instead of the two-photon screen, is carried out in Section 6.3.

Similar focus spot sizes

The size of the linear focusing spot, at the output of the scattering medium, is the typical speckle grain size, that is diffraction-limited. The speckle grain size depends only on the wavelength ($\lambda_{\mathrm{L}} = 800$ nm for the linear signal, and $\lambda_{\mathrm{NL}} = 400-600$ nm for the 2PF signal) and the numerical aperture (NA=0.4) of the imaging system, which are similar for the two incident beams. Therefore spatial-only focusing and spatio-temporal focusing should have the same spot size, that should be different between linear focus and 2PF signal. More precisely, the linear signals should have a spot size on the order of $\lambda_{\mathrm{L}}/(2\mathrm{NA}) = 1\mu$m, while the two-photon signals should have a smaller size $\sim \lambda_{\mathrm{NL}}/(2\mathrm{NA}) \simeq 600$ nm.

In Figure 6.4, we plot the intensity profile of respectively linear images and 2-photon images, in both configuration of spatial and spatio-temporal focusing. As expected, spatial

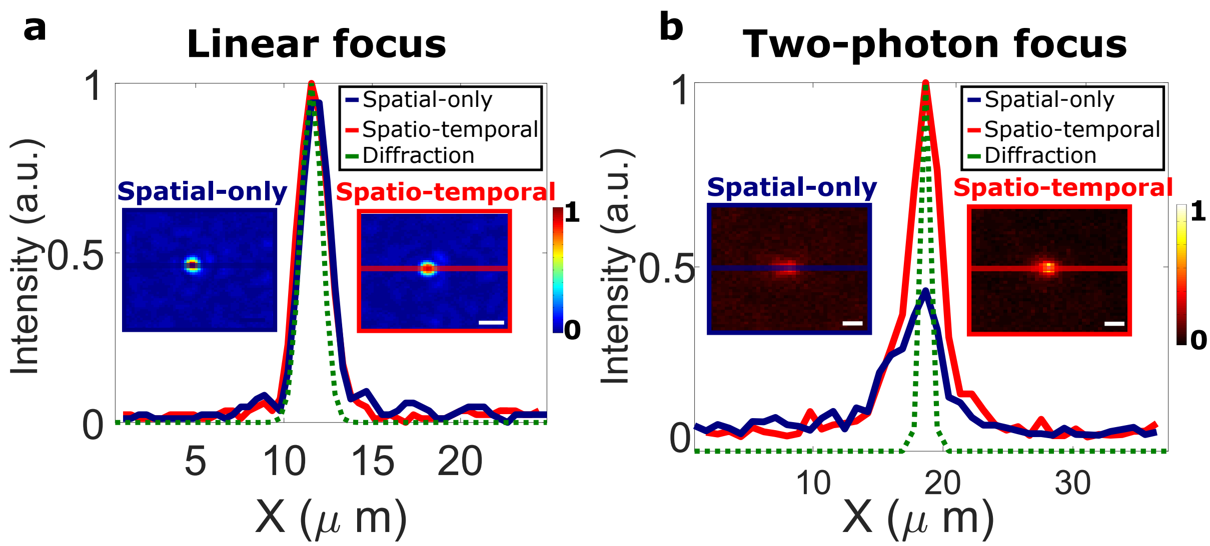

Figure 6.4 – Intensity profiles of both linear and two-photon focus positions, for both spatial-only focusing and spatio-temporal focusing, with the MSTM. Intensity profile of the images from Figure 6.3 are analyzed. **(a)** Intensity profiles of the linear ($\lambda_L = 800$ nm) focus for spatial-only (blue line) focusing and spatio-temporal (red line) focusing. Expected diffraction limit (green line) is fitted with a Gaussian function, with $\lambda_L/(2NA) = 1\mu m$ at FWHM, with NA=0.4. Inset: corresponding CCD images. **(b)** Intensity profiles of the 2-photon ($\lambda_{NL} \simeq 500$ nm) focus for spatial-only (blue line) focusing and spatio-temporal (red line) focusing. Expected diffraction limit (green line) is fitted with a Gaussian function, with $\lambda_{NL}/(2NA) \simeq 600$ nm at FWHM, with NA=0.4. Inset: corresponding EMCCD images. Scale bar: 5 μm.

and spatio-temporal focusing spots have the same linear spot size ($\sim$ 1.5 μm at FWHM), and also the same 2-photon spot size ($\sim$ 3 μm at FWHM).

Although the linear signals are diffraction-limited, the two-photon signals are much larger than the diffraction limit, due to defocus (see Section 6.1.2).

6.2.2 Spatio-temporal focusing at different arrival times with the TRTM

For this set of experiments, we worked with fluorescent microbeads in the experimental setup. They will be used for all the following experiments, instead of the two-photon screen.

In this Section, we complement the study of Section 4.2.3, by analyzing the two-photon signal when focusing the output pulse with the Time-Resolved transmission matrix.

We measure the Time-Resolved transmission matrix of a "thick" scattering medium (See Section 6.1.2), with $N_{SLM} = 1024$ SLM pixels. Figure 6.5 shows the corresponding time-of-flight distribution, measured with ICC technique. The shutter of the external arm is now closed: we only measure temporally-integrated linear signals on the CCD camera, and the corresponding two-photon signal emitted from fluorescent beads.

We focus the output pulse on various beads via single time-gated transmission matrices at different arrival times. We analyze the SBR of focusing from the two-photon signal, for the different arrival times.

Focusing with a single time-gated transmission matrix

Firstly, we extract a single time-gated transmission matrix $\mathbf{H}(\tau_1)$ at arrival time $\tau_1 = 1$ ps (See Figure 6.5). We focus the output pulse, via phase-conjugation, on a single microbead, whose location was identified earlier with a similar protocol as presented in Figure 6.2a.

We then measure the linear speckle on the CCD camera, and the corresponding two-photon signal on the EMCCD camera. Although the two-photon signal comes from a single bead, we consider the two-photon intensity at the focus, $I_{\mathrm{NL,focus}}$, as the spatially integrated signal on the EMCCD camera, as we did to estimate the non-linear background signal in Equation 6.1 (See Section 6.1.2). It is valid because the signal from other beads is negligible. We will use this method to estimate $I_{\mathrm{NL,focus}}$ for all the experiments performed with the fluorescent beads. We thus use the same RoI on the EMCCD camera as in Section 6.1.2. $I_{\mathrm{NL,focus}}$ is calculated, from the EMCCD camera measurement, as follows:

$$I_{\mathrm{NL,focus}} = \sum_{i}^{N_{\mathrm{pixels}}} I_{\mathrm{EMCCD}}(i) - \bar{I}_{\mathrm{noise,bg}} \tag{6.2}$$

The linear SBR is defined as the ratio between the intensity of the focus over the spatially averaged background intensity. The two-photon SBR $\eta_{\mathrm{NL,beads}}$ is defined as:

$$\eta_{\mathrm{NL,beads}} = \frac{I_{\mathrm{NL,focus}}}{\langle I^{\mathrm{beads}}_{\mathrm{NL,background}} \rangle} \tag{6.3}$$

The operation is iterated over 9 different focus positions, corresponding to different microbeads. From this set of data, we extract the average linear SBR $\eta_L(\tau_1) = 25 \pm 2$ and the two-photon SBR $\eta_{NL}(\tau_1) = 45 \pm 8$, that are reported in Figure 6.5, at arrival time τ_1. Error bars are standard deviation of the SBR over the 9 different focus positions. The two-photon SBR is lower than the expected square of the linear SBR. It might be interpreted with the stability of the beads. Although they are supposed to be fixed on the microscope slide, they are immersed in a liquid solution, and thus stable only few hours. Notwithstanding, we note that the two-photon SBR obtained with the beads is much higher than the SBR from the two-photon screen.

Comparison of SBR when focusing with time-gated transmission matrices at different arrival times

We iterate the above protocol for 5 different time-gated transmission matrices, extracted from the TRTM, at their corresponding arrival times. We extract the corresponding SBR ratios of focusing for both linear and two-photon signals, that are averaged over 9 focus positions.

Figure 6.5 presents the result. The linear SBR (blue line) of focus intensity is maximum ($\eta_L(\tau_3) = 34 \pm 2$) at arrival time τ_3 at which the time-of-flight distribution (black line) reaches its maximum, as we already studied in Figure 4.5 and in Section 4.2.3. Consequently, the corresponding two-photon SBR (red line) also reaches its maximum ($\eta_{NL}(\tau_3) = 181 \pm 20$). The two-photon SBR drastically drops for the other arrival times.We will now the study the origin of this drop.

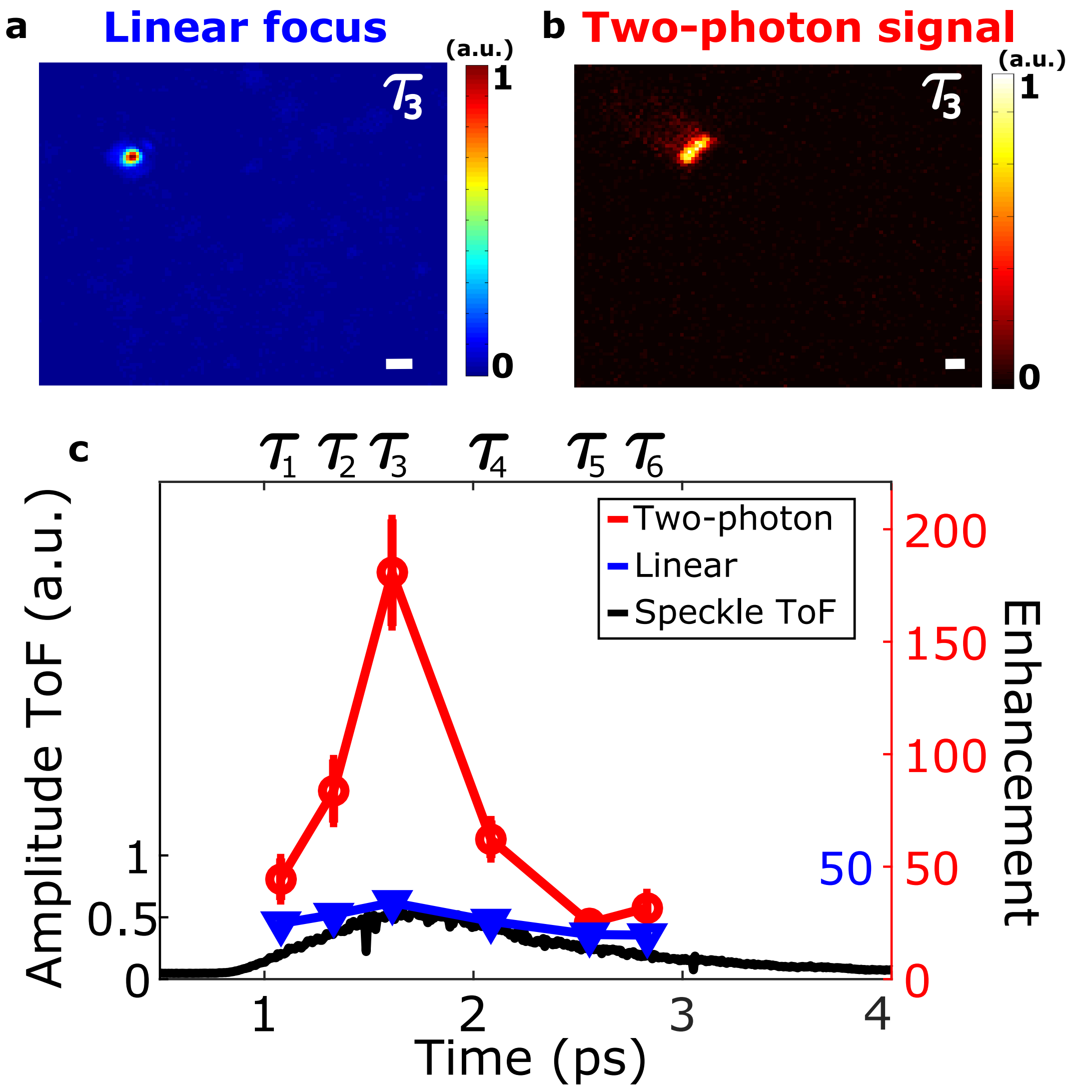

Figure 6.5 – Spatio-temporal focusing with a time-gated transmission matrix $\mathbf{H}(\tau)$: two-photon signal-to-background ratio as a function of arrival time τ. Two-photon signal is emitted from fluorescent microbeads after propagation through a thick scattering sample. **(a)** Temporally-integrated linear focus at arrival time τ_3 (see (c)), measured with the CCD camera, on a microbead. Scale bar: 2 μm. **(b)** Corresponding two-photon signal, measured with the EMCCD camera. Scale bar: 2 μm. **(c)** Black line represents the time-of-flight distribution of photons in the scattering medium. 6 time-gated transmission matrices (TGTM) are measured at arrival times τ_i, with i varying from 1 to 6, that are indicated on top. We focus on 9 different beads with each TGTM: the average linear (blue) and two-photon (red) are both shown, at their corresponding τ_i. Error bars are the corresponding standard deviation.

The two-photon SBR mostly depends on two parameters: intensity of the focus (more precisely its squared value), and duration of the output pulse at the focus position. Figure 4.4 shows that the pulse duration at the focus is approximately conserved for the different arrival times τ. Therefore, the drop of 2PF SBR as a function of τ is mainly due to a lower average intensity at other times than τ_3, which is dictated by the time-of-flight distribution. It is challenging to perform an accurate quantitative analysis, as the measured 2PF enhancements are lower than the squared value of the measured linear enhancements, for reasons that are still under investigations. It might be related to what was discussed in the above Subsection, concerning the low depth of field of the microscope objective, or the method we use in Equation 6.1 and Equation 6.2 to estimate the non-linear intensities. Finally, the non-linear background defined in Equation 6.1 might be underestimated for a bead signal, as it was measured for a single illumination pattern on the SLM due to the long exposure time.

Nonetheless, the main message carried by Figure 6.5 is the following: the highest 2PF signal is measured when the arrival time of the time-gated matrix is set to the delay time when the time-of-flight distribution, that was previously measured, reaches its maximum value. Moreover, the non-linear enhancement is much higher than the linear enhancement.

6.2.3 Effect of quadratic spectral phase on non-linear signal with the MSTM

Non-linear processes are sensitive to the duration of the output pulse. As we studied in the above Sections, spatio-temporal focusing, achieved either with the MSTM or the TRTM, is enhancing 2PF after propagation of the output pulse through the scattering medium. In Section 3.3.3, we deliberately introduced quadratic spectral phase relations on the output pulse, and analyzed with ICC technique the corresponding temporal profiles. In this Section, we qualitatively analyze the two-photon SBR upon under similar chirped pulses, to verify the ability to tune a non-linear effect.

Experimental protocol

In the following, the experimental conditions are exactly similar than in Section 3.3.3: the scattering medium is “thick”. The MSTM is constituted of $N_\lambda = 11$ monochromatic TMs, measured with $N_{\text{SLM}} = 1024$ SLM pixels.

We spatially focus the output pulse on a microbead, and impose a quadratic phase relation between its different spectral components. While the scattering effects are adjusted via the MSTM, this spectral phase relation is adding a controllable dispersion on the output pulse. We then collect both the linear signal and the corresponding 2PF signal. Similarly to the above Section, we extract the focusing SBR ratio for both linear and non-linear signals, for each focus position. The overall SBR are obtained by averaging over 9 different microbeads.

This process is repeated for 8 different quadratic spectral phase profiles (4 positive curvatures and 4 negative curvatures), and a flat spectral phase profile. Figure 6.6a illustrates these different applied spectral phase relation. In Figure 6.6b, the different SBR are shown for the different added group delay dispersions.

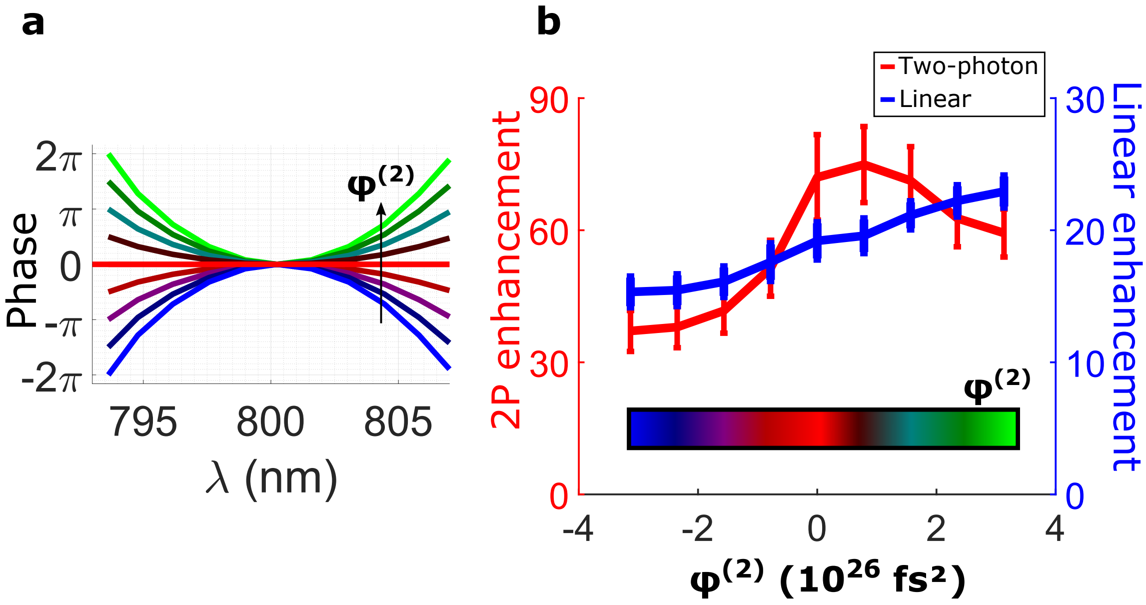

Figure 6.6 – Two photon signal upon an adjustable chirped pulse, via a quadratic spectral phase distribution with the full MSTM. Two-photon signal is emitted from fluorescent beads after propagation through a thick scattering sample. **(a)** Quadratic spectral phase relation applied on the output pulse via the MSTM. **(b)** Measured linear (blue) and two-photon (red) enhancements (SBR) as a function of the added group delay dispersion. Color-bar indicates the correspondence between the curvatures (color lines) in (a) and the x-axis in (b). Error bars are the corresponding standard deviation over 9 different focus positions.

Discussion

First of all, we observe that the maximum two-photon signal is not collected for a flat spectral phase relation, but for a slight positive chirped pulse. Indeed, the imposed flat spectral phase is applied on the CCD camera plane, where the MSTM was measured. However, the 2PF sample is not located in the same plane. According to Figure 2.1, several optical elements, including the fourth microscope objective, are adding dispersion between the 2PF sample plane and the CCD camera plane. Typical microscope objectives, with similar properties (high numerical aperture) than the fourth one, are adding positive group velocity dispersion, that could be pre-compensated with a negative chirp [Müller et al., 1998]. The imposed flat spectral phase relation might then not be flat in the 2PF plane, but slightly quadratic with negative curvature to compensate for the natural positive chirp induced by the microscope objective. Therefore, a positive chirp, corresponding approximately to the group velocity dispersion of the fourth microscope objective, leads in principle to a flat spectral phase relation in the 2PF plane, and thus maximizing the 2PF signal. This chirp value $\varphi^{(2)}_{\text{M.O.}}$ can be retrieved with the duration of the pulse, that is related to our data by the ratio between the 2PF SBR to the corresponding linear SBR squared. This ratio is compared to Equation 3.7 with a chirp $\varphi^{(2)} = \varphi^{(2)}_{\text{applied}} - \varphi^{(2)}_{\text{M.O.}}$, where $\varphi^{(2)}_{\text{applied}}$ corresponds to the added group velocity dispersion presented in Figure 6.6a. It leads to $\varphi^{(2)}_{\text{M.O.}} \sim 3500\ \text{fs}^2 \pm 500\ \text{fs}^2$. This is result is on the same order of magnitude as typical $\varphi^{(2)}_{\text{M.O.}}$ reported in [Müller et al., 1998].

Nonetheless, temperature and humidity stabilities were a notable issue when this experiment was performed. The experiments related to Figure 6.6 were performed from high positive curvatures (green color of $\varphi^{(2)}$, right side of Figure 6.6b) to the lowest negative curvatures (blue color of $\varphi^{(2)}$, left side of Figure 6.6b). The measurement time of a single non-linear focus is $T_e = 10$ s on the EMCCD camera. The average over 9 points, corresponding to a point in Figure 6.6, takes then approximately a couple of minutes. The SBR of linear focusing is indeed decreasing while data were acquired: the MSTM was valid only for couple of hours.

6.3 Comparison of non-linear enhancement between the different transmission matrix approaches

In this Section, we compare the 2PF signal-to-background ratio of focusing, from fluorescent microbeads, for the different transmission matrix (TM) approaches developed in this thesis: the Multi-Spectral TM (Chapter 3), the Time-Resolved TM (Chapter 4) and the Broadband TM (Chapter 5). All the transmission matrices are measured with the same number of SLM pixels (N_{SLM} =1024 SLM pixels.)

We show the comparison for two different multiple scattering samples: a "thin" sample and a "thick" sample (See Section 6.1.2), where the 2PF signal is more challenging to probe, because of the low power per speckle grain, and of the additional temporal spread.

6.3.1 For a "thin" multiple scattering medium

Experimental protocol to compare two-photon signal between the different transmission matrices

The "thin" multiple scattering sample is placed in the experimental setup shown in Figure 2.1. The shutter in the reference arm is opened: measurement of the time-of-flight distribution leads to $\tau_m \sim 550$ fs. We then measure the Multi-Spectral TM (with external reference), with $N_\lambda = 5$ monochromatic TMs, and a single time-gated TM, at time where the time-of-flight distribution reaches its maximum (τ_3 of Figure 6.5), with $N_{\text{SLM}} = 1024$ SLM pixels. The external arm is then closed. The Broadband TM is measured with the same number of SLM pixels.

The measured TMs are exploited for focusing on an isolated microbead. While only one focus is possible with the Broadband TM and the time-gated TM, three different focusing experiments are performed with the Multi-Spectral TM:

- Flat spectral phase (MSTM-flat), leading to spatio-temporal focusing;
- Random spectral phase (MSTM-rand), leading to spatial-only focusing, but the output pulse is temporally broadened;
- Monochromatic focusing, at the central wavelength of the output pulse λ_0, leading also to spatial-only focusing.

From the 5 experiments, we extract the SBR of focusing for both linear and 2PF signal. This process is iterated on 9 different microbeads. Figure 6.7 presents the average SBRs for both signals. Error bars are standard deviation over the 9 different focus positions.

Analysis of the comparison

Several conclusions can be extracted from Figure 6.7. We first note that the linear SBRs are all comparable for the different transmission matrices. Indeed, the linear SBR of focusing, for a given scattering sample (characterized by its number of spectral degrees of freedom N_λ) only depends on the number of spatial degrees of freedom (i.e. N_{SLM}), as we demonstrated in the previous Chapters.

The first striking observation for the non-linear signal is that the time-gated transmission matrix produces the highest two-photon signal. This result is not surprising, as the spatial degrees of freedom are all contributing to focus light arriving only at a chosen delay time. This protocol is clearly the most efficient to obtain spatio-temporal focusing, with a limited inherent background signal resulting from the incoherent sum of the other $(N_\lambda - 1)$ speckle pattern.

The Multi-Spectral TM with a flat spectral phase relation was expected at second rank position in terms of 2PF SBR, behind the time-gated transmission TM. Indeed, the achieved output pulse correspond to a spatio-temporal focusing. Nonetheless, imprecision of the spectral phase measurement, as well as spectral discretization of the MSTM, are increasing the background and the pulse duration. The 2PF SBR for the MSTM-flat, as reported in Figure 6.7, is much lower than the 2PF SBR of the time-gated TM.

Surprisingly, the Broadband TM produces better 2PF than the MSTM-flat, and almost on the same order of magnitude as the time-gated TM. Indeed, the confinement time, $\tau_m \sim 550$ fs, is relatively low regarding the pulse duration ($\delta t \sim 100$ fs). Focusing with the broadband TM leads to a temporal shortening of the output pulse $\tau_{b.f.} = \tau_m/2$, without spatio-temporal focusing, as we studied in Section 5.3.2. Therefore the output pulse has a low average duration $\tau_{b.f.} \sim 250$ fs, leading then to a high 2PF enhancement.

Finally, both the monochromatic TM and the MSTM-rand correspond to spatial-only focus, and a similar temporally broadened pulse (See Figure 3.7). We thus expect similar 2PF enhancement for both approaches, and lower than the previous transmission matrices. Curiously, focusing with MSTM-rand produces a lower linear SBR, and consequently a lower 2PF signal than the monochromatic TM. It might be attributed to the lengthy measurement of the MSTM. Cumulated with the limited stability of the experimental setup (cf Figure 6.6), focusing with the MSTM is then more sensitive to experimental conditions than the other transmission matrices. Moreover, the MSTM is only constituted of $N_\lambda = 5$ monochromatic TMs: fluctuations are high for a low number of spectral degrees of freedom.

6.3.2 For a "thick" multiple scattering medium

The protocol is repeated on a "thick" scattering medium, characterized by $\tau_m \sim 1$ ps. The MSTM is then measured with $N_\lambda = 11$ monochromatic TMs. Figure 6.8 presents the experimental results.

Similarly to Figure 6.7, we first note that the linear signals, for the five different methods, have almost the same SBR of focusing, nonetheless slightly lower than with the "thin" scattering sample. Indeed, the number of spectral degrees of freedom N_λ is twice higher in Figure 6.8 than in Figure 6.7, leading to a reducing of the linear SBR of approximately a factor two. Consequently, the non-linear signal, that is sensitive to the squared linear

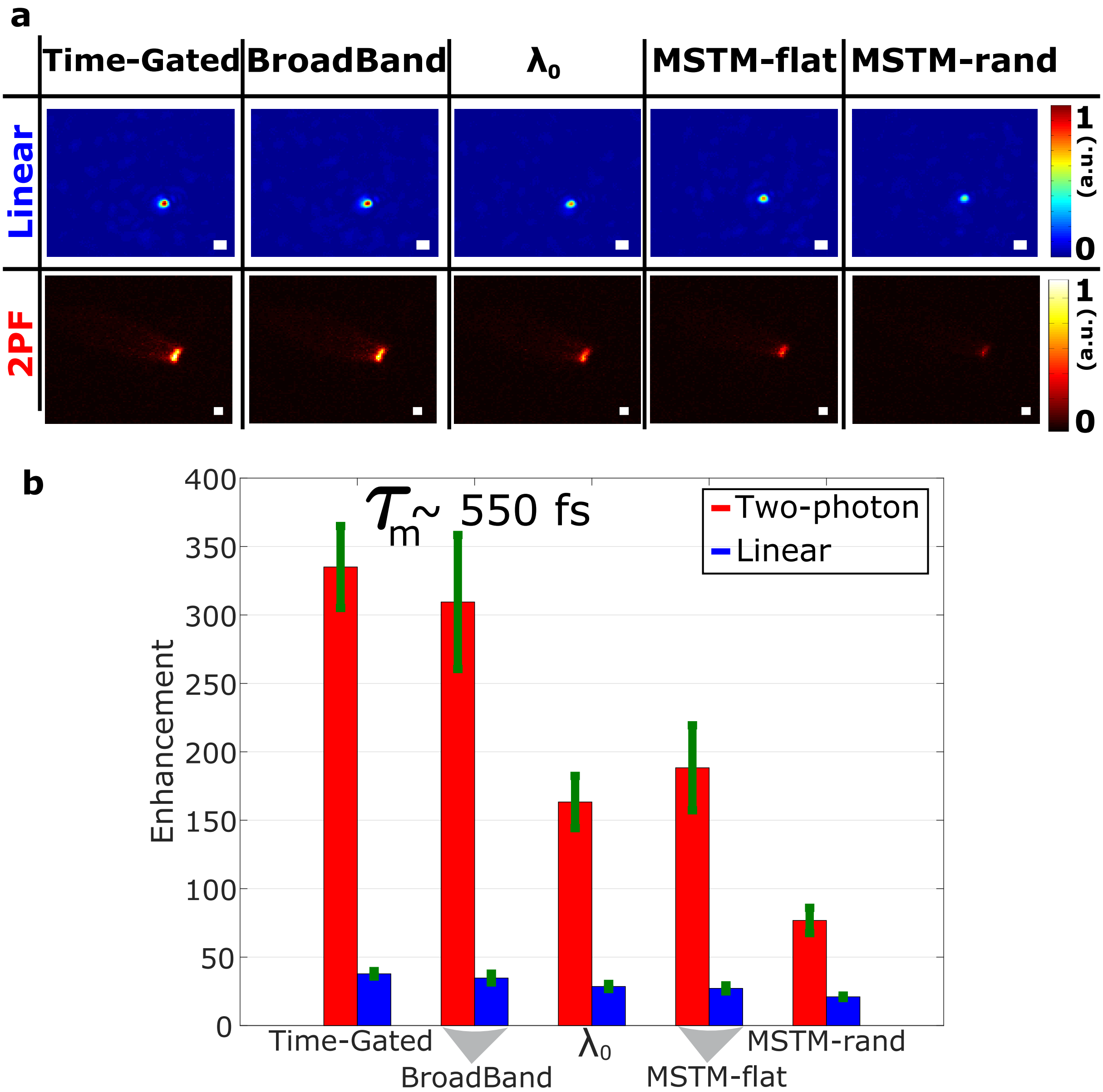

Figure 6.7 – Comparison of two-photon signals between the different transmission matrices, for a "thin" multiple scattering medium. (a) Linear (top line) and two-photon (bottom line) signals, upon focusing on a single fluorescent microbead, for different transmission matrices of a "thin" scattering medium ($\tau_m \sim 550$ fs): Time-Gated, Broadband, monochromatic at λ_0 the central wavelength of the output pulse, and Multi-Spectral for either a flat spectral phase (MSTM-flat) or a random spectral phase (MSTM-rand). Color bar are normalized by maximum value of the Time-Gated images. Scale bars: 2 μm. **(b)** Linear (blue) and two-photon (red) enhancements averaged over 9 different focus positions. Error bars are the corresponding standard deviation.

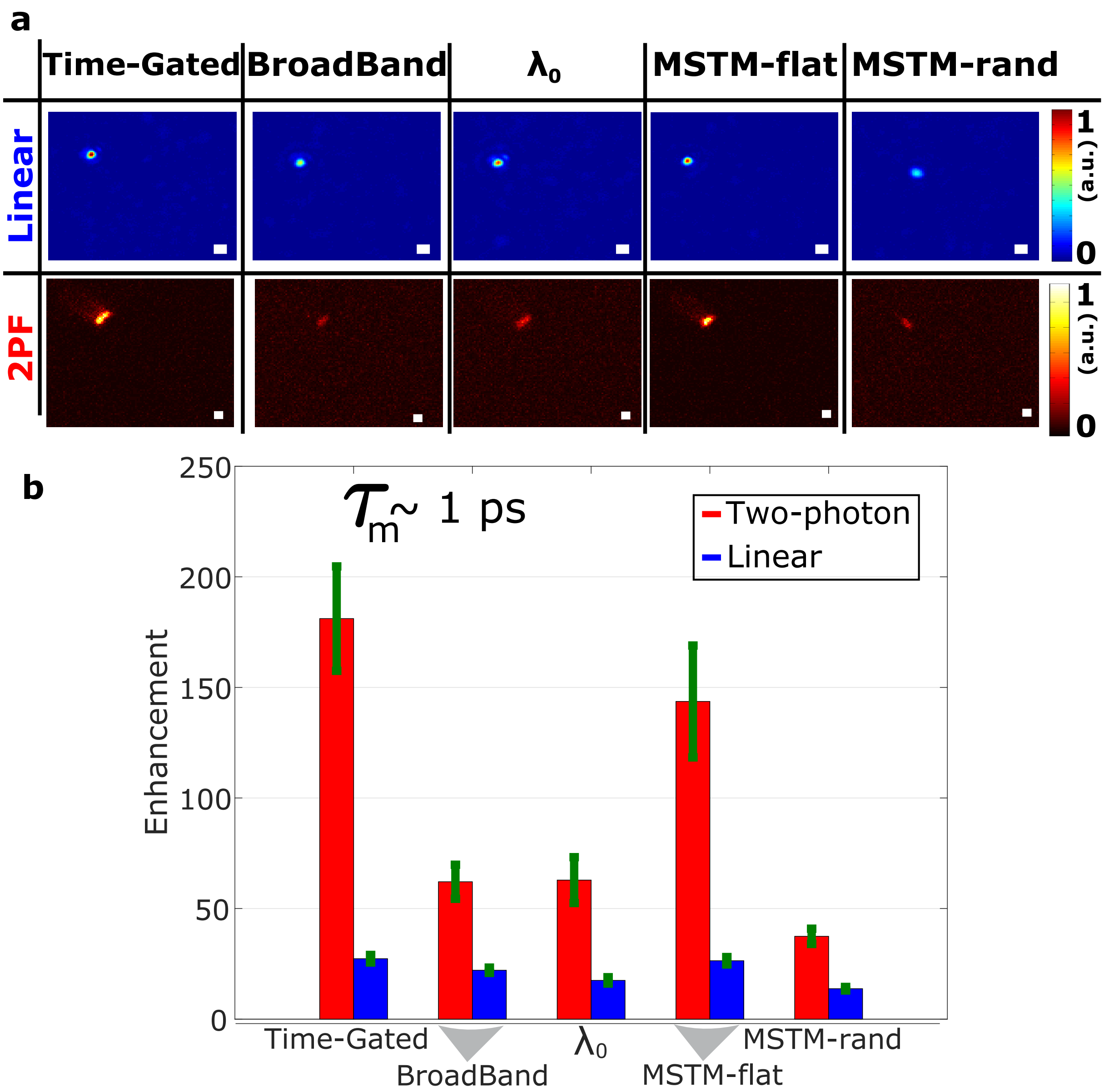

Figure 6.8 – Comparison of two-photon signals between the different transmission matrices, for a "thick" multiple scattering medium. Similar caption than in Figure 6.7, except the scattering medium is now described by $\tau_m \sim 1$ ps.

intensity, is reduced by a factor ~ 4. Although temporal compression is twice more efficient than in Figure 6.7, we expect a decrease of the 2PF SBR for a thicker scattering medium.

Again, the Time-Gated transmission matrix leads to the highest 2PF enhancement. Indeed, analogously to Section 6.3.1, the time-gated TM is the only method that ensures spatio-temporal focusing almost back to Fourier-limited duration with a limited background.

The broadband TM has a lower 2PF enhancement than the MSTM-flat, with this "thick" scattering sample. The expected average duration of the output pulse with the broadband TM, $\tau_{b.f.} = \tau_m/2 \sim 500$ fs, scales much larger than the input pulse duration. Therefore, MSTM-flat focus has a shorter pulse duration. Imprecisions related on the MSTM measurement and the spectral phase are increasing the output pulse duration: MSTM-flat hence produces a 2PF SBR lower than the 2PF SBR with the time-gated TM.

Finally, 2PF SBR with the broadband TM is slightly lower than expected, as its value is on the same order of magnitude than spatial-only focusing, obtained with the monochromatic TM and the MSTM-rand. Interpretation of this result remains elusive as it strongly depends on the experimental conditions.

6.4 Application to non-linear imaging

In the previous Section, we demonstrated that the time-gated transmission matrix $\mathbf{H}(\tau)$, measured at arrival time τ when time-of-flight distribution reaches its maximum, produces the maximum 2PF SBR of focusing. In this Section, we exploit an experimentally measured $\mathbf{H}(\tau)$ for point-scanning imaging purpose, behind a thick scattering material ($\tau_m \sim 1$ ps) where almost no ballistic light is transmitted.

6.4.1 Experimental protocol

In this Section, we use a thick multiple scattering medium. We measure a single time-gated transmission matrix $\mathbf{H}(\tau)$, where τ stands for the delay time where the time-of-flight distribution is maximum. $\mathbf{H}(\tau)$ is measured with $N_{\text{SLM}} = 1024$ SLM segments, over a RoI on the CCD camera $N_{\text{CCD}} = 90$ pixels $\times$ 90 pixels.

Here, we scan the focus using phase-conjugation of $\mathbf{H}(\tau)$, in all the output spatial positions, and we collect the corresponding two-photon signal. In the literature, some point-scanning methods have been developed using the memory-effect of the scattering medium. Such approach was performed in [Vellekoop and Aegerter, 2010] with an iterative optimization on the linear signal and shifting the focus in a 2D zone within the memory effect range, or in a 3D zone with an additional parabolic phase shift [Ghielmetti and Aegerter, 2012]. A memory-effect scanning microscope, with an optimization algorithm on the total back-reflected two-photon signal was realized in [Tang et al., 2012, Katz et al., 2014b]. However, our scattering sample is too thick to exhibit memory effect, in contrast with thinner sample or biological tissues [Schott et al., 2015], as we studied in Section 1.2.3. Indeed, the input phase mask to focus on a single output position is uncorrelated with the input phase mask to focus on a close output position, shifted by a single pixel on the CCD camera. Therefore, we cannot shift the focus by tilting the input wavefront.

Figure 6.9a describes the method for point-scanning imaging with $\mathbf{H}(\tau)$, following the above protocol:

1. We display on the phase-only SLM the pattern to focus the output pulse in the position (x_1, y_1) on the CCD camera (top left corner, see Figure 6.9a), via phase-conjugating the corresponding line of $\mathbf{H}(\tau)$.

2. We check that the output pulse is well focused on the CCD camera, at the corresponding spatial position.

3. We measure the two-photon signal on the EMCCD camera, used as a bucket detector. We use the spatially-integrated two-photon signal for the reconstruction image, at this specific focus position.

4. The process is iterated for all the pixel positions (x_k, y_k) on the CCD camera, with k an integer number ranging from 2 to N_{CCD}.

A similar protocol was developed with a broadband transmission matrix in [de Aguiar et al., 2016], on a thinner multiple scattering sample.

6.4.2 Results of point-scanning imaging with a time-gated transmission matrix

Figure 6.10a shows the mean image after averaging the linear speckle over 100 different random illuminations with the SLM, similarly to Figure 6.2a. In this experiment, 4 isolated microbeads are identified in the field of view. Figure 6.9c presents the measured two-photon signal when the output pulse is focused on a single microbead position. A corresponding bright signal is recorded on the EMCCD camera, localized around the microbead.

Reconstruction image

Reconstruction of the two-photon image, via this point-scanning imaging protocol, is illustrated in Figure 6.10b. We clearly identify 4 microbeads, as in Figure 6.10a. Fluorescent intensity of each microbead differs from each other for several reasons. Firstly, the beads have their own sizes and fluorescence emission cross-sections, that are not rigorously equal for all the beads. Secondly, the focus intensity on the CCD camera is not exactly identical in all the CCD positions, as indicated by the standard deviation of the linear SBR in Figure 6.8. Consequently, the 2PF SBR has a standard deviation (See Figure 6.8). Finally, the experiment is lengthy: the EMCCD camera has an exposure time of 10 seconds per focusing position. It takes ~ 15 hours to measure the two-photon signal for all the focusing positions within the field of view. $\mathbf{H}(\tau)$ might have suffered from inherent decorrelation between the first and the last focus. This long measurement time is only limited by the detection process of the two-photon fluorescence, and not by the SLM itself to scan the focus.

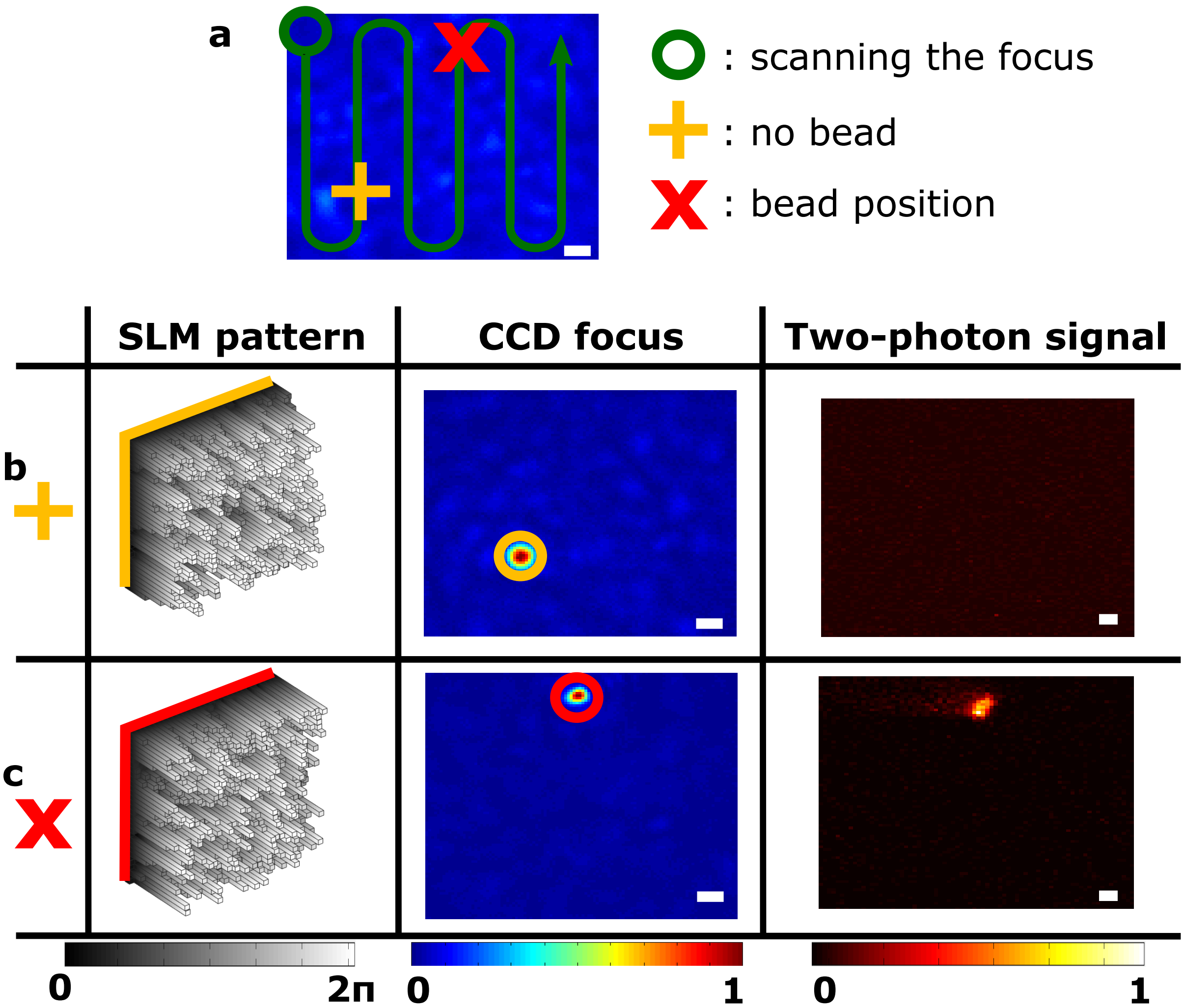

Figure 6.9 – Protocol for point-scanning imaging of fluorescent beads, using a single time-gated transmission matrix. A single time-gated matrix $\mathbf{H}(\tau)$, of a thick scattering medium, is measured. τ corresponds to the delay time where the time-of-flight distribution reaches its maximum. First column: SLM input pattern. Second column: CCD image when focusing with $\mathbf{H}(\tau)$. Third column: corresponding two-photon signal measured on the EMCCD camera. **(a)** (Green line) The achieved focused is scanned, using the phase-conjugation of $\mathbf{H}(\tau)$ in all the output spatial positions. The corresponding spatially-integrated two-photon signal is recorded on the EMCCD camera. **(b)** (Yellow + of (a)) No microbead is detected for this focus position. **(c)** (Red x in (a)) Example of focusing on a microbead: two-photon signal is detected on the EMCCD camera. Scale bars: 2 μm.

Resolution of this point-scanning imaging technique

Intensity profiles of the lower right spot, of both the averaged linear signal and the reconstructed two-photon image, are shown in Figure 6.10c-d. Both intensity profiles peaks have widths $\sim 1\mu$m at FWHM, corresponding to the original bead dimension. Nonetheless, the linear image (Figure 6.10a) cannot be used for resolution purposes, as the contrast comes from both diffraction and scattering from the microbeads. It only enables to identify the number of beads and their respective positions. Resolution of this point-scanning imaging method could be obtained with nanobeads of lower radial dimension. Nonetheless, a compromise must be found between low inner radius of fluorescent beads, and detection of the corresponding two-photon signal. A smaller bead would require a longer exposure time to probe two-photon fluorescence, and a more challenging protocol to detect their positions with the CCD camera. As reported in [Vellekoop and Aegerter, 2010], the resolution should be, in principle, comparable with a widefield microscope resolution. Indeed, the scattering medium is not deteriorating the resolution: on the contrary, we exploit the scattering medium to create a sharper focus, whose size is given by the speckle grain, via the scattering lens effect [Vellekoop et al., 2010].

Our point-scanning method has a larger field of view than typical memory-effect-based scanning microscope. Indeed, our field of view is not limited by the memory-effect range, but only by the dimension N_{CCD} of the measured time-gated transmission matrix $\mathbf{H}(\tau)$.

6.5 Summary

In this Chapter, we exploited the various transmission matrices developed in this thesis, to excite a two-photon fluorescence process. 2PF is enhanced with spatio-temporal focusing, in comparison with both spatial-only focusing and no wavefront shaping. We demonstrated that a time-gated transmission matrix, measured at the arrival time where the time-of-flight distribution reaches its maximum, is the most efficient method among the different transmission matrices, to perform 2PF. We exploited this time-gated transmission matrix to develop a point-scanning imaging technique. It opens interesting perspectives in non-linear imaging in multiple scattering media, for instance using three-photon process for deep imaging in biological tissues [Ouzounov et al., 2017].

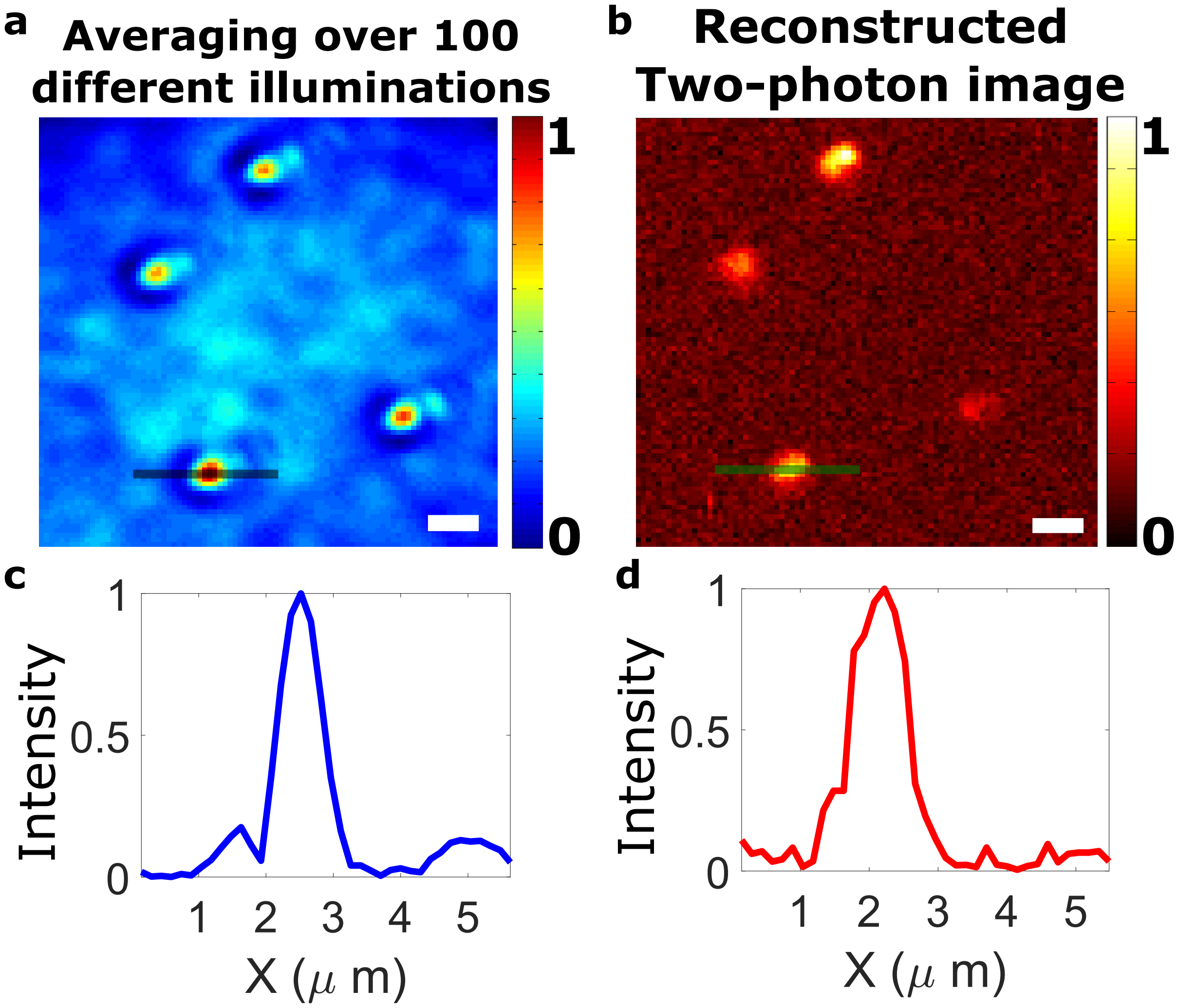

Figure 6.10 – Experimental results of point-scanning imaging of fluorescent beads, using a single time-gated transmission matrix. (a) Mean linear speckle image, obtained by averaging over 100 different random illumination patterns on the SLM, measured with the CCD camera. 4 microbeads are observed in the field of view. Scale bar: 2 μm. **(b)** Reconstructed two-photon image with the point-scanning imaging technique. Scale bar: 2 μm. **(c)** Intensity profile along the black line of (a). **(d)** Intensity profile along the green line of (b).

Conclusion

Light propagation in scattering media is a very complex process. Although statistical properties can be determined, the exact transmitted pattern is almost impossible to predict experimentally. Nonetheless, the control of the output light does not require *a priori* knowledge on the medium. Wavefront control of light propagating through scattering media started 10 years ago with CW light, thanks to the high number of spatial degrees of freedom proposed by spatial light modulators (SLM), and is very promising. Indeed, light that has suffered multiple scattering can be coherently manipulated: the scattering medium is then used as a controllable multi-modal (up to 10^8 modes!) platform. In particular, the ability to focus behind, or through, a scattering material opens interesting perspectives such as deep optical microscopy in biological tissue, where almost no ballistic photons are present, or the study of light-matter interaction in complex media. This active research field has then been extended to different kind of coherent light sources, such as ultrashort pulses. Non-linear optical processes, that mostly rely on the use of ultrashort pulses, are usually inhibited in complex media. Indeed, the transmitted pulse is strongly affected by scattering effects: the output power is several orders of magnitude lower than the input pulse power, and the temporal profile is broadened up to 10-1000 times compared to the initial duration. Recently, the control of both spatial and temporal profiles was demonstrated, based on different techniques such as iterative optimization algorithms, pulse shaping, or digital optical phase conjugation. Nonetheless, those methods do not provide any information on light propagation through the medium, in contrast with the transmission matrix of the medium. The spectral diversity of the scattering medium prevents the use of a monochromatic transmission matrix, the only experimentally measured transmission matrix in previous literature, to control an ultrashort pulse of light. A Multi-Spectral TM approach was developed in our research group before the beginning of this thesis, but temporal control of the output pulse was still elusive.

In this context, we demonstrated in this thesis various transmission matrix (TM) approaches to control the spatio-temporal profile of an ultrashort pulse, that is transmitted through multiple scattering media, with only spatial degrees of freedom of a single phase-only SLM. Using the experimental setup detailed in Chapter 2, we firstly measured the Multi-Spectral TM of a thick layer of white paint in Chapter 3. This 3D tensor is a stack of monochromatic TMs for all the spectral components of the output pulse. We showed the ability to focus different spectral components in different spatial positions, thus using the scattering medium as a controllable dispersive element. Focusing all the spectral components of the output pulse in the same output spatial position, in conjunction with an accurate spectral phase control, enables deterministic control of the output pulse's temporal profile. In addition to spatio-temporal focusing, i.e. focusing the output pulse in a single spatial speckle grain whose temporal profile is close to its Fourier-limited initial duration, we demonstrate that the scattering medium, in conjunction with the SLM, can be exploited as a deterministic pulse shaper, to generate for instance a double pulse with controllable delay.

In Chapter 4, we reported the first measurement of the Time-Resolved TM of a thick layer of paint. This operator is a stack of time-gated TMs, for all the arrival times of photons at the output of the scattering medium. We demonstrated that a single time-gated TM enables spatio-temporal focusing, in contrast with the Multi-Spectral TM that requires the control of the full spectrum to achieve a similar focusing experiment.

Both the Time-Resolved TM and the Multi-Spectral TM need an external reference arm in their respective measurement protocols. We measured the TM with a self-referencing method in Chapter 5, that we coined the BroadBand TM, in contrast with the monochromatic TM measured with CW light. Although spatio-temporal focusing cannot be achieved with this matrix because of its reference field, we interestingly demonstrated a two-fold reduction of the output pulse duration.

Finally, in Chapter 6, we exploited the three different methods to enhance a non-linear process, that is two-photon emission fluorescence. We compared the two-photon signal upon focusing with the three different TMs approaches developed in this thesis. With the most efficient one, the time-gated TM measured when the time-of-flight distribution of photons reaches its maximum, we developed a point-scanning imaging protocol, that we exploited to image fluorescent microbeads.

The various TM approaches developed in this thesis enable deterministic control of a transmitted ultrashort pulse through thick static scattering media. One can focus the output pulse in an arbitrary output spatial position, and define its spectral/temporal properties at will, up to its initial Fourier-limited duration. In addition to the spatial, orbital angular momentum and polarization control, a thick scattering medium (with a SLM) can then be used as a deterministic platform for dispersion control and pulse shaping purposes, which paves the way for light-matter interaction study in complex media. In the following, we propose a list of short-term perspectives that could follow up what was studied in this thesis:

- **Principal modes of a scattering medium.** Over the past two years, several research groups have studied principal modes of optical multi-mode fibers, that have a short temporal duration at the output [Carpenter et al., 2015, Xiong et al., 2016], and its extension to a microwave cavity [Gérardin et al., 2016, Ambichl et al., 2017]. These modes are not distorted, in the first order of frequency variation, by modal dispersion [Fan and Kahn, 2005]: they have a larger spectral correlation bandwidth than without shaping. They are computed from the full scattering matrix, or the transmission matrix if light is not backscattered, such as in a multi-mode fiber. The extension of the principal modes for a scattering medium could be of great interest, both fundamentally and for applications such as transfer of information or light delivery. The experimental setup, shown in Figure 2.1, should in principle enable the study of these principal modes of a scattering medium with the Multi-Spectral TM. We have started preliminary experiments, and the results are still under investigation.
- **Broadband mesoscopic effects in scattering media.** As reported in recent works, the study of broadband mesoscopic effects in scattering media is an active research field. For instance, open channels of a scattering medium upon illumination of a source with large bandwidth have a larger spectral correlation bandwidth than without shaping [Shi and Genack, 2015, Bosch et al., 2016], but temporal properties

have not been studied yet. Focusing with a single time-gated matrix with sufficient mode control, regarding the total number of modes [Goetschy and Stone, 2013], might provide evidence of the presence of open channels if the background increases, in analogy with the spatial study [Vellekoop and Mosk, 2008b]: our experimental setup would enable to measure their temporal profiles. Also, the study of long-range correlations with a broadband source [Hsu et al., 2015, Hsu et al., 2017] could be performed experimentally with the transmission matrix approaches developed in this thesis.

- **Delivery of short pulses for deep optical microscopy.** In a dynamic sample, such as a living biological tissue, the speckle pattern fluctuates with time: the wavefront shaping techniques are available as long as they are much faster than the decorrelation time of the medium [Blochet et al., 2017]. In principle, a very fast SLM could enable the measurement of a time-gated matrix in real time. For instance, measuring a time-gated TM with $N_{SLM} = 1024$ SLM pixels within 100 ms would require a SLM refresh rate on the order of 40 kHz. With the current technology, we can achieve such fast phase modulation using acousto-optic deflectors (AOD) [Akemann et al., 2015] based SLM, MEMS-based SLM or DMD (See Section 1.3.1). Such systems, combined with the different TM approaches, could enable delivery of short pulses deep in tissue, paving the way for multiphotonic imaging in depth.

- **Light-matter interaction in complex media.** The Multi-Spectral TM, in conjunction with the scattering medium and the SLM, enables one to shape at will the temporal profile of the output pulse. It opens interesting perspectives for coherent control [Meshulach and Silberberg, 1998, Cruz et al., 2004] and light-matter interactions [Sapienza et al., 2011] in scattering media.

- **Spectrally-dependent PSF engineering through scattering media.** We demonstrated PSF engineering protocol through a scattering medium, based on the experimentally measured monochromatic TM [Boniface et al., 2017]. This work could be extended to the spectral domain, using the Multi-Spectral TM, or in the temporal domain with the Time-Resolved TM. We would then be able to engineer arbitrary spectrally-dependent, or temporally-dependent, PSFs.

Bibliography

[Aguiar et al., 2017] Aguiar, H. B. d., Gigan, S., and Brasselet, S. (2017). Polarization recovery through scattering media. *Science Advances*, 3(9):e1600743.

[Akbulut et al., 2011] Akbulut, D., Huisman, T. J., Putten, E. G. v., Vos, W. L., and Mosk, A. P. (2011). Focusing light through random photonic media by binary amplitude modulation. *Optics Express*, 19(5):4017–4029.

[Akbulut et al., 2016] Akbulut, D., Strudley, T., Bertolotti, J., Bakkers, E. P. A. M., Lagendijk, A., Muskens, O. L., Vos, W. L., and Mosk, A. P. (2016). Optical transmission matrix as a probe of the photonic strength. *Physical Review A*, 94(4):043817.

[Akemann et al., 2015] Akemann, W., Léger, J.-F., Ventalon, C., Mathieu, B., Dieudonné, S., and Bourdieu, L. (2015). Fast spatial beam shaping by acousto-optic diffraction for 3d non-linear microscopy. *Optics Express*, 23(22):28191–28205.

[Akkermans and Montambaux, 2007] Akkermans, E. and Montambaux, G. (2007). *Mesoscopic Physics of Electrons and Photons*. Cambridge University Press.

[Akkermans et al., 1986] Akkermans, E., Wolf, P. E., and Maynard, R. (1986). Coherent Backscattering of Light by Disordered Media: Analysis of the Peak Line Shape. *Physical Review Letters*, 56(14):1471–1474.

[Ambichl et al., 2017] Ambichl, P., Brandstötter, A., Böhm, J., Kühmayer, M., Kuhl, U., and Rotter, S. (2017). Focusing inside Disordered Media with the Generalized Wigner-Smith Operator. *Physical Review Letters*, 119(3):033903.

[Anderson, 1958] Anderson, P. W. (1958). Absence of Diffusion in Certain Random Lattices. *Physical Review*, 109(5):1492–1505.

[Andreoli, 2014] Andreoli, D. (2014). *Contrôle spatio-temporel multi-spectral de la lumière en milieux complexes*. phdthesis, Université Pierre et Marie Curie - Paris VI.

[Andreoli et al., 2015] Andreoli, D., Volpe, G., Popoff, S., Katz, O., Grésillon, S., and Gigan, S. (2015). Deterministic control of broadband light through a multiply scattering medium via the multispectral transmission matrix. *Scientific Reports*, 5:10347.

[Arrizón et al., 2007] Arrizón, V., Ruiz, U., Carrada, R., and González, L. A. (2007). Pixelated phase computer holograms for the accurate encoding of scalar complex fields. *Journal of the Optical Society of America A*, 24(11):3500.

[Aubry and Derode, 2009] Aubry, A. and Derode, A. (2009). Random Matrix Theory Applied to Acoustic Backscattering and Imaging In Complex Media. *Physical Review Letters*, 102(8):084301.

[Aubry and Derode, 2010] Aubry, A. and Derode, A. (2010). Singular value distribution of the propagation matrix in random scattering media. *Waves in Random and Complex Media*, 20(3):333–363.

[Aulbach et al., 2012a] Aulbach, J., Bretagne, A., Fink, M., Tanter, M., and Tourin, A. (2012a). Optimal spatiotemporal focusing through complex scattering media. *Physical Review E*, 85(1):016605.

[Aulbach et al., 2012b] Aulbach, J., Gjonaj, B., Johnson, P., and Lagendijk, A. (2012b). Spatiotemporal focusing in opaque scattering media by wave front shaping with nonlinear feedback. *Optics Express*, 20(28):29237–29251.

[Aulbach et al., 2011] Aulbach, J., Gjonaj, B., Johnson, P. M., Mosk, A. P., and Lagendijk, A. (2011). Control of Light Transmission through Opaque Scattering Media in Space and Time. *Physical Review Letters*, 106(10):103901.

[Azucena et al., 2011] Azucena, O., Crest, J., Kotadia, S., Sullivan, W., Tao, X., Reinig, M., Gavel, D., Olivier, S., and Kubby, J. (2011). Adaptive optics wide-field microscopy using direct wavefront sensing. *Optics Letters*, 36(6):825–827.

[Babcock, 1953] Babcock, H. W. (1953). The possibility of compensating astronomical seeing. *Publications of the Astronomical Society of the Pacific*, 65(386):229–236.

[Bacot et al., 2016] Bacot, V., Labousse, M., Eddi, A., Fink, M., and Fort, E. (2016). Time reversal and holography with spacetime transformations. *Nature Physics*, 12(10):972–977.

[Badon et al., 2016] Badon, A., Li, D., Lerosey, G., Boccara, A. C., Fink, M., and Aubry, A. (2016). Smart optical coherence tomography for ultra-deep imaging through highly scattering media. *Science Advances*, 2(11):e1600370.

[Beenakker, 1997] Beenakker, C. W. J. (1997). Random-matrix theory of quantum transport. *Reviews of Modern Physics*, 69(3):731–808.

[Berkovits and Feng, 1994] Berkovits, R. and Feng, S. (1994). Correlations in coherent multiple scattering. *Physics Reports*, 238(3):135–172.

[Bertolotti et al., 2012] Bertolotti, J., van Putten, E. G., Blum, C., Lagendijk, A., Vos, W. L., and Mosk, A. P. (2012). Non-invasive imaging through opaque scattering layers. *Nature*, 491(7423):232–234.

[Betzig et al., 2006] Betzig, E., Patterson, G. H., Sougrat, R., Lindwasser, O. W., Olenych, S., Bonifacino, J. S., Davidson, M. W., Lippincott-Schwartz, J., and Hess, H. F. (2006). Imaging Intracellular Fluorescent Proteins at Nanometer Resolution. *Science*, 313(5793):1642–1645.

[Bifano and Stewart, 2005] Bifano, T. G. and Stewart, J. B. (2005). High-speed wavefront control using MEMS micromirrors. volume 5895, pages 58950Q–58950Q–9.

[Blochet et al., 2017] Blochet, B., Bourdieu, L., and Gigan, S. (2017). Focusing light through dynamical samples using fast closed-loop wavefront optimization. *arXiv:1709.07222 [physics]*. arXiv: 1709.07222.

[Boniface et al., 2017] Boniface, A., Mounaix, M., Blochet, B., Piestun, R., and Gigan, S. (2017). Transmission-matrix-based point-spread-function engineering through a complex medium. *Optica*, 4(1):54–59.

[Booth, 2014] Booth, M. J. (2014). Adaptive optical microscopy: the ongoing quest for a perfect image. *Light: Science & Applications*, 3(4):e165.

[Born and Wolf, 2013] Born, M. and Wolf, E. (2013). *Principles of Optics: Electromagnetic Theory of Propagation, Interference and Diffraction of Light*. Elsevier.

[Bosch et al., 2016] Bosch, J., Goorden, S. A., and Mosk, A. P. (2016). Frequency width of open channels in multiple scattering media. *Optics Express*, 24(23):26472–26478.

[Boyd, 2008] Boyd, R. W. (2008). *Nonlinear Optics, Third Edition*. Academic Press, 3rd edition.

[Bridges et al., 1974] Bridges, W. B., Brunner, P. T., Lazzara, S. P., Nussmeier, T. A., O'Meara, T. R., Sanguinet, J. A., and Brown, W. P. (1974). Coherent Optical Adaptive Techniques. *Applied Optics*, 13(2):291–300.

[Burke et al., 2015] Burke, D., Patton, B., Huang, F., Bewersdorf, J., and Booth, M. J. (2015). Adaptive optics correction of specimen-induced aberrations in single-molecule switching microscopy. *Optica*, 2(2):177–185.

[Carpenter et al., 2014] Carpenter, J., Eggleton, B. J., and Schröder, J. (2014). 110x110 optical mode transfer matrix inversion. *Optics Express*, 22(1):96.

[Carpenter et al., 2015] Carpenter, J., Eggleton, B. J., and Schröder, J. (2015). Observation of Eisenbud–Wigner–Smith states as principal modes in multimode fibre. *Nature Photonics*, 9(11):751–757.

[Carpenter et al., 2016] Carpenter, J., Eggleton, B. J., and Schröder, J. (2016). Complete spatiotemporal characterization and optical transfer matrix inversion of a 420 mode fiber. *Optics Letters*, 41(23):5580–5583.

[Cazé et al., 2010] Cazé, A., Pierrat, R., and Carminati, R. (2010). Near-field interactions and nonuniversality in speckle patterns produced by a point source in a disordered medium. *Physical Review A*, 82(4):043823.

[Chaigne et al., 2016] Chaigne, T., Gateau, J., Allain, M., Katz, O., Gigan, S., Sentenac, A., and Bossy, E. (2016). Super-resolution photoacoustic fluctuation imaging with multiple speckle illumination. *Optica*, 3(1):54–57.

[Chaigne et al., 2014] Chaigne, T., Katz, O., Boccara, A. C., Fink, M., Bossy, E., and Gigan, S. (2014). Controlling light in scattering media non-invasively using the photoacoustic transmission matrix. *Nature Photonics*, 8(1):58–64.

[Chandrasekhar, 2013] Chandrasekhar, S. (2013). *Radiative Transfer*. Courier Corporation.

[Cheong et al., 1990] Cheong, W., Prahl, S., and Welch, A. (1990). A review of the optical properties of biological tissues. *IEEE Journal of Quantum Electronics*, 26(12):2166–2185.

[Choi et al., 2017] Choi, W., Jo, Y., Ahn, J., Seo, E., Park, Q.-H., Jhon, Y. M., and Choi, W. (2017). Control of randomly scattered surface plasmon polaritons for multiple-input and multiple-output plasmonic switching devices. *Nature Communications*, 8:14636.

[Choi et al., 2011a] Choi, W., Mosk, A. P., Park, Q.-H., and Choi, W. (2011a). Transmission eigenchannels in a disordered medium. *Physical Review B*, 83(13):134207.

[Choi et al., 2013] Choi, Y., Hillman, T. R., Choi, W., Lue, N., Dasari, R. R., So, P. T. C., Choi, W., and Yaqoob, Z. (2013). Measurement of the Time-Resolved Reflection Matrix for Enhancing Light Energy Delivery into a Scattering Medium. *Physical Review Letters*, 111(24):243901.

[Choi et al., 2011b] Choi, Y., Yang, T. D., Fang-Yen, C., Kang, P., Lee, K. J., Dasari, R. R., Feld, M. S., and Choi, W. (2011b). Overcoming the Diffraction Limit Using Multiple Light Scattering in a Highly Disordered Medium. *Physical Review Letters*, 107(2):023902.

[Choi et al., 2012] Choi, Y., Yoon, C., Kim, M., Yang, T. D., Fang-Yen, C., Dasari, R. R., Lee, K. J., and Choi, W. (2012). Scanner-Free and Wide-Field Endoscopic Imaging by Using a Single Multimode Optical Fiber. *Physical Review Letters*, 109(20):203901.

[Čižmár and Dholakia, 2011] Čižmár, T. and Dholakia, K. (2011). Shaping the light transmission through a multimode optical fibre: complex transformation analysis and applications in biophotonics. *Optics Express*, 19(20):18871–18884.

[Čižmár and Dholakia, 2012] Čižmár, T. and Dholakia, K. (2012). Exploiting multimode waveguides for pure fibre-based imaging. *Nature Communications*, 3:1027.

[Čižmár et al., 2010] Čižmár, T., Mazilu, M., and Dholakia, K. (2010). In situ wavefront correction and its application to micromanipulation. *Nature Photonics*, 4(6):388–394.

[Clark et al., 2016] Clark, T. W., Offer, R. F., Franke-Arnold, S., Arnold, A. S., and Radwell, N. (2016). Comparison of beam generation techniques using a phase only spatial light modulator. *Optics Express*, 24(6):6249–6264.

[Conkey et al., 2012a] Conkey, D. B., Brown, A. N., Caravaca-Aguirre, A. M., and Piestun, R. (2012a). Genetic algorithm optimization for focusing through turbid media in noisy environments. *Optics Express*, 20(5):4840–4849.

[Conkey et al., 2012b] Conkey, D. B., Caravaca-Aguirre, A. M., and Piestun, R. (2012b). High-speed scattering medium characterization with application to focusing light through turbid media. *Optics Express*, 20(2):1733–1740.

[Conkey et al., 2011] Conkey, D. B., Trivedi, R. P., Pavani, S. R. P., Smalyukh, I. I., and Piestun, R. (2011). Three-dimensional parallel particle manipulation and tracking by integrating holographic optical tweezers and engineered point spread functions. *Optics Express*, 19(5):3835.

[Cruz et al., 2004] Cruz, J. M. D., Pastirk, I., Comstock, M., Lozovoy, V. V., and Dantus, M. (2004). Use of coherent control methods through scattering biological tissue to achieve functional imaging. *Proceedings of the National Academy of Sciences of the United States of America*, 101(49):16996–17001.

[Cuche et al., 1999] Cuche, E., Marquet, P., and Depeursinge, C. (1999). Simultaneous amplitude-contrast and quantitative phase-contrast microscopy by numerical reconstruction of Fresnel off-axis holograms. *Applied Optics*, 38(34):6994–7001.

[Cui and Yang, 2010] Cui, M. and Yang, C. (2010). Implementation of a digital optical phase conjugation system and its application to study the robustness of turbidity suppression by phase conjugation. *Optics Express*, 18(4):3444–3455.

[Curry et al., 2011] Curry, N., Bondareff, P., Leclercq, M., van Hulst, N. F., Sapienza, R., Gigan, S., and Grésillon, S. (2011). Direct determination of diffusion properties of random media from speckle contrast. *Optics Letters*, 36(17):3332.

[Dantus and Lozovoy, 2004] Dantus, M. and Lozovoy, V. V. (2004). Experimental Coherent Laser Control of Physicochemical Processes. *Chemical Reviews*, 104(4):1813–1860.

[Das et al., 1993] Das, B. B., Yoo, K. M., and Alfano, R. R. (1993). Ultrafast time-gated imaging in thick tissues: a step toward optical mammography. *Optics Letters*, 18(13):1092–1094.

[Davy et al., 2015] Davy, M., Shi, Z., Wang, J., Cheng, X., and Genack, A. Z. (2015). Transmission Eigenchannels and the Densities of States of Random Media. *Physical Review Letters*, 114(3):033901.

[de Aguiar et al., 2016] de Aguiar, H. B., Gigan, S., and Brasselet, S. (2016). Enhanced nonlinear imaging through scattering media using transmission-matrix-based wave-front shaping. *Physical Review A*, 94(4):043830.

[Débarre et al., 2009] Débarre, D., Botcherby, E. J., Watanabe, T., Srinivas, S., Booth, M. J., and Wilson, T. (2009). Image-based adaptive optics for two-photon microscopy. *Optics Letters*, 34(16):2495–2497.

[Defienne et al., 2014] Defienne, H., Barbieri, M., Chalopin, B., Chatel, B., Walmsley, I. A., Smith, B. J., and Gigan, S. (2014). Nonclassical light manipulation in a multiple-scattering medium. *Optics Letters*, 39(21):6090–6093.

[Defienne et al., 2016] Defienne, H., Barbieri, M., Walmsley, I. A., Smith, B. J., and Gigan, S. (2016). Two-photon quantum walk in a multimode fiber. *Science Advances*, 2(1):e1501054.

[del Hougne et al., 2016] del Hougne, P., Lemoult, F., Fink, M., and Lerosey, G. (2016). Spatiotemporal Wave Front Shaping in a Microwave Cavity. *Physical Review Letters*, 117(13):134302.

[DeMaria et al., 1966] DeMaria, A. J., Stetser, D. A., and Heynau, H. (1966). Self mode-locking of lasers with saturable absorbers. *Applied Physics Letters*, 8(7):174–176.

[Derode et al., 1995] Derode, A., Roux, P., and Fink, M. (1995). Robust Acoustic Time Reversal with High-Order Multiple Scattering. *Physical Review Letters*, 75(23):4206–4209.

[Dickson et al., 1997] Dickson, R. M., Cubitt, A. B., Tsien, R. Y., and Moerner, W. E. (1997). On/off blinking and switching behaviour of single molecules of green fluorescent protein. *Nature*, 388(6640):355–358.

[Diels and Rudolph, 2006] Diels, J.-C. and Rudolph, W. (2006). *Ultrashort Laser Pulse Phenomena: Fundamentals, Techniques, and Applications on a Femtosecond Time Scale*. Academic Press.

[Dorokhov, 1984] Dorokhov, O. N. (1984). On the coexistence of localized and extended electronic states in the metallic phase. *Solid State Communications*, 51(6):381–384.

[Drémeau et al., 2015] Drémeau, A., Liutkus, A., Martina, D., Katz, O., Schülke, C., Krzakala, F., Gigan, S., and Daudet, L. (2015). Reference-less measurement of the transmission matrix of a highly scattering material using a DMD and phase retrieval techniques. *Optics Express*, 23(9):11898–11911.

[Dubois et al., 2004] Dubois, A., Grieve, K., Moneron, G., Lecaque, R., Vabre, L., and Boccara, C. (2004). Ultrahigh-resolution full-field optical coherence tomography. *Applied Optics*, 43(14):2874–2883.

[Dudley et al., 2008] Dudley, J. M., Walmsley, I. A., and Trebino, R. (2008). Measurement of Ultrashort Electromagnetic Pulses. *JOSA B*, 25(6):MU1–MU2.

[Dupré et al., 2015] Dupré, M., del Hougne, P., Fink, M., Lemoult, F., and Lerosey, G. (2015). Wave-Field Shaping in Cavities: Waves Trapped in a Box with Controllable Boundaries. *Physical Review Letters*, 115(1):017701.

[Fan and Kahn, 2005] Fan, S. and Kahn, J. M. (2005). Principal modes in multimode waveguides. *Optics Letters*, 30(2):135.

[Fayard et al., 2015] Fayard, N., Cazé, A., Pierrat, R., and Carminati, R. (2015). Intensity correlations between reflected and transmitted speckle patterns. *Physical Review A*, 92(3):033827.

[Feng et al., 1988] Feng, S., Kane, C., Lee, P. A., and Stone, A. D. (1988). Correlations and Fluctuations of Coherent Wave Transmission through Disordered Media. *Physical Review Letters*, 61(7):834–837.

[Fetterman et al., 1998] Fetterman, M., Goswami, D., Keusters, D., Yang, W., Rhee, J.-K., and Warren, W. (1998). Ultrafast pulse shaping: amplification and characterization. *Optics Express*, 3(10):366.

[Fickler et al., 2017] Fickler, R., Ginoya, M., and Boyd, R. W. (2017). Custom-tailored spatial mode sorting by controlled random scattering. *Physical Review B*, 95(16):161108.

[Fink, 1997] Fink, M. (1997). Time Reversed Acoustics. *Physics Today*, 50(3):34–40.

[Fink, 2010] Fink, M. (2010). Imaging: Sharper focus by random scattering. *Nature Photonics*, 4(5):269–271.

[Fisher and Lee, 1981] Fisher, D. S. and Lee, P. A. (1981). Relation between conductivity and transmission matrix. *Physical Review B*, 23(12):6851–6854.

[Fisher, 2012] Fisher, R. A. (2012). *Optical Phase Conjugation*. Academic Press.

[Fork et al., 1987] Fork, R. L., Cruz, C. H. B., Becker, P. C., and Shank, C. V. (1987). Compression of optical pulses to six femtoseconds by using cubic phase compensation. *Optics Letters*, 12(7):483–485.

[French et al., 2017] French, R., Gigan, S., and Muskens, O. L. (2017). Speckle-based hyperspectral imaging combining multiple scattering and compressive sensing in nanowire mats. *Optics Letters*, 42(9):1820–1823.

[Freund, 1990] Freund, I. (1990). Looking through walls and around corners. *Physica A: Statistical Mechanics and its Applications*, 168(1):49–65.

[Freund et al., 1988] Freund, I., Rosenbluh, M., and Feng, S. (1988). Memory Effects in Propagation of Optical Waves through Disordered Media. *Physical Review Letters*, 61(20):2328–2331.

[Garcia et al., 1992] Garcia, N., Genack, A. Z., and Lisyansky, A. A. (1992). Measurement of the transport mean free path of diffusing photons. *Physical Review B*, 46(22):14475–14479.

[Genack, 1987] Genack, A. Z. (1987). Optical Transmission in Disordered Media. *Physical Review Letters*, 58(20):2043–2046.

[Genack and Drake, 1990] Genack, A. Z. and Drake, J. M. (1990). Relationship between Optical Intensity, Fluctuations and Pulse Propagation in Random Media. *EPL (Europhysics Letters)*, 11(4):331.

[Gérardin et al., 2016] Gérardin, B., Laurent, J., Ambichl, P., Prada, C., Rotter, S., and Aubry, A. (2016). Particlelike wave packets in complex scattering systems. *Physical Review B*, 94(1):014209.

[Gérardin et al., 2014] Gérardin, B., Laurent, J., Derode, A., Prada, C., and Aubry, A. (2014). Full Transmission and Reflection of Waves Propagating through a Maze of Disorder. *Physical Review Letters*, 113(17):173901.

[Ghielmetti and Aegerter, 2012] Ghielmetti, G. and Aegerter, C. M. (2012). Scattered light fluorescence microscopy in three dimensions. *Optics Express*, 20(4):3744.

[Gibson et al., 2004] Gibson, G., Courtial, J., Padgett, M. J., Vasnetsov, M., Pas'ko, V., Barnett, S. M., and Franke-Arnold, S. (2004). Free-space information transfer using light beams carrying orbital angular momentum. *Optics Express*, 12(22):5448–5456.

[Gigan, 2017] Gigan, S. (2017). Optical microscopy aims deep. *Nature Photonics*, 11(1):14–16.

[Gjonaj et al., 2011] Gjonaj, B., Aulbach, J., Johnson, P. M., Mosk, A. P., Kuipers, L., and Lagendijk, A. (2011). Active spatial control of plasmonic fields. *Nature Photonics*, 5(6):360–363.

[Gjonaj et al., 2013] Gjonaj, B., Aulbach, J., Johnson, P. M., Mosk, A. P., Kuipers, L., and Lagendijk, A. (2013). Focusing and Scanning Microscopy with Propagating Surface Plasmons. *Physical Review Letters*, 110(26):266804.

[Goetschy and Stone, 2013] Goetschy, A. and Stone, A. D. (2013). Filtering Random Matrices: The Effect of Incomplete Channel Control in Multiple Scattering. *Physical Review Letters*, 111(6):063901.

[Goodman, 1976] Goodman, J. W. (1976). Some fundamental properties of speckle*. *JOSA*, 66(11):1145–1150.

[Goodman, 2005] Goodman, J. W. (2005). *Introduction to Fourier Optics*. Roberts and Company Publishers.

[Goodman, 2007] Goodman, J. W. (2007). *Speckle Phenomena in Optics: Theory and Applications*.

[Goorden et al., 2014] Goorden, S. A., Bertolotti, J., and Mosk, A. P. (2014). Superpixel-based spatial amplitude and phase modulation using a digital micromirror device. *Optics Express*, 22(15):17999–18009.

[Guan et al., 2012] Guan, Y., Katz, O., Small, E., Zhou, J., and Silberberg, Y. (2012). Polarization control of multiply scattered light through random media by wavefront shaping. *Optics Letters*, 37(22):4663–4665.

[Gustafsson, 2000] Gustafsson, M. G. L. (2000). Surpassing the lateral resolution limit by a factor of two using structured illumination microscopy. *Journal of Microscopy*, 198(2):82–87.

[Harootunian et al., 1986] Harootunian, A., Betzig, E., Isaacson, M., and Lewis, A. (1986). Super-resolution fluorescence near-field scanning optical microscopy. *Applied Physics Letters*, 49(11):674–676.

[Hell and Wichmann, 1994] Hell, S. W. and Wichmann, J. (1994). Breaking the diffraction resolution limit by stimulated emission: stimulated-emission-depletion fluorescence microscopy. *Optics Letters*, 19(11):780–782.

[Helmchen and Denk, 2005] Helmchen, F. and Denk, W. (2005). Deep tissue two-photon microscopy. *Nature Methods*, 2(12):932–940.

[Hillegas et al., 1994] Hillegas, C. W., Tull, J. X., Goswami, D., Strickland, D., and Warren, W. S. (1994). Femtosecond laser pulse shaping by use of microsecond radio-frequency pulses. *Optics Letters*, 19(10):737.

[Hillman et al., 2013] Hillman, T. R., Yamauchi, T., Choi, W., Dasari, R. R., Feld, M. S., Park, Y., and Yaqoob, Z. (2013). Digital optical phase conjugation for delivering two-dimensional images through turbid media. *Scientific Reports*, 3:1909.

[Hsieh et al., 2010] Hsieh, C.-L., Pu, Y., Grange, R., and Psaltis, D. (2010). Digital phase conjugation of second harmonic radiation emitted by nanoparticles in turbid media. *Optics Express*, 18(12):12283–12290.

[Hsu et al., 2015] Hsu, C. W., Goetschy, A., Bromberg, Y., Stone, A. D., and Cao, H. (2015). Broadband Coherent Enhancement of Transmission and Absorption in Disordered Media. *Physical Review Letters*, 115(22):223901.

[Hsu et al., 2017] Hsu, C. W., Liew, S. F., Goetschy, A., Cao, H., and Douglas Stone, A. (2017). Correlation-enhanced control of wave focusing in disordered media. *Nature Physics*, advance online publication.

[Huang et al., 1991] Huang, D., Swanson, E. A., Lin, C. P., Schuman, J. S., Stinson, W. G., Chang, W., Hee, M. R., Flotte, T., Gregory, K., Puliafito, C. A., and Et, A. (1991). Optical coherence tomography. *Science*, 254(5035):1178–1181.

[Hubin and Noethe, 1993] Hubin, N. and Noethe, L. (1993). Active Optics, Adaptive Optics, and Laser Guide Stars. *Science*, 262(5138):1390–1394.

[Ishimaru, 1999] Ishimaru, A. (1999). *Wave Propagation and Scattering in Random Media*. John Wiley & Sons.

[Jang et al., 2015] Jang, M., Ruan, H., Vellekoop, I. M., Judkewitz, B., Chung, E., and Yang, C. (2015). Relation between speckle decorrelation and optical phase conjugation (OPC)-based turbidity suppression through dynamic scattering media: a study on in vivo mouse skin. *Biomedical Optics Express*, 6(1):72–85.

[Jang et al., 2014] Jang, M., Ruan, H., Zhou, H., Judkewitz, B., and Yang, C. (2014). Method for auto-alignment of digital optical phase conjugation systems based on digital propagation. *Optics Express*, 22(12):14054–14071.

[Jang et al., 2017] Jang, M., Yang, C., and Vellekoop, I. M. (2017). Optical Phase Conjugation with Less Than a Photon per Degree of Freedom. *Physical Review Letters*, 118(9):093902.

[Ji, 2017] Ji, N. (2017). Adaptive optical fluorescence microscopy. *Nature Methods*, 14(4):374–380.

[Ji et al., 2012] Ji, N., Sato, T. R., and Betzig, E. (2012). Characterization and adaptive optical correction of aberrations during in vivo imaging in the mouse cortex. *Proceedings of the National Academy of Sciences*, 109(1):22–27.

[Johnson et al., 2003] Johnson, P. M., Imhof, A., Bret, B. P. J., Rivas, J. G., and Lagendijk, A. (2003). Time-resolved pulse propagation in a strongly scattering material. *Physical Review E*, 68(1):016604.

[Judkewitz et al., 2015] Judkewitz, B., Horstmeyer, R., Vellekoop, I. M., Papadopoulos, I. N., and Yang, C. (2015). Translation correlations in anisotropically scattering media. *Nature Physics*, 11(8):684–689.

[Judkewitz et al., 2013] Judkewitz, B., Wang, Y. M., Horstmeyer, R., Mathy, A., and Yang, C. (2013). Speckle-scale focusing in the diffusive regime with time reversal of variance-encoded light (TROVE). *Nature Photonics*, 7(4):300–305.

[Kang et al., 2015] Kang, S., Jeong, S., Choi, W., Ko, H., Yang, T. D., Joo, J. H., Lee, J.-S., Lim, Y.-S., Park, Q.-H., and Choi, W. (2015). Imaging deep within a scattering medium using collective accumulation of single-scattered waves. *Nature Photonics*, advance online publication.

[Katz et al., 2014a] Katz, O., Heidmann, P., Fink, M., and Gigan, S. (2014a). Non-invasive single-shot imaging through scattering layers and around corners via speckle correlations. *Nature Photonics*, 8(10):784–790.

[Katz et al., 2011] Katz, O., Small, E., Bromberg, Y., and Silberberg, Y. (2011). Focusing and compression of ultrashort pulses through scattering media. *Nature Photonics*, 5(6):372–377.

[Katz et al., 2014b] Katz, O., Small, E., Guan, Y., and Silberberg, Y. (2014b). Noninvasive nonlinear focusing and imaging through strongly scattering turbid layers. *Optica*, 1(3):170–174.

[Katz et al., 2012] Katz, O., Small, E., and Silberberg, Y. (2012). Looking around corners and through thin turbid layers in real time with scattered incoherent light. *Nature Photonics*, 6(8):549–553.

[Kim et al., 2012] Kim, M., Choi, Y., Yoon, C., Choi, W., Kim, J., Park, Q.-H., and Choi, W. (2012). Maximal energy transport through disordered media with the implementation of transmission eigenchannels. *Nature Photonics*, 6(9):581–585.

[Kner et al., 2009] Kner, P., Chhun, B. B., Griffis, E. R., Winoto, L., and Gustafsson, M. G. L. (2009). Super-resolution video microscopy of live cells by structured illumination. *Nature Methods*, 6(5):339–342.

[Konforti et al., 1988] Konforti, N., Wu, S.-T., and Marom, E. (1988). Phase-only modulation with twisted nematic liquid-crystal spatial light modulators. *Optics Letters*, 13(3):251–253.

[Krausz and Ivanov, 2009] Krausz, F. and Ivanov, M. (2009). Attosecond physics. *Reviews of Modern Physics*, 81(1):163–234.

[Lagendijk et al., 2009] Lagendijk, A., Tiggelen, B. v., and Wiersma, D. S. (2009). Fifty years of Anderson localization. *Physics Today*, 62(8):24–29.

[Lagendijk and van Tiggelen, 1996] Lagendijk, A. and van Tiggelen, B. A. (1996). Resonant multiple scattering of light. *Physics Reports*, 270(3):143–215.

[Leith and Upatnieks, 1966] Leith, E. N. and Upatnieks, J. (1966). Holographic Imagery Through Diffusing Media. *JOSA*, 56(4):523–523.

[Lemoult et al., 2009] Lemoult, F., Lerosey, G., de Rosny, J., and Fink, M. (2009). Manipulating Spatiotemporal Degrees of Freedom of Waves in Random Media. *Physical Review Letters*, 103(17):173902.

[Leonardo and Bianchi, 2011] Leonardo, R. D. and Bianchi, S. (2011). Hologram transmission through multi-mode optical fibers. *Optics Express*, 19(1):247–254.

[Lepetit et al., 1995] Lepetit, L., Chériaux, G., and Joffre, M. (1995). Linear techniques of phase measurement by femtosecond spectral interferometry for applications in spectroscopy. *Journal of the Optical Society of America B*, 12(12):2467.

[Lerosey et al., 2007] Lerosey, G., Rosny, J. d., Tourin, A., and Fink, M. (2007). Focusing Beyond the Diffraction Limit with Far-Field Time Reversal. *Science*, 315(5815):1120–1122.

[Liu et al., 2015] Liu, Y., Lai, P., Ma, C., Xu, X., Grabar, A. A., and Wang, L. V. (2015). Optical focusing deep inside dynamic scattering media with near-infrared time-reversed ultrasonically encoded (TRUE) light. *Nature Communications*, 6:5904.

[Liu et al., 2017] Liu, Y., Ma, C., Shen, Y., Shi, J., and Wang, L. V. (2017). Focusing light inside dynamic scattering media with millisecond digital optical phase conjugation. *Optica*, 4(2):280–288.

[Lueder, 2010] Lueder, E. (2010). *Liquid Crystal Displays: Addressing Schemes and Electro-Optical Effects*. John Wiley & Sons.

[Macfaden and Wilkinson, 2017] Macfaden, A. J. and Wilkinson, T. D. (2017). Characterization, design, and optimization of a two-pass twisted nematic liquid crystal spatial light modulator system for arbitrary complex modulation. *JOSA A*, 34(2):161–170.

[Marčenko and Pastur, 1967] Marčenko, V. A. and Pastur, L. A. (1967). Distribution of eigenvalues for some sets of random matrices. *Mathematics of the USSR-Sbornik*, 1(4):457.

[Martinez et al., 2017] Martinez, J. L., Fernandez, E. J., Prieto, P. M., and Artal, P. (2017). Chromatic aberration control with liquid crystal spatial phase modulators. *Optics Express*, 25(9):9793–9801.

[Matthews et al., 2011] Matthews, T. E., Piletic, I. R., Selim, M. A., Simpson, M. J., and Warren, W. S. (2011). Pump-Probe Imaging Differentiates Melanoma from Melanocytic Nevi. *Science Translational Medicine*, 3(71):71ra15–71ra15.

[Maurer et al., 2011] Maurer, C., Jesacher, A., Bernet, S., and Ritsch-Marte, M. (2011). What spatial light modulators can do for optical microscopy. *Laser & Photonics Reviews*, 5(1):81–101.

[McCabe et al., 2011] McCabe, D. J., Tajalli, A., Austin, D. R., Bondareff, P., Walmsley, I. A., Gigan, S., and Chatel, B. (2011). Spatio-temporal focusing of an ultrafast pulse through a multiply scattering medium. *Nature Communications*, 2:447.

[McDowell et al., 2010] McDowell, E. J., Cui, M., Vellekoop, I. M., Senekerimyan, V., Yaqoob, Z., and Yang, C. (2010). Turbidity suppression from the ballistic to the diffusive regime in biological tissues using optical phase conjugation. *Journal of Biomedical Optics*, 15(2):025004–025004–11.

[Merali, 2015] Merali, Z. (2015). Optics: Super vision. *Nature News*, 518(7538):158.

[Meshulach and Silberberg, 1998] Meshulach, D. and Silberberg, Y. (1998). Coherent quantum control of two-photon transitions by a femtosecond laser pulse. *Nature*, 396(6708):239–242.

[Meshulach and Silberberg, 1999] Meshulach, D. and Silberberg, Y. (1999). Coherent quantum control of multiphoton transitions by shaped ultrashort optical pulses. *Physical Review A*, 60(2):1287–1292.

[Mie, 1908] Mie, G. (1908). Beiträge zur Optik trüber Medien, speziell kolloidaler Metallösungen. *Annalen der Physik*, 330(3):377–445.

[Monmayrant et al., 2010] Monmayrant, A., Weber, S., and Chatel, B. (2010). A newcomer's guide to ultrashort pulse shaping and characterization. *Journal of Physics B: Atomic, Molecular and Optical Physics*, 43(10):103001.

[Morales-Delgado et al., 2015] Morales-Delgado, E. E., Farahi, S., Papadopoulos, I. N., Psaltis, D., and Moser, C. (2015). Delivery of focused short pulses through a multimode fiber. *Optics Express*, 23(7):9109.

[Mosk et al., 2012] Mosk, A. P., Lagendijk, A., Lerosey, G., and Fink, M. (2012). Controlling waves in space and time for imaging and focusing in complex media. *Nature Photonics*, 6(5):283–292.

[Moulton, 1986] Moulton, P. F. (1986). Spectroscopic and laser characteristics of Ti:Al_2O_3. *JOSA B*, 3(1):125–133.

[Mounaix et al., 2017] Mounaix, M., Aguiar, H. B. d., and Gigan, S. (2017). Temporal recompression through a scattering medium via a broadband transmission matrix. *Optica*, 4(10):1289–1292.

[Mounaix et al., 2016a] Mounaix, M., Andreoli, D., Defienne, H., Volpe, G., Katz, O., Grésillon, S., and Gigan, S. (2016a). Spatiotemporal Coherent Control of Light through a Multiple Scattering Medium with the Multispectral Transmission Matrix. *Physical Review Letters*, 116(25):253901.

[Mounaix et al., 2016b] Mounaix, M., Defienne, H., and Gigan, S. (2016b). Deterministic light focusing in space and time through multiple scattering media with a time-resolved transmission matrix approach. *Physical Review A*, 94(4):041802.

[Müller et al., 1998] Müller, Squier, Wolleschensky, Simon, and Brakenhoff (1998). Dispersion pre-compensation of 15 femtosecond optical pulses for high-numerical-aperture objectives. *Journal of Microscopy*, 191(2):141–150.

[Noll, 1976] Noll, R. J. (1976). Zernike polynomials and atmospheric turbulence*. *JOSA*, 66(3):207–211.

[Ntziachristos, 2010] Ntziachristos, V. (2010). Going deeper than microscopy: the optical imaging frontier in biology. *Nature Methods*, 7(8):603–614.

[Ojambati et al., 2016] Ojambati, O. S., Hosmer-Quint, J. T., Gorter, K.-J., Mosk, A. P., and Vos, W. L. (2016). Controlling the intensity of light in large areas at the interfaces of a scattering medium. *Physical Review A*, 94(4):043834.

[Osnabrugge et al., 2017] Osnabrugge, G., Horstmeyer, R., Papadopoulos, I. N., Judkewitz, B., and Vellekoop, I. M. (2017). Generalized optical memory effect. *Optica*, 4(8):886–892.

[Ouzounov et al., 2017] Ouzounov, D. G., Wang, T., Wang, M., Feng, D. D., Horton, N. G., Cruz-Hernández, J. C., Cheng, Y.-T., Reimer, J., Tolias, A. S., Nishimura, N., and Xu, C. (2017). In vivo three-photon imaging of activity of GCaMP6-labeled neurons deep in intact mouse brain. *Nature Methods*, 14(4):388–390.

[Padgett and Bowman, 2011] Padgett, M. and Bowman, R. (2011). Tweezers with a twist. *Nature Photonics*, 5(6):343–348.

[Papadopoulos et al., 2012] Papadopoulos, I. N., Farahi, S., Moser, C., and Psaltis, D. (2012). Focusing and scanning light through a multimode optical fiber using digital phase conjugation. *Optics Express*, 20(10):10583–10590.

[Patterson et al., 1989] Patterson, M. S., Chance, B., and Wilson, B. C. (1989). Time resolved reflectance and transmittance for the noninvasive measurement of tissue optical properties. *Applied Optics*, 28(12):2331–2336.

[Paudel et al., 2013] Paudel, H. P., Stockbridge, C., Mertz, J., and Bifano, T. (2013). Focusing polychromatic light through strongly scattering media. *Optics Express*, 21(14):17299–17308.

[Pesce et al., 2015] Pesce, G., Volpe, G., Maragó, O. M., Jones, P. H., Gigan, S., Sasso, A., and Volpe, G. (2015). Step-by-step guide to the realization of advanced optical tweezers. *Journal of the Optical Society of America B*, 32(5):B84.

[Pierrat et al., 2014] Pierrat, R., Ambichl, P., Gigan, S., Haber, A., Carminati, R., and Rotter, S. (2014). Invariance property of wave scattering through disordered media. *Proceedings of the National Academy of Sciences*, 111(50):17765–17770.

[Platt and Shack, 2001] Platt, B. C. and Shack, R. (2001). History and Principles of Shack-Hartmann Wavefront Sensing. *Journal of Refractive Surgery*, 17(5):S573–S577.

[Plöschner et al., 2015] Plöschner, M., Tyc, T., and Čižmár, T. (2015). Seeing through chaos in multimode fibres. *Nature Photonics*, 9(8):529–535.

[Popoff et al., 2010a] Popoff, S., Lerosey, G., Fink, M., Boccara, A. C., and Gigan, S. (2010a). Image transmission through an opaque material. *Nature Communications*, 1:81.

[Popoff et al., 2011a] Popoff, S. M., Aubry, A., Lerosey, G., Fink, M., Boccara, A. C., and Gigan, S. (2011a). Exploiting the Time-Reversal Operator for Adaptive Optics, Selective Focusing, and Scattering Pattern Analysis. *Physical Review Letters*, 107(26):263901.

[Popoff et al., 2014] Popoff, S. M., Goetschy, A., Liew, S. F., Stone, A. D., and Cao, H. (2014). Coherent Control of Total Transmission of Light through Disordered Media. *Physical Review Letters*, 112(13):133903.

[Popoff et al., 2010b] Popoff, S. M., Lerosey, G., Carminati, R., Fink, M., Boccara, A. C., and Gigan, S. (2010b). Measuring the Transmission Matrix in Optics: An Approach to the Study and Control of Light Propagation in Disordered Media. *Physical Review Letters*, 104(10):100601.

[Popoff et al., 2011b] Popoff, S. M., Lerosey, G., Fink, M., Boccara, A. C., and Gigan, S. (2011b). Controlling light through optical disordered media: transmission matrix approach. *New Journal of Physics*, 13(12):123021.

[Prada and Fink, 1994] Prada, C. and Fink, M. (1994). Eigenmodes of the time reversal operator: A solution to selective focusing in multiple-target media. *Wave Motion*, 20(2):151–163.

[Prada et al., 1996] Prada, C., Manneville, S., Spoliansky, D., and Fink, M. (1996). Decomposition of the time reversal operator: Detection and selective focusing on two scatterers. *The Journal of the Acoustical Society of America*, 99(4):2067–2076.

[Psaltis and Papadopoulos, 2012] Psaltis, D. and Papadopoulos, I. N. (2012). Imaging: The fog clears. *Nature*, 491(7423):197–198.

[Putten et al., 2008] Putten, E. G. v., Vellekoop, I. M., and Mosk, A. P. (2008). Spatial amplitude and phase modulation using commercial twisted nematic LCDs. *Applied Optics*, 47(12):2076–2081.

[Rahimi-Keshari et al., 2013] Rahimi-Keshari, S., Broome, M. A., Fickler, R., Fedrizzi, A., Ralph, T. C., and White, A. G. (2013). Direct characterization of linear-optical networks. *Optics Express*, 21(11):13450–13458.

[Redding et al., 2013] Redding, B., Liew, S. F., Sarma, R., and Cao, H. (2013). Compact spectrometer based on a disordered photonic chip. *Nature Photonics*, 7(9):746–751.

[Roddier, 1999] Roddier, F. (1999). *Adaptive Optics in Astronomy*. Cambridge University Press.

[Rotter and Gigan, 2017] Rotter, S. and Gigan, S. (2017). Light fields in complex media: Mesoscopic scattering meets wave control. *Reviews of Modern Physics*, 89(1):015005.

[Sansone et al., 2006] Sansone, G., Benedetti, E., Calegari, F., Vozzi, C., Avaldi, L., Flammini, R., Poletto, L., Villoresi, P., Altucci, C., Velotta, R., Stagira, S., De Silvestri, S., and Nisoli, M. (2006). Isolated Single-Cycle Attosecond Pulses. *Science*, 314(5798):443–446.

[Sapienza et al., 2011] Sapienza, R., Bondareff, P., Pierrat, R., Habert, B., Carminati, R., and van Hulst, N. F. (2011). Long-Tail Statistics of the Purcell Factor in Disordered Media Driven by Near-Field Interactions. *Physical Review Letters*, 106(16):163902.

[Sapienza et al., 2007] Sapienza, R., García, P. D., Bertolotti, J., Martín, M. D., Blanco, Á., Viña, L., López, C., and Wiersma, D. S. (2007). Observation of Resonant Behavior in the Energy Velocity of Diffused Light. *Physical Review Letters*, 99(23):233902.

[Sardesai et al., 1998] Sardesai, H., Chang, C.-C., and Weiner, A. (1998). A femtosecond code-division multiple-access communication system test bed. *Journal of Lightwave Technology*, 16(11):1953–1964.

[Sarma et al., 2016] Sarma, R., Yamilov, A. G., Petrenko, S., Bromberg, Y., and Cao, H. (2016). Control of Energy Density inside a Disordered Medium by Coupling to Open or Closed Channels. *Physical Review Letters*, 117(8):086803.

[Savage, 2009] Savage, N. (2009). Digital spatial light modulators. *Nature Photonics*, 3(3):170–172.

[Scheffold and Maret, 1998] Scheffold, F. and Maret, G. (1998). Universal Conductance Fluctuations of Light. *Physical Review Letters*, 81(26):5800–5803.

[Schott et al., 2015] Schott, S., Bertolotti, J., Léger, J.-F., Bourdieu, L., and Gigan, S. (2015). Characterization of the angular memory effect of scattered light in biological tissues. *Optics Express*, 23(10):13505–13516.

[Segev et al., 2013] Segev, M., Silberberg, Y., and Christodoulides, D. N. (2013). Anderson localization of light. *Nature Photonics*, 7(3):197–204.

[Serabyn et al., 2010] Serabyn, E., Mawet, D., and Burruss, R. (2010). An image of an exoplanet separated by two diffraction beamwidths from a star. *Nature*, 464(7291):1018–1020.

[Shapiro, 1986] Shapiro, B. (1986). Large Intensity Fluctuations for Wave Propagation in Random Media. *Physical Review Letters*, 57(17):2168–2171.

[Shapiro, 1999] Shapiro, B. (1999). New Type of Intensity Correlation in Random Media. *Physical Review Letters*, 83(23):4733–4735.

[Shen et al., 2016] Shen, Y., Liu, Y., Ma, C., and Wang, L. V. (2016). Focusing light through biological tissue and tissue-mimicking phantoms up to 9.6 cm in thickness with digital optical phase conjugation. *Journal of Biomedical Optics*, 21(8):085001–085001.

[Shi et al., 2015] Shi, Z., Davy, M., and Genack, A. Z. (2015). Statistics and control of waves in disordered media. *Optics Express*, 23(9):12293–12320.

[Shi and Genack, 2012] Shi, Z. and Genack, A. Z. (2012). Transmission Eigenvalues and the Bare Conductance in the Crossover to Anderson Localization. *Physical Review Letters*, 108(4):043901.

[Shi and Genack, 2015] Shi, Z. and Genack, A. Z. (2015). Dynamic and spectral properties of transmission eigenchannels in random media. *Physical Review B*, 92(18):184202.

[Silberberg, 2009] Silberberg, Y. (2009). Quantum Coherent Control for Nonlinear Spectroscopy and Microscopy. *Annual Review of Physical Chemistry*, 60(1):277–292.

[Sinefeld et al., 2015] Sinefeld, D., Paudel, H. P., Ouzounov, D. G., Bifano, T. G., and Xu, C. (2015). Adaptive optics in multiphoton microscopy: comparison of two, three and four photon fluorescence. *Optics Express*, 23(24):31472–31483.

[Skipetrov and Goetschy, 2011] Skipetrov, S. E. and Goetschy, A. (2011). Eigenvalue distributions of large Euclidean random matrices for waves in random media. *Journal of Physics A: Mathematical and Theoretical*, 44(6):065102.

[Small et al., 2012] Small, E., Katz, O., Guan, Y., and Silberberg, Y. (2012). Spectral control of broadband light through random media by wavefront shaping. *Optics Letters*, 37(16):3429–3431.

[Stöckmann, 2006] Stöckmann, H.-J. (2006). *Quantum Chaos: An Introduction*. Cambridge University Press.

[Strudley et al., 2013] Strudley, T., Zehender, T., Blejean, C., Bakkers, E. P. A. M., and Muskens, O. L. (2013). Mesoscopic light transport by very strong collective multiple scattering in nanowire mats. *Nature Photonics*, 7(5):413–418.

[Tajalli et al., 2012] Tajalli, A., McCabe, D. J., Austin, D. R., Walmsley, I. A., and Chatel, B. (2012). Characterization of the femtosecond speckle field of a multiply scattering medium via spatio-spectral interferometry. *JOSA B*, 29(6):1146–1151.

[Tang et al., 2012] Tang, J., Germain, R. N., and Cui, M. (2012). Superpenetration optical microscopy by iterative multiphoton adaptive compensation technique. *Proceedings of the National Academy of Sciences*, 109(22):8434–8439.

[Tanter et al., 2000] Tanter, M., Thomas, J.-L., and Fink, M. (2000). Time reversal and the inverse filter. *The Journal of the Acoustical Society of America*, 108(1):223–234.

[Tao et al., 2015] Tao, X., Bodington, D., Reinig, M., and Kubby, J. (2015). High-speed scanning interferometric focusing by fast measurement of binary transmission matrix for channel demixing. *Optics Express*, 23(11):14168–14187.

[Thompson et al., 1997] Thompson, C. A., Webb, K. J., and Weiner, A. M. (1997). Diffusive media characterization with laser speckle. *Applied Optics*, 36(16):3726.

[Thouless, 1977] Thouless, D. J. (1977). Maximum Metallic Resistance in Thin Wires. *Physical Review Letters*, 39(18):1167–1169.

[Tikhonov, 1963] Tikhonov, A. (1963). Solution of Incorrectly Formulated Problems and the Regularization Method. *Soviet Math. Dokl.*, 5:1035/1038.

[Tomita and Matsumoto, 1995] Tomita, M. and Matsumoto, T. (1995). Observation and formulation of two-dimensional speckle in the space and the time domains. *JOSA B*, 12(1):170–174.

[Trebino et al., 1997] Trebino, R., DeLong, K. W., Fittinghoff, D. N., Sweetser, J. N., Krumbügel, M. A., Richman, B. A., and Kane, D. J. (1997). Measuring ultrashort laser pulses in the time-frequency domain using frequency-resolved optical gating. *Review of Scientific Instruments*, 68(9):3277–3295.

[Tripathi et al., 2012] Tripathi, S., Paxman, R., Bifano, T., and Toussaint, K. C. (2012). Vector transmission matrix for the polarization behavior of light propagation in highly scattering media. *Optics Express*, 20(14):16067–16076.

[Tripathi and Toussaint, 2013] Tripathi, S. and Toussaint, K. C. (2013). Quantitative control over the intensity and phase of light transmitted through highly scattering media. *Optics Express*, 21(22):25890–25900.

[Tyson, 2015] Tyson, R. K. (2015). *Principles of Adaptive Optics, Fourth Edition.* CRC Press.

[van Albada et al., 1991] van Albada, M. P., van Tiggelen, B. A., Lagendijk, A., and Tip, A. (1991). Speed of propagation of classical waves in strongly scattering media. *Physical Review Letters*, 66(24):3132–3135.

[van Beijnum et al., 2011] van Beijnum, F., van Putten, E. G., Lagendijk, A., and Mosk, A. P. (2011). Frequency bandwidth of light focused through turbid media. *Optics Letters*, 36(3):373.

[van Putten et al., 2011] van Putten, E. G., Akbulut, D., Bertolotti, J., Vos, W. L., Lagendijk, A., and Mosk, A. P. (2011). Scattering Lens Resolves Sub-100 nm Structures with Visible Light. *Physical Review Letters*, 106(19):193905.

[van Rossum and Nieuwenhuizen, 1999] van Rossum, M. C. W. and Nieuwenhuizen, T. M. (1999). Multiple scattering of classical waves: microscopy, mesoscopy, and diffusion. *Reviews of Modern Physics*, 71(1):313–371.

[Vellekoop, 2015] Vellekoop, I. M. (2015). Feedback-based wavefront shaping. *Optics Express*, 23(9):12189–12206.

[Vellekoop and Aegerter, 2010] Vellekoop, I. M. and Aegerter, C. M. (2010). Scattered light fluorescence microscopy: imaging through turbid layers. *Optics Letters*, 35(8):1245–1247.

[Vellekoop et al., 2012] Vellekoop, I. M., Cui, M., and Yang, C. (2012). Digital optical phase conjugation of fluorescence in turbid tissue. *Applied Physics Letters*, 101(8):081108.

[Vellekoop et al., 2010] Vellekoop, I. M., Lagendijk, A., and Mosk, A. P. (2010). Exploiting disorder for perfect focusing. *Nature Photonics*, 4(5):320–322.

[Vellekoop and Mosk, 2007] Vellekoop, I. M. and Mosk, A. P. (2007). Focusing coherent light through opaque strongly scattering media. *Optics Letters*, 32(16):2309–2311.

[Vellekoop and Mosk, 2008a] Vellekoop, I. M. and Mosk, A. P. (2008a). Phase control algorithms for focusing light through turbid media. *Optics Communications*, 281(11):3071–3080.

[Vellekoop and Mosk, 2008b] Vellekoop, I. M. and Mosk, A. P. (2008b). Universal Optimal Transmission of Light Through Disordered Materials. *Physical Review Letters*, 101(12):120601.

[Walmsley and Dorrer, 2009] Walmsley, I. A. and Dorrer, C. (2009). Characterization of ultrashort electromagnetic pulses. *Advances in Optics and Photonics*, 1(2):308–437.

[Wang and Genack, 2011] Wang, J. and Genack, A. Z. (2011). Transport through modes in random media. *Nature*, 471(7338):345–348.

[Wang et al., 2014] Wang, K., Milkie, D. E., Saxena, A., Engerer, P., Misgeld, T., Bronner, M. E., Mumm, J., and Betzig, E. (2014). Rapid adaptive optical recovery of optimal resolution over large volumes. *Nature Methods*, 11(6):625–628.

[Weiner and Heritage, 1987] Weiner, A. and Heritage, J. (1987). Picosecond and femtosecond Fourier pulse shape synthesis. *Revue de Physique Appliquée*, 22(12):1619–1628.

[Weiner et al., 1992] Weiner, A., Leaird, D., Patel, J., and Wullert, J. (1992). Programmable shaping of femtosecond optical pulses by use of 128-element liquid crystal phase modulator. *IEEE Journal of Quantum Electronics*, 28(4):908–920.

[Weiner, 2000] Weiner, A. M. (2000). Femtosecond pulse shaping using spatial light modulators. *Review of Scientific Instruments*, 71(5):1929–1960.

[Weiner, 2011] Weiner, A. M. (2011). Ultrafast optics: Focusing through scattering media. *Nature Photonics*, 5(6):332–334.

[Weiner et al., 1988] Weiner, A. M., Heritage, J. P., and Kirschner, E. M. (1988). High-resolution femtosecond pulse shaping. *Journal of the Optical Society of America B*, 5(8):1563.

[Wolf and Maret, 1985] Wolf, P.-E. and Maret, G. (1985). Weak Localization and Coherent Backscattering of Photons in Disordered Media. *Physical Review Letters*, 55(24):2696–2699.

[Wolterink et al., 2016] Wolterink, T. A. W., Uppu, R., Ctistis, G., Vos, W. L., Boller, K.-J., and Pinkse, P. W. H. (2016). Programmable two-photon quantum interference in ${10}^{3}$ channels in opaque scattering media. *Physical Review A*, 93(5):053817.

[Woutersen et al., 1997] Woutersen, S., Emmerichs, U., and Bakker, H. J. (1997). Femtosecond Mid-IR Pump-Probe Spectroscopy of Liquid Water: Evidence for a Two-Component Structure. *Science*, 278(5338):658–660.

[Xiong et al., 2016] Xiong, W., Ambichl, P., Bromberg, Y., Redding, B., Rotter, S., and Cao, H. (2016). Spatiotemporal Control of Light Transmission through a Multimode Fiber with Strong Mode Coupling. *Physical Review Letters*, 117(5):053901.

[Xu et al., 1996] Xu, C., Zipfel, W., Shear, J. B., Williams, R. M., and Webb, W. W. (1996). Multiphoton fluorescence excitation: new spectral windows for biological non-linear microscopy. *Proceedings of the National Academy of Sciences*, 93(20):10763–10768.

[Xu et al., 2011] Xu, X., Liu, H., and Wang, L. V. (2011). Time-reversed ultrasonically encoded optical focusing into scattering media. *Nature Photonics*, 5(3):154–157.

[Yamaguchi and Zhang, 1997] Yamaguchi, I. and Zhang, T. (1997). Phase-shifting digital holography. *Optics Letters*, 22(16):1268–1270.

[Yao and Wang, 2000] Yao, G. and Wang, L. (2000). Propagation of polarized light in turbid media: simulated animation sequences. *Optics Express*, 7(5):198.

[Yaqoob et al., 2008] Yaqoob, Z., Psaltis, D., Feld, M. S., and Yang, C. (2008). Optical phase conjugation for turbidity suppression in biological samples. *Nature Photonics*, 2(2):110–115.

[Yariv, 1976] Yariv, A. (1976). On transmission and recovery of three-dimensional image information in optical waveguides*. *JOSA*, 66(4):301–306.

[Yariv et al., 1979] Yariv, A., Fekete, D., and Pepper, D. M. (1979). Compensation for channel dispersion by nonlinear optical phase conjugation. *Optics Letters*, 4(2):52–54.

[Yılmaz et al., 2013] Yılmaz, H., Vos, W. L., and Mosk, A. P. (2013). Optimal control of light propagation through multiple-scattering media in the presence of noise. *Biomedical Optics Express*, 4(9):1759–1768.

[Yu et al., 2013] Yu, H., Hillman, T. R., Choi, W., Lee, J. O., Feld, M. S., Dasari, R. R., and Park, Y. (2013). Measuring Large Optical Transmission Matrices of Disordered Media. *Physical Review Letters*, 111(15):153902.

[Yu et al., 2017] Yu, H., Lee, K., and Park, Y. (2017). Ultrahigh enhancement of light focusing through disordered media controlled by mega-pixel modes. *Optics Express*, 25(7):8036–8047.

[Zipfel et al., 2003] Zipfel, W. R., Williams, R. M., and Webb, W. W. (2003). Nonlinear magic: multiphoton microscopy in the biosciences. *Nature Biotechnology*, 21(11):1369–1377.